Coggon, R.M., Teagle, D.A.H., Sylvan, J.B., Reece, J., Estes, E.R., Williams, T.J., Christeson, G.L., and the Expedition 390/393 Scientists
Proceedings of the International Ocean Discovery Program Volume 390/393
publications.iodp.org

Site U1557[1]

R.M. Coggon, J.B. Sylvan, E.R. Estes, D.A.H. Teagle, J. Reece, T.J. Williams, G.L. Christeson, M. Aizawa, C. Borrelli, J.D. Bridges, E.J. Carter, J. Dinarès-Turell, J.D. Estep, W.P. Gilhooly III, L.J.C. Grant, M.R. Kaplan, P.D. Kempton, C.M. Lowery, A. McIntyre, C.M. Routledge, A.L. Slagle, M. Takada, L. Tamborrino, Y. Wang, K. Yang, E. Albers, C. Amadori, T.M. Belgrano, T. D'Angelo, N. Doi, A. Evans, G.M. Guérin, M. Harris, V.M. Hojnacki, G. Hong, X. Jin, M. Jonnalagadda, D. Kuwano, J.M. Labonte, A.R. Lam, M. Latas, W. Lu, P. Moal-Darrigade, S.F. Pekar, C. Robustelli Test, J.G. Ryan, D. Santiago Ramos, A. Shchepetkina, A. Villa, S.Y. Wee, S.J. Widlansky, W. Kurz, M. Prakasam, L. Tian, T. Yu, and G. Zhang[2]

[1] Coggon, R.M., Sylvan, J.B., Estes, E.R., Teagle, D.A.H., Reece, J., Williams, T.J., Christeson, G.L., Aizawa, M., Borrelli, C., Bridges, J.D., Carter, E.J., Dinarès-Turell, J., Estep, J.D., Gilhooly, W.P., III, Grant, L.J.C., Kaplan, M.R., Kempton, P.D., Lowery, C.M., McIntyre, A., Routledge, C.M., Slagle, A.L., Takada, M., Tamborrino, L., Wang, Y., Yang, K., Albers, E., Amadori, C., Belgrano, T.M., D'Angelo, T., Doi, N., Evans, A., Guérin, G.M., Harris, M., Hojnacki, V.M., Hong, G., Jin, X., Jonnalagadda, M., Kuwano, D., Labonte, J.M., Lam, A.R., Latas, M., Lu, W., Moal-Darrigade, P., Pekar, S.F., Robustelli Test, C., Ryan, J.G., Santiago Ramos, D., Shchepetkina, A., Villa, A., Wee, S.Y., Widlansky, S.J., Kurz, W., Prakasam, M., Tian, L., Yu, T., and Zhang, G., 2024. Site U1557. In Coggon, R.M., Teagle, D.A.H., Sylvan, J.B., Reece, J., Estes, E.R., Williams, T.J., Christeson, G.L., and the Expedition 390/393 Scientists, South Atlantic Transect. Proceedings of the International Ocean Discovery Program, 390/393: College Station, TX (International Ocean Discovery Program). https://doi.org/10.14379/iodp.proc.390393.105.2024
[2] **Expedition 390/393 Scientists' affiliations.**

Contents

Keywords
International Ocean Discovery Program, IODP, *JOIDES Resolution*, Expedition 390, Expedition 393, Expedition 390C, Expedition 395E, South Atlantic Transect, Biosphere Frontiers, Earth Connections, Mid-Atlantic Ridge, Site U1557

Core descriptions

Supplementary material

References (RIS)

MS 390393-105
Published 23 January 2024

Funded by NSF OCE1326927

1. Background and objectives

Site U1557 (30°56.4651′S, 26°37.7892′W, proposed Site SATL-56A) is in the central South Atlantic Ocean at a water depth of ~5011 meters below sea level (mbsl) ~1243 km west of the Mid-Atlantic Ridge (see Figure **F1** and Tables **T1**, **T2**, all in the Expedition 390/393 summary chapter [Coggon et al., 2024d]) on crust that formed at a slow half spreading rate of ~13.5 mm/y, which is the slowest spreading rate in the study region (Kardell et al., 2019; Christeson et al., 2020) (see Figure **F7** in the Expedition 390/393 summary chapter [Coggon et al., 2024d]; Reece et al., 2016; Reece and Estep, 2019). With an estimated age of 60.7 Ma, Site U1557 is just about the oldest location of the South Atlantic Transect (SAT) campaign (International Ocean Discovery Program [IODP] Expeditions 390C, 395E, 390, and 393). Site U1557 is more heavily sedimented than Site U1556, which is located 6.5 km west of Site U1557 on 61.2 Ma ocean crust. Together, both sites allow for investigation of the effect of sediment thickness on crustal evolution.

1.1. Geologic setting

Site U1557 is located on the approximately east-west–trending (094) Crustal Reflectivity Experiment Southern Transect (CREST) Seismic Line 1A/1B at Common Depth Point 4470 about 5.7 km east of the north-south–trending (358.5) CREST crossing Line 05 (Figures **F1**, **F2**; Reece et al., 2016; Reece and Estep, 2019). Interpretation of multichannel seismic and ocean-bottom seismograph data in this region suggests that the ocean crust is anomalously thin at the site (~3.6 km; Christeson et al., 2020) compared to normal ocean crust (~6.15 ± 0.93 km; Christeson et al., 2019). Reasons for the thin crust could be the proximity to the plume-derived Rio Grande Rise (see Figure **F1** in the Expedition 390/393 summary chapter [Coggon et al., 2024d]) and a potentially reduced magma supply. With a water depth of 5011 m and 564 m of sediment, the basement at Site U1557 is significantly deeper than predicted by simple lithospheric cooling models (see Figure **F4** in the Expedition 390/393 summary chapter [Coggon et al., 2024d]) (e.g., Parsons and Slater, 1977; Korenaga and Korenaga, 2008; Marty and Cazenave, 1989).

Site U1557 is located toward the eastern end of a ~17.5 km wide basin that is filled with sediments to a uniform bathymetric level of ~5000 mbsl (Figure **F1**). The basin sits between two near north-south–trending, strongly faulted basement ridges that have steep flanks and very thin or no

sediment cover (Figures **F1**, **F2A**). Basement topography changes significantly within this basin, resulting in large differences in sedimentary cover. Site U1557 is located in a 2 km wide subbasin including the deepest point of the basin (~565 m) (Figure **F2**). This subbasin is east of the basement ridge on which Sites U1556 and U1561 are located. The north–south crossing line does not pass over Site U1557 directly but runs 5.7 km west of Site U1557 (Figure **F2**).

The ocean crust at Site U1557 has a sediment cover of 564 m, which is thicker than the global average overburden thickness for basement of this age (~200 m; Spinelli et al., 2004) (see Figure **F3** in the Expedition 390/393 summary chapter [Coggon et al., 2024d]) and the reported mean sedi-

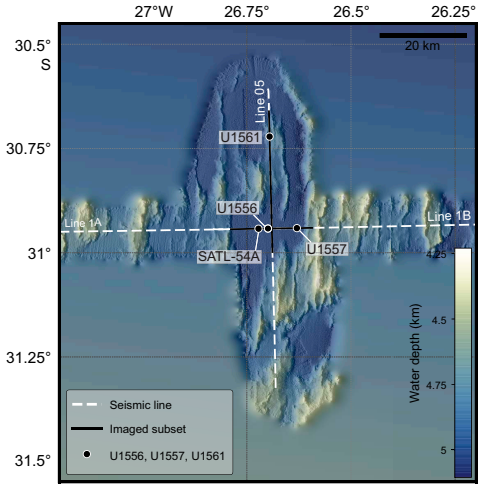

Figure F1. Bathymetric map of ~61 Ma SAT study area showing locations of Sites U1556, U1557, and U1561 and multichannel seismic (MCS) reflection Lines 1A/1B and 05 (Christeson and Reece, 2020). Seismic reflection profiles were acquired during CREST cruise (Reece et al., 2016). Solid black lines = locations of wide-angle MCS profiles for which seismic images are shown in Figure F2.

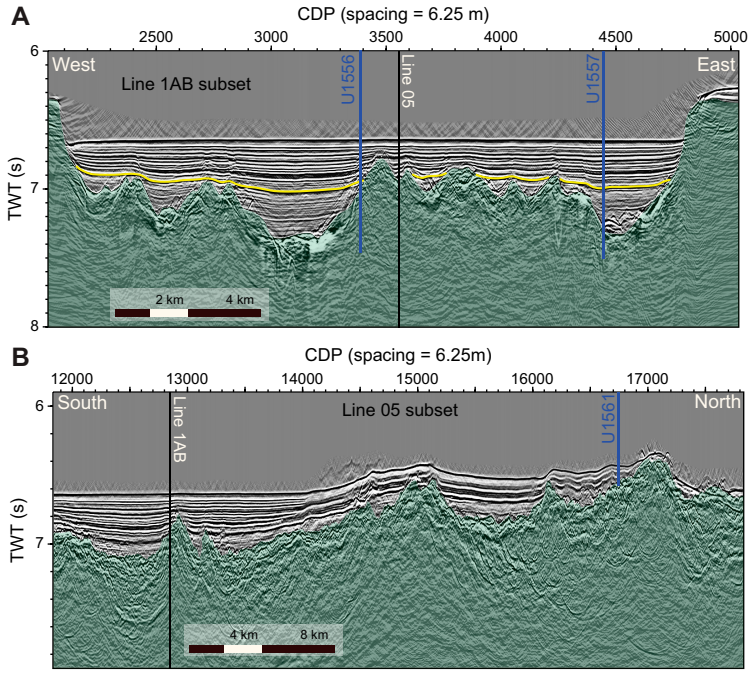

Figure F2. Multichannel seismic (MCS) reflection profiles for SAT sites on ~61 Ma crust showing local basement topography. A. West–east MCS reflection profile CREST Line 1A/1B that crosses CREST Line 05 ~5.7 km south of Site U1561. B. North–south MCS reflection profile CREST Line 05. Black lines = intersections of MCS reflection profiles, blue lines = site locations. CDP = common depth point, TWT = two-way traveltime.

ment thickness encountered along CREST Seismic Lines 1B (48–63 Ma) and 1A (63–70 Ma) of 132 and 223 m, respectively (Estep et al., 2019). This thicker-than-normal sediment cover is due to the location of this site in a deep subbasin. A recent sedimentation thickness global synthesis suggests though that ~60 Ma ocean crust should host around 460 m of sediment (cf. Olson et al., 2016), although there are very large ranges in global and regional estimates of sediment thickness with crustal age (e.g., ~560 m; Straume et al., 2019).

Backscatter reflections from multibeam profiles (Figure **F3**) reveal that a significant proportion of the seafloor in this basin near Site U1557 boasts continuous sediment cover, which is in contrast to other sites along the SAT. Therefore, ventilation of the volcanic rocks of the upper ocean crust through the ingress of seawater and egress of seawater-derived low-temperature hydrothermal fluids may be reduced compared to other sites. However, the relatively steep flanks of the faulted basement ridges and sometimes also crests of the Site U1557 region are unsedimented, as can be seen by the high normalized reflectivity (Figure **F3**) and may influence the local fluid flow system with consequent impacts on heat flow, sediment pore waters, basement hydrothermal alteration, and microbial communities in both the marine sediments and underlying basalts. Basement at Site U1557 was predicted to be ~60.7 Ma based on CREST site survey magnetic data (Kardell et al., 2019) and preliminary biostratigraphy analyses from Hole U1557B sampled during Expedition 390C.

Site U1557 was first occupied during engineering Expeditions 390C and 395E. During Expedition 390C, Hole U1557B was cored using the advanced piston corer (APC) and extended core barrel (XCB) systems to a total depth of 574 meters below seafloor (mbsf), penetrating the entire sediment succession and ~10 m into basement (Figure **F4**; Table **T1**) (see Table **T2** in the Expedition 390/393 summary chapter [Coggon et al., 2024d]; Estes et al., 2021), and Hole U1557D was drilled to 64.2 mbsf. During Expedition 395E, Hole U1557D was deepened to 576.6 mbsf and a reentry system with 10¾ inch casing was installed to 571.6 mbsf (Figure **F5**). In Hole U1557D, the sediment/basement contact was encountered at 566.6 mbsf.

1.2. Objectives

The operational objectives at Site U1557 during Expedition 390 were to (1) core 250 m into basement with the rotary core barrel (RCB) system in Hole U1557D to collect material that addresses the petrologic, geochemical, and microbiological objectives of the SAT expeditions; and (2) collect a comprehensive suite of wireline geophysical logging data through the basement section (Coggon et al., 2022b).

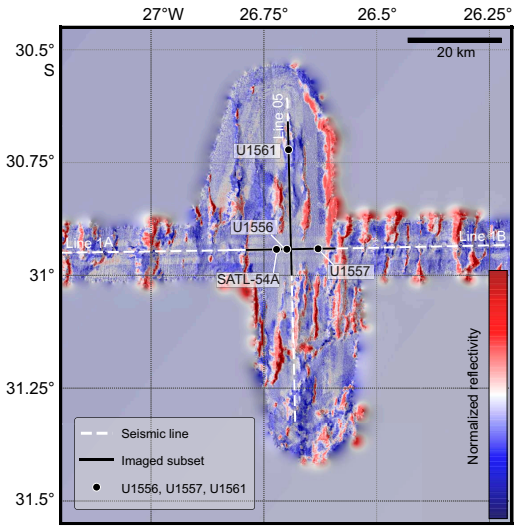

Figure F3. Backscatter reflections from region around Sites U1556, U1557, and U1561 collected during CREST site survey cruise (Reece et al., 2016; Reece and Estep, 2019; Christeson et al., 2020). Red = higher normalized reflectivity values, blue = lower normalized reflectivity values. Solid black lines = locations of wide-angle multichannel seismic profiles for which seismic images are shown in Figure F2.

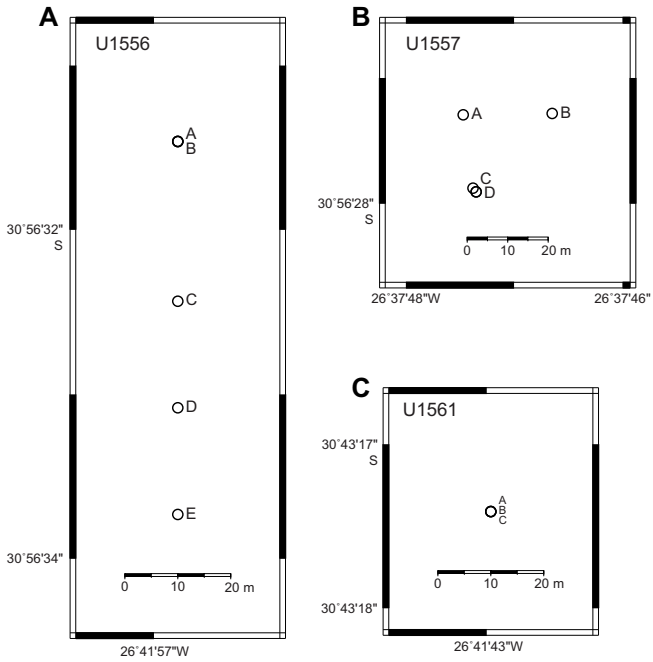

Figure F4. Map of holes drilled at Sites (A) U1556, (B) U1557, and (C) U1561.

2. Operations

Site U1557 was visited during engineering Expeditions 390C and 395E, as well as Expedition 390. Hole U1557A was a missed mudline, but Hole U1557B (Expedition 390C) completed APC/XCB coring through the sediment column to the basement interface. In Hole U1557C, a casing jet-in test was conducted during Expedition 390C that concluded that the casing would need to be drilled in. A reentry system and casing were installed during Expedition 390C, starting Hole U1557D, and the casing was extended into basement during Expedition 395E. During Expedition 390, RCB coring in Hole U1557D cored a 109.1 m interval of basement to 684.7 mbsf, extending to ~120 m into basement (see **Stratigraphic unit summary**). The drill bit was dropped on the seafloor to establish Hole U1557D as a legacy hole for potential future deepening and the installation of a borehole observatory.

2.1. Expeditions 390C and 395E

Site U1557 was first visited during Expedition 390C, an engineering leg with the goal of coring a single hole with the APC and XCB systems to basement for gas safety monitoring and installing a reentry system with casing through sediment to ~5 m into basement (Estes et al., 2021). We opted to replace proposed primary Site SATL-54A with proposed alternate Site SATL-56A because the thinner sediment (estimated to be 510 m at Site SATL-56A instead of 640 m at Site SATL-54A) would allow installation of casing to basement. Stress calculations indicated that casing could only be installed to 600 m without exceeding the safe utilization threshold of the drill pipe, given the water depth. The reentry system and casing installation was planned as two stages. First, the reentry cone and five joints of 16 inch casing would be jetted in to ~60 mbsf. Then, 10¾ inch casing string would be drilled into basement.

After a missed mudline in Hole U1557A, Hole U1557B penetrated to 574.0 mbsf, contacting basement at 564.0 mbsf, with an overall recovery of 414.94 m of sediment as well as the sediment/basement interface (72% recovery; Table **T1**) (Estes et al., 2021). In Hole U1557C, a jet-in test determined that we would not be able to jet in the Dril-Quip reentry system and five joints of 16 inch casing. Instead, the reentry system and 16 inch casing was drilled into Hole U1557D. The casing could not be extended during Expedition 390C because of a subsea camera system failure.

Table T1. Core summary, Site U1557. DRF = drilling depth below rig floor, DSF = drilling depth below seafloor, CSF = core depth below seafloor, CSF-A = core depth below seafloor, Method A. Core type: H = advanced piston corer (APC), R = rotary core barrel (RCB), X = extended core barrel (XCB), numeric core type = drilled interval. ROP = rate of penetration. (Continued on next page.) **Download table in CSV format.**

Hole U1557A
Expedition: 390C
Latitude: 30°56.4549′S
Longitude: 26°37.7912′W
Water depth (m): 5012.28
Date started (UTC): 01 Nov 2020; 0740 h
Date finished (UTC): 01 Nov 2020; 1345 h
Time on hole (days): 0.25
Seafloor depth DRF (m): 5023.4
Seafloor depth est. method: OFFSET
Rig floor to sea level (m): 11.12
Penetration DSF (m): 9.5
Cored interval (m): 9.5
Recovered length (m): 9.63
Recovery (%): 101.37
Drilled interval (m): 0
Drilled interval (*N*): 0
Total cores (*N*): 1
APC cores (*N*): 1

Hole U1557B
Expedition: 390C
Latitude: 30°56.4547′S
Longitude: 26°37.7775′W
Water depth (m): 5012.28
Date started (UTC): 01 Nov 2020; 1345 h
Date finished (UTC): 09 Nov 2020; 0110 h
Time on hole (days): 7.48
Seafloor depth DRF (m): 5023.4
Seafloor depth est. method: APC_CALC
Rig floor to sea level (m): 11.12
Penetration DSF (m): 574
Cored interval (m): 574
Recovered length (m): 414.94
Recovery (%): 72.29
Drilled interval (m): 0
Drilled interval (*N*): 0
Total cores (*N*): 66
APC cores (*N*): 11
XCB cores (*N*): 55

Hole U1557C
Expedition: 390C
Latitude: 30°56.4646′S
Longitude: 26°37.7897′W
Water depth (m): 5012.28
Date started (UTC): 09 Nov 2020; 0110 h
Date finished (UTC): 09 Nov 2020; 1835 h
Time on hole (days): 0.73
Seafloor depth DRF (m): 5023.4
Seafloor depth est. method: OFFSET
Rig floor to sea level (m): 11.12
Penetration DSF (m): 3
Cored interval (m): 0
Recovered length (m): 0
Recovery (%): 0
Drilled interval (m): 3
Drilled interval (*N*): 1
Total cores (*N*): 0

Hole U1557D
Expedition: 390C
Latitude: 30°56.4651′S
Longitude: 26°37.7892′W
Water depth (m): 5010.66
Date started (UTC): 09 Nov 2020; 1835 h
Date finished (UTC): 12 Nov 2020; 0808 h
Time on hole (days): 2.56
Seafloor depth DRF (m): 5021.9
Seafloor depth est. method: TAGGED
Rig floor to sea level (m): 11.24
Penetration DSF (m): 64.2
Cored interval (m): 0
Recovered length (m): 0
Recovery (%): 0
Drilled interval (m): 64.2
Drilled interval (*N*): 1
Total cores (*N*): 0

Hole U1557D
Expedition: 395E
Latitude: 30°56.4651′S
Longitude: 26°37.7892′W
Water depth (m): 5010.66
Date started (UTC): 29 Apr 2021; 2215 h
Date finished (UTC): 05 May 2021; 0630 h
Time on hole (days): 5.34
Seafloor depth DRF (m): 5021.9
Seafloor depth est. method: TAGGED
Rig floor to sea level (m): 11.24
Penetration DSF (m): 576.6
Cored interval (m): 0
Recovered length (m): 0
Recovery (%): 0
Drilled interval (m): 516.6
Drilled interval (*N*): 1
Total cores (*N*): 0

Hole U1557D
Expedition: 390
Latitude: 30°56.4651′S
Longitude: 26°37.7892′W
Water depth (m): 5010.66
Date started (UTC): 11 May 2022; 1330 h
Date finished (UTC): 19 May 2022; 0420 h
Time on hole (days): 7.62
Seafloor depth DRF (m): 5021.9
Seafloor depth est. method: TAGGED
Rig floor to sea level (m): 11.24
Penetration DSF (m): 684.7
Cored interval (m): 109.1
Recovered length (m): 71.28
Recovery (%): 65.33
Drilled interval (m): 575.6
Drilled interval (*N*): 2
Total cores (*N*): 13
RCB cores (*N*): 13

Core, type	Date	Time on deck UTC (h)	Top depth drilled DSF (m)	Bottom depth drilled DSF (m)	Advanced (m)	Top depth cored CSF (m)	Bottom depth recovered CSF-A (m)	Recovered length (m)	Curated length (m)	Recovery (%)	Sections (*N*)	Real ROP (m/h)
390C-U1557A-												
1H	01 Nov 2020	1420	0.0	9.5	9.5	0.0	9.63	9.63	9.63	101	8	0.0
390C-U1557B-												
1H	01 Nov 2020	1545	0.0	4.1	4.1	0.0	4.07	4.07	4.07	99	4	8.0
2H	01 Nov 2020	1720	4.1	13.6	9.5	4.1	10.54	6.44	6.44	68	6	114.0
3H	01 Nov 2020	1840	13.6	23.1	9.5	13.6	17.68	4.08	4.08	43	5	114.0
4H	01 Nov 2020	2005	23.1	32.6	9.5	23.1	32.84	9.74	9.74	103	8	114.0
5H	01 Nov 2020	2120	32.6	42.1	9.5	32.6	41.62	9.02	9.02	95	7	114.0
6H	01 Nov 2020	2235	42.1	51.6	9.5	42.1	51.91	9.81	9.81	103	8	114.0
7H	02 Nov 2020	0010	51.6	61.1	9.5	51.6	60.63	9.03	9.03	95	8	114.0
8H	02 Nov 2020	0125	61.1	70.6	9.5	61.1	70.92	9.82	9.82	103	8	114.0
9H	02 Nov 2020	0240	70.6	80.1	9.5	70.6	80.43	9.83	9.83	103	8	114.0
10H	02 Nov 2020	0415	80.1	89.6	9.5	80.1	89.90	9.80	9.80	103	8	114.0
11H	02 Nov 2020	0715	89.6	99.1	9.5	89.6	98.91	9.31	9.31	98	8	6.0
12X	02 Nov 2020	0940	99.1	104.1	5.0	99.1	99.90	0.80	0.80	16	2	15.0
13X	02 Nov 2020	1125	104.1	113.7	9.6	104.1	113.73	9.63	9.63	100	8	16.5
14X	02 Nov 2020	1300	113.7	123.3	9.6	113.7	122.35	8.65	8.65	90	7	16.5
15X	02 Nov 2020	1455	123.3	132.9	9.6	123.3	132.98	9.68	9.68	101	8	16.5
16X	02 Nov 2020	1630	132.9	142.5	9.6	132.9	139.25	6.35	6.35	66	6	19.2
17X	02 Nov 2020	1815	142.5	152.1	9.6	142.5	151.21	8.71	8.71	91	7	16.5
18X	02 Nov 2020	1955	152.1	161.7	9.6	152.1	161.53	9.43	9.43	98	8	19.2
19X	02 Nov 2020	2140	161.7	171.3	9.6	161.7	169.96	8.26	8.26	86	7	19.2
20X	02 Nov 2020	2330	171.3	180.9	9.6	171.3	180.36	9.06	9.06	94	8	16.5
21X	03 Nov 2020	0135	180.9	190.5	9.6	180.9	190.53	9.63	9.63	100	8	12.8
22X	03 Nov 2020	0340	190.5	200.1	9.6	190.5	191.61	1.11	1.11	12	2	11.5
23X	03 Nov 2020	0550	200.1	209.7	9.6	200.1	209.03	8.93	8.93	93	7	14.4
24X	03 Nov 2020	0755	209.7	219.3	9.6	209.7	216.98	7.28	7.28	76	6	16.5

Table T1 (continued).

Core, type	Date	Time on deck UTC (h)	Top depth drilled DSF (m)	Bottom depth drilled DSF (m)	Advanced (m)	Top depth cored CSF (m)	Bottom depth recovered CSF-A (m)	Recovered length (m)	Curated length (m)	Recovery (%)	Sections (*N*)	Real ROP (m/h)
25X	03 Nov 2020	1000	219.3	228.9	9.6	219.3	228.76	9.46	9.46	99	8	19.2
26X	03 Nov 2020	1140	228.9	238.5	9.6	228.9	235.93	7.03	7.03	73	6	16.5
27X	03 Nov 2020	1340	238.5	248.1	9.6	238.5	248.28	9.78	9.78	102	8	11.5
28X	03 Nov 2020	1625	248.1	257.7	9.6	248.1	251.58	3.48	3.48	36	4	11.5
29X	03 Nov 2020	1920	257.7	267.3	9.6	257.7	267.50	9.80	9.80	102	8	9.6
30X	03 Nov 2020	2205	267.3	276.9	9.6	267.3	267.86	0.56	0.56	6	2	9.6
31X	04 Nov 2020	0110	276.9	286.5	9.6	276.9	285.80	8.90	8.90	93	7	12.8
32X	04 Nov 2020	0355	286.5	296.1	9.6	286.5	293.08	6.58	6.58	69	6	11.5
33X	04 Nov 2020	0620	296.1	305.7	9.6	296.1	303.49	7.39	7.39	77	6	19.2
34X	04 Nov 2020	0915	305.7	315.3	9.6	305.7	311.94	6.24	6.24	65	5	16.5
35X	04 Nov 2020	1215	315.3	324.9	9.6	315.3	320.70	5.40	5.40	56	5	10.5
36X	04 Nov 2020	1445	324.9	334.5	9.6	324.9	332.26	7.36	7.36	77	6	14.4
37X	04 Nov 2020	1725	334.5	344.1	9.6	334.5	343.64	9.14	9.14	95	7	14.4
38X	04 Nov 2020	2005	344.1	353.7	9.6	344.1	351.49	7.39	7.39	77	6	11.5
39X	04 Nov 2020	2235	353.7	363.3	9.6	353.7	362.49	8.79	8.79	92	7	11.5
40X	05 Nov 2020	0125	363.3	372.9	9.6	363.3	369.61	6.31	6.31	66	6	10.5
41X	05 Nov 2020	0345	372.9	382.5	9.6	372.9	375.91	3.01	3.01	31	3	19.2
42X	05 Nov 2020	0645	382.5	392.1	9.6	382.5	388.58	6.08	6.08	63	5	14.4
43X	05 Nov 2020	0945	392.1	401.7	9.6	392.1	398.12	6.02	6.02	63	5	16.5
44X	05 Nov 2020	1245	401.7	411.3	9.6	401.7	407.16	5.46	5.46	57	5	10.5
45X	05 Nov 2020	1550	411.3	420.9	9.6	411.3	416.63	5.33	5.33	56	5	8.2
46X	05 Nov 2020	1905	420.9	430.5	9.6	420.9	429.99	9.09	9.09	95	7	6.8
47X	05 Nov 2020	2220	430.5	438.6	8.1	430.5	434.41	3.91	3.91	48	4	5.4
48X	06 Nov 2020	0135	438.6	448.2	9.6	438.6	444.24	5.64	5.64	59	5	7.2
49X	06 Nov 2020	0520	448.2	457.8	9.6	448.2	454.24	6.04	6.04	63	5	5.2
50X	06 Nov 2020	0900	457.8	467.4	9.6	457.8	463.70	5.90	5.90	61	5	6.4
51X	06 Nov 2020	1205	467.4	474.5	7.1	467.4	472.12	4.72	4.72	66	4	7.1
52X	06 Nov 2020	1505	474.5	484.1	9.6	474.5	477.34	2.84	2.84	30	2	10.5
53X	06 Nov 2020	1755	484.1	493.7	9.6	484.1	484.41	0.31	0.31	3	1	9.6
54X	06 Nov 2020	2145	493.7	501.0	7.3	493.7	500.38	6.68	6.68	92	6	4.0
55X	07 Nov 2020	0135	501.0	509.6	8.6	501.0	506.82	5.82	5.82	68	5	4.3
56X	07 Nov 2020	0545	509.6	519.2	9.6	509.6	516.05	6.45	6.45	67	6	4.3
57X	07 Nov 2020	1010	519.2	527.3	8.1	519.2	522.09	2.89	2.89	36	3	4.1
58X	07 Nov 2020	1300	527.3	532.8	5.5	527.3	530.15	2.85	2.85	52	3	6.6
59X	07 Nov 2020	1710	532.8	542.4	9.6	532.8	535.78	2.98	2.98	31	3	5.0
60X	07 Nov 2020	2110	542.4	546.7	4.3	542.4	545.84	3.44	3.44	80	3	2.2
61X	08 Nov 2020	0130	546.7	552.8	6.1	546.7	553.10	6.40	6.40	105	6	3.1
62X	08 Nov 2020	0550	552.8	562.4	9.6	552.8	557.16	4.36	4.36	45	4	5.0
63X	08 Nov 2020	1010	562.4	567.9	5.5	562.4	566.01	3.31	3.61	60	3	2.8
64X	08 Nov 2020	1410	567.9	569.4	1.5	567.9	568.83	0.67	0.93	45	1	0.8
65X	08 Nov 2020	1745	569.4	571.9	2.5	569.4	570.02	0.57	0.62	23	1	1.8
66X	08 Nov 2020	2130	571.9	574.0	2.1	571.9	574.22	2.09	2.32	100	2	1.4
				Hole U1557B totals:	574.00			414.94	415.78	72		
390C-U1557C-												
11	09 Nov 2020	0430	0.0	3.0		*****Drilled from 0.0 to 3.0 mbsf*****					0	1.7
390C-U1557D-												
11	11 Nov 2020	1315	0.0	64.2		*****Drilled from 0.0 to 64.2 mbsf*****					0	24.1
395E-U1557D-												
12	30 Apr 2021	1600	64.2	575.6		*****Drilled from 64.2 to 575.6 mbsf*****					0	17.0
390-U1557D-												
2R	12 May 2022	1725	575.6	581.7	6.1	575.6	577.98	1.98	2.38	32	2	1.5
3R	12 May 2022	2200	581.7	587.4	5.7	581.7	587.67	5.04	5.97	88	5	2.1
4R	13 May 2022	0330	587.4	597.1	9.7	587.4	594.79	6.17	7.39	64	6	2.8
5R	13 May 2022	0920	597.1	606.9	9.8	597.1	603.66	5.54	6.56	57	5	2.5
6R	13 May 2022	1420	606.9	616.6	9.7	606.9	615.07	7.39	8.17	76	6	2.9
7R	13 May 2022	1940	616.6	626.3	9.7	616.6	622.08	4.82	5.48	50	4	2.9
8R	14 May 2022	0215	626.3	636.1	9.8	626.3	632.59	5.30	5.99	54	5	2.1
9R	14 May 2022	0500	636.1	637.1	1.0	636.1	636.97	0.57	0.87	57	1	1.7
10R	16 May 2022	1605	637.1	645.8	8.7	637.1	646.33	8.47	9.23	97	7	1.9
11R	16 May 2022	2330	645.8	655.5	9.7	645.8	649.94	3.67	4.14	38	3	1.8
12R	17 May 2022	0625	655.5	665.3	9.8	655.5	665.09	8.83	9.59	90	9	2.0
13R	17 May 2022	1240	665.3	675.0	9.7	665.3	673.32	6.87	8.02	71	6	2.2
14R	17 May 2022	1940	675.0	684.7	9.7	675.0	682.66	6.63	7.66	68	6	1.9
				Hole U1557D totals:	109.10			71.28	81.45	65		

Expedition 395E returned to Hole U1557D and installed 10¾ inch casing to a depth of 571.6 mbsf, with the hole reaching a depth of 576.6 mbsf (Figure **F5**) (Williams et al., 2021).

2.2. Expedition 390 Hole U1557D

Expedition 390 arrived at Site U1557 on 12 May 2022 after moving over from Site U1556 in dynamic positioning (DP) mode. Pipe was tripped toward the seafloor, stopping twice to fill the drill pipe with water. At 0415 h, the subsea camera system was deployed through the moonpool to guide reentry into Hole U1557D. The Conductivity-Temperature-Depth (CTD) sensor was attached to the subsea camera frame. We located and reentered Hole U1557D at 0653 h, recovered the subsea camera system, and began tripping pipe through the casing to the hole bottom. Core 390-U1557D-2R was the first recovered core in this hole following the two drilled intervals, and it arrived on deck at 1925 h. Coring continued smoothly through Core 8R; Core 9R had advanced only 1 m when it was recovered because of poor weather and drilling conditions. We then pulled out of the hole, with the bit reaching the seafloor at 0930 h on 14 May, and tripped pipe up to 3327 meters below rig floor (mbrf), where we positioned to wait for weather conditions to improve.

Operations resumed at 1800 h on 15 May after waiting on weather for 1.5 days. The subsea camera system was deployed at 2130 h to guide reentry in Hole U1557D, with a successful reentry accomplished at 0246 h on 16 May. With the top drive in, we tripped pipe inside the casing to 637.1 mbsf. The top drive was then set back to replace the wash pipe. After this repair, we continued coring from 637.1 mbsf with Core 390-U1557D-10R. Core 14R was the final core for the site and advanced to 684.7 mbsf; after its recovery, we began tripping out of the hole to drop the bit on the seafloor and reenter for logging. Excluding Cores 2R, 3R, and 9R, all cores were full length. A mud sweep was pumped after every core following Core 5R. Additional mud (50 bbl) was pumped during the final mud sweep to prepare the hole for logging. Penetration rates were <3.0 m/h throughout the hole. In total, coring in Hole U1557D during Expedition 390 advanced 109.1 m and recovered 71.28 m (65%).

The drill pipe cleared the seafloor at 0025 h on 18 May, and the bit was dropped on the seafloor using the mechanical bit release (MBR) at 0220 h. The decision to drop the bit on the seafloor allows future reentry, deepening of the hole, and the potential for installation of a borehole observatory at this site. Subsequent logging operations confirmed Hole U1557D to be stable, with no washouts, further confirming its suitability as a legacy hole for any future operations.

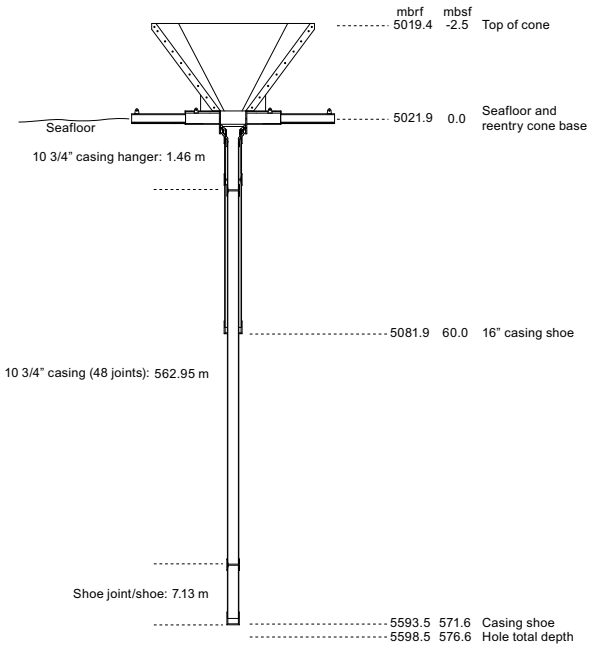

Figure F5. Reentry system, casing, and bottom-hole assembly, Hole U1557.

The subsea camera system was then deployed through the moonpool to guide reentry into Hole U1557D for logging operations. Reentry occurred at 0437 h on 18 May, the subsea camera system was recovered, and the end of the drill pipe was positioned at 30 mbsf. The triple combo tool string, including tools for measuring formation density, resistivity, magnetic susceptibility (MS), and the borehole caliper was deployed at 0919 h and lowered to the hole bottom. Two upward passes covering the basement section of the hole were completed, and then the sediment section of the hole was logged through casing as the tools were pulled back to the surface. We elected to not deploy the other two logging drill strings to recover time lost to weather and to prioritize operations at Site U1559. The tools were back on deck by 1735 h, and we tripped pipe out of the hole and performed a slip and cut of the drilling line before tripping back to the surface. By 0644 h on 19 May, the bottom-hole assembly had been recovered and laid out and the thrusters were raised and secured. The vessel transitioned into cruise mode from DP mode at 0648 h and began the 600 nmi transit to Site U1559. Operations time at Site U1557 totaled 7.6 days during Expedition 390.

3. Stratigraphic unit summary

The cores recovered at Site U1557 comprise two sedimentary units overlying a single basement unit identified on the basis of macro- and microscopic visual observations combined with mineralogical analyses by X-ray diffraction (XRD), spectral color analyses, and MS data. The units are numbered from the top of the hole, with units in the sedimentary section designated by Roman numerals (e.g., I and II) and basement units designated by Arabic numerals (e.g., 1 and 2); subunits are designated with letters (e.g., IA, IIA, 2a, and 2b).

3.1. Sedimentary units

Sediments recovered at Site U1557 from a single core in Hole U1557A and an ~565 m sequence cored to basement in Hole U1557B are a mix of biogenic (predominantly calcareous nannofossils and foraminifera) and siliciclastic (predominantly clay-rich) sediments (Figure **F6**). Lithologic Unit I is composed of ~290 m of Eocene to recent alternating silty clay and nannofossil ooze layers and is divided into five subunits (IA–IE; Table **T2**) based on alternations in the proportions of biogenic carbonates (mostly nannofossil ooze) and siliciclastic sediments (silty clays). Unit II is composed of ~275 m of Paleocene to Eocene nannofossil/calcareous chalk and is also divided into five subunits (IIA–IIE; Table **T2**). In contrast to Unit I, siliciclastic lithologies are absent in Unit II, with the exception of Subunit IIC, which is a distinct ~0.8 m thick interval composed of layers of silty clay and calcareous nannofossil chalk with distinct colors (brown, light brown, and light greenish gray), likely deposited during the Paleocene/Eocene Thermal Maximum (PETM). The other Unit II subunits are defined by differences in sediment color (likely controlled by the abundance of clay minerals), the dominant biogenic components of the lithology, and the sediment age.

3.2. Basement units

The basement rocks cored at Site U1557 are sedimentary breccias that contain a range of basaltic clast types derived predominantly from pillow lavas. Ubiquitous volcanic glass clasts are almost all completely altered with rare fresh glass. Hole U1557B penetrated the sediment/basement interface at 564.77 mbsf, below which 9.5 m of sedimentary breccia was cored. A further ~109 m of sedimentary breccia was cored in Hole U1557D between ~10 and ~120 meters subbasement (msb). Although some variation in clast lithology is observed downhole, systematic variations are not observed, and the entire sequence of rocks recovered is defined as a single lithologic unit (1; Figure **F6**). Unit 1 is divided into three lithologic subunits based on variations in the relative proportions and mineralogy of both the breccia matrix and cement.

3.3. Sediment/basement interface

At Site U1557, the sediment/basement interface was only recovered in Hole U1557B in interval 390C-U1557B-63X-2, 87 cm, at 564.77 m core depth below seafloor, Method B (CSF-B). This interface is defined by the shallowest occurrence of basalt in the hole, comprising a <10 cm interval of basalt rubble (pieces <4 cm in diameter) underlying the nannofossil-rich chalk of Subunit

IIE. The uppermost basement unit (Subunit 1a; 564.77–567.9 mbsf) is a transitional unit that comprises both pelagic sedimentary material and volcanic clasts (see **Igneous petrology**). The pelagic component of these rocks occurs as the matrix between basalt blocks (>10 cm diameter) and is predominantly composed of indurated calcareous sediment that likely formed from a foraminifera-bearing nannofossil chalk lithified through circulation of hydrothermal fluids combined with burial diagenesis.

3.3.1. Sediment/basement interface depth

The sediment/basement interface was not recovered in Hole U1557D because the cased reentry system in this hole was deliberately drilled into basement (see **Operations**). During its installation during engineering Expedition 395E, hard rock was encountered at ~566 mbsf, casing was installed ~5 m into basement, and the drilled interval reached ~10 m into basement. A distinct horizon that shares physical properties characteristics with core-based data was observed in downhole logs through the casing at ~558 m wireline log matched depth below seafloor (WMSF) (see **Physical properties and downhole measurements**).

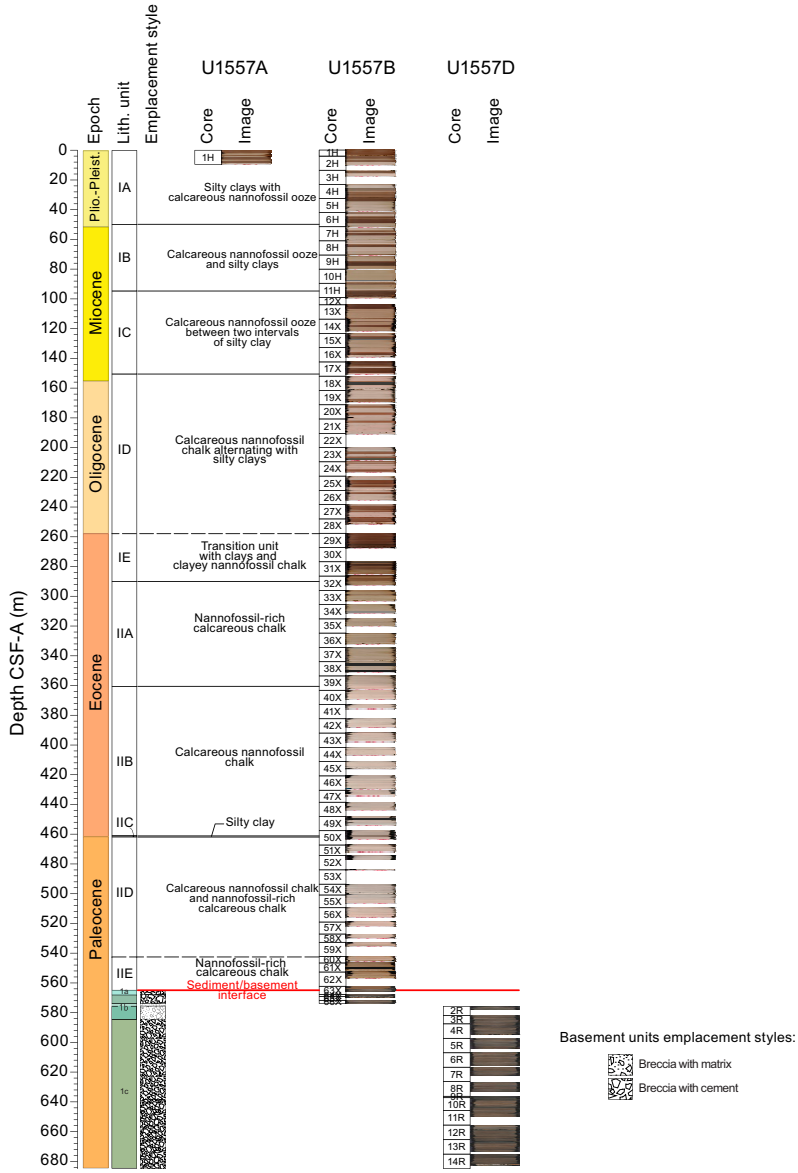

Figure F6. Stratigraphic unit summary, Site U1557. Lith. unit column on left uses unit thicknesses in Holes U1557B (0–574 m CSF-B) and U1557D (575–683 m CSF-B). Chronostratigraphy is based on the biostratigraphy and paleomagnetic stratigraphy of Hole U1557B (0–574 m CSF-B) (see Biostratigraphy and Paleomagnetism).

Table T2. Sedimentary units and subunits, contacts, and thicknesses, Site U1557. There are gaps in recovery between Subunits ID/IE and IID/IIE. **Download table in CSV format.**

Lith. unit	Hole	Depth CSF-B (m)	Thickness (m)	Age	Core, section, interval (cm)	Lithologic summary
	390C-					
IA	U1557A	0–9.63	9.63	Pliocene/Pleistocene	1H-1, 0, to 1H-CC, 13	Silty clays with pinkish white calcareous nannofossil ooze.
	U1557B	0–49.66	49.66		1H-1, 0, to 6H-6, 6.5	
IB	U1557B	49.67–94.55	44.88	Late Miocene to Pliocene	6H-6, 6.5, to 11H-4, 45.3	Calcareous nannofossil ooze and silty clays.
IC	U1557B	94.55–150.38	55.83	mid-Miocene	11H-4, 45.3, to 17X-6, 37	Nannofossil ooze between two relatively thick layers of dark brown silty clays.
ID	U1557B	150.38–251.53	101.15	late Oligocene to mid-Miocene	17X-6, 37, to 28X-CC, 20	Calcareous nannofossil chalk alternating with reddish brown silty clays.
IE	U1557B	257.70–289.84	32.14	early Eocene	29X-1, 0, to 32X-3, 45	Dark brown clays and brown clayey nannofossil chalk.
IIA	U1557B	289.84–360.37	70.53	early Eocene	32X-3, 45, to 39X-6, 65.5	Light brownish gray nannofossil-rich calcareous chalk.
IIB	U1557B	360.37–460.86	100.49	early Eocene	39X-6, 65.5, to 50X-3, 6	Pinkish white calcareous nannofossil chalk.
IIC	U1557B	460.86–461.66	0.80	late Paleocene	50X-3, 6, to 50X-3, 86	PETM light brown silty clay layer.
IID	U1557B	461.66–535.73	74.07	late Paleocene (?)	50X-3, 86, to 59X-CC, 21	Pinkish white/gray calcareous nannofossil chalk; nannofossil-rich calcareous chalk.
IIE	U1557B	542.40–564.77	22.36	early to middle Paleocene?	60X-1, 0, to 63X-2, 86	Yellowish brown nannofossil-rich calcareous chalk.
1a	U1557B	564.80–567.90	9.50	Transition unit	63X-2, 86, to 63X-3, 115	Transition unit.

At many of the SAT sites, there is >10 m of basement topography between closely spaced (20–30 m) holes. For stratigraphic correlation between SAT sites and with other sections of upper ocean crust recovered by scientific ocean drilling, we have therefore defined a site basement/sediment interface depth for each of the SAT sites. For consistency, this is taken as the curated depth of the top of the shallowest occurrence of basalt in the hole with the greatest basement penetration at each site. Because the interface was deliberately not recovered in Hole U1557D, for Site U1557 we define it as the curated depth of the top of the shallowest occurrence of basalt in Hole U1557B (564.77 m CSF-B). This is in good agreement with the depth of the sediment/basement interface in Hole U1557D based on drilling parameters (see **Operations**), indicating minimal basement topography between Holes U1557B and U1557D.

4. Sedimentology

The sediments recovered at Site U1557 mainly come from Hole U1557B, which was cored to basement at 564.76 mbsf. Sediments from Holes U1557A (only 0–9.63 m CSF-B) and U1557B contain of a mix of biogenic (predominantly calcareous nannofossils and foraminifera) and siliciclastic (predominantly clay-rich) sediments (Figure **F7**). Visual core descriptions (VCDs) summarize observations recorded in the shipboard DESClogik program, including assessment of sediment color, grain size, sedimentary structures, bioturbation, and drilling disturbance. Sediment colors reported here are defined according to the Munsell color system (color codes are provided in the VCDs). The color of the sediment primarily reflects its lithologic characteristics; sediments composed mainly of nannofossil and calcareous ooze are generally pinkish white, whereas silty clays range from brown/dark brown where carbonate is absent to reddish brown where the carbonate content is higher (Figure **F11**). Holes U1557A and U1557B were cored in November 2020 during Expedition 390C but were not described until April 2022 during Expedition 390. We observed some differences in color on the digital color images obtained using the Section Half Imaging Logger (SHIL) during Expedition 390C (see **Physical properties and downhole measurements** in the Expedition 390/393 methods chapter [Coggon et al., 2024c]) and the visual color determinations made during Expedition 390, likely reflecting changes such as postcoring drying and/or oxidation of the sediments.

Smear slides (Figure **F10**) and XRD (Figures **F9**, **F14**) were used to confirm lithologic composition. In general, the alternations between nannofossil ooze/chalk and silty clays are well correlated with MS and the luminosity (L*) color reflectance parameter, as well as with natural gamma radiation (NGR) (see **Physical properties and downhole measurements**) (Figure **F7**). The bioturbation

index (see **Sedimentology** in the Expedition 390/393 methods chapter [Coggon et al., 2024c]) ranges from absent to heavy in Holes U1557A and U1557B, but bioturbation is generally sparse throughout Site U1557 sediments.

In addition to the major lithologies (nannofossil ooze/chalk and silty clay), several minor distinct sedimentologic features are observed (Figure **F11**) including greenish white foraminifera layers/lenses, microstructural deformation (faulting and folding), and a unique clay-bearing layer in the long sequence of nannofossil-rich calcareous chalk of Unit II.

Two lithologic sedimentary units and ten subunits are defined at Site U1557 based on a combination of visual observations of sedimentologic characteristics (color, sedimentary structures, bioturbation, and general appearance), microscopic examination of smear slides, and bulk mineralogical analysis by XRD (see **Sedimentology** in the Expedition 390/393 methods chapter [Coggon et al., 2024c]) integrated with MS and color spectral observations (see **Physical properties and downhole measurements** in the Expedition 390/393 methods chapter [Coggon et al., 2024c]). Ages were assigned to each subunit based on micropaleontology results and magnetostratigraphy (see **Age model and mass accumulation rates**).

4.1. Unit descriptions

4.1.1. Unit I

Intervals: 390C-U1557A-1H-1, 0 cm, to 1H-CC, 13 cm; 390C-U1557B-1H-1, 0 cm, to 32X-3, 45 cm
Depths: Hole U1557A = 0–9.63 m CSF-B; Hole U1557B = 0–289.84 m CSF-B
Thickness: Hole U1557A = 9.63 m; Hole U1557B = 289.84 m
Age: Eocene to recent
Lithology: nannofossil ooze/chalk, silty clay

Unit I is composed of 289.84 m of upper Eocene to Pleistocene silty clay and calcareous nannofossil ooze (Figure **F7**). Unit I is divided into five subunits based on alternations between biogenic carbonates (mostly nannofossil ooze) and siliciclastic sediments (silty clays) (Figure **F8**). In detail, the top of Unit I comprises ~50 m of Pliocene–Pleistocene brown silty clays with minor pinkish white nannofossil ooze intervals (Subunit IA). Below this interval, nannofossil oozes are more common but have a different color (light gray), defining Subunit IB (49.67–94.55 m CSF-B; Late Miocene–Pliocene). Two relatively thick intervals (>5 m) of dark brown clays split by a sequence of pinkish gray nannofossil ooze characterize most of the Miocene sediments (Subunit IC; 94.55–150.38 m CSF-B). Below 150.38 m CSF-B, reddish brown silty clays alternate with pink nannofossil chalk for ~56 m, with the color and mineralogy (Figure **F9**) indicative of a partially marly composition of the two major lithologies in this subunit (Subunit ID; Oligocene). Below Subunit ID, unconsolidated oozes turn into moderately consolidated chalks, reflecting diagenetic burial processes. Dark brown to black silty clays and brown clayey nannofossil chalk occur at the bottom of Unit I (Subunit IE; 276.90–289.84 m CSF-B) around the level identified as the Eocene–Oligocene transition (see **Biostratigraphy** and **Age model and mass accumulation rates**).

The lithologic contacts vary between bioturbated, gradational, and planar, with less common sharp or irregular contacts. Centimeter-thick intervals or lenses of greenish white foraminifera-rich nannofossil ooze often occur at the boundaries between silty clays and nannofossil ooze, likely indicative of changes in environmental conditions (selective deposition of foraminifera by bottom currents and/or selective dissolution of the nannofossil shells). The bioturbation index in Unit I ranges from absent to high, although it is most commonly absent or sparse. Drilling disturbance manifests as slight uparching throughout Unit I. Toward the bottom of Unit I, drilling gaps are more common, likely reflecting both the change from the APC system to the XCB system in Core 390C-U1557B-12X (see **Operations**) and/or a change in sediment rheology.

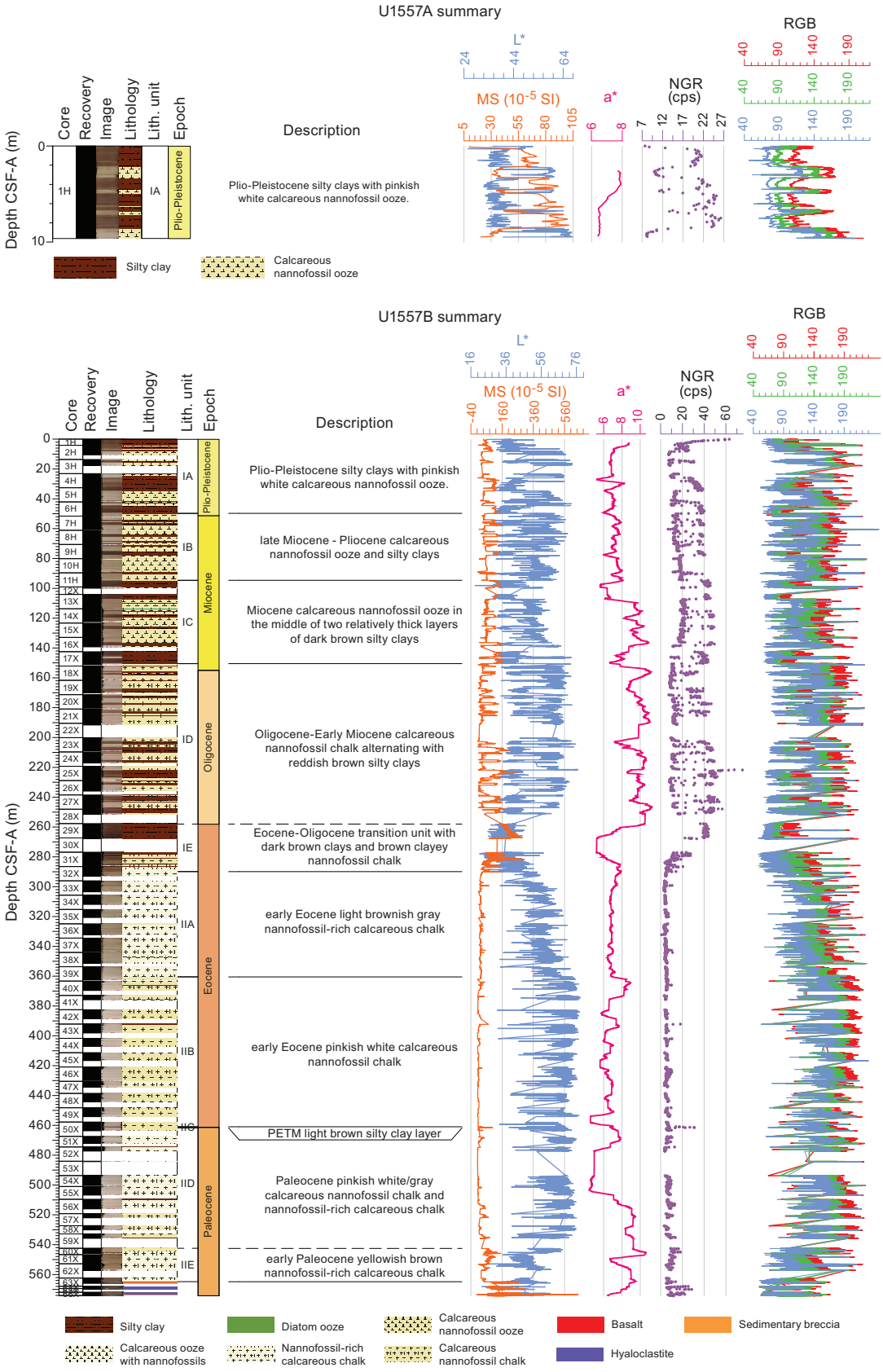

Figure F7. Lithologic summary, Holes (A) U1557A and (B) U1557B. For epochs, see Age model and mass accumulation rates. For physical properties analyses, see Physical properties and downhole measurements. MS = point magnetic susceptibility; a* = red–green value (greater value = redder) smoothed with a 100-point moving average. cps = counts per second. RGB is graphed in machine units.

4.1.1.1. Subunit IA

Intervals: 390C-U1557A-1H-1, 0 cm, to 1H-CC, 13 cm; 390C-U1557B-1H-1, 0 cm, to 6H-6, 6.5 cm
Depths: Hole U1557A = 0–9.63 m CSF-B; Hole U1557B = 0–49.66 m CSF-B
Thickness: Hole U1557A = 9.63 m; Hole U1557B = 49.66 m
Age: Pliocene–Pleistocene
Lithology: silty clays, calcareous nannofossil ooze, diatom-rich biosiliceous ooze

Subunit IA is composed mainly of brown silty clay interrupted by pinkish white calcareous nannofossil ooze intervals. Thin (<4 cm) diatom-rich biosiliceous ooze layers within a silty clay interval occur in Sections 390C-U1557A-1H-1 and 390C-U1557B-1H-1. Diatoms are predominantly concentrated in pale green laminations. Bioturbation is generally sparse throughout Subunit IA. Some organic-rich laminations occur in silty clay intervals in Cores 390C-U1557B-4H through 6H.

The Lithologic Subunit IA/IB boundary is located at Section 390C-U1557B-6H-6, 6.5 cm (49.66 m CSF-B), where there is a sharp transition from brown silty clay at the base of Subunit IA to light gray calcareous nannofossil ooze at the top of Subunit IB that is visually distinct from the pinkish white calcareous nannofossil ooze observed in Cores 1H–6H.

4.1.1.2. Subunit IB

Interval: 390C-U1557B-6H-6, 6.5 cm, to 11H-4, 45.3 cm
Depth: 49.67–94.55 m CSF-B
Thickness: 44.88 m
Age: Late Miocene to Pliocene
Lithology: calcareous nannofossil ooze, silty clay

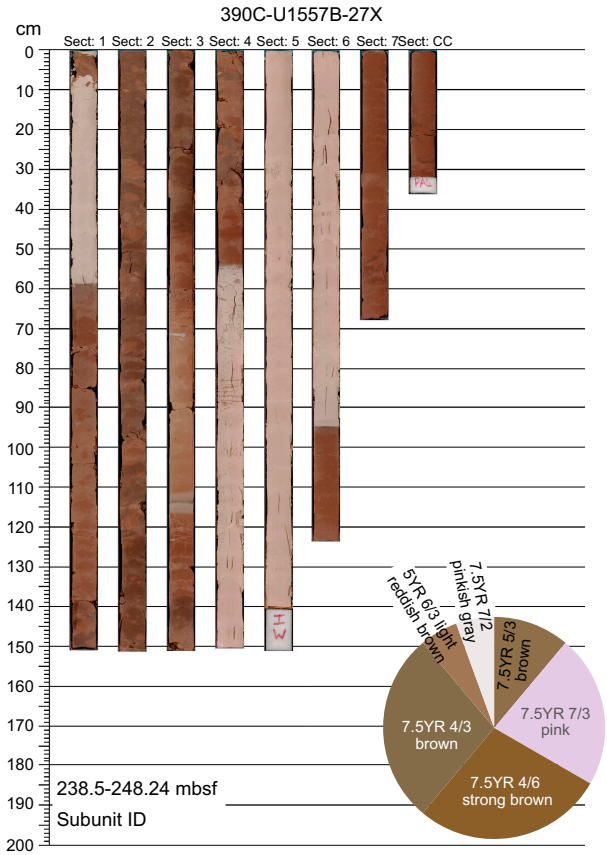

Figure F8. Characteristic lithology and color alternations, Unit I. Pie chart shows relative proportions of colors in Core 390C-U1557B-27X as described according to Munsell color system.

Subunit IB is mostly composed of light gray/pinkish white calcareous nannofossil ooze with minor brown silty clay intervals. Foraminifera are rare (<10%) in the nannofossil ooze (Figure **F10**). Light greenish gray foraminiferal ooze occurs near the bottom of Subunit IB (Figure **F11**) at 94.49–94.55 m CSF-B. Bioturbation is generally sparse throughout Subunit IB.

The Lithologic Subunit IB/IC boundary is located at Section 390C-U1557B-11H-4, 45.3 cm (94.553 m CSF-B), where there is a sharp transition between calcareous nannofossil ooze at the base of Subunit IB and the brown silty clay at the top of Subunit IC.

4.1.1.3. Subunit IC

Interval: 390C-U1557B-11H-4, 45.3 cm, to 17X-6, 37 cm
Depth: 94.55–150.38 m CSF-B
Thickness: 55.83 m
Age: Middle Miocene
Lithology: calcareous nannofossil ooze, silty clays

Subunit IC is composed of two relatively thick (>5 m) brown silty clays that bookend a thicker layer (>43 m) of pinkish gray calcareous nannofossil ooze with minor silty clays intervals (~1 cm to ~1 m thickness). Foraminifera are rare (<10%) in the nannofossil ooze intervals (Figure **F11**). The bioturbation index is generally sparse to low throughout Subunit IC.

The Lithologic Subunit IC/ID boundary is located at Section 390C-U1557B-17X-6, 37 cm (150.38 m CSF-B), where there is a sharp transition between brown silty clay at the base of Subunit IC and pink calcareous nannofossil chalk at the top of Subunit ID. Subunits IC and ID have different colors for calcareous nannofossil ooze/chalk (Subunit IC = pinkish gray; Subunit ID = pink) and silty clays (Subunit IC = brown; Subunit ID = reddish brown).

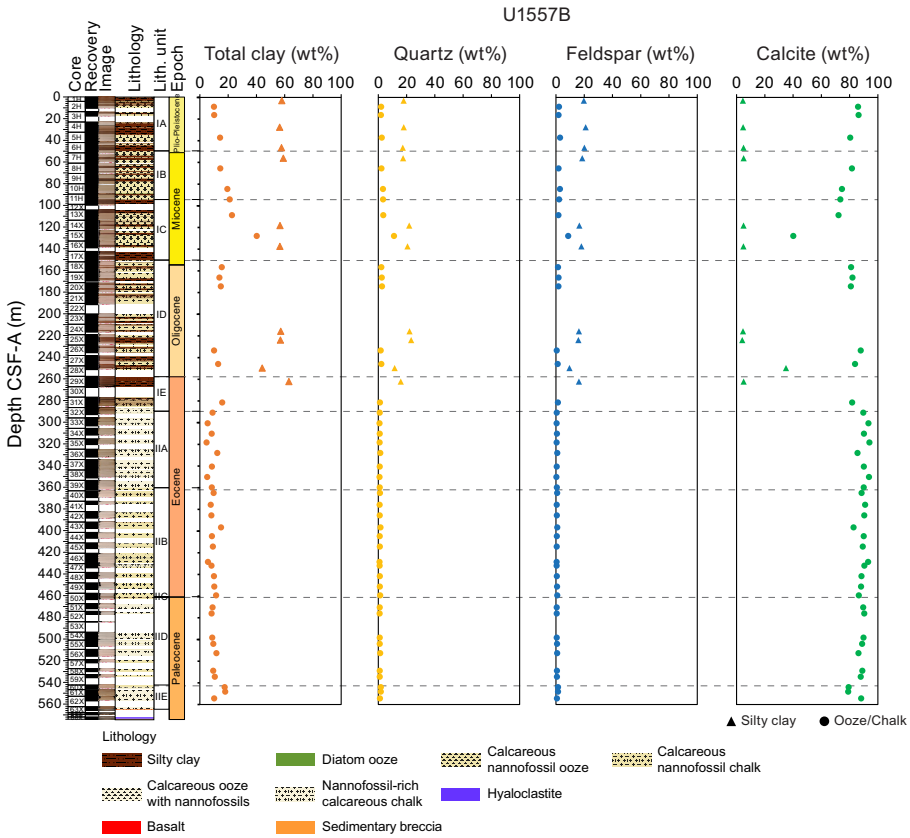

Figure F9. Downhole changes in mineralogy based on XRD results shown in Figure F14, Hole U1557B. Silty clays are only in Lithologic Unit I. Values are normalized such that total clay minerals (smectite + illite + chlorite + kaolinite) + quartz + feldspar (plagioclase + K-feldspar) + calcite = 100%.

4.1.1.4. Subunit ID

Interval: 390C-U1557B-17X-6, 37 cm, to 28X-CC, 20 cm
Depth: 150.38–251.53 m CSF-B
Thickness: 101.15 m
Age: late Oligocene to Middle Miocene
Lithology: calcareous nannofossil chalk, silty clays

Subunit ID is mostly composed of pink calcareous nannofossil chalk with reddish brown silty clay intervals (2–3 per core; ~1 m average thickness). Trace to abundant foraminifera are observed in the nannofossil ooze intervals. The bioturbation index is generally absent to sparse throughout Subunit ID.

The Lithologic Subunit ID/IE boundary is located at Section 390C-U1557B-28X-CC, 20 cm (251.53 m CSF-B), where a sharp transition between pink nannofossil chalk at the base of Subunit ID and brown/very dark brown silty clay at the top of Subunit IE also corresponds to a gap in core recovery.

4.1.1.5. Subunit IE

Interval: 390C-U1557B-29X-1, 0 cm, to 32X-3, 45 cm
Depth: 257.70–289.84 m CSF-B
Thickness: 32.14 m
Age: early to late? Eocene
Lithology: silty clay, organic-rich silty clay, clayey nannofossil chalk

Subunit IE predominantly comprises dark brown silty clay or clay (Figure F7), which is particularly abundant in the upper portion of the subunit (251.39–277.94 m CSF-B). Brown clayey calcareous chalk mostly characterizes the lower portion of Subunit IE (277.94–289.84 m CSF-B). Black organic-rich silty clay layers (~5 cm average thickness) are common throughout Core 390C-

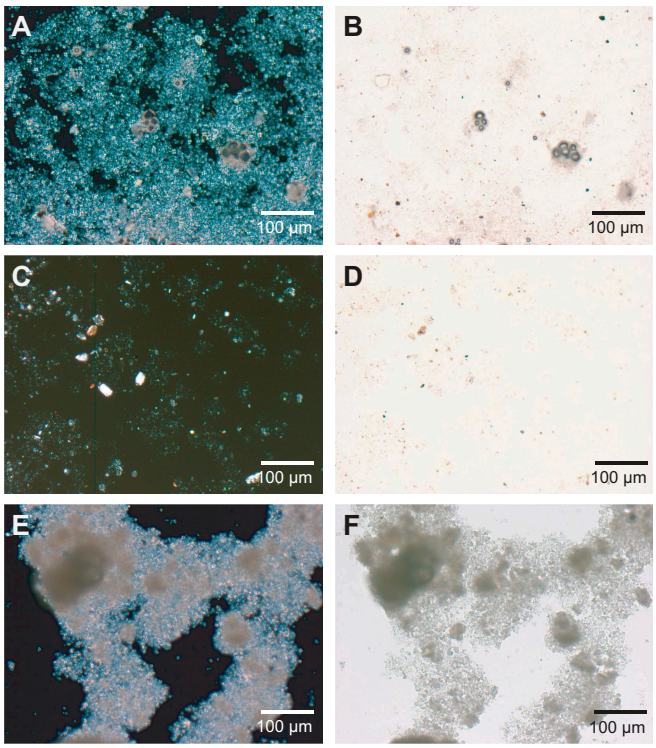

Figure F10. Main sedimentary components, Hole U1557B. A, B. Calcareous nannofossil ooze with few foraminifera (6H-7, 33 cm). C, D. Silty clay (11H-5, 60 cm). E, F. Nannofossil-rich calcareous chalk (59X-1, 100 cm). A, C, E = cross-polarized light (XPL); B, D, F = plane-polarized light (PPL).

U1557B-31X. Foraminifera are only observed in a prominent ~4 cm thick layer in interval 32X-1, 134–138 cm, within very pale brown calcareous foraminiferal ooze with nannofossils. Prominent organic-rich intense laminations are observed in Section 31X-6.

The Lithologic Subunit IE/IIA boundary is located at Section 390C-U1557B-32X-3, 45 cm (289.84 m CSF-B), at a bioturbated contact between a 5 cm thick unit of brown silty clay (Subunit IE) and pale brown nannofossil-rich calcareous chalk (Subunit IIA). Subunit IE represents the transition from Unit I to Unit II; the latter is characterized by the almost complete absence of siliciclastic lithologies.

4.1.2. Unit II

Interval: 390C-U1557B-32X-3, 45 cm, to 63X-2, 86 cm
Depth: 289.84–564.76 m CSF-B
Thickness: 274.92 m
Age: middle Paleocene to early Eocene
Lithology: nannofossil chalk with or without foraminifera, nannofossil-rich calcareous chalk with or without foraminifera, organic-rich silty clay with nannofossil, silty clay

Unit II is composed of ~275 m of Paleocene to early Eocene sediments, predominantly nannofossil-rich calcareous chalk or calcareous nannofossil chalk (Figures **F7**, **F12**). Unit II is divided into five subunits (Figure **F7**). Foraminifera are more common throughout Unit II than in Unit I, especially below ~400 m CSF-B. In contrast to Unit I, siliciclastic lithologies are almost

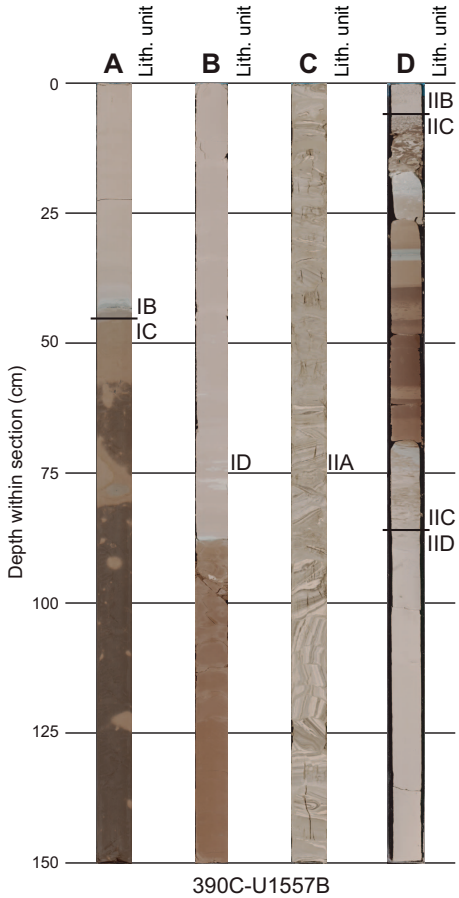

Figure F11. Selected core sections, Hole U1557B. A. Brown silty clays with sparse bioturbation underlying pinkish gray nannofossil ooze (11H-4; 94.10–95.60 m CSF-B). B. Reddish brown silty clays underlying pinkish gray nannofossil chalk (20X-4; 175.55–180.31 m CSF-B; Subunit ID). C. Very pale brown nannofossil-rich chalk with laminations, microfaulting, and folding (35X-3; 318.31–319.81 m CSF-B). D. Brown calcareous silty clay interval (unique in Unit II; interpreted to be PETM) hosting a greenish gray layer of calcareous nannofossil chalk with foraminifera (50X-3; 460.80–462.31 m CSF-B).

absent in Unit II (Figures **F8**, **F13**). Subunit IIA also hosts a notable section (390C-U1557B-35X-3; Figure **F11**) of material exhibiting complex synsedimentary deformation (folding and microfaulting) associated with different rheological behaviors of the sediment (degree of lithification). Subunit IIB (360.37–460.86 m CSF-B) is predominantly composed of nannofossil-rich calcareous chalk with variable foraminifera abundance (from trace to common; see **Sedimentology** in the Expedition 390/393 methods chapter [Coggon et al., 2024c]). In the middle of the ooze/chalk of Unit II, Subunit IIC is a distinct layer bearing brown clays associated with calcareous nannofossil chalk and colors (brown, light brown, and light greenish gray) that was likely deposited during the PETM (see **Biostratigraphy**; Figure **F11D**). Subunit IID cores are dominated by pinkish white nannofossil chalk with minor (up to 5 cm thick) pinkish gray foraminifera-rich intervals. Subunit IIE primarily comprises grayish brown nannofossil-rich calcareous chalk with foraminifera and yellowish brown calcareous nannofossil chalk.

The lithologic subunit boundaries of Unit II vary between bioturbated, gradational, and planar, with less common sharp or irregular contacts. The bioturbation index in Unit II ranges from absent to high, although it is generally absent or sparse. Drilling disturbance manifests as slight

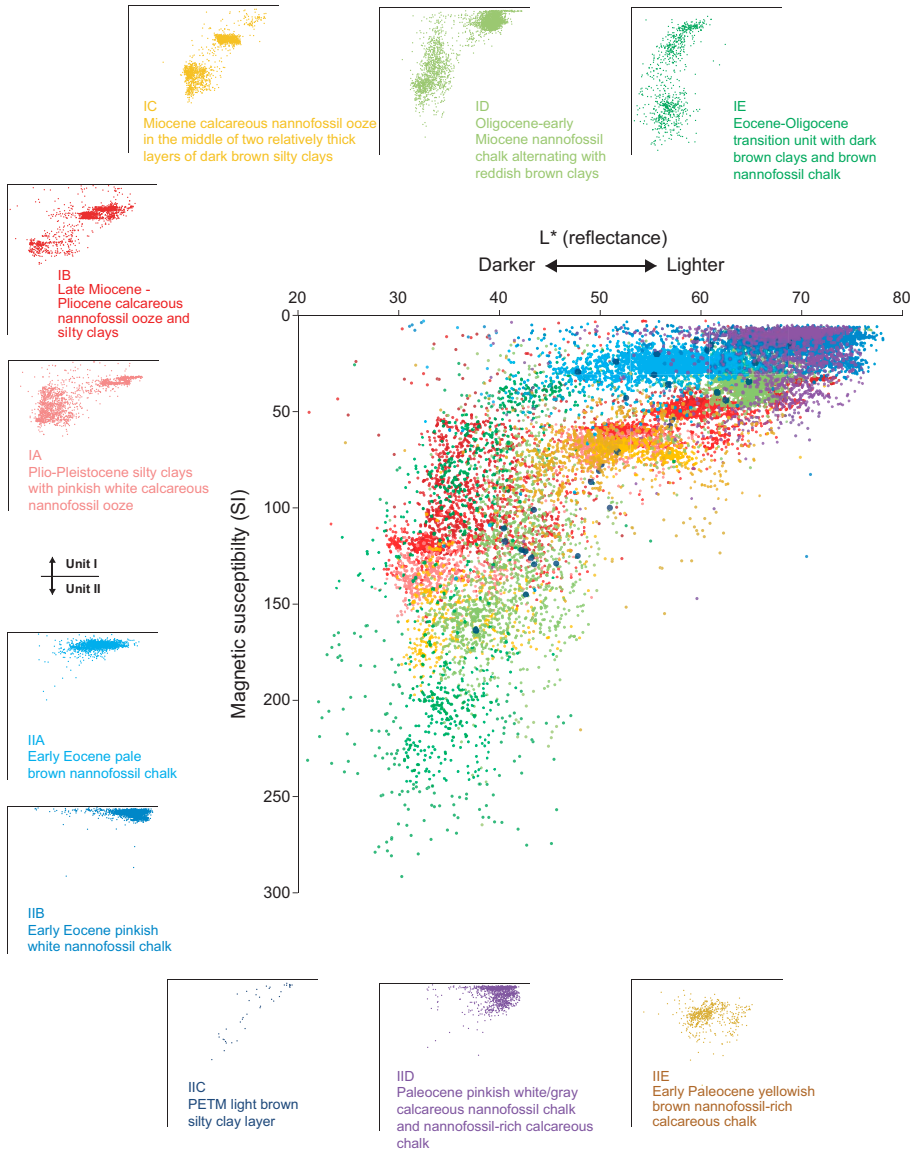

Figure F12. Scatter plots of SHMSL MSP and L* (reflectance), Site U1557. (See Sedimentology in the Expedition 390/393 methods chapter [Coggon et al., 2024c].) Insets above, below, and on left: properties of individual subunits with brief descriptions.

biscuiting throughout much of Unit II. However, toward the bottom of Unit II, particularly in Subunit IID, biscuits are commonly surrounded by ooze that appears unconsolidated because of the drilling disturbance, and the original sedimentary characteristics (e.g., bioturbation and color changes) are only preserved in the centers of the biscuits.

4.1.2.1. Subunit IIA

Intervals: 390C-U1557B-32X-3, 45 cm, to 39X-6, 65.5 cm
Depth: 289.84–360.37 m CSF-B
Thickness: 70.53 m
Age: early Eocene
Lithology: nannofossil-rich calcareous chalk

Subunit IIA primarily consists of nannofossil-rich calcareous chalk that varies in color between very pale brown, brown, light brownish gray, and pinkish gray. In addition, Subunit IIA contains minor amounts of foraminiferal calcareous chalk with nannofossils, nannofossil-rich calcareous chalk with foraminifera, and calcareous nannofossil chalk with foraminifera that collectively exhibit a similar color range to the primary lithology. Sections 390C-U1557B-35X-1 and 35X-2 contain particularly noteworthy pods of sediment that consist of millimeter-sized volcanic basalt/glass clasts surrounded by halos of subcentimeter-wide very pale brown sediment. In addition, the lower portion of Core 35X (Sections 35X-2 [~70 cm] through 35X-CC) exhibits complex synsedimentary deformation (folding and microfaulting; Figure **F11C**) associated with the variable rheological properties of the sediment (lithification degree). Within the deformed sediments in Sections 35X-2 through 35X-CC, the nannofossil-rich calcareous chalk is on average light brownish gray (10YR 6/2), hosting thin to thick laminations (see **Sedimentology** in the Expedition 390/393 methods chapter [Coggon et al., 2024c]) with different colors (e.g., light brownish gray and very pale brown). The bioturbation index is generally absent or sparse throughout Subunit IIA except for a few intervals where it is low to high.

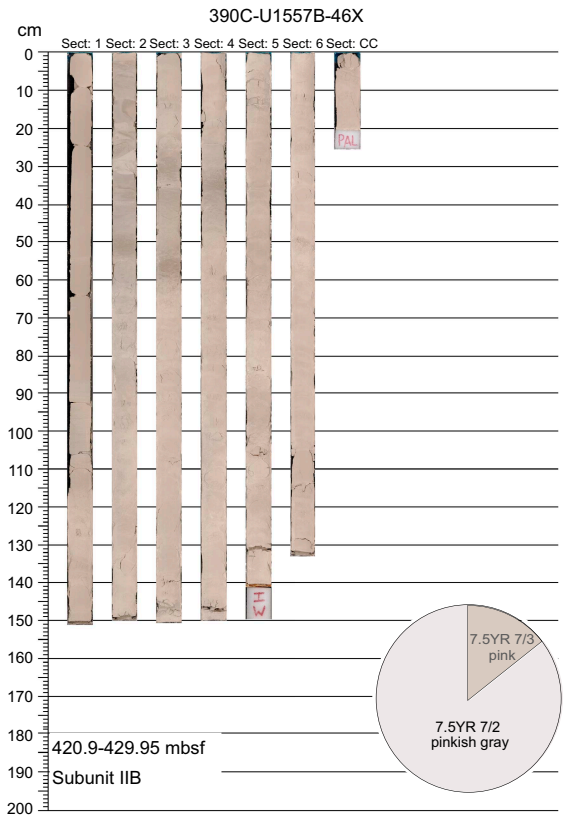

Figure F13. Characteristic lithology and color alternations, Unit II. Pie chart shows relative proportions of colors in Core 390C-U1557B-46X as described according to Munsell color system.

4.1.2.2. Subunit IIB

Interval: 390C-U1557B-39X-6, 65.5 cm, to 50X-3A, 6 cm
Depth: 360.37–460.86 m CSF-B
Thickness: 100.49 m
Age: early Eocene
Lithology: calcareous nannofossil chalk

Subunit IIB primarily comprises pink or pinkish white calcareous nannofossil chalk (Figure **F13**). The abundance of foraminifera is variable (trace to common) throughout Subunit IIB. Three thin (<2 cm) layers bearing volcaniclastic material (dark brown to greenish black volcanic ash/glass with sandy silt grain sizes) are observed near the top of Subunit IIB (362.09–362.1, 373.45–373.47, and 382.68–382.76 m CSF-B). Thin laminations occur sparsely throughout Subunit IIB. The bioturbation index is almost always either absent or sparse throughout Subunit IIB except for rare intervals with low intensity.

The Lithologic Subunit IIB/IIC boundary is located at Section 390C-U1557B-50X-3, 6 cm (454.18 m CSF-B), where there is a transition between pinkish white calcareous nannofossil ooze with foraminifera at the base of Subunit IIB and generally light brown, brown, and greenish gray units in Subunit IIC.

4.1.2.3. Subunit IIC

Interval: 390C-U1557B-50X-3, 6–86 cm
Depth: 460.86–461.66 m CSF-B
Thickness: 0.8 m
Age: latest Paleocene
Lithology: calcareous nannofossil chalk, calcareous nannofossil chalk with clay, calcareous silty clay

Subunit IIC is composed of light brown to brown calcareous silty clays and calcareous nannofossil chalk with clay. Subunit IIC is a unique interval in Unit II because it contains a relatively high content of clayey material (Figures **F7**, **F11D**) compared to the rest of Unit II. From 460.97 to 461.06 m CSF-B, light greenish gray calcareous nannofossil chalk occurs with foraminifera. From 461.12 to 461.14 m CSF-B, there are <1 cm thick greenish gray, grayish green, and pinkish white layers of calcareous nannofossil chalk; within these layers, there is a grayish green ~0.1 cm laminae. Below the greenish gray and grayish green layers, light brown calcareous nannofossil chalk with clay and brown calcareous silty clay are interstratified from 461.14 to 461.45 m CSF-B and interpreted to be the PETM. The bioturbation index is generally absent to sparse or low.

The Lithologic Subunit IIC/IID boundary is located at Section 390C-U1557B-50X-3, 86 cm (461.66 m CSF-B), at a transition from pale brown and light greenish gray calcareous nannofossil chalk (with clay or foraminifera) to the underlying pervasive pink and pinkish white calcareous nannofossil chalk with foraminifera.

4.1.2.4. Subunit IID

Interval: 390C-U1557B-50X-3, 86 cm, to 59X-CC, 21 cm
Depth: 461.66–535.73 m CSF-B
Thickness: 74.07 m
Age: late Paleocene (?)
Lithology: nannofossil-rich calcareous chalk, calcareous nannofossil chalk

Subunit IID is mainly composed of pinkish white nannofossil-rich calcareous chalk and pinkish gray calcareous nannofossil chalk. Thin to medium organic-rich laminations (gray to dark bluish gray) are observed in Core 390C-U1557B-56X. Prominent <2.5 cm thick layers of calcareous nannofossil chalk with bluish gray organic particles occur in Core 57X. Prominent silty clay beds <10 cm thick occur at the bottom of Core 59X. Relatively organic rich, ~10–15 cm (and one 2 cm) thick layers that are likely associated with bioturbation also occur in Core 59X. A bed of calcareous nannofossil chalk (535.06–535.2 m CSF-B) bearing fine bluish gray volcaniclasts and medium lam-

inations of light olive-brown ferromagnesian oxides are observed (Section 59X-2). The bioturbation index is generally sparse to moderate.

Drilling disturbance (biscuiting) commonly turned the nannofossil chalk into unconsolidated material (ooze) throughout cores in Subunit IID. Only in the center of the biscuits, where undisturbed sediment still exists, can original sedimentary characteristics (e.g., bioturbation and color changes) be observed.

The Lithologic Subunit IID/IIE boundary is located at Section 390C-U1557B-59X-CC, 21 cm (535.73 m CSF-B), where there is a transition between pinkish gray calcareous nannofossil chalk (Subunit IID) and dark grayish brown nannofossil-rich calcareous chalk (Subunit IIE), which also corresponds to a gap in core recovery.

4.1.2.5. Subunit IIE

Interval: 390C-U1557B-60X-1, 0 cm, to 63X-2, 87 cm
Depth: 542.40–564.77 m CSF-B
Thickness: 22.36 m
Age: early to middle Paleocene?
Lithology: nannofossil-rich calcareous chalk, calcareous nannofossil chalk

Subunit IIE is composed mainly of pinkish gray calcareous nannofossil chalk (542.40–553.38 m CSF-B) and yellowish brown or dark grayish brown nannofossil-rich calcareous chalk with foraminifera (553.38–564.76 m CSF-B). Minor (from a few millimeters up to 10 cm) intervals of bluish gray nannofossil-rich calcareous chalk containing igneous clasts (up to sand sizes) occur in Core 390C-U1557B-60X. Sections 61X-3, 61X-4, and 62X-3 contain organic-rich laminations <5 cm thick. Silt-sized medium laminae contain strong brown ferromagnesian oxide grains at 556.70–557.16 m CSF-B. The bioturbation index is generally sparse to moderate throughout Subunit IIE except near the bottom, where it is high (Sections 63X-1 and 63X-2) to intense (Section 60X-CC).

The lithologic boundary between Subunit IIE and basement Unit 1 (see **Igneous petrology**) is located at Section 390C-U1557B-63X-2, 87 cm (564.77 m CSF-B), and is the shallowest occurrence of igneous basement lithologies (basalt cobbles).

4.1.3. Unit 1

Interval: 390C-U1557B-63X-2, 86 cm, to 63X-3, 115 cm
Depth: 564.8–567.9 mbsf
Thickness: 9.5 m
Age: late Paleocene (?)
Sedimentary lithology: indurated calcareous sediment
Basement lithology: basalt, hyaloclastite

Below the sediment/basement interface in Hole U1557B, which is defined as 564.77 m CSF-B at Site U1557 based on the shallowest occurrence of basalt material cored in Hole U1557B (see **Stratigraphic unit summary**), the uppermost basement unit is a transitional unit that comprises both pelagic sedimentary material and volcanic clasts (see **Igneous petrology**). The sediment occurs as the matrix among basalt blocks (>10 cm diameter) in the sedimentary breccias (Subunit 1a; 564.88–566.01 and 573.32–574.22 m CSF-B) as well as hyaloclastite layers (volcanic glass clasts; sizes <1 mm to ~10 cm) at 567.90–573.32 m CSF-B (Subunit 1b). In both lithologies, the sediment is mostly composed of indurated calcareous sediment, likely from nannofossil chalk that was lithified by hydrothermal fluids. This indurated calcareous sediment is pale brown, dark brown, or reddish yellow, and its color is probably indicative of different degrees of hydrothermal alteration. Sparse, submillimeter-sized dark particles (altered sediment particles or igneous clasts) are embedded in the indurated calcareous sediment. Sedimentary textures are mostly absent or limited except for rare bioturbation features (burrows). Sparse secondary calcite veins (millimeter to subcentimeter thickness) crosscut the sedimentary matrix of Unit 1 (see **Alteration petrology**).

4.2. X-ray diffraction

Bulk powder XRD analyses results are summarized in Figures **F9** and **F14** and Table **T3**. Powder samples were collected from every interstitial water (IW) geochemistry whole-round residue section (see **X-ray diffraction analysis** in the Expedition 390/393 methods chapter [Coggon et al., 2024c]) during Expedition 390C. In Lithologic Unit II, IW sampling was only carried out in the chalk layers and no analysis of any silty clay lithology was conducted. Most of the XRD samples were collected from homogeneous intervals (e.g., silty clay and ooze/chalk), and the differences in mineral assemblages between samples of similar lithologies were negligible. Downhole variations in the mineral assemblages within the silty clay and ooze/chalk sediments, respectively, are also relatively small (Figures **F9**, **F14**).

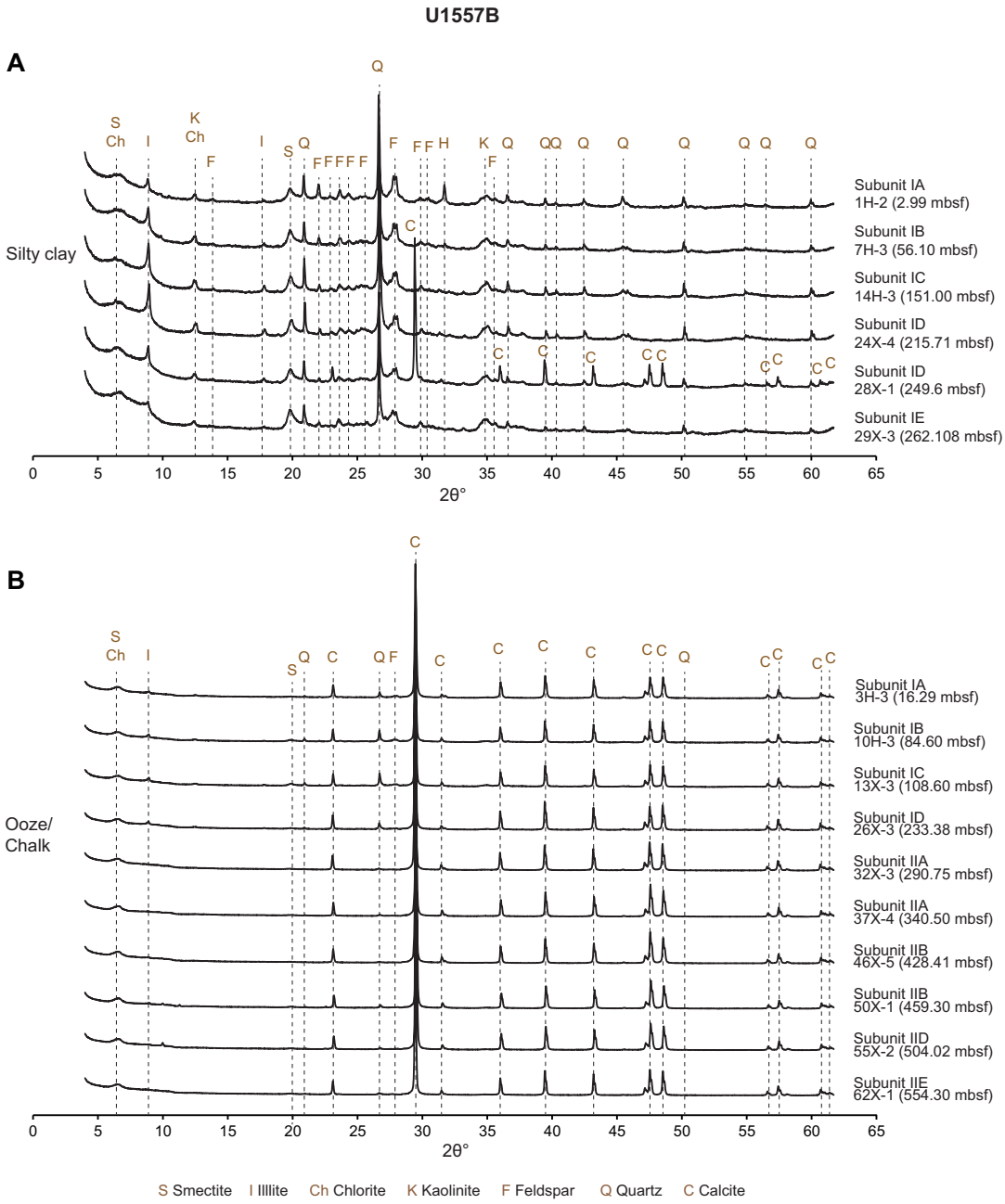

Figure F14. Representative X-ray diffractograms of bulk sediments, Hole U1557B. A. Silty clay lithology. B. Carbonate (ooze/chalk) lithology.

The average mineral composition of the silty clay intervals from Unit I is as follows:

- Total clay minerals = 57.64 wt%.
- Quartz = 20.10 wt%.
- Feldspar = 17.67 wt%.
- Calcite = 4.59 wt%.

Table T3. Results from quantitative mineral phase analyses (accuracy <3%) based on XRD diffractograms of samples from Hole U1557B. All samples were collected on whole-round IW residues. **Download table in CSV format.**

Core, section	Depth (mbsf)	Lith. unit	Lithologic description	Total clay (wt%)	Quartz (wt%)	Feldspar (wt%)	Calcite (wt%)
390C-U1557B-							
1H-2	2.99	IA	Dark yellowish brown silty clay	57.9	17.9	19.7	4.5
2H-3	8.60	IA	Pinkish white calcareous ooze	9.9	2.0	2.1	86.0
3H 3	16.29	IA	Pinkish white calcareous ooze	10.1	1.8	1.8	86.3
4H-3	27.50	IA	Brown silty clay	56.4	18.0	21.0	4.6
5H-3	37.11	IA	Pinkish gray calcareous nannofossil ooze	14.3	2.4	2.9	80.4
6H-3	46.46	IA	Very dark grayish brown silty clay	57.7	17.3	20.1	4.9
7H-3	56.10	IB	Brown silty clay	59.0	17.5	18.6	5.0
8H-3	65.45	IB	Light gray calcareous nannofossil ooze	14.4	2.2	1.8	81.7
10H-3	84.46	IB	Light gray calcareous nannofossil ooze	19.4	3.2	2.8	74.6
11H-3	94.10	IB	Pink calcareous nannofossil ooze	21.0	3.3	2.2	73.4
13H-3	108.59	IC	Pinkish gray calcareous nannofossil ooze	22.6	3.4	1.8	72.2
14H-3	118.21	IC	Brown silty clay	56.7	21.9	16.6	4.9
15X-3	127.77	IC	Pinkish gray calcareous nannofossil ooze	40.2	11.0	8.7	40.2
16X-3	137.41	IC	Brown silty clay	56.6	20.7	17.9	4.8
18X-3	156.60	ID	Pink calcareous nannofossil chalk	15.5	2.1	1.4	81.0
19X-3	166.20	ID	Pink calcareous nannofossil chalk	13.8	2.4	1.8	82.0
20X-2	174.28	ID	Pink calcareous nannofossil chalk	14.8	2.6	1.7	80.9
24X-4	215.71	ID	Brown nannofossil-rich silty clay	57.2	22.0	16.2	4.5
25X-3	223.81	ID	Reddish brown silty clay	57.0	23.2	15.8	4.0
26X-3	233.38	ID	Pink calcareous nannofossil chalk	10.0	1.6	0.5	87.9
27X-5	245.88	ID	Pink calcareous nannofossil chalk	12.9	2.1	1.2	83.8
28X-1	249.60	ID	Brown silty clay	44.0	11.5	9.5	35.0
29X-3	262.11	IE	Brown silty clay	62.9	15.8	16.2	5.0
31X-3	281.42	IE	Brown calcareous nannofossil chalk	15.8	1.1	1.3	81.8
32X-3	290.75	IIA	Pale brown nannofossil-rich calcareous chalk	8.9	0.9	0.5	89.7
33X-3	300.59	IIA	Pale brown nannofossil-rich calcareous chalk	5.5	0.8	0.4	93.4
34X-3	310.20	IIA	Very pale brown nannofossil-rich calcareous chalk	8.3	0.9	0.6	90.1
35X-2	318.31	IIA	Light brownish gray nannofossil-rich calcareous chalk	4.7	0.9	0.4	94.0
36X-2	327.91	IIA	Light yellowish brown nannofossil-rich calcareous chalk	12.2	1.3	0.9	85.6
37X 4	340.50	IIA	Pale brown nannofossil-rich calcareous chalk	8.5	0.9	0.5	90.1
38X-4	350.11	IIA	Pinkish gray nannofossil-rich calcareous chalk	5.1	0.8	0.3	93.7
39X-4	359.72	IIA	Pinkish gray nannofossil-rich calcareous chalk	8.4	1.0	0.6	90.0
40X-1	364.80	IIB	Pink calcareous nannofossil chalk	9.7	1.1	0.8	88.5
41X-2	375.71	IIB	Pink calcareous nannofossil chalk	7.6	0.9	0.5	91.0
42X-2	385.50	IIB	Pink calcareous nannofossil chalk	8.1	1.0	0.6	90.4
43X-3	396.59	IIB	Pinkish white calcareous nannofossil chalk	14.9	1.5	0.9	82.8
44X-2	404.70	IIB	Pinkish white calcareous nannofossil chalk	8.5	1.0	0.6	90.0
45X-2	414.29	IIB	Pinkish white calcareous nannofossil chalk	9.1	1.0	0.6	89.3
46X 5	428.41	IIB	Pinkish white calcareous nannofossil chalk	5.7	0.8	0.4	93.1
47X-1	431.92	IIB	Pinkish white calcareous nannofossil chalk	8.8	0.9	0.5	90.5
48X-2	441.60	IIB	Pinkish white calcareous nannofossil chalk	9.9	1.1	0.6	88.4
49X-2	451.21	IIB	Pinkish white calcareous nannofossil chalk	10.1	1.0	0.7	88.1
50X-1	459.30	IIB	Pinkish white calcareous nannofossil chalk with foraminifera	11.4	1.3	0.9	86.5
51X-2	470.39	IID	Pinkish white nannofossil-rich calcareous chalk	8.9	0.9	0.5	89.6
52X-1	476.00	IID	Pinkish white nannofossil-rich calcareous chalk with foraminifera	8.2	0.9	0.5	90.4
54X-3	498.20	IID	Pinkish white nannofossil-rich calcareous chalk	8.7	1.0	0.5	89.9
55X-2	504.02	IID	Pinkish white nannofossil-rich calcareous chalk	9.5	1.0	0.7	88.8
56X-2	512.61	IID	Pinkish white nannofossil-rich calcareous chalk	11.7	1.2	0.8	86.3
58X-1	528.78	IID	Pinkish white calcareous nannofossil chalk	9.4	1.0	0.7	89.0
59X-1	534.30	IID	Pinkish gray calcareous nannofossil chalk	10.5	1.0	0.7	87.8
60X-1	543.90	IIE	Pinkish gray calcareous nannofossil chalk	17.5	1.8	1.4	79.3
61X-1	548.11	IIE	Dark grayish brown nannofossil-rich calcareous chalk	17.9	1.7	1.5	79.0
62X-1	554.30	IIE	Yellowish brown nannofossil-rich calcareous chalk with foraminifera	10.1	1.1	0.7	88.2

The average mineral composition of the calcareous ooze from Unit I is as follows:

- Total clay minerals = 15.54 wt%.
- Quartz = 2.52 wt%.
- Feldspar = 1.71 wt%.
- Calcite = 80.23 wt%.

On average, the calcareous chalk from Unit II contains the following:

- Total clay minerals = 9.00 wt%.
- Quartz = 1.00 wt%.
- Feldspar = 0.62 wt%.
- Calcite = 89.39 wt%.

The alternation of silty clays and calcareous ooze in Unit I is well highlighted by the quantitative mineral composition. Compared to Unit II, however, the calcareous ooze of Unit I hosts a higher amount of siliciclastic minerals, perhaps indicative of the shifts between the two lithologies in Unit I.

4.3. Spectrophotometry and point source magnetic susceptibility

Comparisons of spectral data, specifically reflectance and color space (L* a* b*) (see **Sedimentology** in the Expedition 390/393 methods chapter [Coggon et al., 2024c]), and point magnetic susceptibility (MSP) measured on the Section Half Multisensor Logger (SHMSL) (see **Physical properties and downhole measurements** in the Expedition 390/393 methods chapter [Coggon et al., 2024c]) confirm that the subunits exhibit different respective physical properties (Figures **F12**, **F15**). Essentially, the silty clays, which are more dominant in Lithologic Unit I than in Unit II, have lower reflectance and higher MSP than the carbonate oozes/chalks. For example, for Subunits IA–ID, which comprise alternating silty clays and nannofossil ooze/chalk (Figure **F8**), reflectance and MSP values are grouped into two clusters. In Figures **F12** and **F15**, Unit I subunits overlap with Unit II subunits, but ooze dominates in the latter. Notably, Subunit IE, which contains low reflectance and chromaticity and the highest MSP, represents the Eocene–Oligocene transition and is dominated by dark brown silty clay. Subunits IIB and IID, which are predominantly chalk with a high proportion of calcite (Figures **F9**, **F14**), only display high reflectance and high a*/b* ratios (e.g., less yellow or red). Subunit IIC, which contains the PETM, displays a wide range of reflectance, color, and related MSP values, reflecting its varied lithology.

4.4. Comparison with DSDP Leg 3 lithologic formations

Given that Site U1557 was the longest record obtained in Expeditions 390/393 back to the Paleocene (Coggon et al., 2022a), we provide a comparison with the earlier Deep Sea Drilling Project (DSDP) Leg 3 findings in the area from more than 50 y ago. The general sedimentologic characteristics and ages of the subunits in Lithologic Units I and II can be tentatively correlated with the lithologic formations and sediments spot-cored during Leg 3 (The Shipboard Scientific Party, 1970). Leg 3 sediments were divided into nine lithologic formations. We interpret Leg 3 formations at DSDP Sites 15, 19, and 20 (see Figure **F1** in the Expedition 390/393 summary chapter [Coggon et al., 2024d]) to correspond to Site U1557 sediments (Table **T4**).

Leg 3 lithologic formations were inferred to be represented across the central South Atlantic Basin (or at least at the sites cored); relative to Site U1557, Site 15 is ~800 km east, Site 19 is ~400 km northeast, and Site 20 is ~250 km north. Sites 19 and 20 have a water depth (>4500 m) and distance (>1000 km) from the axis of the Mid-Atlantic Ridge that make them comparable to Site U1557. The poor recovery of post-Oligocene sediment at these sites during Leg 3 does not allow any correlation with Lithologic Subunits IA and IC of Site U1557. However, it seems that Subunit IB resembles the coeval sediments described at Site 15 (Challenger/Blake ooze). The poor recovery/incomplete coring of sediment sections during Leg 3 also prevented the collection of cores lithologically equivalent to Site U1557 Subunits IIC and IIE. Additionally, the Eocene–Oligocene transition in Subunit IE seems to only partially overlap with Gazelle ooze, likely indicat-

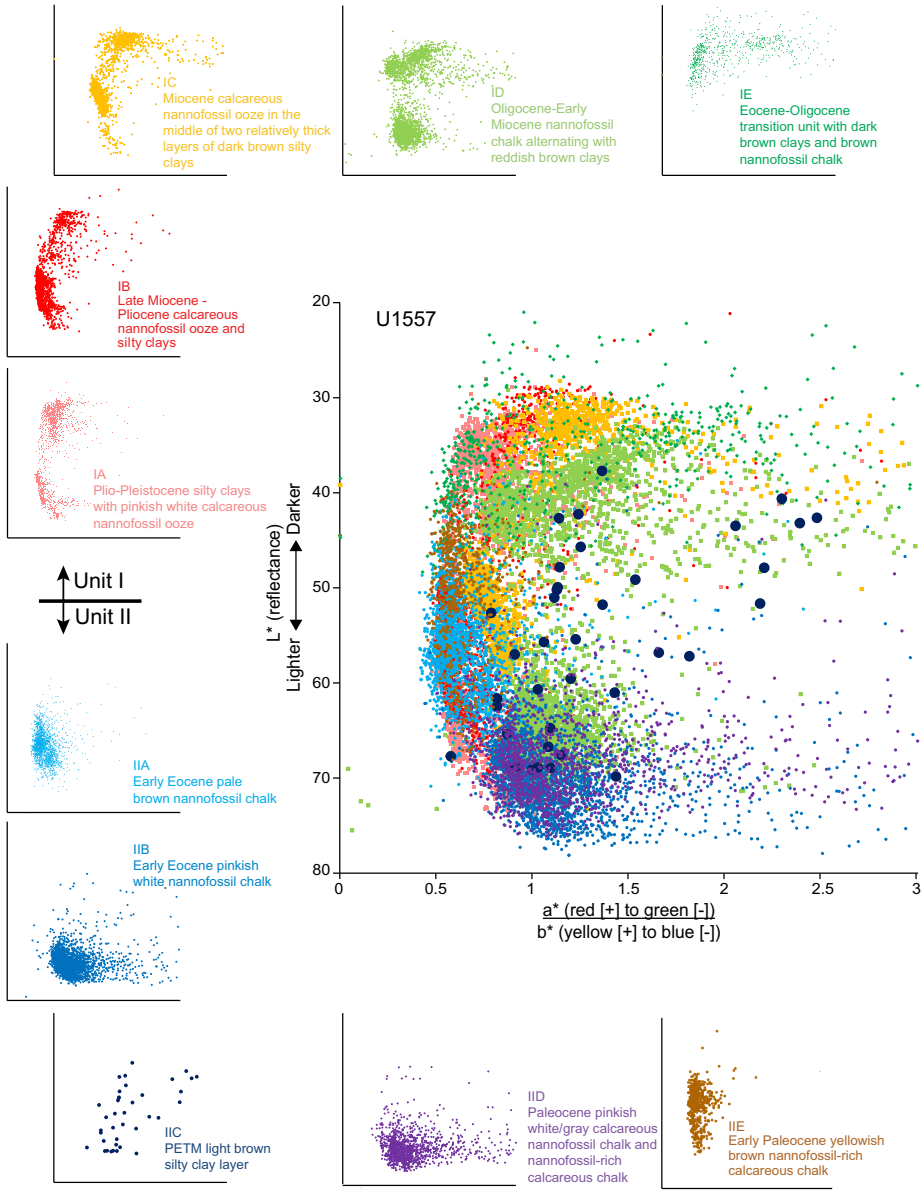

Figure F15. Scatter plots of SHMSL color reflectance data, including L* (reflectance) and chromaticity a*/b*, Site U1557. (See Sedimentology in the Expedition 390/393 methods chapter [Coggon et al., 2024c].) Insets above, below, and on left: properties of individual subunits with brief descriptions.

Table T4. Possible correlations between subunits defined at Site U1557 with DSDP Leg 3 lithologic formations. **Download table in CSV format.**

Lith. subunit	Possible correlation with these Leg 3 lithologic formations	Age	Description of Site U1557 subunit	Description of DSDP Leg 3 lithologic formation
IB	Challenger Blake ooze	Late Miocene/Pliocene	Calcareous nannofossil ooze and silty clays.	Nannofossil chalk ooze, marly in various shades of brown. White nannofossil chalk ooze (with local red clays).
ID	Endeavor ooze	Oligocene/Miocene	Calcareous nannofossil chalk alternating with reddish brown silty clays.	Nannofossil chalk and marls, brown with red clays locally.
	Discovery clays			Red clays, zeolitic, marly ooze interbeds present locally.
IE	Gazelle ooze (partial correlation)	late Eocene	Eocene/Oligocene transition unit, dark brown clays and brown clayey nannofossil chalk.	Nannofossil marl oozes and clays, brown.
IIA	Grampus ooze	Eocene	Light brownish gray nannofossil-rich calcareous chalk.	Foraminiferal nannofossil chalk oozes, darker and richer in foraminifera near the base.
IIB–IID	Hirondelle ooze	Paleocene/early Eocene	Pinkish white/gray calcareous nannofossil chalk and nannofossil-rich calcareous chalk.	Nannofossil chalk oozes partly recrystallized pink.

ing a lower recovery of the identifying dark brown silty clay material (indeed, core recovery gaps also occurred during operations in Hole U1557B; see **Operations**).

5. Igneous petrology

Two holes at Site U1557 recovered basement rocks in the form of sedimentary breccia. In Hole U1557B, 9.5 m of sedimentary breccia was cored after basement, marked by the shallowest presence of lithified/volcanic rock, was reached at 564.8 mbsf. A reentry system was installed in Hole U1557D during engineering Expeditions 390C and 395E, with the casing installed ~5 m into basement and the open hole below the casing reaching ~10 m into basement (575.6 mbsf) (see **Operations**). Expedition 390 cored 109.1 m of basement in Hole U1557D, recovering sedimentary breccia throughout the depth of the hole.

The breccia recovered in Hole U1557D consists of a range of basaltic clast types derived predominantly from pillow lavas. The clasts are all moderately to highly altered (see **Alteration petrology**), making it difficult to discriminate reliably among all clasts based on primary igneous lithology alone. Therefore, for the purposes of macroscopic core description, we have distinguished between altered glass and basalts (cryptocrystalline to microcrystalline) and grouped the basalts into three categories based on color that broadly reflect different degrees of alteration: gray, brown, and orange (Figure **F16**) (see **Alteration petrology**). In general, gray basalts are the least altered and most diverse lithologically; they range from cryptocrystalline to microcrystalline and from aphyric to highly plagioclase-olivine-clinopyroxene phyric, although aphyric textures are most common. Brown and orange basalts are typically aphyric to sparsely plagioclase or olivine phyric. In addition, orange basalts are typically associated with textures indicative of an origin in a pillow chilled margin. With few exceptions, basaltic glass is completely altered throughout the core. Although some variation in clast lithology is observed downhole (see **Clast petrology**), systematic variations were not identified, and the entire sequence of rocks recovered is defined as a single lithologic unit. It is divided into three lithologic subunits based on variations in breccia

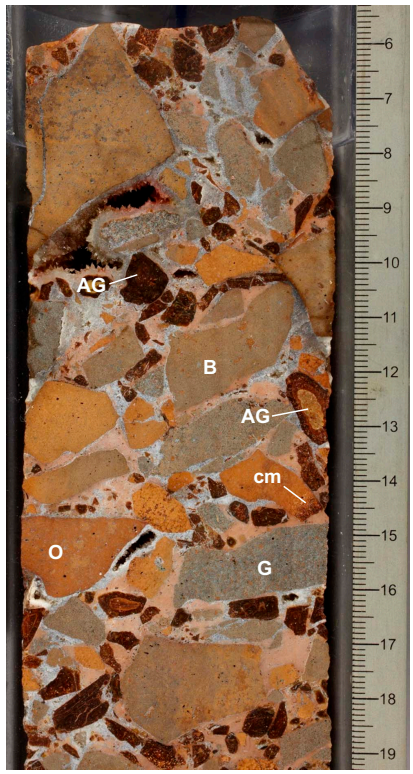

Figure F16. Various clast types encountered at Site U1557 (390-U1557D-6R-1 [Piece 2, 6–19 cm]). G = gray basalt, B = brown basalt, O = orange basalt, AG = altered glass, cm = chilled margin.

matrix and cement: Lithologic Subunit 1a in Sections 390C-U1557B-63X-2, 86 cm, through 63X-3; Subunit 1b in Sections 64X-1 through 66X-2 and 390-U1557D-2R-1 through 3R-2; and Subunit 1c in Sections 390-U1557D-3R-3 through 14R-6 (Figure **F17**).

In this section, we describe each of the igneous subunits and provide our interpretation of the entire basement succession.

5.1. Unit descriptions

5.1.1. Unit 1

5.1.1.1. Subunit 1a

Interval: 390C-U1557B-63X-2, 86 cm, through 63X-3, 115 cm
Depth: 564.8–567.9 mbsf
Lithology: sedimentary breccia with pelagic sediment matrix

Subunit 1a was recovered only in Hole U1557B. It is a 3.1 m interval of sedimentary breccia that ranges from matrix to clast supported (Figure **F18**). It consists of moderately sorted basaltic clasts in a pelagic calcareous sediment matrix that is pinkish gray (7.5YR 7/2) to white. The clasts, which are up to 7 cm, are predominantly aphyric and moderately altered and range in color from gray to brown. Chilled margin textures are recovered in some clasts, suggesting they originated as pillow lavas. Altered glass, although present, is in low abundance.

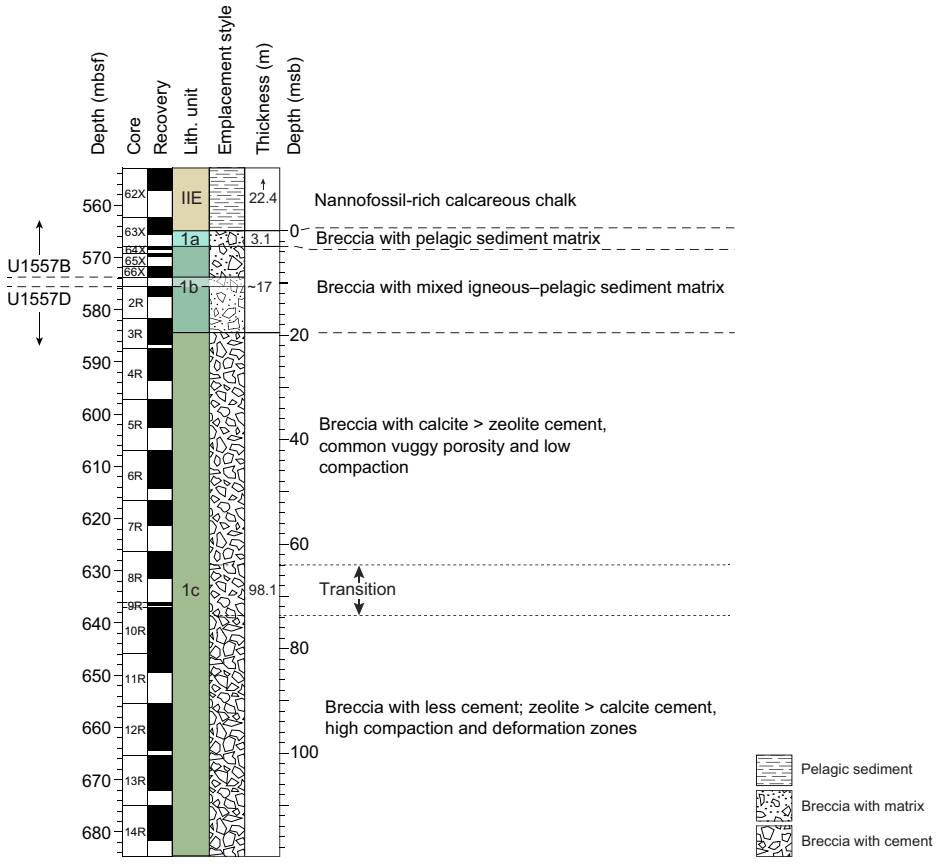

Figure F17. Basement stratigraphic summary, Site U1557. Composite based on Hole U1557B for Subunit 1a and Hole U1557D for Subunits 1b and 1c. Calcite cement and vuggy porosity tends to be greater in uppermost part of Subunit 1c relative to more zeolite-rich cement and compaction toward bottom of subunit. Broad transitional region is indicated. Although real changes are present, Subunit 1c was not further divided because variations are subtle, gradational, and not unidirectional. Subunit 1c remains sedimentary breccia throughout, with similar clast types present from top to bottom.

5.1.1.2. Subunit 1b

Intervals: 390C-U1557B-64X-1 through 66X-2; 390-U1557D-2R-1 through 3R-2
Depths: Hole U1557B = 567.9–574.22 mbsf (base of subunit not recovered); Hole U1557D = 575.6–584.52 mbsf
Lithology: Sedimentary breccia with mixed igneous–pelagic sediment matrix

Subunit 1b is a clast-supported, poorly sorted sedimentary breccia. It occurs in both Holes U1557B and U1557D; 6.3 m was cored in Hole U1557B (in which the base of this subunit was not penetrated), and 8.9 m was cored in Hole U1557D. Subunit 1b differs from Subunit 1a in that the matrix is more variable in composition. It consists of pelagic sediment that hosts a range of millimeter- to centimeter-sized altered glass clasts as well as submillimeter dark particles of altered volcaniclastic material (Figure **F19**). Foraminifera are preserved in the matrix (Figure **F19A**), and locally the micritic matrix is partially recrystallized to a microsparry calcite (Figure **F19B**). Many of the clasts included in the sediment are lithics consisting of altered glass and cryptocrystalline basalt cemented by zeolite (Figure **F19C, F19D**). This indicates that at least some of the clasts are derived from a unit that had already undergone zeolite cementation.

The color of the pelagic sediment matrix changes in response to the variable clast load. It is more reddish yellow where altered glass clasts are abundant and more pale brown to brown where they are not (Figure **F20**). Variations in alteration also have an impact on overall breccia appearance, with colors ranging from orange-brown to greenish gray, depending on the alteration style (see **Alteration petrology**) (Figure **F21**). Aside from the increase in altered glass abundance, clast types are similar to those in Subunit 1a, consisting predominantly of aphyric gray, brown, and

Figure F18. Representative sedimentary breccia, Subunit 1a (390C-U1557B-63X-3, 35–56 cm). PS = pelagic sediment (indurated calcareous sediment) matrix.

orange basalts, some with chilled margins (Figures **F20C**, **F21**). Locally, sparry calcite veins cross-cut the breccia (Figure **F22**), but they are in relatively low abundance (see **Alteration petrology**).

5.1.1.3. Subunit 1c

Interval: 390-U1557D-3R-3 through 14R-6
Depth: 584.52–682.66 mbsf
Lithology: sedimentary breccia with carbonate and zeolite cement

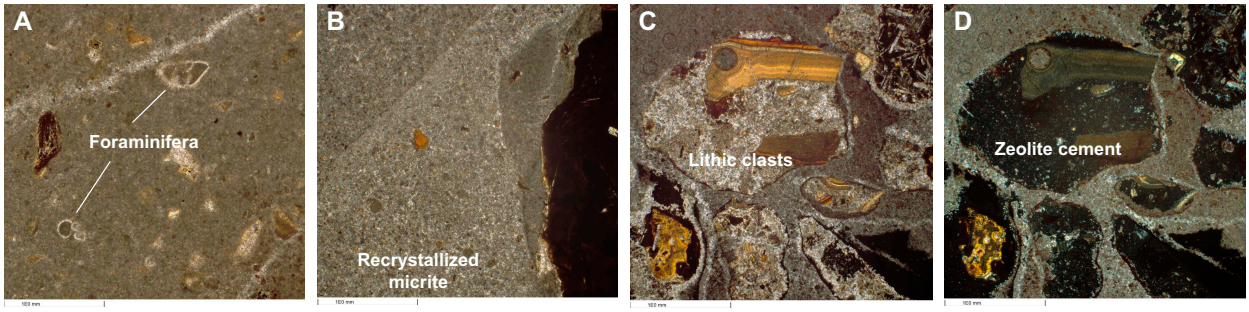

Figure F19. Sedimentary breccia, Subunit 1b (390-U1557D-2R-1 [Piece 16, 97–99 cm]). A. Pelagic sediment matrix showing fossil foraminifera (PPL). B. Partial recrystallization/neomorphism of carbonate sediment (PPL). Note island of unrecrystallized matrix adjacent to basalt clast on right. C, D. Lithic clasts of altered glass and cryptocrystalline basalt cemented by zeolite (C: PPL, D: XPL).

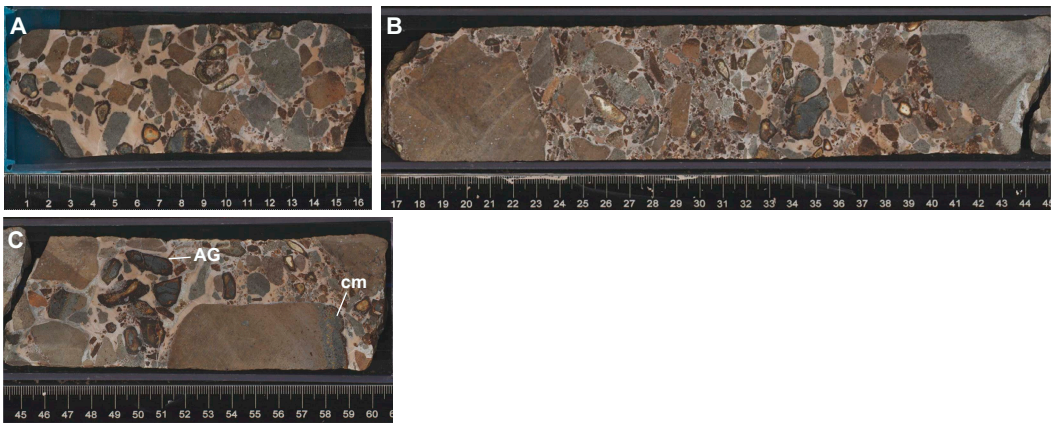

Figure F20. Representative sedimentary breccia showing variation in clast type and grain size, Hole U1557D Subunit 1b. A. 3R-1 (Piece 1A). B. 3R-1 (Piece 1B). C. 3R-1 (Piece 1C). Note chilled margin (cm) on large brown basalt clast and relatively unaltered cores of some altered glass (AG) clasts. Although these cores are not glass, they are very fine grained spherulitic zones of chilled margins. Such fresh glassy material is rare at Site U1557, particularly deeper in the hole.

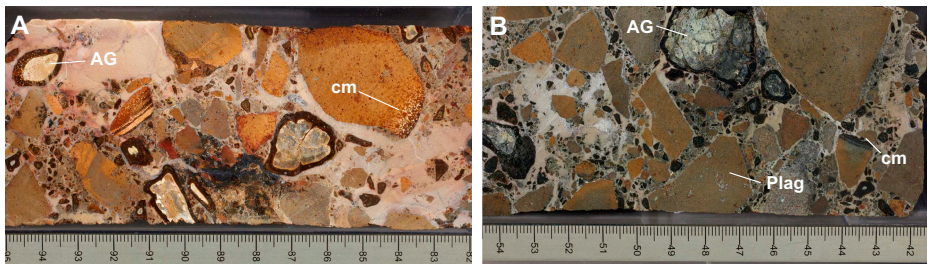

Figure F21. Representative sedimentary breccia showing impact of differing styles of alteration on appearance of rock, Hole U1557D Subunit 1b. A. More oxidative alteration style (2R-1 [Piece 16, 82–95 cm]). Note chilled margin (cm) in orange basalt and concentric zoning of alteration in altered glass (AG) clasts with white to pale yellow cores. B. More reducing alteration style (2R-2 [Piece 4, 41–55 cm]). Note altered glass cores are more pale green to gray. Plagioclase phyric clast (Plag) is relatively uncommon among Site U1557 breccias.

Subunit 1c was recovered only in Hole U1557D. It is a 98.1 m thick interval of sedimentary breccia, variably cemented by carbonate and zeolites. In many respects, it is similar to Subunits 1a and 1b. The deposit is poorly sorted and clast supported. The clasts are predominantly aphyric basalts and include the gray, brown, and orange varieties; altered glass is common throughout and locally abundant (e.g., intervals 390-U1557D-7R-1, 14–28 cm, and 10R-1, 34–47 cm; Figure **F23**). The main difference between Subunits 1b and 1c is the absence of pelagic sediment matrix and the presence of calcite and zeolite cements instead. Calcite cementation is first present in Section 3R-1 (Subunit 1b), but it becomes the dominant cement material starting in Section 3R-3 (Figure **F24**), which defines the boundary between the two subunits. In Sections 3R-3 through 8R-2, the

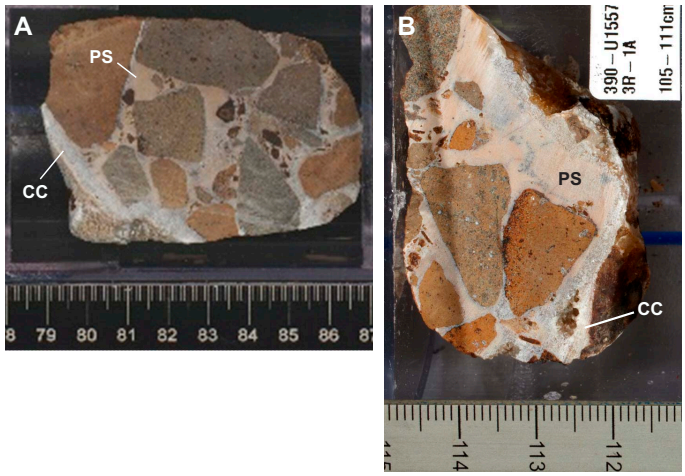

Figure F22. Sparry calcite vein, Subunit 1b. A. 390-U1557D-3R-1 (Piece 4, 79–85 cm). B. 3R-1 (Piece 6, 105–111 cm). PS = pelagic sediment, CC = calcite cement.

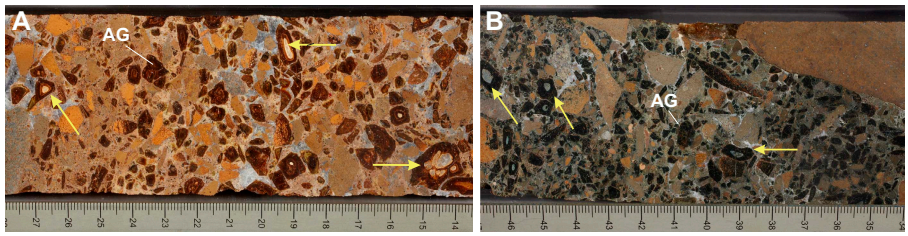

Figure F23. Intervals with high modal proportions of altered glass (AG), Subunit 1c. Yellow arrows = altered glass clasts showing particularly good concentric zoning. A. 390-U1557D-7R-2 (Piece 1, 14–28 cm). B. 10R-2 (Piece 3, 14–28 cm).

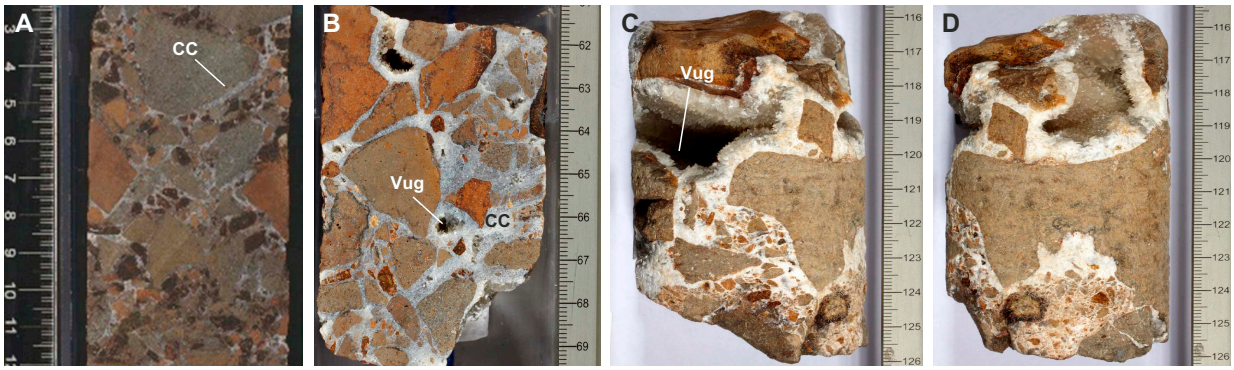

Figure F24. Variation in calcite cement styles, Subunit 1c. A. Calcite forms thin, clast-rimming cement (390-U1557D-4R-1 [Piece 1, 0–12 cm]). B–D. Calcite occurs as coarse-grained sparry calcite associated with vuggy porosity. (B: 3R-4 [Piece 6, 61–70 cm], C, D: 5R-1 [Piece 12, 116–126 cm]). Note that in C and D, vug connects from one side of core to the other.

calcite ranges from thin, clast-rimming cement to coarse calcite spar that can be associated with significant vuggy porosity (Figure **F24**) (**Alteration petrology**). Throughout this interval, patches of pinkish gray (5YR 7/2) to light brown (7.5YR 6/3) clay-sized material occur that superficially resemble pelagic sediment in the core (Figure **F25**). This material is commonly associated with areas where fine-grained igneous detritus concentration is high (Figure **F25B**). However, thin section analysis shows that this material is not pelagic sediment. Rather, the detritus-rich areas are typically cemented by a zeolite ± micritic or microsparry calcite (Figure **F26**). The zeolite is commonly relatively coarse grained, subhedral to euhedral, with a bladed habit in which the blades

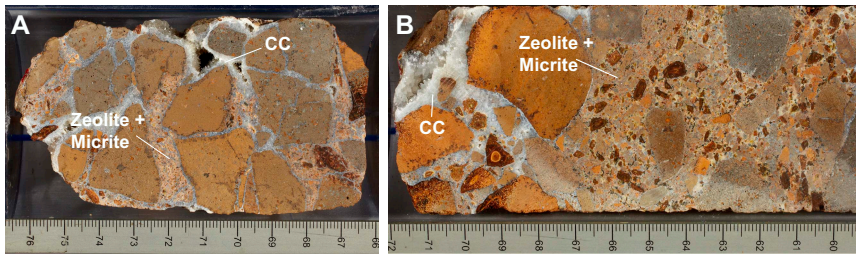

Figure F25. Patches of zeolite-cemented igneous detritus with sparry calcite cements (CC), Subunit 1c. A. 390-U1557D-4R-5 (Piece 11, 66–76 cm). B. 7R-3 (Piece 7, 60–71 cm).

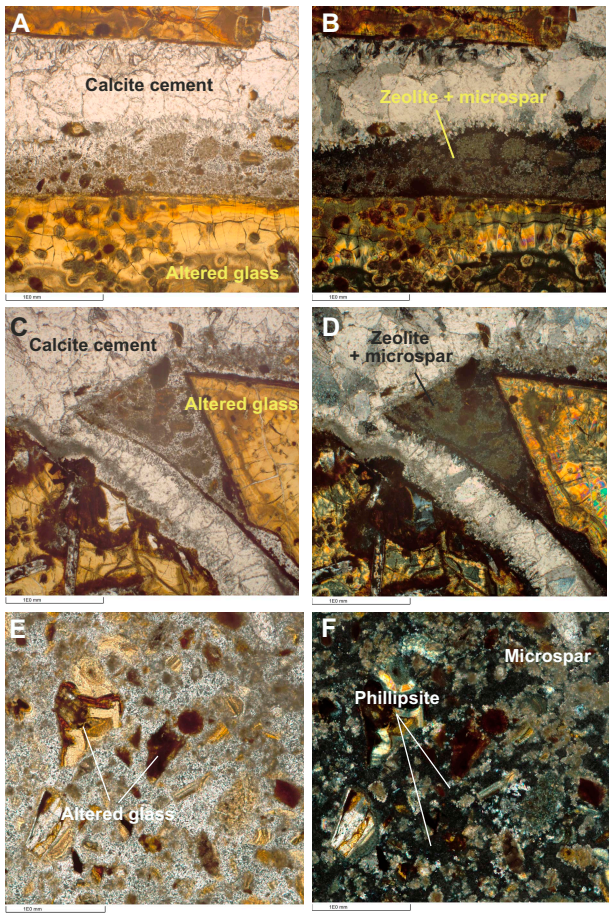

Figure F26. Zeolite cement, Subunit 1c. A, B. Layer of igneous detritus between altered glass clast and sparry calcite vein (390-U1557D-5R-3 [Piece 13, 109–111 cm]; A: PPL, B: XPL). Detritus is cemented by zeolites. C, D. Patch of igneous detritus that appears to be truncated by two calcite veins (5R-3 [Piece 13, 109–111 cm]; C: PPL, D: XPL). At edges of sediment patch, zeolites exhibit bladed habit with euhedral terminations that project into calcite vein. E, F. Common association between igneous detritus–rich areas and cementation by zeolites (10R-3 [Piece 1, 22–24 cm]; E: PPL, F: XPL). Micritic or microspar calcite may also contribute to cementation.

grow perpendicular to clast surfaces (Figure **F27**). In some cases, the crystals are large enough for sector twinning to be observable (Figure **F27A, F27B**), a growth habit that is typical of the zeolite phillipsite. Phillipsite has been confirmed by XRD analysis, and it is the predominant zeolite in Site U1557 basement (see **Alteration petrology**).

The coarse-grained, bladed growth habit is primarily observed in association with altered glass (Figures **F26**, **F27**), which is not surprising because altered glass is a common source of the dissolved silica and aluminum required for phillipsite crystallization (Kastner, 1979). Where phillipsite is the cementing material, in areas with high modal proportions of silt- and sand-sized igneous particles (Figure **F26C–F26F**), its habit is anhedral and/or cryptocrystalline, but the two morphologies grade from one to the other. Sample 390-U1557D-10R-1 (Piece 9, 122–124 cm), for example, shows a patch of fine-grained igneous detritus adjacent to an altered glass clast; it is cemented by fine-grained, anhedral phillipsite that grows outward as blades with euhedral terminations against sparry calcite that fills the center of a vein (Figure **F27E, F27F**).

Although phillipsite is one of the most common zeolite minerals in marine systems (Kastner, 1979; Walton and Schiffman, 2003), it generally does not occur below 500 m in the sediment column. The presence of phillipsite throughout this hole may, therefore, have implications for the origin and diagenesis of the Site U1557 breccias. Phillipsite is a hydrated K-Na-(Ca)-rich aluminosilicate that forms during low-temperature (<150°C) diagenesis. It requires a source of dissolved silica and aluminum to form, and it is usually assumed that altered glass and/or smectite are the main min-

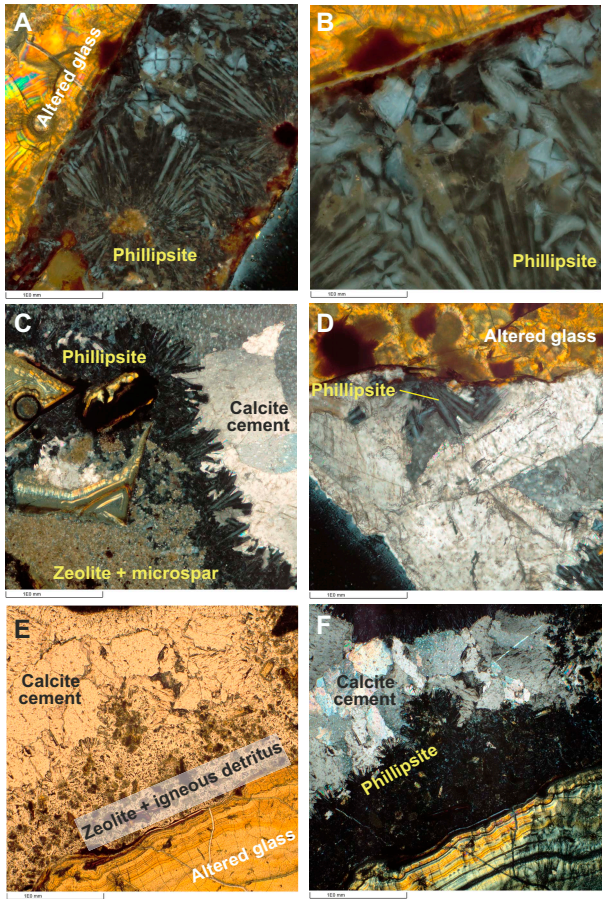

Figure F27. Phillipsite cement styles in breccias, Hole U1557D. A. Coarse-grained phillipsite showing bladed habit adjacent to altered glass (5R-3 [Piece 13, 109–111 cm]; XPL). B. Phillipsite exhibiting sector twinning (5R-3 [Piece 13, 109–111 cm]; XPL). C. Phillipsite varying from cryptocrystalline habit adjacent to altered glass clast to bladed habit with euhedral terminations against sparry calcite in the vein (6R-1 [Piece 2, 34–36 cm]; XPL). D. Euhedral phillipsite crystals growing from altered glass clast and projecting into sparry calcite vein (5R-3 [Piece 13, 109–111 cm]). E, F. Igneous detritus cemented by cryptocrystalline phillipsite that transitions into bladed morphology with euhedral terminations projecting into sparry calcite cement (10R-1 [Piece 9, 122–124 cm]; E: PPL, F: XPL).

eral precursors. The strong association of phillipsite with altered glass at Site U1557 (Figures **F26**, **F27**) is consistent with this assumption. Moreover, we observe examples of spongy disintegration of altered glass where phillipsite occupies the pore spaces created by the breakdown of the altered glass (Figure **F28**). Depending on the sequence of diagenetic events, this could have implications for element mass balance during alteration of oceanic crust. Some studies of seafloor alteration of basaltic glass propose that the process leads to the complete loss of Si and alkali elements to seawater (Kruber et al., 2008). However, crystallization of phillipsite may fix some of the Si (along with Na, K, and some incompatible trace elements) released within the altered crust and/or sequester some of it from seawater. Indeed, preliminary analysis based on portable X-ray fluorescence (pXRF) data (see **Clast petrology**) shows significant enrichment in K in the detrital basalt clasts at Site U1557.

Breakdown of the altered glass also appears to contribute to the silt- and sand-sized fraction within the rocks, even after deposition (Figure **F28A, F28B, F28E, F28F**). Although the bladed rimming morphology is most commonly observed in association with altered glass, it is also present surrounding highly altered basaltic clasts (Figure **F29A, F29B**), where it has been shown to derive the silica it needs to stabilize its growth from secondary minerals such as smectite (Kastner, 1979).

Growth relationships observed in thin section indicate that phillipsite precedes sparry calcite in the diagenetic history of the Site U1557 breccias. The euhedral terminations on the bladed phillipsite crystals suggest growth into open space unopposed by other minerals, and Figures **F26**,

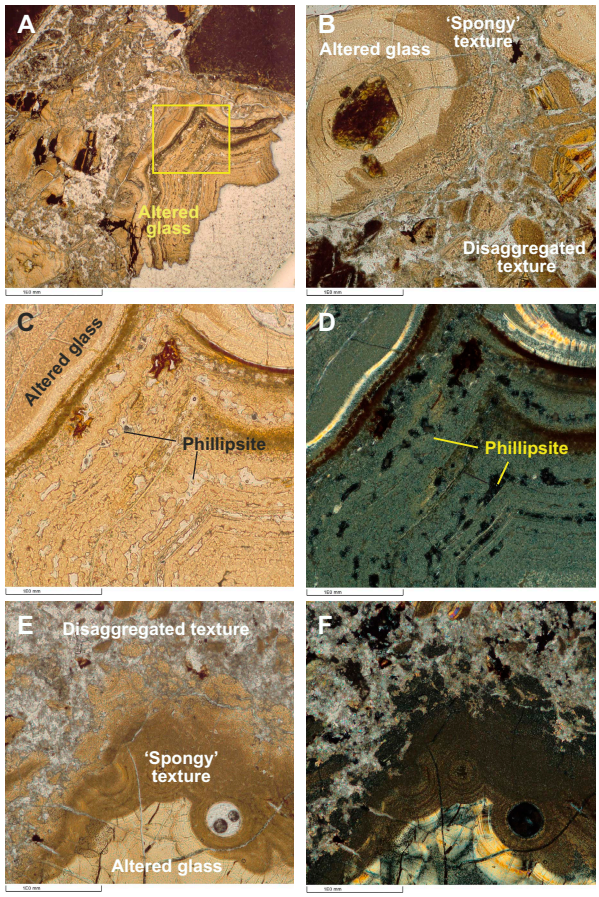

Figure F28. Spongy disintegration of altered glass, Hole U1557D. A. Fibrous palagonite shows concentric zoning (14R-4 [Piece 5, 110–112 cm]; PPL). Yellow box = area enlarged in C and D. B. Spongy disintegration of altered glass (13R-4 [Piece 1, 28–30 cm]; PPL). Note sea of altered glass fragments to right of spongy boundary. C, D. Close-up images of spongy altered glass shown in A (C: PPL, D: XPL). Pore spaces created by spongy disintegration are filled with phillipsite. E, F. Spongy altered glass from higher in hole where phillipsite typically occurs in association with micritic or microspar calcite (7R-2 [Piece 2, 85–87 cm]; E: PPL, F: XPL).

F27, and F28 show that calcite commonly occupies the centers of the veins or voids into which the blades of phillipsite grew. In addition, patches of silt- and sand-sized igneous detritus that have been cemented by phillipsite appear to behave like clasts themselves where they were later disrupted by the calcite veining (Figure F29D). In Sample 390-U1557D-6R-6 (Piece 1, 1–3 cm), the calcite veining has detached not only some of the rimming phillipsite cement but also a sliver of the basalt to which it was attached (Figure F29E, F29F).

Although both calcite and zeolite cements occur between Sections 390-U1557D-3R-3 and 8R-2, calcite is almost always the dominant cement. However, between Sections 8R-3 and 10R-2 there are breccia intervals where the clasts are more highly compacted (e.g., higher ratio of clasts to matrix and some apparent preferred alignment of clasts) (Figure F30) and zeolite cements dominate over calcite. From Section 10R-3 to the bottom of the hole, several characteristics of the breccia change in concert: (1) the degree of compaction increases, (2) the reduction in calcite cement continues, and (3) there is evidence for deformation (Figure F31). Microscopic examination shows that these structural features have resulted in significant comminution of clasts (Figure F32A), and at least some of the deformation must have occurred after calcite cementation because the deformation has produced rounding of sparry calcite crystals in the zone of movement (Figure F32B). The deformation has also led to realignment of clasts into preferred orientations and cataclasis (Figure F32C–F32F). Detailed structural measurements were not made during shipboard macroscopic description because of time constraints; however, aside from a small fault in Section

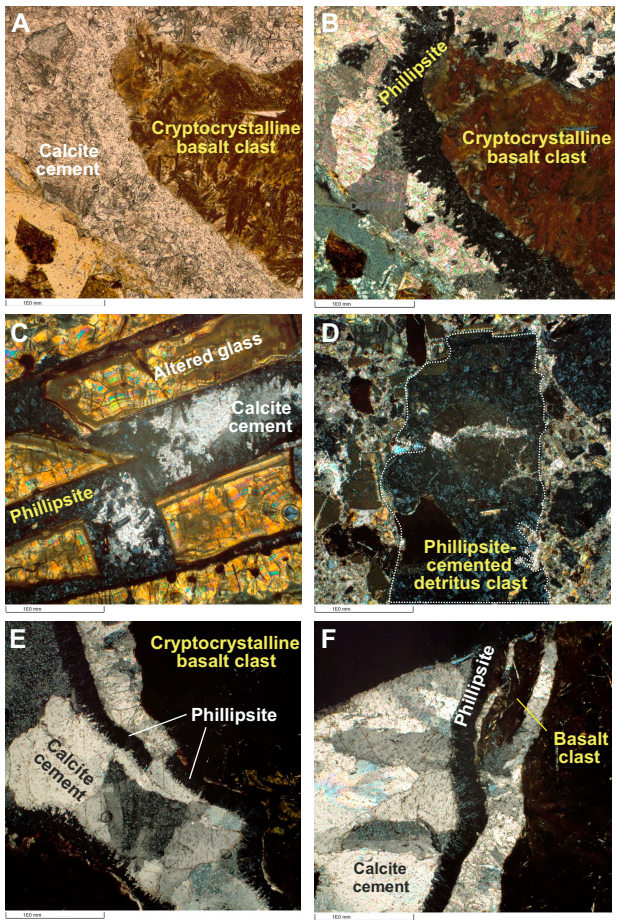

Figure F29. Phillipsite cement styles in breccias, Hole U1557D. A, B. Phillipsite rimming cryptocrystalline basalt clast with euhedral crystal terminations projecting into calcite vein (8R-3 [Piece 4, 102–106 cm]; A: PPL, B: XPL). C. Phillipsite growing radially from altered glass clasts with euhedral terminations projecting into calcite cement (5R-3 [Piece 13, 109–111 cm]). D. Detritus-rich area, cemented by phillipsite, that was later disrupted by calcite veining and cementation such that the phillipsite-cemented area behaves like a clast (10R-3 [Piece 5, 131–134 cm]). E. Phillipsite rimming cement that has detached from basalt clast and broken in two by sparry calcite veining (6R-6 [Piece 1, 1–3 cm]; XPL). F. Rimming phillipsite cement has been detached from basalt clast along with a sliver of basalt (6R-6 [Piece 1, 1–3 cm]; XPL).

11R-2, most of the deformation features observed were relatively small scale (less than a few centimeters thick) and gently to steeply dipping (Figure **F31**). The role of fluids in facilitating the deformation may have been significant because there are low-angle to subhorizontal calcite veins parallel to deformation surfaces (Figure **F33**), particularly from Section 13R-3 to the bottom of the hole. Whether these structural elements represent the base of the talus deposit at Site U1557 or more localized, smaller scale features will require detailed shore-based research.

Subunit 1c is defined by the overall absence of pelagic sediment matrix. However, during microscopic analysis of the core, two fragments of foraminifera are present in the lowermost two cores of the hole (Sections 390-U1557D-13R-2 and 14R-2; Figure **F34**). We do not take these fossil fragments as evidence that there was ever a significant quantity of pelagic sediment in Subunit 1c, however. As seen at Site U1556, it is not uncommon for pelagic sediment to be intercalated within the chilled margins of pillow basalts. The fossil fragments could simply have been entrained along with the basalt and altered glass clasts when the breccia was formed.

5.1.2. Stratigraphic interpretation

The Site U1557 breccias formed as a talus pile adjacent to fault scarps that bound the sediment basin in which it now occurs. Our observations are not consistent with eruption of basaltic magma

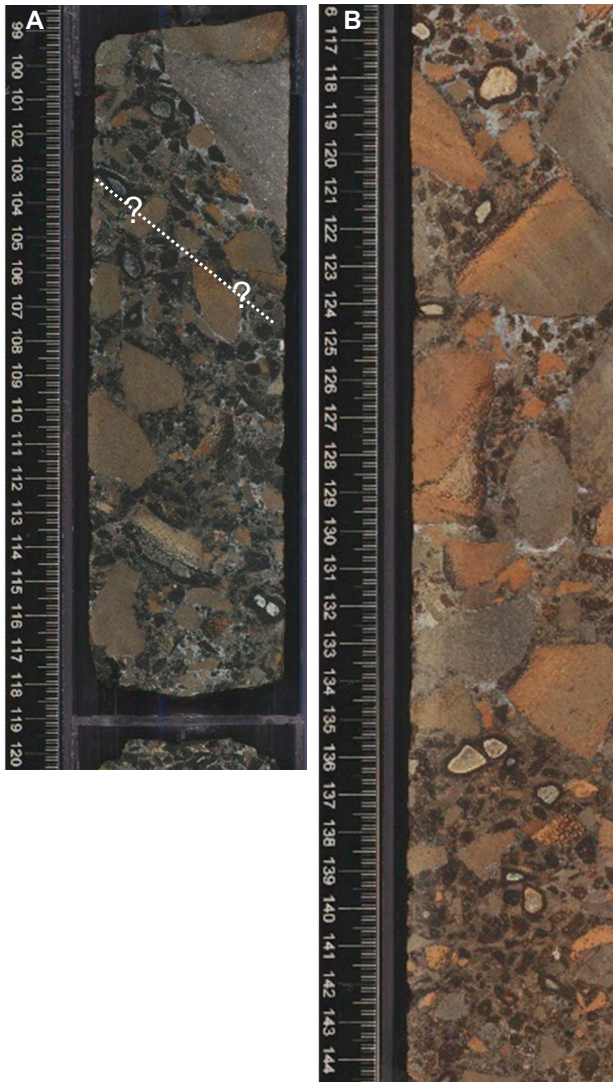

Figure F30. Increase in compaction toward bottom of Hole U1557D. A. 10R-1, 99–118 cm. White dashed line = possible preferred alignment of clasts created by compaction and/or deformation. B. 10R-2, 116–144 cm. See Figures F16, F20, F21, F22, and F25 for examples of rock textures higher in hole.

into a sediment pond or even deposition of the basalt clasts into a thick sequence of pelagic sediment. Significant amounts of pelagic sediment are limited in occurrence to the uppermost ~10 m of the deposit. The sediments in this interval could have infiltrated from the top during deposition of the overlying pelagic sedimentary sequence. Moreover, to support the widespread crystallization of phillipsite within the breccias, there must have been considerable pore space available in between breccia clasts because phillipsite is known to form where sedimentation rates are low (Kastner, 1979). Whether the breccia deposit formed as a single mass wasting event or accumulated gradually will require detailed shore-based research to resolve.

5.2. Clast petrology

5.2.1. Clast type variation with depth

Although the basement rocks at Site U1557 are essentially a sedimentary deposit, we examined the breccia clasts recovered in terms of their igneous petrology based on macroscopic core descriptions, thin section analysis, and geochemistry (as determined by pXRF) (see **Igneous petrology** in the Expedition 390/393 methods chapter [Coggon et al., 2024c]). The purpose of this analysis was to assess whether there were any systematic variations in clast type with depth that

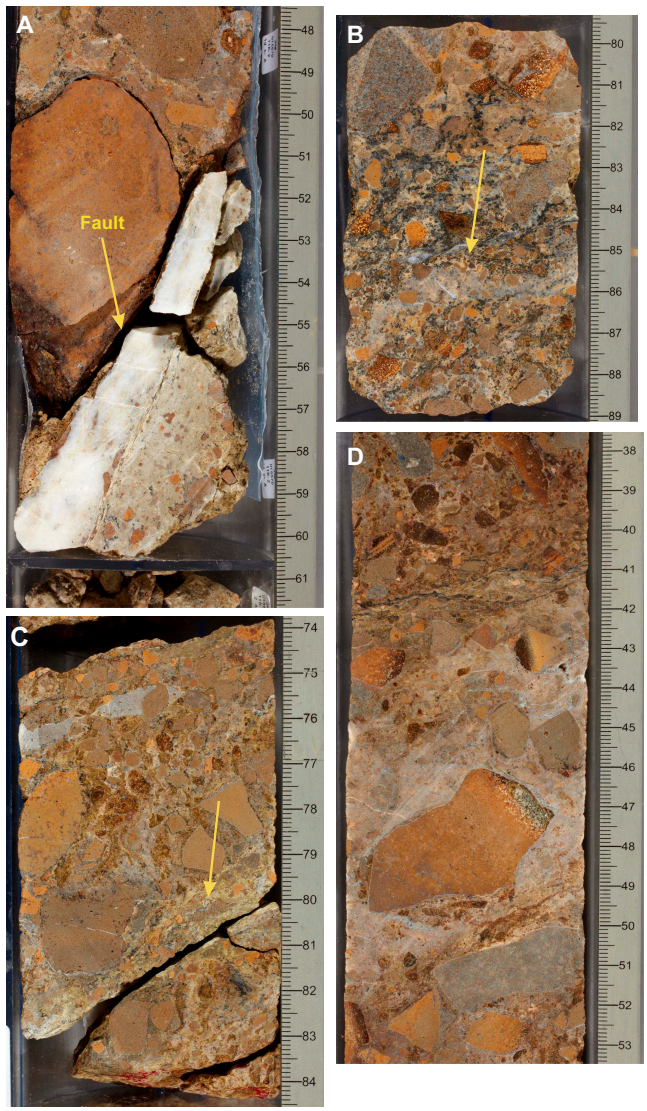

Figure F31. Deformation features, Hole U1557D. A. Fault surface is lined by thick calcite vein, with fault gouge below and to the right (11R-2, 48–61 cm). B, C. Zone of most intense deformation in a ~1 cm wide interval (B: 12R-9, 60–89 cm, C: 14R-4, 74–84 cm). D. Interval of deformation spans ~7 cm (13R-3, 38–53 cm).

might affect physical properties (see **Physical properties and downhole measurements**). In addition, at Site U1556 we observed that volcanostratigraphic sequences maintained similar physical characteristics over tens (possibly hundreds) of meters. As such, depending on the depositional mechanism, the breccia deposit at Site U1557 might record the stratigraphy of the uplifted fault blocks from which it was derived. Such information could provide insights into whether the breccia formed as a single depositional event or accumulated gradually. We also wanted to assess whether the basalts at Site U1557 encompassed the same lithologies as those observed at Site U1556, particularly the presence or absence of alkali basalts.

Time constraints limited us to only a very qualitative assessment of clast abundance. Using the three color-based categories that emerged from macroscopic core description, we ranked the clasts from most to least abundant (or absent) based on visual estimates down the hole (i.e., the exercise resulted in a qualitative ranking, not a quantitative assessment of modal proportions). We did not include altered glass as a clast for this analysis because it commonly occurs as small pebbles or sand- to silt-sized particles in the matrix. It was also not possible to link the altered glass to a specific basalt lithology based on macroscopic observation, which limited its utility in this context.

Figure **F35** shows the results of the analysis. In general, all three clast types (gray, brown, or orange) are present throughout the hole, and there are no significant gaps or trends in occurrence. However, we note that gray clasts tend to be either the most abundant lithology in a given interval or in very low abundance to absent. In contrast, orange clasts are rarely the most abundant, and only below Core 390-U1557D-6R, but they were the least likely to be entirely absent. Brown clasts tended to be the most abundant, ranking first or second in abundance more often than either gray or orange basalts.

As a first-order qualitative analysis, we believe the lack of systematic stratigraphic variations is inconsistent with the talus pile forming through the progressive erosion of a stratigraphic succession from an adjacent fault scarp. If it were, we would expect to see long intervals that represent a more limited range of clast types. Instead, the Site U1557 breccia probably formed as one or more

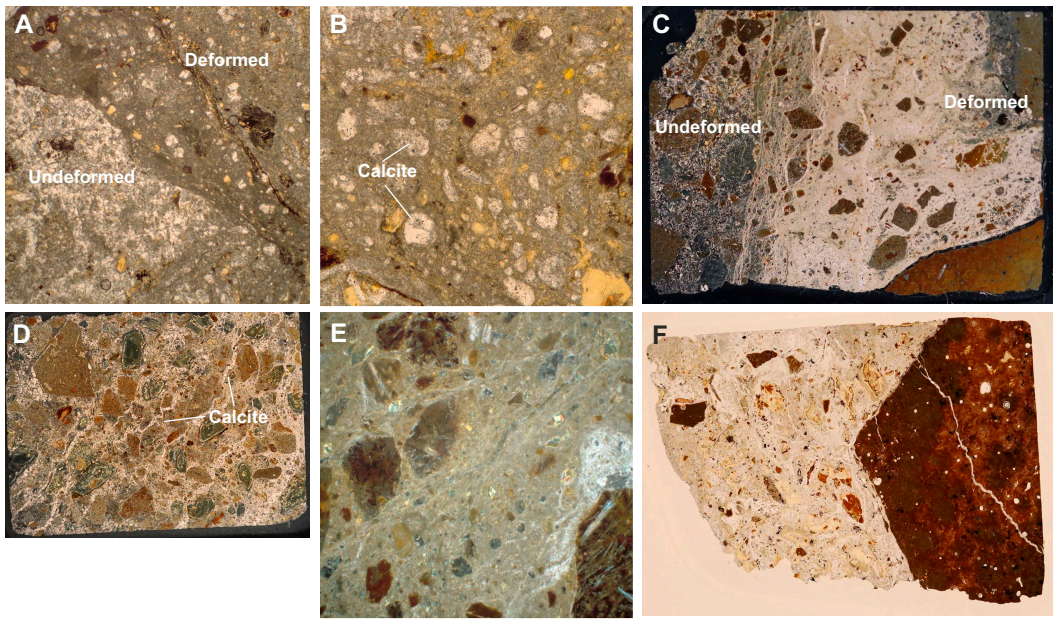

Figure F32. Comminution and preferred alignment of grains in response to deformation, Hole U1557D (PPL). A. Lower left area is relatively undeformed vs. upper right, which has undergone considerable grain size reduction (12R-6 [Piece 2, 50–53 cm]). B. Rounding of isolated calcite crystals indicates deformation occurred after calcite cementation (12R-6 [Piece 2, 50–53 cm]). C. Boundary between deformed and undeformed breccia (12R-6 [Piece 2, 50–53 cm]). D. Significant grain size reduction and realignment in zone of deformation (11R-2 [Piece 4, 81–84 cm]). E. Preferential alignment of elongate grains parallel to direction of deformation (10R-3 [Piece 5, 131–134 cm]). F. Coincidence of deformation and some calcite veins (14R-2 [Piece 2, 26–29 cm]).

slump/mass wasting events that mixed lithologies over multiple stratigraphic (magmatic) sequences.

5.2.2. Petrographic observations

The basalt clasts at Site U1557 are predominantly aphyric; however, where phenocrysts (or microphenocrysts) are present, the rocks are predominantly plagioclase phyric or olivine phyric. Highly or even moderately plagioclase-olivine-clinopyroxene phyric basalts like those present at Site U1556 and other sites along the SAT are uncommon. Green clinopyroxenes (i.e., diopside) are rare

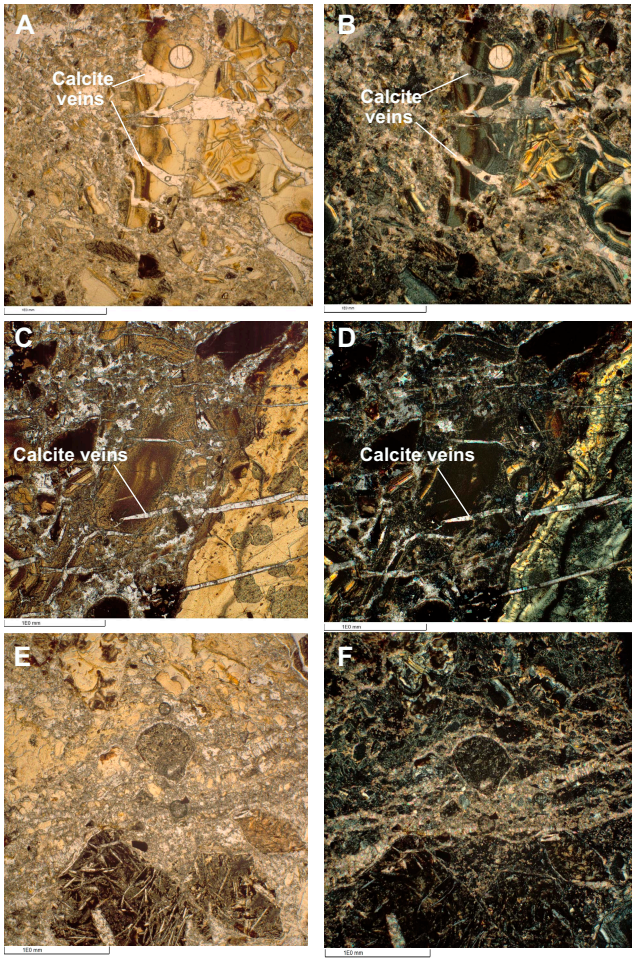

Figure F33. Association of deformation with calcite veins, Hole U1557D. A, B. 13R-2 (Piece 5, 34–36 cm). C, D. 13R-4 (Piece 1, 28–30 cm). E, F. 12R-6 (Piece 2, 50–53 cm). A, C, E = PPL; B, D, F = XPL.

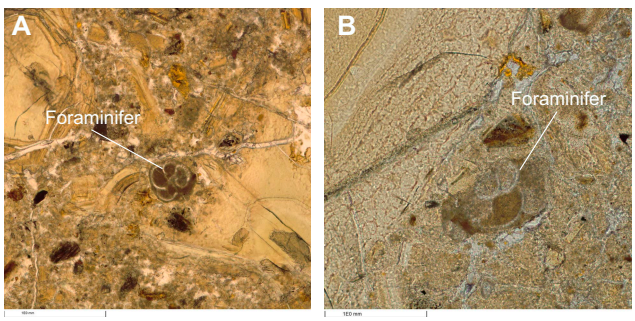

Figure F34. Fossil foraminifera associated with altered glass clasts within breccia deposit, Hole U1557D (PPL). A. 13R-2 (Piece 5, 34–36 cm). B. 14R-2 (Piece 2, 26–29 cm).

in the core, and thin section analysis confirmed that titanaugite is not present. The latter indicates that alkali basalts were not recovered at Site U1557, and this observation is confirmed by the pXRF analyses (see **Insights from pXRF analysis** and **Geochemistry**). In this sense, the rocks are more typical of mid-ocean-ridge basalts (MORBs; i.e., tholeiitic). Compositionally, this makes them most similar to Stratigraphic Sequence C at the bottom of Hole U1556B. Although plagioclase phenocrysts/macrocrysts are rare, where they are seen, they exhibit a multistage history, having older cores that were partially resorbed and enclosed in a younger phase of plagioclase crystallization (Figure **F36A**), similar to plagioclase macrocrysts in highly plagioclase-olivine-pyroxene phyric (H-POPP) basalts at Site U1556.

We also encountered basalts with microcrystalline textures that were not observed at Site U1556 (Figure **F36C**). These are typically gray basalts that range from aphyric to sparsely plagioclase ± olivine phyric. In thin section, they exhibit subophitic textural relationships between clinopyroxene and plagioclase (Figure **F36D**).

Finally, although olivine was observed to contain small equant crystals of Cr-spinel in several samples from Site U1556, much larger Cr-spinels are present as discrete crystals in at least two samples from Site U1557 (Samples 390-U1557D-6R-4 [Piece 5, 104–105 cm] and 14R-3 [Piece 3, 85–87 cm]) (Figure **F36B**). The composition of Cr-spinel is known to be a good indicator of the melt composition from which it crystallized (Kamenetsky et al., 2001). These crystals can, therefore, provide information on preeruptive petrogenetic events, such as magma chamber recharge. In a deposit where the basalts are as thoroughly altered as those from Site U1557, Cr-spinel composition could be a useful tool for reconstructing at least some of the primary igneous petrogenesis.

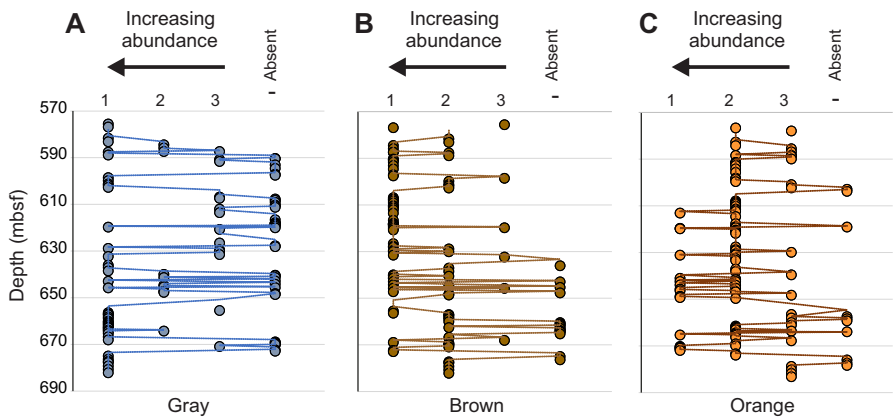

Figure F35. Clast modal abundance ranking for (A) gray, (B) brown, and (C) orange basalts, Hole U1557D. 1 = most abundant, 3 = least abundant. If clast type was not observed, it was listed as absent rather than least abundant.

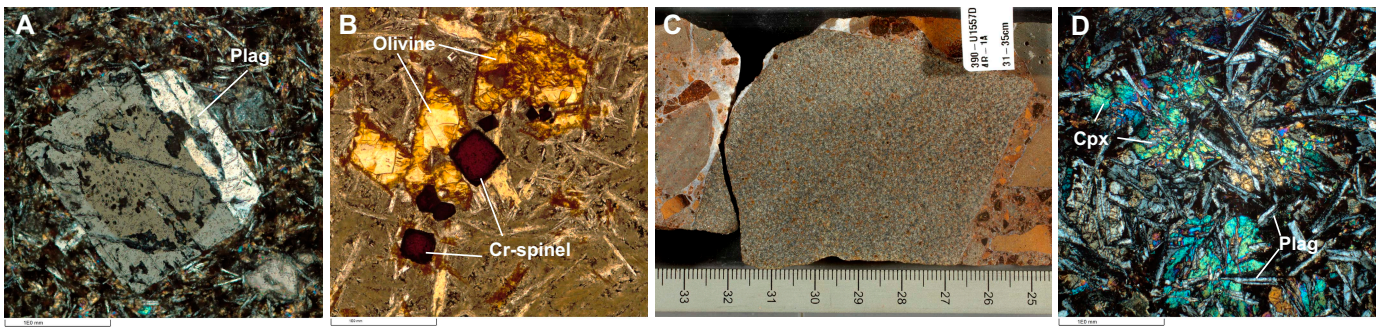

Figure F36. A. Plagioclase (Plag) phenocryst/macrocryst (390-U1557D-6R-4 [Piece 5, 104–105 cm]; XPL). B. Discrete Cr-spinel crystals (14R-3 [Piece 3, 85–87 cm]; PPL). C. Representative microcrystalline basalt clast (4R-1, 24–33 cm). D. Typical microcrystalline basalt groundmass texture (4R-1 [Piece 13, 124–127 cm]; XPL). Cpx = clinopyroxene.

5.2.3. Insights from pXRF analysis

Petrologic interpretations made from macroscopic core descriptions and thin section observations were corroborated using geochemical data produced by pXRF (see **Geochemistry**). A total of 53 analyses of 44 discrete basaltic clasts were determined from the archive half of the core along with 52 analyses of 20 sample powders prepared for inductively coupled plasma–atomic emission spectroscopy (ICP-AES). Our sampling includes clasts from all groups (i.e., gray, brown, and orange). As explained in the **Site U1556** chapter [Coggon et al., 2024a], in our usage of the pXRF we found that most elements were insufficiently precise and/or accurate or too mobile in response to alteration to be useful for examining aspects of primary igneous petrogenesis (see **Geochemistry**). We have, therefore, relied on the ratio of Zr to Ti, normalized to the average normal MORB (N-MORB) composition of Sun and McDonough (1989) (i.e., $[Zr/Ti]_N$), for our analysis. Note that we have applied the same correction procedure to the samples from Site U1557 as we did for Site U1556 (see **Igneous petrology** in the Site U1556 chapter [Coggon et al., 2024a]). Our results are shown in Figure **F37** relative to the data for basalts from Site U1556.

Basalt breccia clasts from Site U1557 have $[Zr/Ti]_N$ values similar to N-MORB and overlap the compositions of Stratigraphic Sequence C (H-POPP) basalts, although with considerably more scatter. Three of the more extreme high values, one from a brown basalt (Section 390-U1557D-2R-2, 36 cm) and two from orange clasts (Sections 4R-4, 88 cm, and 4R-5, 142 cm) overlap the compositions of alkali basalts from Site U1556 (Stratigraphic Sequences A and B) even though petrographic evidence indicates that these basaltic clasts are not of this lithologic type. Conversely, one sample (11R-2, 22 cm) has the lowest $[Zr/Ti]_N$ value measured during Expedition 390, which is significantly lower than N-MORB (Figure **F37**). These extreme values should be considered with caution, however, considering the ~1 cm^2 analytical footprint of the pXRF instrument and hence its propensity for perturbation by inadvertent analysis of phenocrysts.

The data are plotted in Figure **F37B** on an expanded scale relative to Figure **F37A** and distinguished by clast color so that variations within each color group can be seen more easily. The data show that the gray clasts (i.e., those that are least altered) have the smallest range of $[Zr/Ti]_N$ values. The average value for the gray basalt clasts (0.92 ± 0.06) is slightly lower than average N-MORB but overlaps the compositions of H-POPP basalts from Site U1556 (0.91 ± 0.03). Somewhat surprisingly, the brown clasts, which were assumed to be the next least altered, extend to both significantly higher and lower values than both the gray and the orange basalts; the range for brown clasts is 0.51–1.69, whereas the range for orange clasts is 0.71–1.36.

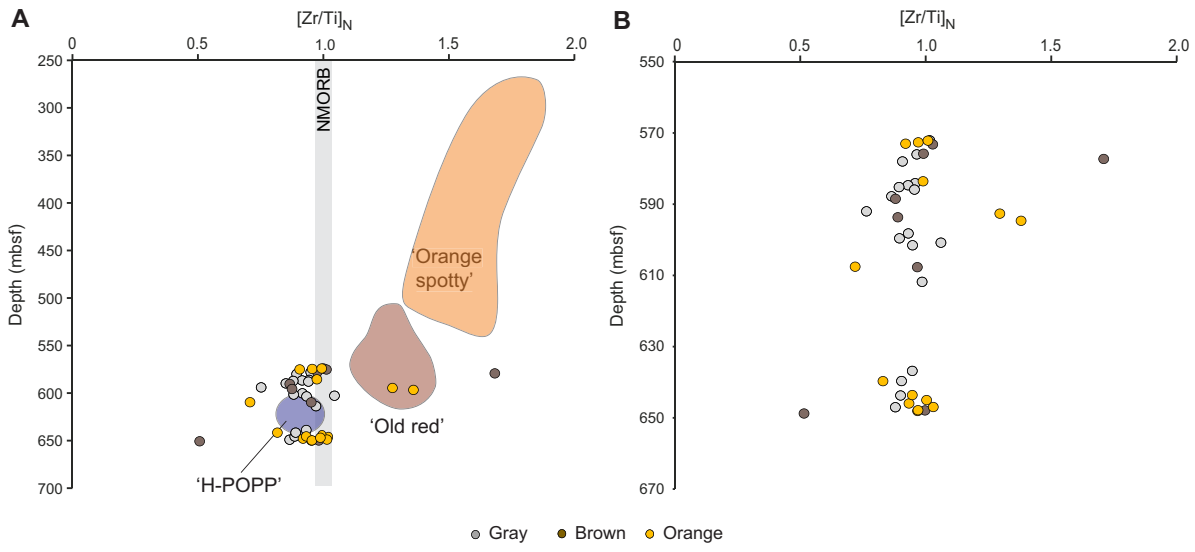

Figure F37. A. $[Zr/Ti]_N$ for Site U1557 basalt breccia clasts compared with Site U1556 basalts (shaded areas). Note that we used depth below seafloor rather than subbasement depth because we are interested in assessing stratigraphic equivalence to rocks recovered at Site U1556. Average N-MORB normalization from Sun and McDonough (1989). B. Data for Site U1557 basalt breccia clasts on expanded scale so that compositional variations within each group can be seen more easily. See Geochemistry in the Expedition 390/393 methods chapter (Coggon et al., 2024c) for details of data quality analysis and data correction procedures.

The data suggest that the $[Zr/Ti]_N$ ratio may have been affected by alteration in some samples, and the variation appears to be related more to the behavior of Ti than to Zr. The samples with the anomalously high $[Zr/Ti]_N$ (Samples 390-U1557D-2R-2, 36 cm; 4R-4, 88 cm; and 4R-5, 142 cm) have much lower TiO_2 concentrations than is typical for the basalt clasts (~0.5–0.6 wt% corrected concentration as compared to ~1.0 ± 0.1 wt% for basalt clasts on average). Conversely, the sample with the anomalously low $[Zr/Ti]_N$ (Sample 11R-2, 22 cm) has a corrected concentration of ~1.5 wt% TiO_2. In contrast, the average corrected Zr concentration for the basalt clasts is 54 ± 5 ppm, and all four anomalous clasts have Zr concentrations within that range.

These data indicate that, despite assumptions to the contrary, the concentration of Ti appears to have been affected by alteration in some cases, suggesting that caution should be used when assuming high field strength element immobility during alteration. The impacts of alteration are even more dramatic for some of the large ion lithophile elements (LILEs), namely elements that are well known to be fluid mobile. Figure **F38** shows the variation in the concentration of K relative to $[Zr/Ti]_N$ for the Site U1557 basalt clasts compared with the data for basalts from Site U1556 (Stratigraphic Sequences A–C). Not surprisingly, the alkali basalts from Stratigraphic Sequence A ("orange spotty") have high K concentrations, which is consistent with their alkali basalt compositions. The "old red" basalts (Stratigraphic Sequence B) have lower K concentrations, which is more consistent with an origin as an enriched MORB (E-MORB). The K concentrations for H-POPP basalts (Stratigraphic Sequence C) were too low to be determined by pXRF, but results of ICP-AES analysis indicate concentrations <2000 ppm. By comparison, all of the basalt clasts from the Site U1557 breccia have K concentrations greater than ~3000 ppm. This is five times the K concentration of N-MORB (~600 ppm [Sun and McDonough, 1989]). The highly altered clast with the lowest $[Zr/Ti]_N$ also has the highest K concentration we have measured (>35,000 ppm), which is equivalent to a K_2O content of more than 4 wt%. These high concentrations are potentially consistent with the abundance of phillipsite throughout the core, as discussed above. Other LILEs, such as Sr, do not show these extreme enrichments, even among the most altered basalt breccia clasts (Figure **F38B**). This may be because the data reported here are for basalt clasts only. We did not analyze the breccia matrix separately or attempt whole-rock analysis, given the lithologic heterogeneity of the breccia. Shore-based research is obviously required to understand the full panoply of element fluxes into and out of the breccias at Site U1557.

In summary, if we focus on the least altered samples from Site U1557, the data suggest that there is no systematic variation in clast composition with depth. The overlap in $[Zr/Ti]_N$ compositions of the gray breccia clasts and the H-POPP rocks from Site U1556 and their similarity to N-MORB

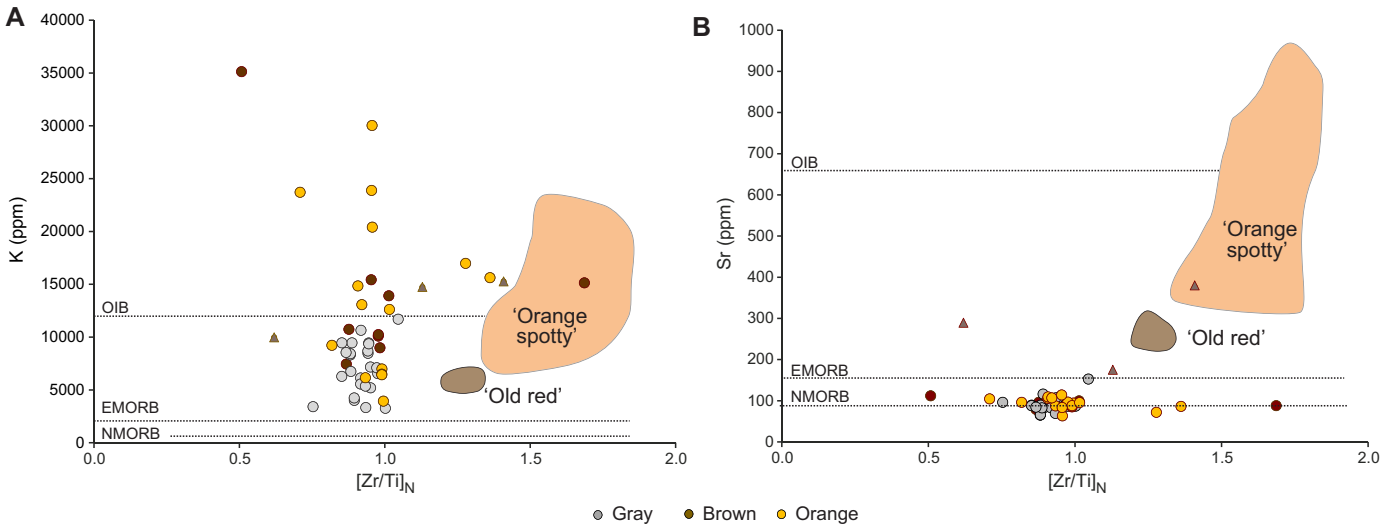

Figure F38. (A) K and (B) Sr vs. $[Zr/Ti]_N$ for Site U1557 basalt breccia clasts compared to basalts from Site U1556 (shaded areas). Brown triangles = highly altered samples of old red (Site U1556 Stratigraphic Sequence B) that do not plot within field as drawn. Average N-MORB, E-MORB, and OIB compositions from Sun and McDonough (1989). See Geochemistry in the Expedition 390/393 methods chapter (Coggon et al., 2024c) for details of data quality analysis and data correction procedures.

(Figure **F37**) suggest they are most likely derived from a mantle source that is similar to that of N-MORB. Alkali basalt compositions like those seen in Stratigraphic Sequences A and B (i.e., orange spotty and old red) at Site U1556 are not observed. Therefore, the breccia clasts at Site U1557 were not derived from the stratigraphic succession observed at Site U1556 6.5 km west of Site U1557. At a spreading rate of 13.5 mm/y for Site U1557 (see **Background and objectives**), there could have been ~500,000 y between the events that formed the seafloor at Sites U1557 and U1556. Whatever the origin of the alkali basalts at Site U1556, the conditions that gave rise to them have been lost in the space (and time) that has been traversed to Site U1557.

6. Alteration petrology

Alteration of the breccias at Site U1557 is variable, with evidence of alteration within the breccia pile as well as earlier alteration prior to brecciation and deposition. A range of different alteration styles are evident, from oxide-rich halos to apparently more reducing conditions characterized by green clay minerals. Alongside alteration of the igneous clasts, there is extensive cementation and filling of void spaces by carbonate and zeolite.

The overall range of alteration is very similar in color, extent, and mineralogy to that present in Hole U1556B, ~6.5 km to the west. However, the basalts at Site U1557 are fragmented and juxtaposed as clasts in a talus breccia where they were further altered. This history gives rise to a number of hybrid styles of alteration and adds complexity to the tasks of logging and interpreting the alteration petrology (Figure **F40**).

The interclast space of the breccias is variably filled with pelagic sediment, sparry carbonate, fine-grained igneous material (glass and basalt), and/or authigenic zeolite + micritic sediment with open millimeter- to centimeter-scale porosity common throughout much of the hole. The volume proportion of porosity and cements decreases downhole (Figure **F55**).

Macroscopic observations of secondary mineralogy were refined using thin section observations and XRD analyses of vein-filling minerals and breccia cements (34 mineral samples + 21 whole-rock powder samples) (Tables **T5**, **T6**). Full alteration and vein logs are available in DESC_WKB in **Supplementary material**; piece logs are available in ALTPET in **Supplementary material**.

6.1. Types of alteration

Alteration in the breccias results from two or more stages, with a range of alteration pre- and post-brecciation histories apparent in the clasts throughout the hole. This dual-stage alteration is most macroscopically apparent in the occurrence of several meter-scale intervals of pervasive dark green alteration that clearly overprint earlier oxidative alteration. These contrast with the rest of the basement cores, where orange alteration colors and mineralogy indicate primarily oxidative alteration.

As in rocks at Site U1556, the expression of alteration in a given rock is partly a function of its primary igneous characteristics, principally grain size and primary mineralogy. Cryptocrystalline rocks are more commonly altered to intense bright orange, whereas coarser grained equivalents may preserve more fresh material and appear grayer in color.

6.1.1. Background alteration

6.1.1.1. Orange speckled background alteration

Orange speckled background alteration represents the freshest material in Hole U1557D. It is defined macroscopically by the occurrence of orange or red speckling in an otherwise moderately altered gray (dark gray [GLEY 1 4/N]) to gray-brown (dark gray [2.5Y 4/1]) groundmass. This type of alteration corresponds to the gray clasts described in **Igneous petrology**. The speckling results from pseudomorphic alteration of olivine to a mixture of smectite and Fe oxyhydroxides (± carbonate), which is often referred to as iddingsite and likely similar to the cryptocrystalline red-brown material replacing groundmass in orange halos (Figure **F39**). The major difference between this and other observed oxidative alteration styles is that alteration of the groundmass is princi-

Table T5. XRD mineral analysis, Site U1557. * = minor phase, † = uncertain, ** = highly uncertain. **Download table in CSV format.**

Core, section, interval (cm)	Top depth CSF-A (m)	Bottom depth CSF-A (m)	Minerals identified	Comments	Sample comments
390C-U1557B-					
66X-2, 71–72	573.92	573.93	Phillipsite (83%) + Calcite (7%) + clays		Pinkish noncarbonate mineral overgrowing vug calcite
390-U1557D-					
2R-1, 88–89	576.48	576.49	Montmorillonite + Calcite + phillipsite		Dark slightly metallic patch - FeMn crust?
2R-1, 115–119	576.75	576.79	Calcite (3% Mg) + zeolite P + *smectite		Orange carbonate sediment matrix
2R-2, 0–12	576.88	577.00	Calcite (6% Mg) + zeolite P + beidellite + phillipsite		Green sediment matrix
3R-1, 87–92	582.57	582.62	Phillipsite + calcite (6% Mg) + †tobermorite/smectite + †merlinoite		Cream massive mineral overgrowing sparry carbonate
3R-2, 34–38	583.52	583.56	Calcite (6% Mg) + *smectite		Dark brown mineral coating sparry vug carbonate
5R-2, 45–50	599.03	599.08	Anorthite + diopside + smectite + *illite + **manganese nickel oxide + amorphous		Unusual blotchy brown thin vein (Fe oxide?)
5R-3, 20–23	600.08	600.11	Calcite + anorthite + †birnessite ($MgMnO_2(H_2O)_{0.8}$)		Dark brown material from thin coating on basalt carb cement contact
7R-4, 103–125	621.78	622.00	Anorthite + diopside + **sanidine + smectite + *illite + amorphous		Whole-round khaki altered basalt from rubble bin
8R-3, 89–90	629.75	629.76	Calcite (6% Mg) + phillipsite + montmorillonite + anorthite + some illite + amorphous		Red mineral in breccia cement
8R-4, 28–30	630.37	630.39	Calcite + †asbolane ($CoH_4Mn_2O_7$) + montmorillonite		Black waxy mineral overgrowing carb in vug
8R-5, 19–24	631.73	631.78	Calcite + phillipsite + smectite + *illite + amorphous		Dark brown lining to carb vein
8R-5, 94–95	632.48	632.49	Calcite (6% Mg) + smectite + †tobermorite + **talc		Carbonate + saponite vein cutting clast
10R-2, 15–30	638.68	638.83	Calcite + phillipsite + *smectite + *illite		White poorly crystalline carbonate bearing cement in green breccia (from rubble bin)
10R-4, 77–82	642.16	642.21	Calcite + pyrolusite (MnO_2) + †magnesioferrite		Gray-black mineral intergrown with sparry carbonate in vug
10R-4, 141–142	642.80	642.81	Saponite + calcite + †tobermorite + **nontronite		Beige/white nodule with orange to red rim overgrowing carbonate
10R-4, 146–147	642.85	642.86	Calcite + pyrolusite (MnO_2) + †tobermorite		Very dark slightly metallic mineral overgrowing carbonate in vug
10R-5, 74–75	643.61	643.62	Montmorillonite + †amesite + †beidellite + †talc		Pale green core of altered green glass
11R-1, 17–20	645.97	646.00	Montmorillonite + calcite + ramsdellite (MnO_2)		Gray-black slightly metallic mineral forming wide stripes with carbonate in vein
11R-2, 38–43	647.62	647.67	Calcite + phillipsite + montmorillonite + †rectorite		Slickensided green and brownish vein
11R-2, 70–73	647.94	647.97	Calcite + phillipsite + †sanidine + †zeolite Y		Fault vein/fault gouge
11R-2, 81–86	648.05	648.10	Calcite + montmorillonite + phillipsite + zeolite P		Green/yellow-gray fault gouge (from rubble bin)
11R-2, 123–124	648.47	648.48	Calcite (6% Mg) + phillipsite + **blodite (sulfate)		Sediment from below fault zone for comparison with fault gouge
12R-2, 76–79	657.20	657.23	Montmorillonite + calcite (10% Mg) + †beidellite + **MnO,OH	Unusually ordered montmorillonite pattern	Nodules of black mineral, sparkly/velvety?
12R-5, 36–38	659.30	659.32	Phillipsite + smectite + amorphous + †chabazite		Pale green from core of green glass clast
12R-6, 114–116	661.20	661.22	Calcite (6% Mg) + phillipsite + smectite + chabazite		Botryoidal pale yellow core of glass clast
12R-9, 84–85	664.73	664.74	Calcite (6% Mg) + phillipsite + smectite + amorphous + **blodite		Black flecked yellow sediment FeMn, clay, oxides?
13R-3, 92–93	669.02	669.03	Calcite + †asbolane + montmorillonite		Very dark brownish gray clay overgrowing vug carbonate (same as one mistaken for mud)
13R-4, 24–25	669.84	669.85	Montmorillonite + mostly amorphous	Very poor pattern	Brown not orange glass (from core of clast)
13R-4, 46–48	670.06	670.08	Montmorillonite + saponite + **sepiolite + amorphous	Very poor pattern	Orange core of glass clast
13R-5, 109–110	672.01	672.02	Phillipsite + chabazite + †tobermorite/smectite + *amorphous		Yellow-green botryoidal core of glass
13R-6, 9–10	672.46	672.47	Calcite (6% Mg) + montmorillonite + phillipsite		Yellow-gray carbonate-bearing core of glass
14R-1, 113–115	676.13	676.15	Calcite + anorthite + montmorillonite + phillipsite + augite	Igneous minerals likely from lithic clasts	Dark altered sediments from very brown altered zone (2 cores)
14R-4, 85–92	680.11	680.18	Calcite + phillipsite + montmorillonite + †celadonite		Fault gouge? greenish yellowish gray (from rubble bin)

pally to smectite clays with relatively little reddening from Fe oxyhydroxides. The distinction between orange speckled background alteration and khaki-brown (gray [7.5YR 5/1]) background alteration (see **Khaki-brown background alteration**) is gradational in macroscopic color and secondary mineralogy.

6.1.1.2. Khaki-brown background alteration

The most abundant alteration type in Hole U1557D is basalt altered to a distinct khaki-brown color (gray [2.5Y 5/1] to brown [10YR 5/3]) (Figure **F40**). This type of alteration corresponds to the brown clasts described in **Igneous petrology**. Olivine phenocrysts, if present, are ubiquitously altered to brick-red, similar to orange speckled background. At the scale of individual clasts, this style of alteration can appear quite variable and commonly grades into intense orange halos or, more rarely, grayer orange speckled background. Nonetheless, allowing for differences in the expression of alteration by basalts of different grain size, the color and macroscopic appearance of

Table T6. XRD mineral analysis of ICP-AES powder preparations, Site U1557. * = minor phase, † = uncertain. **Download table in CSV format.**

Core, section, interval (cm)	Top depth CSF-A (m)	Bottom depth CSF-A (m)	Minerals identified	Sample comments
390C-U1557B-				
65X-1, 15–17	569.55	569.57	Ca albite + diopside + smectite + †*illite	Piece 2
390-U1557D-				
2R-1, 37.5–39.5	575.98	576.00	Anorthite + diopside + montmorillonite + *illite	
3R-2, 56.5–58.5	583.75	583.77	Anorthite + augite + †zeolite A + lots of smectite + *illite	Piece 3A
3R-2, 58.5–61	583.77	583.79	Ca albite + augite + †zeolite A + lots of smectite + *illite	Piece 3A
3R-3, 128–130	585.80	585.82	Anorthite + diopside + montmorillonite + *illite	
4R-1, 28–30	587.68	587.70	Anorthite + diopside + montmorillonite + *illite	Piece 1B
4R-1, 124–127	588.64	588.67	Ca albite + diopside + montmorillonite + *illite	
5R-3, 107–109	600.95	600.97	Anorthite + diopside + smectite + *illite	Piece 12
5R-4, 108–109	602.36	602.37	Anorthite + diopside + smectite + *illite	Piece 12
6R-4, 101–103	611.60	611.62	Anorthite + diopside + montmorillonite + *illite	Piece 5
8R-3, 39–41	629.25	629.27	Anorthite + diopside + montmorillonite + *illite	Piece 1C
8R-5, 94–97	632.48	632.51	Anorthite + diopside + smectite + *illite	Piece 11B
9R-1, 41.5–43	636.52	636.53	Ca albite + augite + smectite + *illite	Piece 7
10R-2, 82–84	639.33	639.37	Ca albite + augite + smectite + *illite	Piece 4
10R-6, 138–140	645.62	645.64	Anorthite + †augite + smectite + *illite	Piece 8
11R-1, 89–91	646.69	646.71	Diopside + anorthite + smectite + *illite	Piece 2C
11R-2, 121–123	648.45	648.47	Anorthite + augite + smectite + *illite	Piece 8
12R-3, 61–63	657.95	657.97	Ca albite + augite + smectite + *illite	Piece 1B
13R-2, 36–37	667.13	667.14	Ca albite + diopside + smectite + *illite	Piece 5A
13R-3, 6.5–8.5	668.17	668.19	Ca albite + augite + smectite + *illite	Piece 1
14R-6, 0–4	682.19	682.23	Diopside + anorthite + smectite + *illite	Piece 1

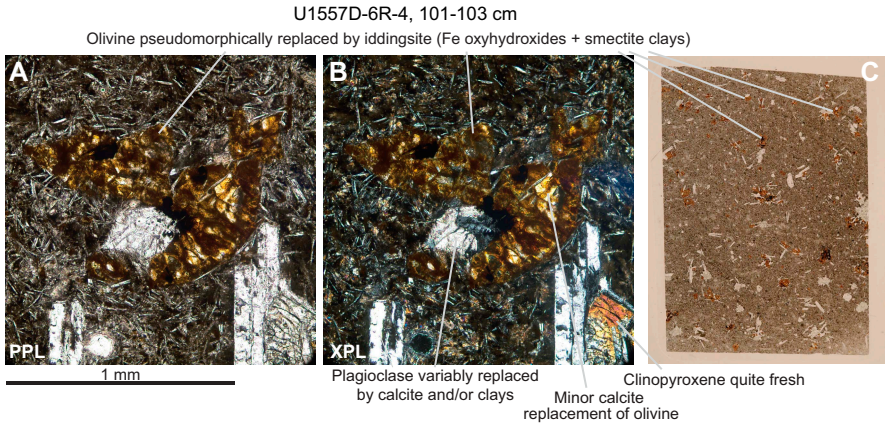

Figure F39. A–C. Pseudomorphic replacement of olivine by iddingsite (Fe oxyhydroxides + smectite clay) and minor calcite with moderately altered plagioclase and groundmass and mostly fresh clinopyroxene (C: PPL), Hole U1557D. Pseudomorphic alteration of olivine in this fashion is typical of orange speckled background alteration.

khaki-altered clasts is quite homogeneous at the scale of a core section. This homogeneity of alteration contrasts with the variable intensity and clear gradients of alteration apparent in clasts with orange halo alteration (see **Orange halos**). There are also examples where khaki alteration has developed as concentric halos in larger clasts, indicating alteration occurred after brecciation and hence most likely in situ.

In thin section, the khaki-altered mesostasis is characterized by patchy but intense alteration to cryptocrystalline, dusty, grayish clays, as well as moderately intense reddening from replacement of plumose quench crystals (likely olivine and/or clinopyroxene) and olivine phenocrysts by Fe oxyhydroxides (Figure **F41**). The result is a distinctive dark, dull brown appearance of the groundmass in thin section.

Compared to orange speckled background alteration, khaki alteration shows more intense reddening of groundmass in thin section, reflecting a greater abundance of red-brown clays + Fe oxyhydroxides replacing groundmass, but not as intense or pervasive as in the orange halos. Bright yellow clays are also common throughout the rock, replacing groundmass and lining or filling vesicles. Similar yellow clays from Hole U1556B cores were only observed in orange halos around

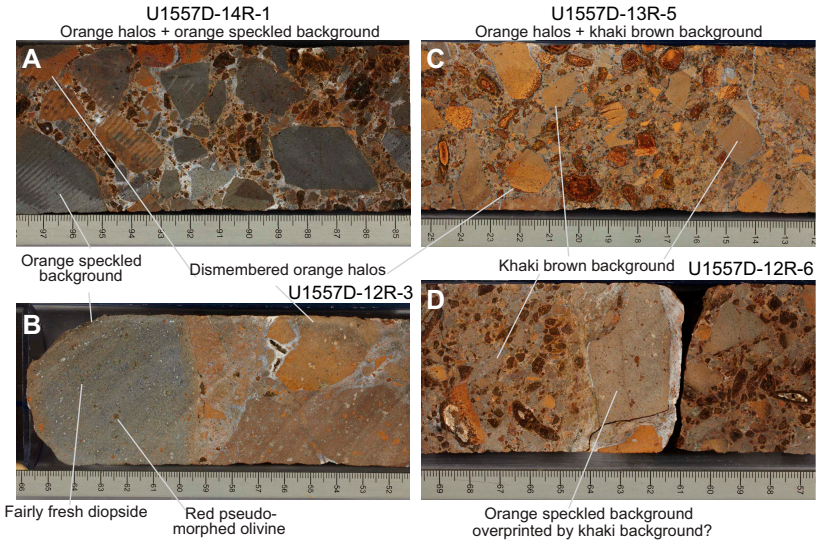

Figure F40. Examples of orange speckled and khaki-brown backgrounds (both with fragments of orange halo), Hole U1557D. A, B. Gray fragments of orange speckled background altered basalt with reddened olivine phenocrysts. C, D. Breccias with similar assemblages of clasts to A and B that have been pervasively altered to khaki-brown.

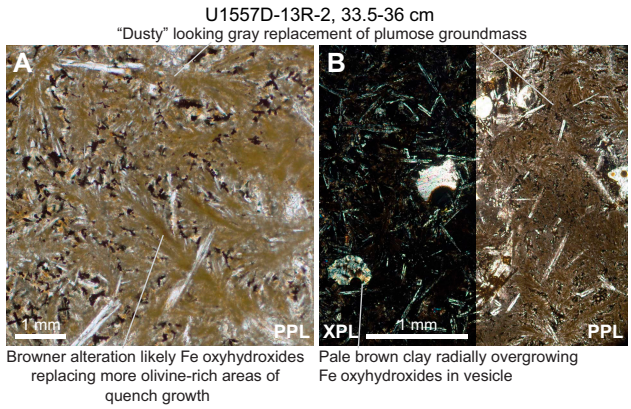

Figure F41. A, B. Typical khaki-brown alteration, Hole U1557D. Pervasive replacement of groundmass by both grayish dusty looking clays and brown-red Fe oxyhydroxide with coexisting pale brown clay (possibly saponite) and carbonate in vesicles overgrowing oxidative alteration phases.

veins or pillow margins. In vesicles, pale brown clays, sometimes over/intergrown with a fibrous mineral phase (possibly a zeolite), overgrow green clay and yellow to brown clay ± Fe oxyhydroxide. In rare examples, these pale brown clays have been patchily stained orange-brown (Figure **F42**). Similar phases overgrow iddingsite after olivine (Figure **F43**).

6.1.1.3. Dark green background alteration

One of the most marked features of the Hole U1557D breccias is the occurrence of numerous intervals of pervasive dark green alteration. These consist of ~0.5–2.0 m intervals in which glass is altered to (macroscopically) dark green clay, sediment is greenish beige, and basalt clasts have a gray to olive- or blue-green hue to their groundmass, superimposed on any orange halo or orange speckled alteration (Figure **F44A, F44D**). Vesicles in basalt are commonly filled with pale greenish

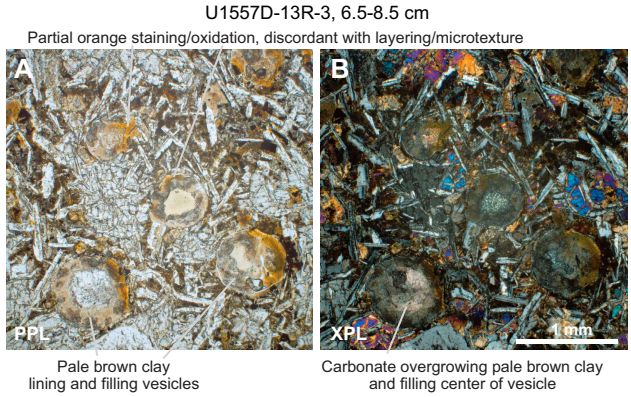

Figure F42. A, B. Evidence for oxidative overprinting of pale brown clay (possibly saponite) filling vesicles and replacing groundmass mesostasis resulting in patchy orange-brown staining, discordant with concentric lining of vesicles and with microtexture of saponite clays, Hole U1557D.

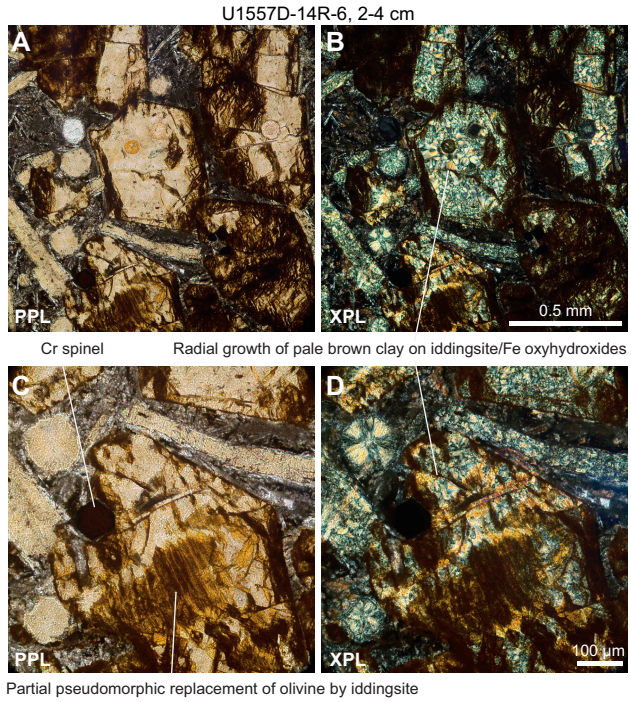

Figure F43. Pale brown clay overgrowing Fe oxyhydroxides/iddingsite that originally pseudomorphically replaced olivine in moderately orange speckled background altered basalt, Hole U1557D. A, B. Olivine altered to brown iddingsite that is itself overgrown by fibrous pale brown clay, which also fills vesicles and replaces groundmass and plagioclase lathes. C, D. Pale brown clay growing out radially from iddingsite replacement of olivine.

to dark green minerals. Orange halos (see **Orange halos**) are largely unaffected by the green alteration, and only the patches or minerals not already altered to Fe oxyhydroxides are green hued (Figures **F44A, F44D**, **F45**). This is especially true in cryptocrystalline rocks, where orange halos are most strongly developed.

Similar meter-scale green alteration zones occur in Hole U1556B and are characterized by very dark gray alteration colors in olivine phyric basalts and the presence of black or very dark green altered glass. In Hole U1557D (and at the bottom of Hole U1556B), this alteration style is typically expressed as paler gray-green altered basalt groundmass (intermediate between Munsell colors GLEY 1 4/N and GLEY 1 5/5GY). The difference in color appears to relate to the grain size of the rocks and their plagioclase phyric nature.

In thin section, green alteration of basalts is characterized by the presence of pale green clay (Figure **F46**) that occurs as a pseudomorphic replacement for olivine and plagioclase and as a vesicle-filling phase. Carbonate is also present filling vesicles (typically without other phases) and replacing small patches of groundmass. The groundmass mesostasis is gray and dusty in plane-polarized light with variable proportions of reddish Fe oxyhydroxide (Figure **F46**). Where Fe oxyhydroxides occur in dark green background, they are related to overprinting of orange halos or orange speckled background by green alteration.

Bright green clays occur in thin section in the green altered basalts but only as narrow fronts to orange halos (see **Green halos**). Wherever bright green clays coexist with pale green clays, the latter overgrow the former. These pale green/brown clays also typically overgrow oxidative phases such as Fe oxyhydroxides or iddingsite pseudomorphing olivine (Figure **F43**) and are apparently unaffected by a yellow clay overprint commonly developed on the green clays (Figure **F47**).

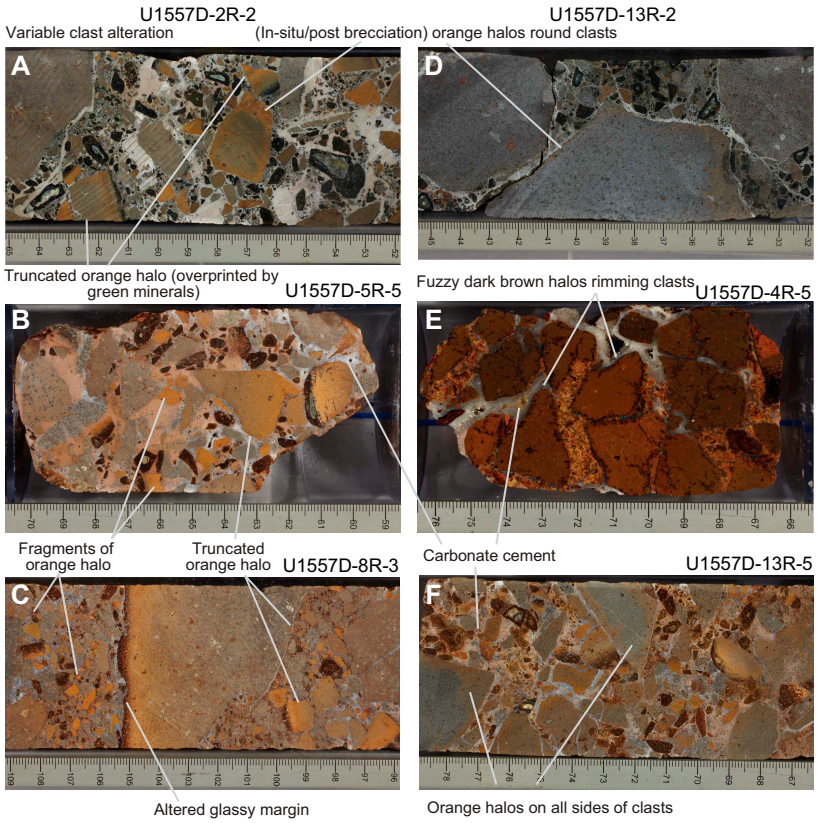

Figure F44. Variety of alteration styles in breccia pile, Hole U1557D. A. Clasts with variety of oxidative orange halo alteration overprinted (in situ) by green background alteration affecting less altered portions and glass. B, C. Various fragments of orange halo–altered basalts truncated by clast edges, some with attached glassy margins. D. Orange halos around large clast (center) juxtaposed with clast of similar grain size and lithology showing no halo (left). E. Fuzzy/dendritic dark brown halos around clasts of highly altered basalt. F. Concentric orange halos paralleling edges of variably altered basalt clasts.

The intervals of dark green background alteration occur at all levels in the basement, although they are more numerous in the lower part below Core 390-U1557D-7R (~620–680 mbsf) (Figure **F48**). Where it was recovered, the boundary between orange and green alteration typically consists of a sharp front (Figure **F49**), though some intervals show more gradual transitions (e.g., interval 10R-5, 68–82 cm). These boundaries are clearest where they cut across the fine-grained matrix and can be subhorizontal or moderately dipping (<45°).

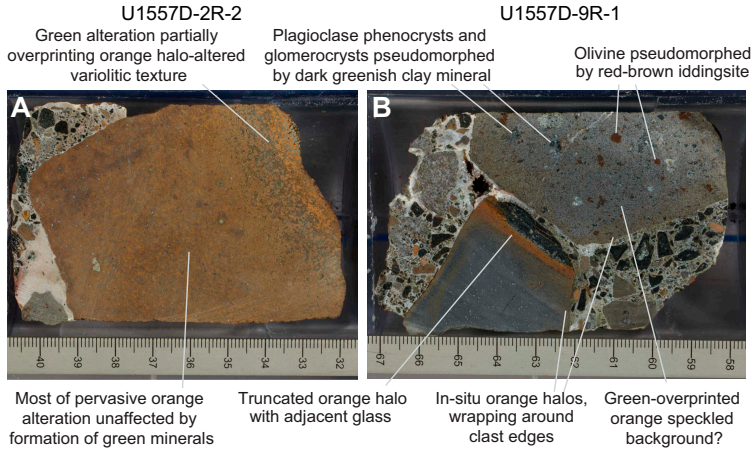

Figure F45. Green alteration only partially overprinting earlier oxidative alteration, Hole U1557D. A. Intense orange halo mostly unaffected by formation of green clays except between altered spherules in variolitic chilled margin (see Igneous petrology in the Site U1556 chapter [Coggon et al., 2024a]). B. Two different clasts in green alteration zone. Upper clast appears to have been altered to orange speckled background before alteration mainly of plagioclase to greenish clay; lower is finer grained and has orange halo parallel to truncated glassy margin; green alteration is mainly manifest as pale green vesicle-filling minerals. Both clasts have in situ orange halo around their edges, apparently developed prior to green alteration.

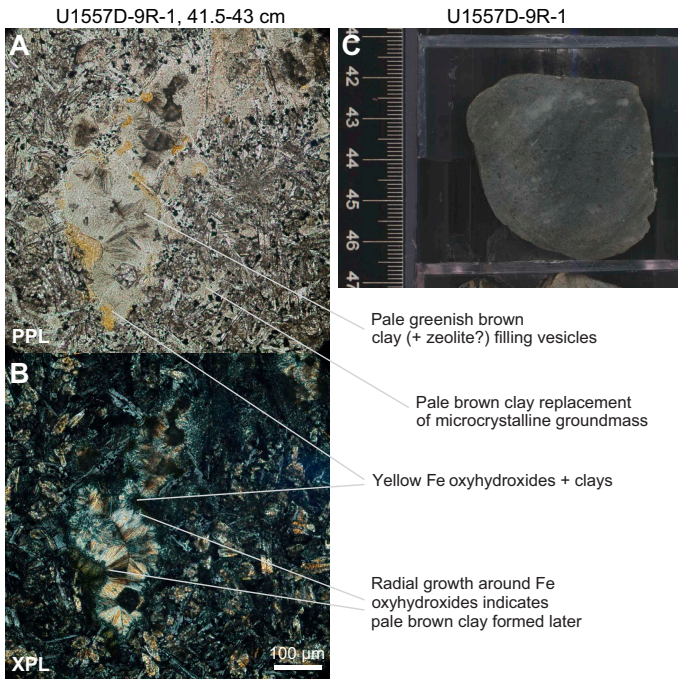

Figure F46. A, B. Pale greenish brown clay (possibly intergrown with fibrous phase) occurs abundantly in dark green background and is likely responsible for greenish hue of rock in hand specimen, Hole U1557D. C. Macroscopic dark gray-green alteration color of rock.

6.1.2. Alteration halos

6.1.2.1. Orange halos

One of the most distinctive types of alteration seen in Hole U1557D are orange halos, which occur abundantly throughout the core (Figures **F40**, **F44**). These occur most commonly in clasts of cryptocrystalline basalt that are highly altered to a strong orange (brown [7.5YR 5/4] to reddish yellow [7.5YR 6/6]) similar to the intense alteration seen along the interior of the chilled margins

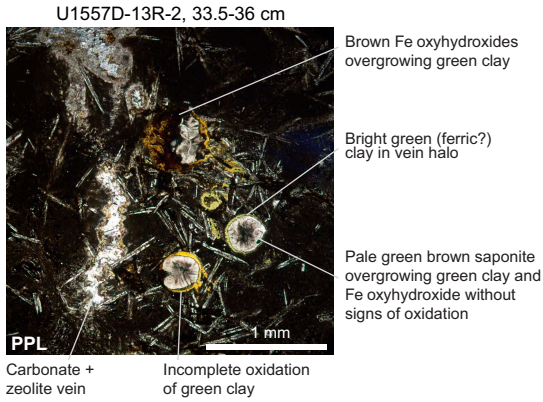

Figure F47. Several phases of overprinting alteration, Hole U1557D. Early green clays are partially oxidized to yellow-orange and overgrown by brown Fe oxyhydroxides. Overgrowing both these phases is dusty looking pale brownish clay showing no signs of oxidation.

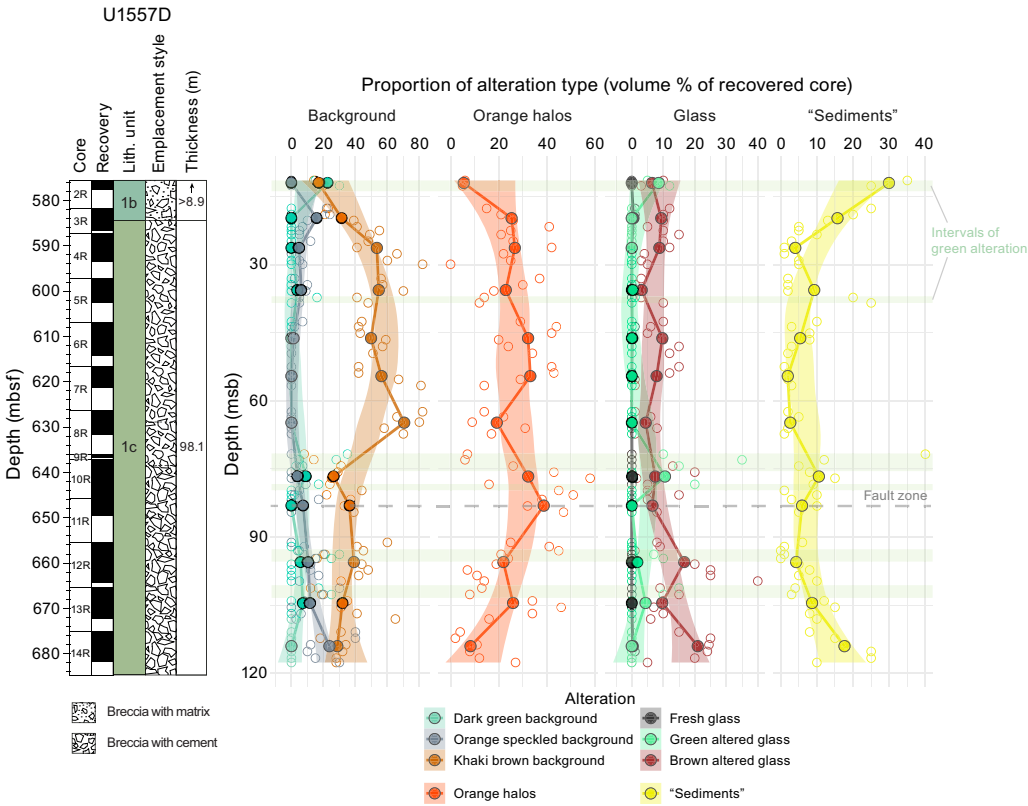

Figure F48. Alteration types, Hole U1557D. msb = meters subbasement assuming basement/sediment interface = 564.77 mbsf. Open symbols = raw data logged at section level, solid symbols = averages for each core (except for Core 9R, which only has one section and was averaged together with Core 10R). Smoothed downhole trend of section data (calculated using locally estimated scatter plot smoothing [LOESS] function) is shown for each alteration type. Green shading = intervals of predominantly green alteration, dashed line = fault zone in Section 390-U1557D-11R-2.

of pillow basalts in Hole U1556B. This type of alteration corresponds to the orange clasts described in **Igneous petrology**. Orange halos commonly occur as fragments with a gradient in the intensity of alteration color and, more rarely, may have remnants of a glassy margin paralleling the alteration gradient. Such gradients are commonly truncated by the broken edges of the clast, indicating formation prior to brecciation. Conversely, there are numerous examples of clasts that show orange halos paralleling their edges, which appear to have formed after brecciation. These are commonly juxtaposed with clasts of similar lithology and grain size showing no orange halos (Figure **F44A**, **F44D**).

In thin section, orange halos are defined by intense and near-complete replacement of the cryptocrystalline quench groundmass by red-brown Fe oxyhydroxides and clays (Figure **F50**). This type of oxidative alteration appears highly resistant to overprinting or overgrowth by later phases of alteration (except by more Fe oxyhydroxides). As such, orange halos are almost completely unaffected when their host breccia is pervasively altered to deep green (Figure **F44A**) (see **Dark green background alteration**).

6.1.2.2. Green halos

Green halos are defined by the presence of clays that appear bright green in thin section and very dark green or black in hand specimen. These were only observed in thin section in Hole U1557D and were not recognized during core description except when cross-checked with thin section observations. Similar micro- and macroscopic colors were exhibited by green altered glass in Hole U1556B (see **Alteration petrology** in the Site U1556 chapter [Coggon et al., 2024a]).

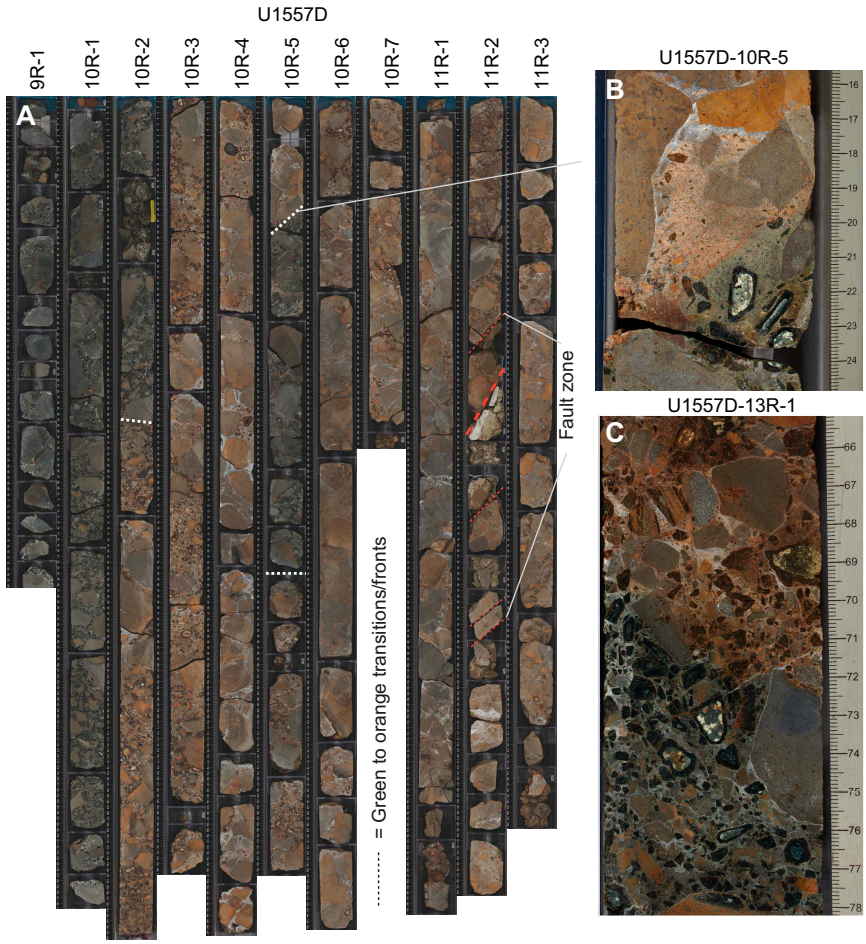

Figure F49. A. Macroscopic alternation between green and khaki-brown/orange alteration zones (390-U1557D-9R through 11R). White dashed lines = transitions between green and brown alteration zones that are sharp fronts where recovered, red dashed lines = thick white carbonate fault vein and several thinner subparallel slickensided veins. B, C. Sharp green to khaki-brown alteration fronts.

In thin section, the clays appear bright green and optically clear in plane-polarized light but cryptocrystalline or feathery in texture under crossed nichols (Figure **F51**). Green halos occur most commonly along one or more edges of a clast or, less commonly, within a narrow halo along a vein. Within such halos, green clays fill or line vesicles or less commonly replace groundmass. Where the relative order of secondary mineral formation is clear, such as concentric growth layers in filled vesicles, the green clays are the first stage of alteration (e.g., Figure **F47**).

6.1.2.3. Dark brown fuzzy halos

Some intervals are characterized by abundant but thin (typically 2–3 mm) dark brown halos with a fuzzy, blotchy, or dendritic appearance that form around the edges of clasts and along thin veins and in isolated patches within the clasts (Figure **F52**). The affected clasts are typically highly altered cryptocrystalline fragments of orange halo (Figure **F52B**). In thin section, the fuzzy appearance is defined by abundant opaque clays + Fe oxyhydroxides that grow from the edges of the clast inward, nucleating along and spreading from pseudomorphed relics of elongate quench groundmass phases (likely originally olivine; Figure **F53**). Similar features occur as vein halos and isolated patches in Hole U1556B, principally in highly altered aphyric pillow basalts of Stratigraphic Sequence B (see **Igneous petrology** in the Site U1556 chapter [Coggon et al., 2024a]). The concentric pattern of these halos fringing the outer portion of clasts indicates that they principally formed postbrecciation. XRD analysis of the dark material coating such clasts (similar to the halo-forming phases) suggests that it is smectite with a large proportion of amorphous material that

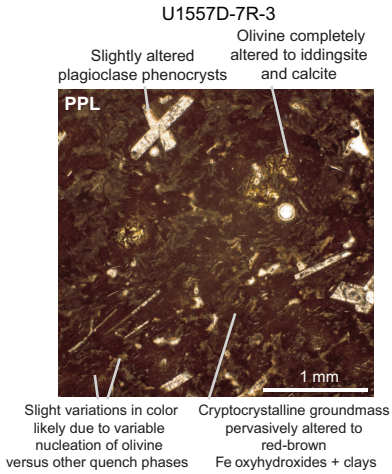

Figure F50. Example of well-developed orange halo showing almost complete replacement of cryptocrystalline groundmass to red-brown Fe oxyhydroxides + clays (390-U1557D-7R-3, 51.5–55.5 cm).

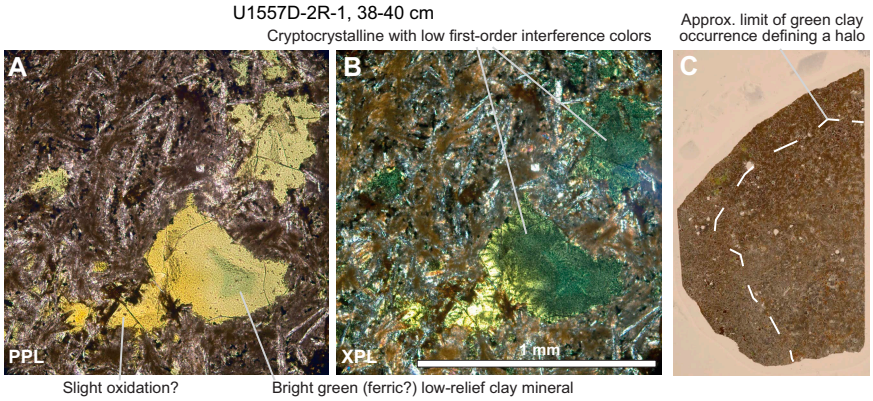

Figure F51. A. Bright green, likely ferric clays filling vesicles in halo on one edge of basaltic breccia clast, Hole U1557D. B. Bright green absorption color in center of vesicle. Apparent first-order interference colors partly obscured by green absorption color of mineral. C. Approximate limit of bright green clay occurrence (PPL).

may be Fe oxyhydroxides (Table **T5**). Some samples display peaks that indicate the presence of Mn oxide or oxyhydroxide (see **Manganese oxides**).

6.1.3. Authigenic zeolite-bearing sediment

In Hole U1557D, the breccia matrix consists of pale yellow, pink, or brown carbonate-bearing, fine-grained, massively textured or laminated material and typically fills interclast pore space in gravity-controlled positions. During alteration logging, the proportion of this material in each section was recorded together with the various types of alteration of the basalt and glass clasts and treated as distinct from crystalline cements (mostly carbonate) that grew in the pore space (recorded as breccia cements in the vein log; see DESC_WKB in **Supplementary material**). In thin section, it is clear that much of this material, especially below Core 390-U1557D-3R, constitutes authigenic zeolites and carbonates rather than pelagic sediment (see **Igneous petrology**). To maintain consistency with the alteration and vein logs, in this section both pelagic sediment and authigenic material are referred to collectively throughout as sediment. This also allows us to retain the meaningful petrologic distinction between authigenic microspar + zeolite matrix and crystalline void-filling calcite (and other mineral) cements in the data and downhole plots.

6.2. Downhole variations in alteration

During alteration logging, the area proportions of the alteration types described above—background (orange speckled, dark green, and khaki-brown), halos (orange and dark/fuzzy), altered and unaltered glass (brown, green, and fresh), and sediment matrix (see **Authigenic zeolite-bearing sediment**)—were estimated for each section of core (see **Alteration petrology** in the Expedition 390/393 methods chapter [Coggon et al., 2024c]). These data are averaged as a weighted mean by recovered length for each core in Hole U1557D (Figure **F48**). The most abun-

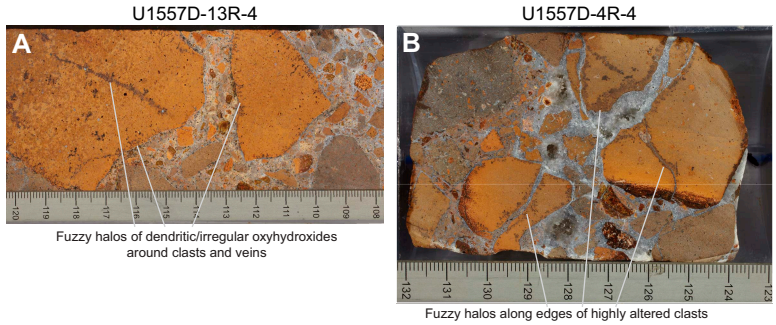

Figure F52. A. Typical macroscopic appearance of fuzzy dark brown halos growing along clast edges and veins in highly oxidized clasts of orange halo altered basalts, Hole U1557D. B. Fuzzy halos growing along edges of highly altered clasts and less pronounced or absent in less altered, coarser grained basalts.

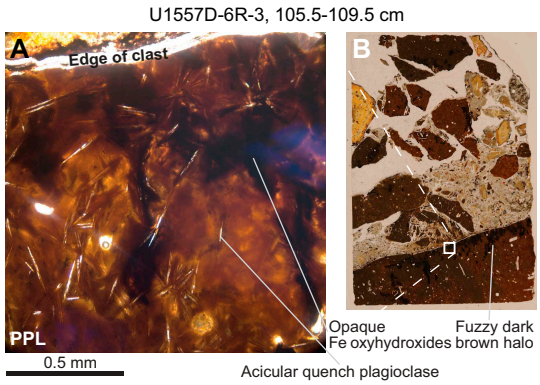

Figure F53. A. Typical fuzzy dark brown halos formed of opaque Fe oxyhydroxides growing along elongate quench crystals at clast edges, Hole U1557D. B. Context of A within fuzzy halo (PPL).

dant alteration types are khaki-brown background and orange halos, which constitute approximately 20%–70% and 5%–40%, respectively, of the rock by area per core.

The proportion of green altered glass and green background alteration show several spikes in six intervals spaced throughout the hole. Several of these intervals appear to correspond to intervals of elevated K-derived NGR identified from downhole logging (Figure **F93**).

Below ~75 msb (~640 mbsf), both altered glass and sediment become more abundant (Figure **F48**). This depth corresponds to a 3 m unrecovered interval between Cores 390-U1557D-8R and 9R. The same interval corresponds to an apparent transition in physical properties including NGR and resistivity logs, which broadly increase and decrease, respectively, over a similar depth range (~630–645 mbsf) (see **Physical properties and downhole measurements**) (Figures **F92**, **F93**).

The proportion of orange halos shows apparent cyclicity in the upper part of the hole (above 75 msb), although this appears to be largely an artifact of minor variations in the proportions of various other alteration types/components (including glass and sediment). Below ~75 msb, the proportion of orange halos decreases. This trend is more clearly seen where orange halos are plotted as a proportion of the total area of basalt clasts (i.e., data normalized to exclude glass and sediment) (Figure **F54A**). The proportion of orange halos increases slightly at ~75 msb, below which it decreases steadily downhole. Plotting the proportion of khaki-brown alteration as a proportion of all background alteration (khaki and orange speckled background) shows a similar change at ~75 msb, with the relative proportion of khaki alteration uniform above this horizon but steadily decreasing downhole (Figure **F54B**). These trends might reflect decreasing intensity of both prebrecciation (orange halo) and postbrecciation (khaki background) alteration downhole.

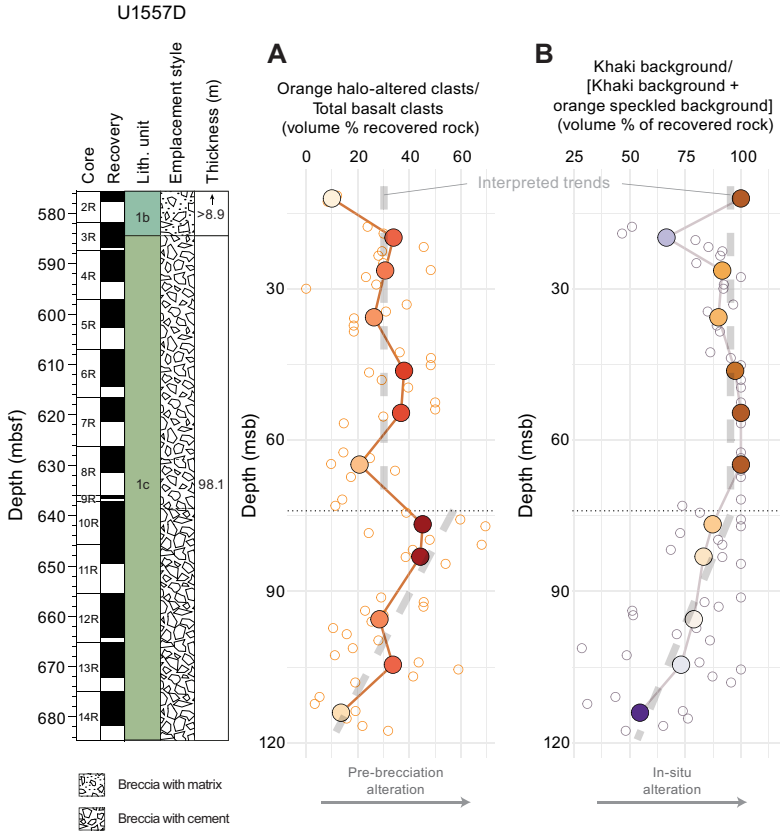

Figure F54. Alteration type abundance ratios, Hole U1557D. msb = meters subbasement assuming abasement/sediment interface = 564.77 mbsf. A. Abundance of orange halos in all basalt clasts. B. Area proportion of khaki-brown background alteration in total khaki + orange speckled background alteration. Open symbols = raw data logged at section level, solid symbols = averages for each core. Core averages were computed as a weighted mean by recovered length of core in each section of core (except for Core 9R, which only has one section and was averaged together with Core 10R). Dotted line = inferred discontinuity in breccia sedimentation and/or alteration, bold dashed line = broad interpreted trends.

6.3. Order of alteration events

The earliest alteration event, which is only preserved in some altered basalt clasts, appears to be green halo development, characterized in thin section by the presence of bright green clays (see **Green halos**). Where these occur, a partial oxidative overprint is commonly manifested in alteration of the color of green clays to bright yellow, with these apparent oxidation gradients cutting discordantly across patches and vesicles filled by green clay (Figure **F47**).

Almost all samples show oxidative alteration, characterized in thin section by replacement of groundmass, cryptocrystalline quench phases, and olivine phenocrysts by various red-brown, orange, or yellow clay + Fe oxyhydroxide mixtures. This oxidative alteration is generally followed by formation of pale green to pale brown clays, possibly saponitic in composition, that overgrow iddingsite, replace groundmass, and fill vesicles. In thin section, these pale clays occur ubiquitously throughout the basalts showing khaki-brown background, dark green background, and orange speckled background alteration (Figures **F41**, **F46**, **F49**). Wherever pale brown/green clays, bright green clays, and brown Fe oxyhydroxides occur together in thin section, the sequence of formation begins with bright green clays that are overgrown by red-yellow-brown clay ± Fe oxyhydroxides and finally by pale brown clay. The pale brown clays are mostly, although not universally, unaffected by oxidative overprints that commonly alter the color of the bright green clays to yellow or orange (Figure **F47**; cf. Figure **F42**). In rare examples, there is evidence for multiple generations of pale brown/green clay alteration (e.g., Sample 390-U1557D-13R-3, 7–9 cm). When present, carbonate typically represents the latest forming phase seen in thin section, overgrowing pale brown clays in vesicles (Figure **F42**).

6.3.1. Relative timing of orange halo alteration and brecciation

Orange halos show evidence for formation both along the original chilled margins of pillows and around the edges of fragments of basalt (Figure **F44A, F44D**). In many cases, the former are sharply truncated by the broken edges of clasts. Various clasts, including those with truncated halos, concentric halos around their edges, and no halos, are commonly juxtaposed in the breccias. Some clasts show both truncated and concentric halos (Figure **F45B**).

These observations suggest that extensive oxidative alteration, manifest by the formation of orange halos, occurred both prior to and following brecciation. Formation of orange halos prior to incorporation in the breccia pile would have to have proceeded rapidly given the 60.76–61.27 Ma age of basal sediments at Site U1557 (see **Biostratigraphy**). Intact basalts from young oceanic crust, including those from Site U1559, do not typically show such intense alteration (see **Alteration petrology** in the Site U1559 chapter [Coggon et al., 2024e]), implying some extra mechanism is needed for their alteration. This could include partial brecciation of basalts in a rubble pile and/or localization of fluid flow. The apparent truncation of orange pillow margin halos could also partly reflect the interaction of postbrecciation alteration with primary igneous grain size variation, with cryptocrystalline portions being more easily altered or more strongly expressing intense orange alteration colors. Another alternative is that early-forming alteration halos (e.g., dark gray halos seen in young crust; see **Alteration petrology** in the Site U1559 chapter [Coggon et al., 2024e]) might alter the mineralogy or microstructure of the rock to promote later oxidation.

6.3.2. Formation of zones of dark green background alteration

Zones of dark green background alteration clearly formed in situ within the breccia and overprint orange halos in basalt clasts (Figure **F44A**) and, where present, represent the latest phase of alteration. Green intervals lack voluminous carbonate cement and open porosity (Figure **F55**). Rather, they are characterized by comparatively sparse cement, with few open vugs (e.g., compare Sections 390-U1557D-9R-1 and 10R-4; Figure **F49**). Outside of these intervals of low porosity, orange halo, khaki background, and orange speckled background alteration predominate, likely reflecting relatively more oxidizing conditions.

6.4. Vein logging

The area proportion of the core that is filled by veins and breccia cements and vesicles, together with the mineralogy of these features, was quantitatively logged in the basement cores from Holes

U1557B and U1557D. Vein density (as number of veins per meter of recovered core) is plotted downhole in Figure **F56**, and the corresponding mean, median, and maximum vein width are plotted in Figure **F57**. The volume proportions of selected secondary minerals in breccia cements and vesicle fills are plotted downhole in Figures **F55** and **F58**, respectively. The abundance of veins in Hole U1557D is unsurprisingly low compared to Site U1556, with only 334 veins recorded, corresponding to an average of 4.8 veins/m of recovered core (68.95 m). The low abundance reflects the fact that fractures or veins present in basalts prior to brecciation and redeposition will have been preferentially fractured and now form the outside surfaces of clasts.

The density of veins in Hole U1557D broadly increases downhole, with a sharp increase in carbonate vein density (from ~1 to 5 veins/m) coinciding with a discontinuity in the alteration style at ~75–85 msb identified in alteration logs (Figure **F56**) and physical properties downhole logging (see **Downhole variations in alteration**). Across the same interval, the mean and median width of veins also increases (Figure **F57**). This change correlates with tighter packing of the breccias and the disappearance of open porosity (Figure **F55**); below 75 msb, veins were more commonly observed cutting both clasts and matrix than in the upper part of the hole (Figure **F59**).

Throughout the core, breccia cements were the most abundant type of secondary mineral fill recorded. The vast majority of these consisted of vuggy crystalline carbonate filling the interclast void spaces, often with significant centimeter-scale open porosity remaining (Figures **F55**, **F60**). In 26 carbonate-bearing samples analyzed using XRD for their mineralogy, the fitted mineral spectra always included calcite (Table **T5**). Vesicles in basalt clasts are sparsely present throughout the hole and show no clear downhole trends in their distribution (Figure **F58**).

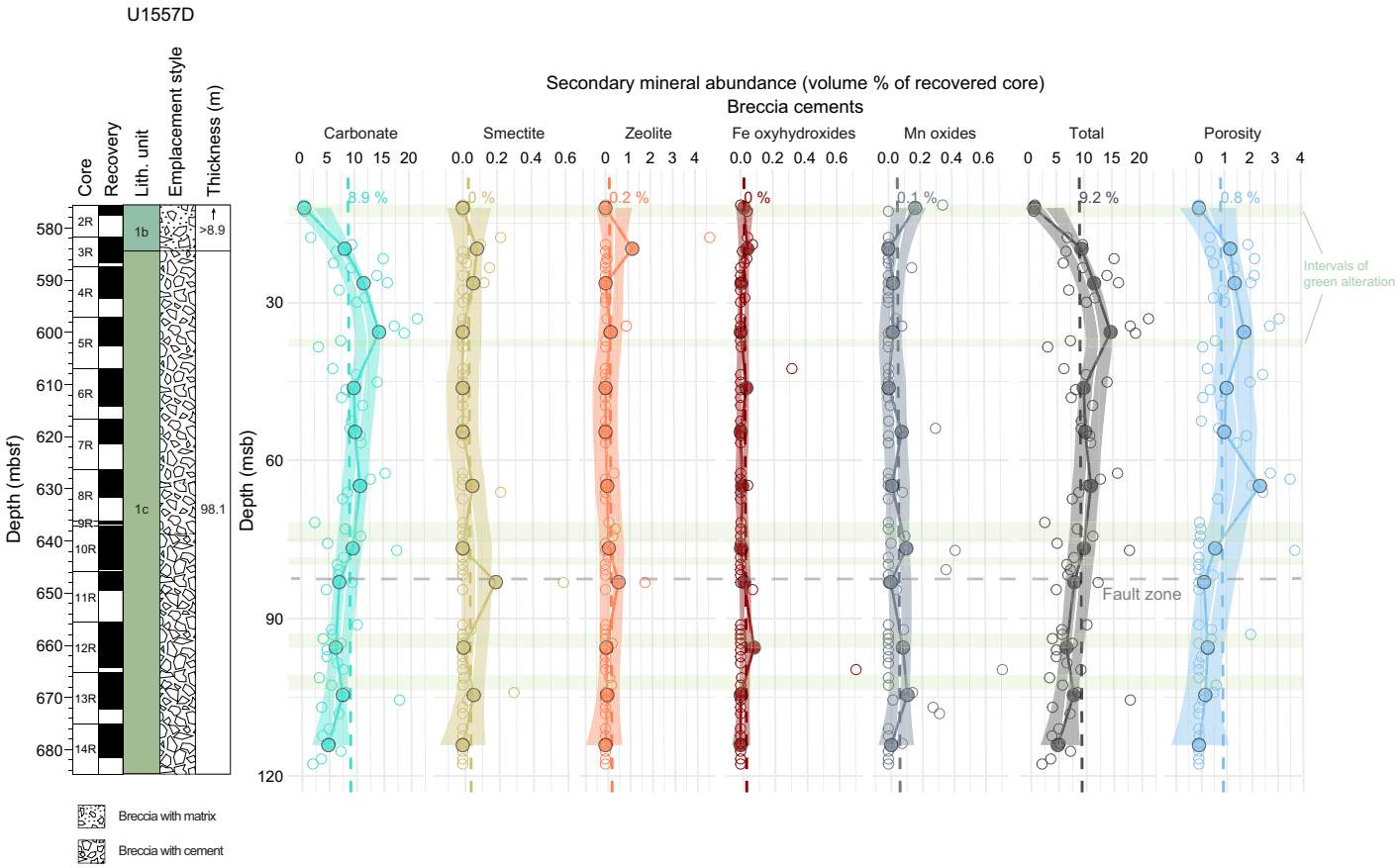

Figure F55. Proportion of secondary minerals and porosity in breccia cements, Hole U1557D. msb = meters subbasement assuming basement/sediment interface = 564.77 mbsf. Open symbols = raw data logged at section level, solid symbols = averages for each core. Core and section values were computed as total volume of logged secondary divided by recovered volume of core. Smoothed downhole trend of core data (calculated using locally estimated scatter plot smoothing [LOESS] function) is shown for each secondary mineral. Dashed vertical lines = average secondary mineral contents for entire hole, green shading = intervals of predominantly green alteration, dashed horizontal line = fault zone in 390-U1557D-11R-2.

6.4.1. Abundance of carbonate in the breccias

The volume proportion of carbonate in the cores was determined for each section and logged as a proportion of recovered core, assuming that area percentage and volume percentage are proportional to one another (see DESC_WKB in **Supplementary material**). Carbonate abundance, expressed as the volume proportion of carbonate in recovered core, is plotted downhole in Figure **F61**.

The volume proportion of recovered rock made up of carbonate breccia cement is high throughout Hole U1557D, averaging 8.9 vol% of the recovered rock (calculated as a weighted mean by recovered length of rock). Carbonate cement abundance is low in the uppermost cores (Cores 390-U1557D-2R and 3R), where sediment commonly fills much of the interclast space but increases rapidly with depth, reaching a maximum between about 30 and 40 msb. Some core sections have 15–20 vol% carbonate in this interval, below which its abundance gradually decreases to about 5 vol% at the bottom of the hole. This trend parallels the proportion of open porosity, which ranges 0–4 vol% in the upper part of the hole but decreases to near zero below 75 msb (Figure **F55**). This suggests that carbonate cements have filled existing porosity in the breccias (Figure **F57**). As such, the proportion of remaining porosity is a fairly constant (and low) proportion of the original interclast pore space.

Authigenic carbonate + zeolite matrix (see **Authigenic zeolite-bearing sediment**) also represents a reservoir of carbonate in the rock. Based on thin section observations, its carbonate abundance has been conservatively estimated as 50 vol%. Assuming this value, the proportion of sediment matrix–hosted carbonate has been calculated downhole from the alteration log (see DESC_WKB in **Supplementary material**), together with the total of breccia cement and sediment matrix

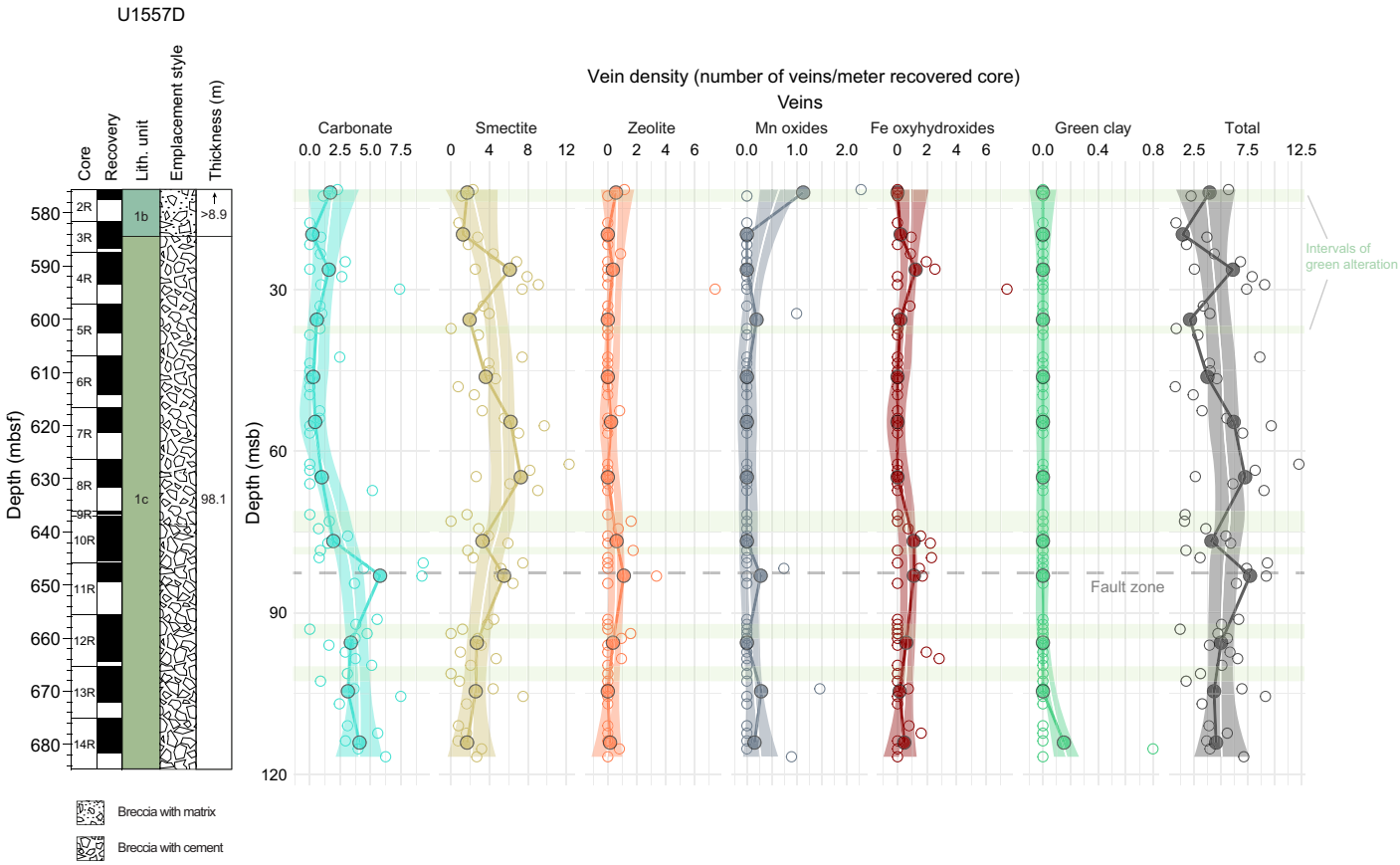

Figure F56. Vein density, Hole U1557D. msb = meters subbasement assuming basement/sediment interface = 564.77 mbsf for selected secondary mineral fills. Open symbols = raw data logged at section level, solid symbols = averages for each core. Core averages were computed as total number of veins divided by recovered length of core. Smoothed downhole trend of core data (calculated using locally estimated scatter plot smoothing [LOESS] function) is shown for each secondary mineral. Green shading = intervals of predominantly green alteration, dashed line = fault zone in 390-U1557D-11R-2.

carbonate (Figure **F61**). Based on these very approximate calculations, the average carbonate content for Hole U1557D could be as high as 12.9 vol% of the recovered rock.

6.4.2. Fault zone and associated veins

A notable feature in Hole U1557D was a small fault zone recovered in interval 390-U1557D-11R-2, 39–95 cm (647.63–648.19 mbsl). The fault zone consists of a 2 cm thick, massive, white carbonate vein dipping 57° with a marble-like appearance markedly different from the translucent sparry carbonate cements (Figures **F49**, **F62**). This feature is underlain by at least 50 cm of greenish yellow, highly fissile fault gouge containing angular clastic material. The clasts are formed of the same variably altered igneous materials that form the rest of the breccias. Their grain size decreases approaching the thick white vein (Figure **F63A**). Several 0.5–1 mm thick greenish veins with slickensided surfaces and slip lineations parallel to their maximum dip occur in the fault gouge and adjacent rocks. Slickenside surfaces reflect both normal and reverse movement senses. One of these is in the same core piece as the thick white vein and parallels it (Figure **F49A**). Although the relative rotation of other pieces is unknown, their dips are all slightly gentler than but broadly consistent with that of the thick carbonate vein (dips 25°–50°).

The mineralogies of the slickensided veins and fault gouge, determined using XRD and confirmed in a thin section of the fault gouge, are all very similar and consist of calcite and phillipsite with abundant smectite clays as well as other zeolite species and/or mixed layer clays possibly present (Table **T5**). This assemblage is similar to the mineralogy of the authigenic sediment matrix sampled adjacent to the fault zone at the base of Section 390-U1557D-11R-2, but the fault gouge has more abundant clays. No hint of primary igneous minerals was recorded on the XRD pattern (Table **T5**). Although alteration within the ~50 cm thick fault zone appears to be high, there is no indication of substantial alteration in the surrounding rocks outside the immediate fault zone.

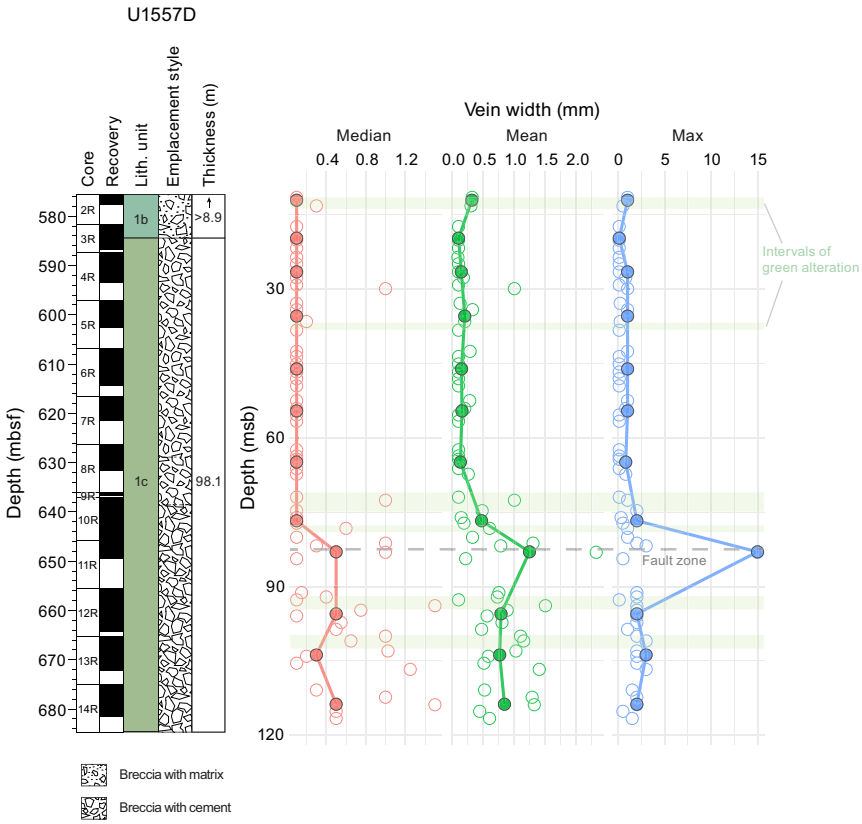

Figure F57. Vein widths, Hole U1557D. msb = meters subbasement assuming basement/sediment interface = 564.77 mbsf. Open symbols = raw data logged at section level, solid symbols = averages for each core. Green shading = intervals of predominantly green alteration, dashed line = fault zone in 390-U1557D-11R-2.

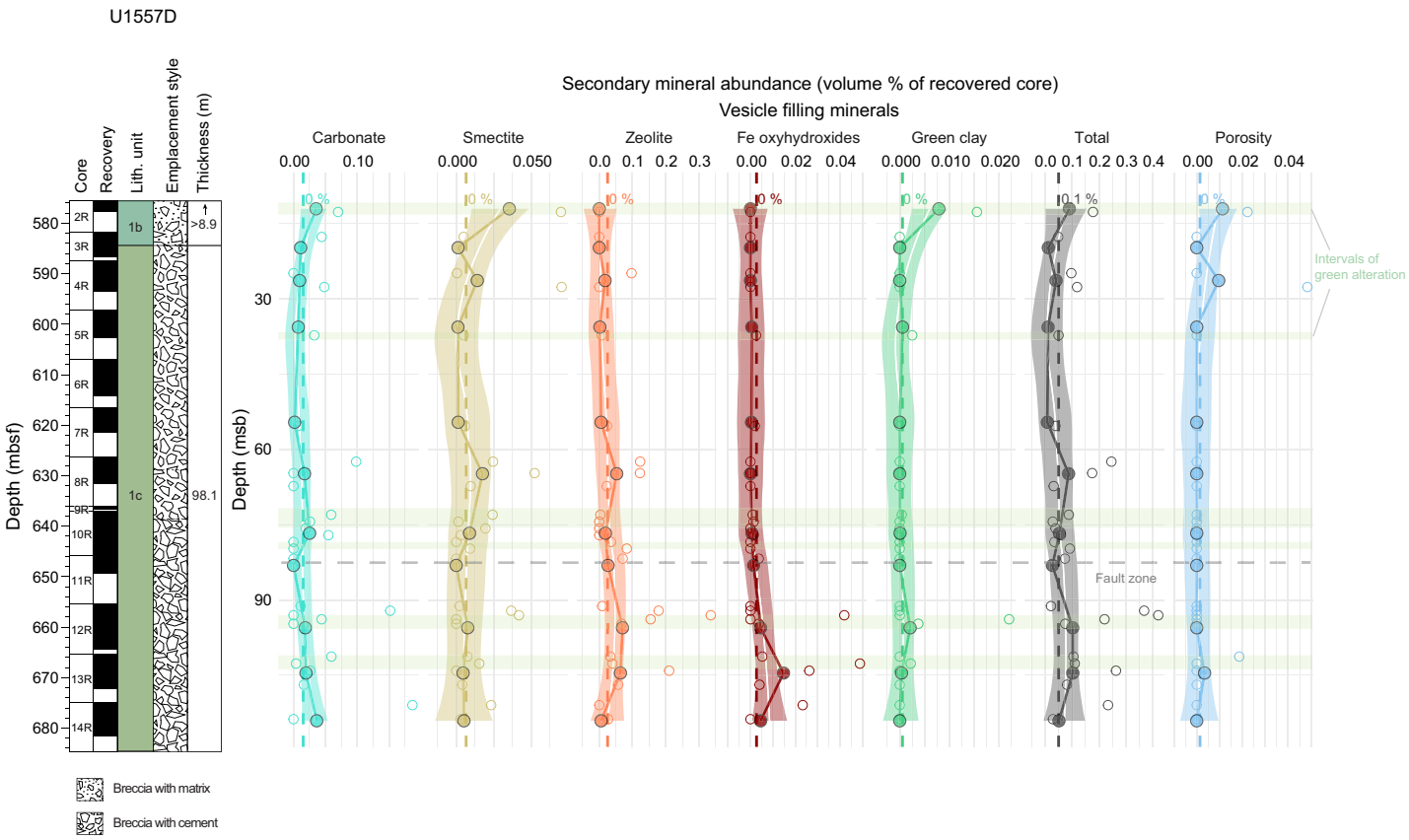

Figure F58. Proportion of secondary minerals and porosity in vesicles, Hole U1557D. msb = meters subbasement assuming basement/sediment interface = 564.77 mbsf. Open symbols = raw data logged at section level, solid symbols = averages for each core. Core and section values were computed as total volume of logged secondary minerals divided by recovered volume of core. Smoothed downhole trend of core data (calculated using locally estimated scatter plot smoothing [LOESS] function) is shown for each secondary mineral. Dashed vertical lines = average secondary mineral contents for entire hole, green shading = intervals of predominantly green alteration, dashed horizontal line = fault zone in 390-U1557D-11R-2.

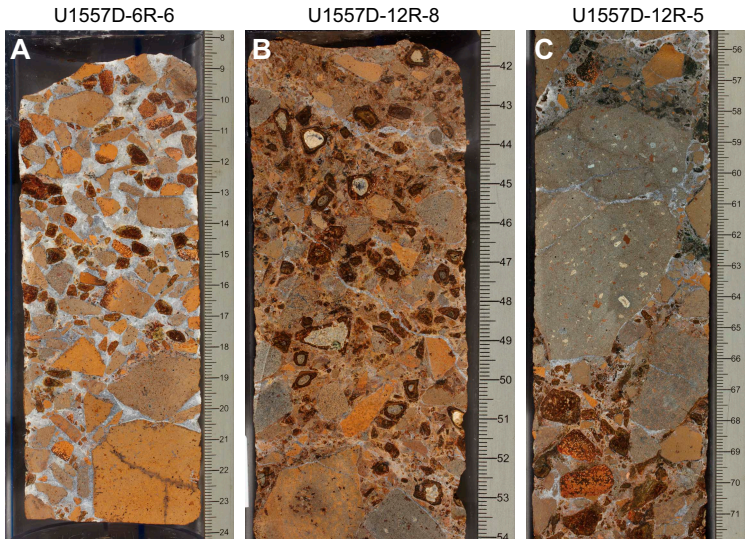

Figure F59. Development of through-going veins in breccia matrix, Hole U1557D. A. Porosity-filling carbonate cement in upper part of hole. B. Subplanar veins cutting through tightly packed matrix. C. Rare occurrence of vein cutting into a clast in lower part of hole.

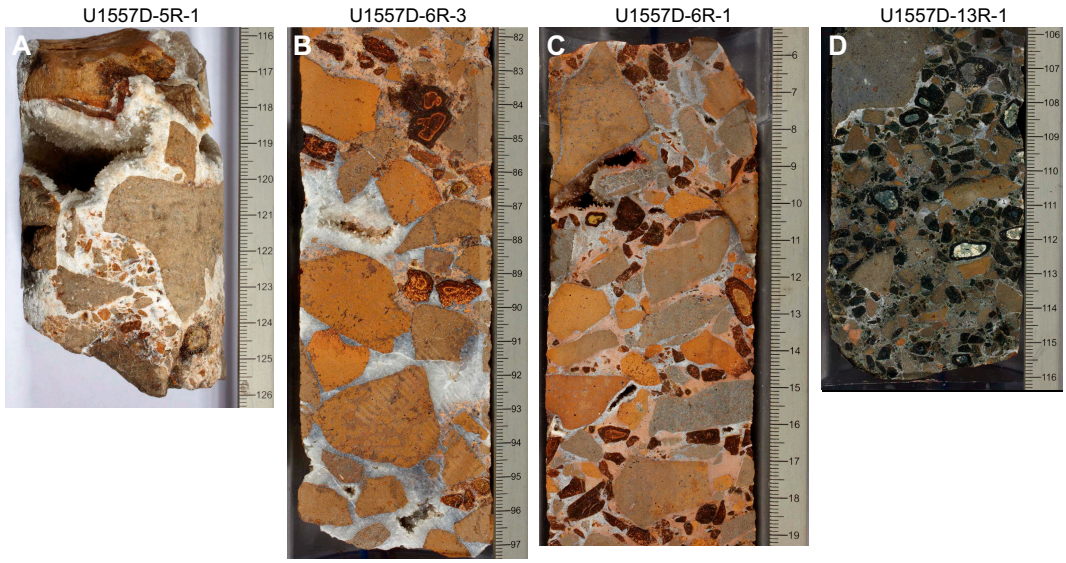

Figure F60. Typical carbonate breccia cements, Hole U1557D. A. Vuggy crystalline calcite fill with abundant open interclast void space (5R-1, 116–126 cm). B. Vuggy calcite fill with sparse sediment/matrix in gravity traps and coating calcite spars in void (6R-3, 82–97 cm). C. Relatively sediment/matrix-rich breccia with remaining pore space cemented by vuggy calcite with open void (6R-1, 6–19 cm). D. Typical matrix-rich breccia characteristic of green alteration intervals and much of lower part of hole (13R-1, 106–116 cm).

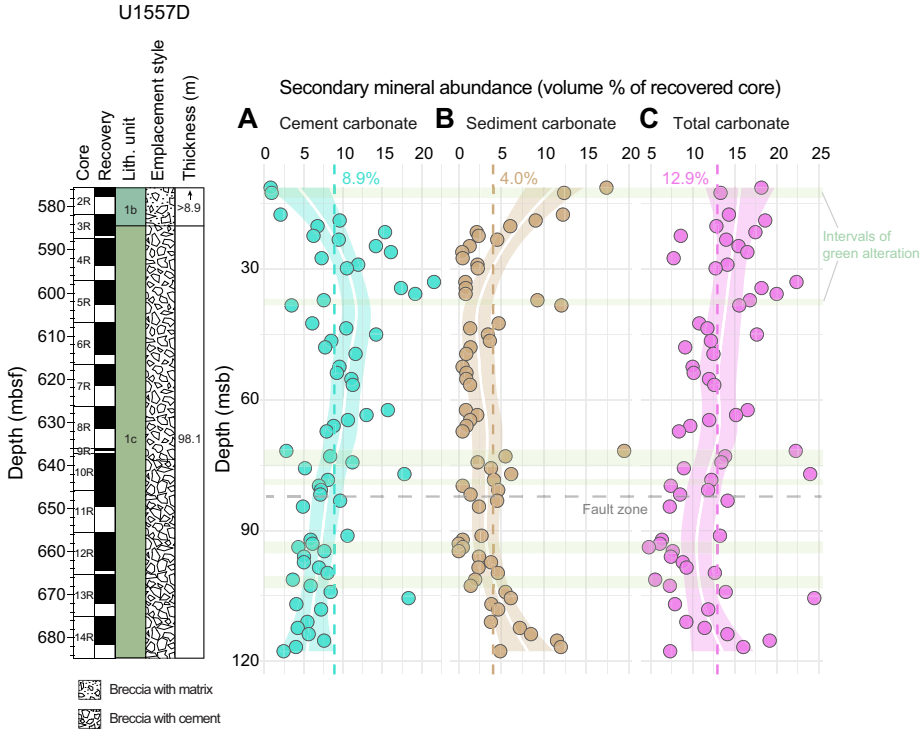

Figure F61. Estimated proportion of carbonate in (A) breccia cements, (B) authigenic zeolite + calcite matrix (assuming 50 vol% carbonate), and (C) total of breccia cements and authigenic matrix, Hole U1557D. msb = meters subbasement assuming basement/sediment interface = 564.77 mbsf. Smoothed downhole trend of core data (calculated using locally estimated scatter plot smoothing [LOESS] function) is shown for each secondary mineral. Dashed vertical lines = average carbonate contents for entire hole, green shading = intervals of predominantly green alteration, dashed horizontal line = fault zone in 390-U1557D-11R-2.

6.4.3. Manganese oxides

Dark gray to black secondary minerals occur throughout Hole U1557D. These phases exhibit a range of properties, with luster ranging from graphitic/submetallic to sparkly black to dull and hardness ranging from very hard to soft. They occur as thin coatings, nodules, or amorphous overgrowths to vuggy calcite, as well as veins and more cryptic intergrowths within carbonate cements (Figure **F63**). These minerals are always extremely dark in color and occur as late phases, either intergrown with or overgrowing carbonate. They occur throughout Hole U1557D but are slightly more common in the lower half of the hole (Figure **F55**). XRD analyses of several examples hinted at the presence of a variety of Mn oxide and hydroxide phases, commonly coexisting with smectite clays (Table **T5**), but were inconclusive and will require more detailed research to identify precisely.

6.5. Summary

The breccias recovered at Site U1557 show evidence for alteration under a range of conditions, resulting in a sequence of overprinting events manifested as replacement and void filling by a

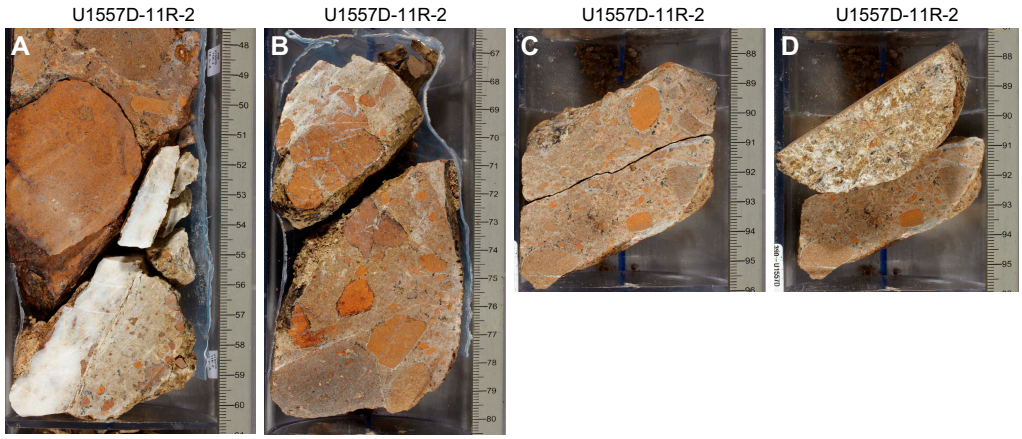

Figure F62. Fault veins and associated fault gouge, Hole U1557D. A. Thick, massive white carbonate fault vein underlain by greenish fault gouge in which clasts decrease in size approaching the vein. B. Fracture/vein and associated fault gouge with similar dip to A. C. Minor vein in greenish fault gouge with slickensided surface. D. Surface of vein in C.

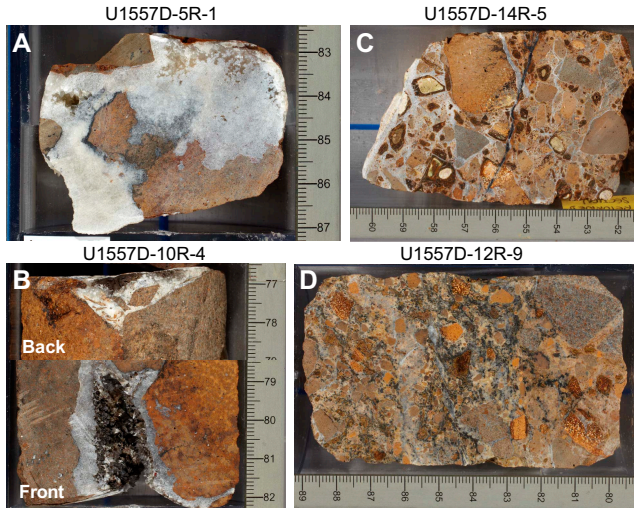

Figure F63. Examples of manganese oxide and associated minerals, Hole U1557D. A. Dark material lining and intergrown with white calcite cement. B. Amorphous accumulation of massive dark smectite clays likely in association with Mn oxides or oxyhydroxides in vug and coating sparry calcite. C. Mn oxide and calcite vein crosscutting calcite breccia cement. D. Abundant black flecks in yellow authigenic sediment matrix.

range of secondary minerals. Petrographic observations indicate a sequence of events from (oldest to youngest) green, possibly ferric clays; red-yellow-brown clays + Fe oxyhydroxides; pale brown to green clays (possibly saponite) ± zeolite; carbonate cements; and manganese oxide ± clay. There are, however, exceptions to this broad sequence of alteration that point to greater complexity. Macroscopic alteration colors and textural relationships, including fragmented orange halos and meter-scale zones of overprinting green alteration, indicate that alteration of the basalt clasts likely occurred both prior to and following their brecciation and deposition.

The breccias host few veins but are ubiquitously cemented by sparry calcite, which partially fills millimeter- to centimeter-scale open space between the clasts. These cements are highly abundant, constituting altogether 8.9 vol% of the recovered rock in Hole U1557D and making up as much as 22 vol% in individual core sections. If the carbonate in these cements derives from seawater, breccias such as these in fault-bounded basins along slow-spread crust may represent important overlooked sinks in the global carbon cycle.

7. Biostratigraphy

The 564.76 m thick sedimentary succession of pelagic ooze, chalk, and clay in Hole U1557B ranges in age from Pleistocene to middle Paleocene. Samples analyzed from Holes U1557A (terminated after one core) and U1557B were primarily core catcher samples sent to the science party biostratigraphers following Expedition 390C (see **Background and objectives**). These samples were supplemented shipboard during Expedition 390 by additional nannofossil smear slides taken from the archive halves of cores from Hole U1557B as well as working-half foraminiferal samples directly above basement from previously unsplit Core 390C-U1557B-63X. An integrated calcareous nannoplankton and planktic foraminiferal biozonation for Site U1557 is summarized in Table **T7** and Figure **F64**. An age-depth plot of biostratigraphic datums and paleomagnetic reversals can be found in Figure **F81**. Benthic foraminifera are present and indicate an abyssal paleodepth throughout. A summary of microfossil preservation and abundance is shown in Figure **F65**.

Planktic and benthic foraminifera and calcareous nannoplankton are present in varying abundances in the oozes and chalks but are mostly absent from the clays at this site. The Hole U1557B mudline sample is barren and thus the Holocene was not observed, but sedimentation appears to be continuous from the Pleistocene to early Oligocene. A 12.94 m thick condensed interval composed of dark brown pelagic clay and spanning the middle Eocene to early Oligocene occurs in Cores 390C-U1557B-29X through 31X (Figure **F66**). Thin horizons that visually appear to have higher carbonate content (i.e., lighter in color) were sampled for nannofossil analysis in this interval, but all samples are barren or contain few non-age-diagnostic taxa. Below this interval, sedimentation appears to be continuous, although there are significant gaps in recovery through to the bottom of the hole. We interpret a prominent reddish brown clay in Section 50X-3 (~461 m CSF-B) to represent the PETM based on the occurrence of the calcareous nannofossil genus *Rhomboaster*, which is characteristic of the PETM interval, as well as sedimentologic and physical properties data indicating a significant drop in carbonate content (see **Sedimentology** and **Physical properties and downhole measurements**). These observations are strong evidence that a PETM section was recovered at Site U1557. Below this hyperthermal event, continuous sedimentation is observed through to the sediment/basement interface.

7.1. Age of basement

One sample analyzed directly above basement (Sample 390C-U1557B-63X-2, 78–80 cm; 564.15–564.17 m CSF-B) is assigned to planktic foraminiferal Zone P4a (60.54–60.76 Ma; Gradstein et al., 2020) and calcareous nannofossil Zone CNP7 (60.76–61.27 Ma; Gradstein et al., 2020), both of which are in good agreement with the projected crustal age of 61 Ma at Site U1557 and which correlate well to nearby Sites U1556 and U1561 (see **Background and objectives**; also see **Biostratigraphy** in the Site U1556 chapter and **Biostratigraphy** in the Site U1561 chapter [Coggon et al., 2024a, 2024b]).

7.2. Calcareous nannofossils

Calcareous nannofossil biostratigraphy is based on analysis of core catcher samples and additional smear slide samples from the Hole U1557B archive halves. Biostratigraphic datums used for the age-depth model are shown in Table **T7**, and calcareous nannofossil occurrence data are shown in Table **T8**. Note that the distribution chart is biased toward age-diagnostic and other notable taxa; a plate of photomicrographs including many of these taxa is shown in Figure **F67**.

At Site U1557, the preservation of calcareous nannofossils varies from poor to good and abundance varies from barren to abundant depending on lithology. Throughout Lithologic Units I and II (see **Sedimentology**), nannofossils are abundant and moderately to well preserved in the nannofossil ooze and chalk intervals, but nannofossils are rare to common and poorly to moderately preserved in the pelagic clay intervals. Where core catcher samples comprise pelagic clays (mostly in Lithologic Unit I) and nannofossil preservation is poor and/or samples were barren or

Table T7. Integrated calcareous nannoplankton and planktic foraminiferal datums, Site U1557. * = *Ch. adriatica* is uncalibrated, just "in O5," so this midpoint is between 26.9 and 28.0 ± 0.55 My. † = *G. siakensis* is uncalibrated, just "in O3," so this midpoint is 29.2 and 30.3 Ma ± 0.55 My. ** = *A. alticonica* is uncalibrated, just "in E7." B of *T. frontosa* in sample below constrains this to Zone E7b, so this datum age is top of Zone E7b to top of Zone E7a, or midpoints of 46.24 to 48.62 ± 1.19 My. T = top, B = base, Bc = base common. **Download table in CSV format.**

Biozone	Event	Datum age (Ma)	Core, section, interval above (cm)	Sample above CSF-A (m)	Sample above CSF-B (m)	Core, section, interval below (cm)	Sample below CSF-A (m)	Sample below CSF-B (m)	Average depth (m)	Depth error (± m)
			390C-U1557B-			390C-U1557B-				
CNPL4	T *Discoaster tamalis*	2.76				1H-CC	4.02	4.02	2.01	2.01
in CNPL3	T *Amaurolithus* spp.	3.93	2H-CC	10.49	10.49	3H-3, 120	15.99	15.99	13.24	2.75
in CNPL1	B *Ceratolithus cristatus*	5.08	6H-2, 20	43.80	43.75	6H-CC	51.86	51.55	47.65	3.90
CNM18	T *Nicklithus amplificus*	5.98	6H-CC	51.86	51.55	7H-3, 92	55.52	55.52	53.535	1.985
CNM17	B *Nicklithus amplificus*	6.82	8H-5, 96	68.06	67.83	8H-CC	70.85	70.53	69.18	1.35
CNM16	B *Amaurolithus* spp.	7.45	8H-CC	70.85	70.53	9H-5, 120	77.80	77.56	74.045	3.515
in CNM13	B *Minylitha convallis*	9.75	10H-4, 135	85.95	85.77	10H-CC	89.85	89.55	87.66	1.89
in CNM12	B *Discoaster bellus*	10.64	11H-2, 65	91.75	91.75	11H-CC	98.86	98.86	95.305	3.555
in CNM8	B *Calcidiscus macintyrei*	13.16	14X-3, 66	117.36	117.36	14X-CC	122.30	122.30	119.83	2.47
CNM4	B *Sphenolithus belemnos*	19.01	17X-3, 50	146.00	146.00	17X-CC	151.16	151.16	148.58	2.58
CNM1	B *Sphenolithus disbelemnos*	22.9	18X-2, 75	154.35	154.35	18X-4, 20	156.80	156.80	155.575	1.225
in CNO4	B *Sphenolithus ciperoensis*	27.13	23X-3, 139	204.49	204.49	23X-CC	208.98	208.98	206.735	2.245
CNO3	B *Sphenolithus distentus*	30	26X-CC	235.88	235.88	27X-4, 64	243.66	243.57	239.725	3.845
CNE21	Bc *Clausicoccus subdistichus*	33.88	28X-3, 28	251.04	251.04	28X-CC	251.53	251.53	251.285	0.245
CNE6	T *Discoaster lodoensis*	48.22	29X-CC	267.37	267.17	31X-1, 47	277.37	277.37	272.27	5.10
CNE3	Bc *Discoaster lodoensis*	52.93	32X-CC	293.03	293.03	33X-4, 135	301.94	301.94	297.485	4.455
in CNE3	B *Discoaster lodoensis*	53.58	34X-CC	311.89	311.89	35X-3, 121	319.52	319.52	315.705	3.815
in CNE3	B *Toweius gammation*	53.67	36X-4, 138	330.79	330.79	36X-CC	332.21	332.21	331.50	0.71
in CNE3	B *Sphenolithus radians*	54.12	37X-3, 110	338.60	338.60	37X-CC	343.59	343.59	341.095	2.495
inCNE2	B *Tribrachiatus orthostylus*	54.3	41X-1, 60	373.50	373.50	41X-CC	375.86	375.86	374.68	1.18
in CNE2	B *Discoaster diastypus*	54.89	45X-3, 43	414.72	414.72	45X-CC	416.58	416.58	415.65	0.93
CNP11	B *Rhomboaster* spp.	56	50X-3, 45	461.25	461.25	50X-3, 60	461.40	461.40	461.325	0.075
in CNP11	T *Ericsonia robusta* (>9 µm)	57.11	51X-CC	472.07	472.07	52X-1, 100	475.50	475.50	473.785	1.715
CNP10	Bc *Discoaster multiradiatus*	57.32	55X-3, 123	505.25	505.25	55X-CC	506.77	506.77	506.01	0.76
in CNP10	B *Ericsonia robusta* (>9 µm)	57.54	58X-1, 24	527.54	527.54	58X-2, 57	529.35	529.35	528.445	0.905
in CNP9	T *Heliolithus kleinpellii*	58.8	58X-CC	530.10	530.10	59X-1, 60	533.40	533.40	531.75	1.65
CNP8	B *Discoaster mohleri*	58.97	59X-2, 91	535.21	535.21	59X-CC	535.73	535.73	535.47	0.26
in CNP8	B *Heliolithus kleinpellii*	59.36	60X-2, 64	544.54	544.54	60X-CC	545.79	545.79	545.165	0.625
in CNP7	T *Fasciculithus pileatus*	60.76	61X-CC	553.05	552.36	62X-1, 70	553.50	553.50	552.93	0.57
PL2	T *Globorotalia margaritae*	3.85	2H-CC	10.49	10.49	3H-CC	17.63	17.63	14.06	3.57
in M14	B *Globorotalia margaritae*	6.09	5H-CC	41.57	41.57	10H-CC	89.85	89.55	65.56	23.99
in O7	T *Tenuitella gemma*	23.53	12X-CC	99.85	99.85	18X-CC	161.48	161.48	130.665	30.815
in O5	T *Chiloguembelina adriatica*	27.45*	18X-CC	161.48	161.48	21X-CC	190.48	190.45	175.965	14.485
in O3	B *Globorotalia siakensis*	29.75†	21X-CC	190.48	190.45	22X-CC	191.56	191.56	191.005	0.555
in O2	B *Paragloborotalia opima*	30.71	22X-CC	191.56	191.56	23X-CC	208.98	208.98	200.27	8.71
in O1	T *Pseudohastigerina micra*	33.9	28X-CC	251.53	251.53	29X-CC	267.45	267.25	259.39	7.86
in E7b	T *Acarinina alticonica*	47.43**	29X-CC	267.45	267.25	32X-CC	293.03	293.03	280.14	12.89
E7a	B *Turborotalia frontosa*	48.62	32X-CC	293.03	293.03	33X-CC	303.44	303.44	298.235	5.205
in E5	T *Morozovella formosa*	50.81	34X-CC	311.89	311.89	35X-CC	320.65	320.65	316.27	4.38
E4	B *Morozovella subbotinae*	54.12	35X-CC	320.65	320.65	40X-CC	369.56	369.56	345.105	24.455
in E2	B *Pearsonites broedermanni*	55.34	49X-CC	454.19	454.19	50X-CC	463.65	463.65	458.92	4.73
P4c	T *Globanomalina pseudomenardii*	57.1	51X-CC	472.07	472.07	53X-CC	484.36	484.36	478.215	6.145
in P4b	T *Morozovella acutispira*	57.59	56X-CC	516.00	516.00	57X-CC	522.04	522.04	519.02	3.02
P4a	T *Parasubbotina variospira*	60.54	58X-CC	530.10	530.10	59X-CC	535.73	535.73	532.915	2.815

rare to common in abundance, additional nannofossil samples were taken to refine the age model. There is common reworking of Paleogene and Neogene taxa throughout Lithologic Unit I and common reworking of Paleogene taxa throughout Lithologic Unit II; therefore, top occurrences were considered carefully before being included in the age model.

The uppermost sediments in Holes U1557A and U1557B (Samples 390C-U1557A-1H-CC, 8–13 cm [9.50 m CSF-B], and 390C-U1557B-1H-CC, 13–18 cm, to 2H-CC, 8–13 cm [4.02–10.49 m CSF-B]) contain abundant well-preserved nannofossils that we judged to be Pliocene–Pleistocene in age (Zone CNPL4). Several species of *Discoaster* are present, including *Discoaster brouweri, Discoaster triradiatus, Discoaster pentaradiatus, Discoaster surculus*, and *Discoaster tamalis* and

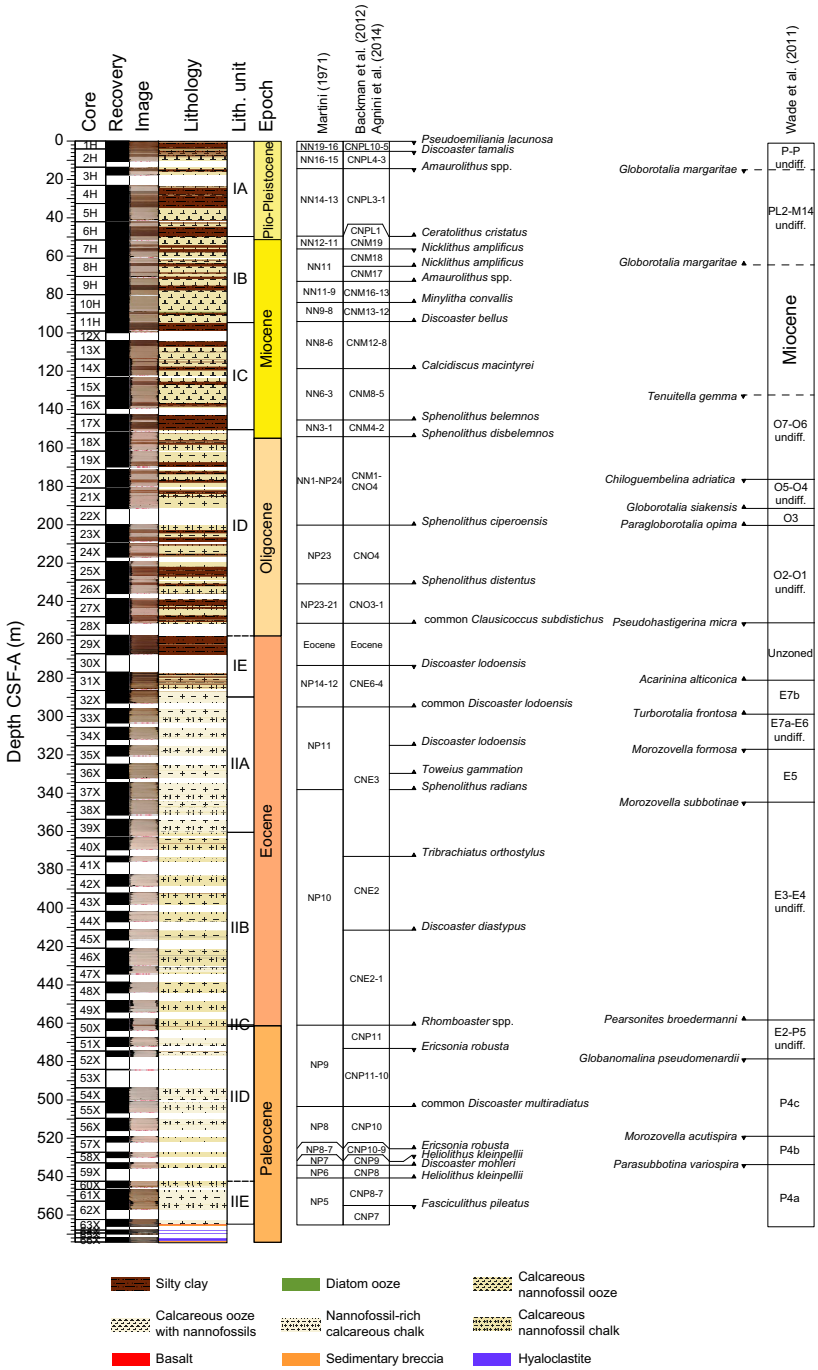

Figure F64. Calcareous nannofossil and planktic foraminiferal biostratigraphic zones and datums, Site U1557. Upward arrows = bioevent base, downward arrows = bioevent top.

abundant small reticulofenestrids. This suggests a very condensed Pleistocene section at Site U1557 that encompasses nannofossil Zones CNPL10–CNPL5.

The interval below these occurrences (15.99–85.77 m CSF-B) in Hole U1557B represents the mid-Pliocene through Late Miocene (nannofossil Zones CNPL3–CNM13) based on the top of *Amaurolithus* spp. in Sample 390C-U1557B-3H-3, 120 cm (15.99 m CSF-B), base of *Ceratolithus cristatus* in Sample 6H-CC, 13–18 cm (51.55 m CSF-B), top of *Nicklithus amplificus* in Sample 7H-3, 92 cm (55.52 m CSF-B), and base of *N. amplificus* in Sample 8H-5, 96 cm (67.83 m CSF-B). The top of Zone CNM16 is marked by the base of *Amaurolithus* spp. in Sample 8H-CC, 15–20 cm (70.53 m CSF-B), whereas the base of *Minylitha convallis* in Sample 10H-4, 135 cm (85.77 m CSF-B), falls within Zone CNM16.

The Early–Middle Miocene (Zones CNM13–CNM2) is recognized between Samples 390C-U1557B-11H-2, 65 cm, and 18X-2, 75 cm (91.75–154.35 m CSF-B), by the following nannofossil events: the base of *Discoaster bellus* (Sample 11H-2, 65 cm; 91.75 m CSF-B), base of *Calcidiscus macintyrei* (Sample 14X-3, 66 cm; 117.36 m CSF-B), base of *Sphenolithus belemnos* (Sample 17X-3, 50 cm; 146.00 m CSF-B), and base of *Sphenolithus disbelemnos* (Sample 18X-2, 75 cm; 154.35 m CSF-B). The late Oligocene, including the Oligocene/Miocene boundary, is poorly constrained in Hole U1557B in part because of lithology, sampling resolution, and reworking of nannofossil marker taxa; thus, top occurrences of bioevents were not used in this interval. The first useful Oligocene bioevent identified is the base of *Sphenolithus ciperoensis* in Sample 23X-3, 139 cm (204.49 m CSF-B), which is within Zone CNO4. The base of *Sphenolithus distentus* occurs in Sample 25X-CC, 13–18 cm (228.71 m CSF-B), marking the top of Zone CNO3.

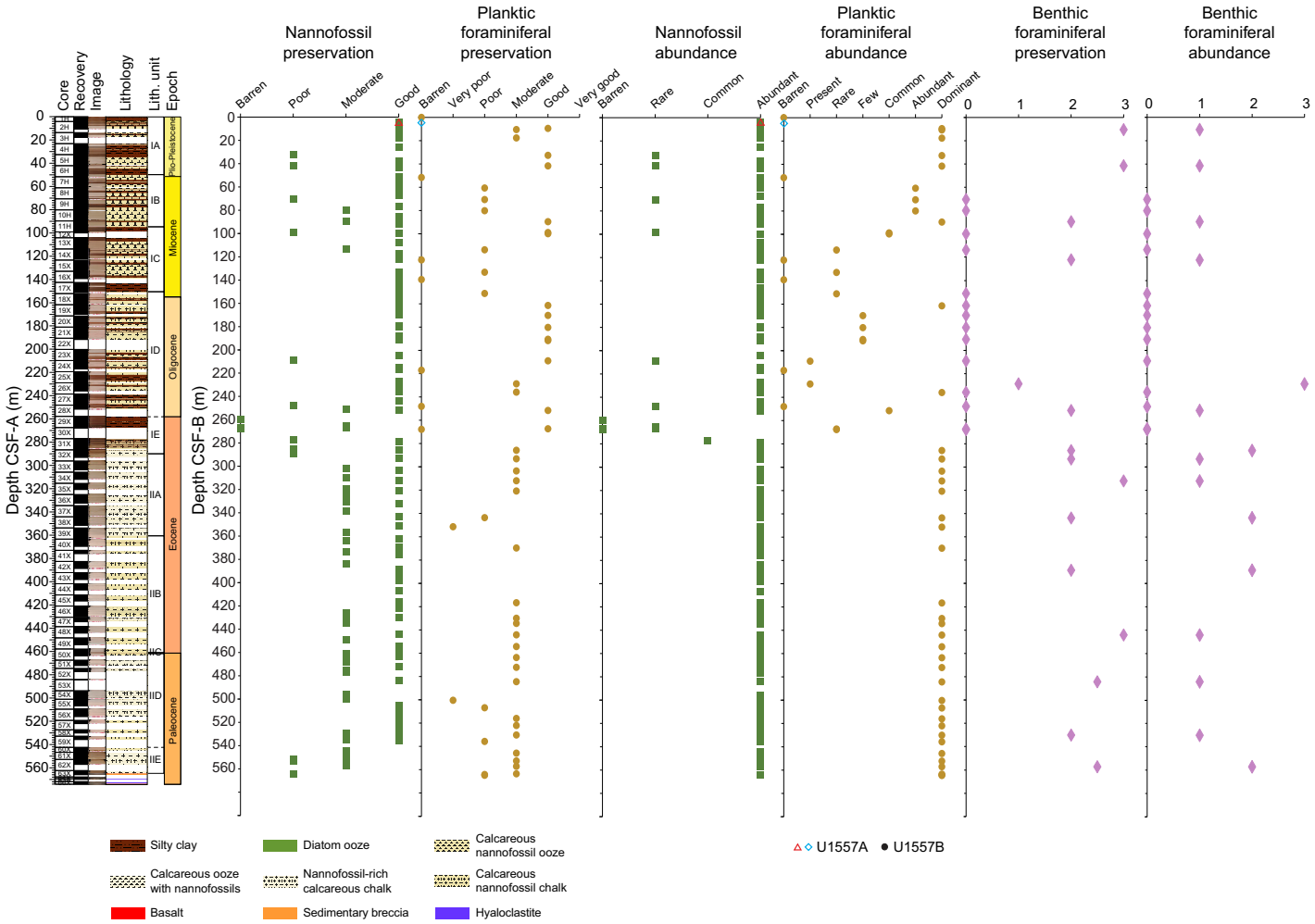

Figure F65. Group abundance and preservation of calcareous nannofossils and planktic and benthic foraminifera, Site U1557.

Sample 390C-U1557B-28X-3, 28 cm (251.04 m CSF-B), is assigned to earliest Oligocene Zone CNO1 by the base common of *Clausicoccus subdistichus*, which is the closest event to the Eocene/Oligocene boundary identified at this site. Sample 28X-CC, 20–25 cm (251.53 m CSF-B), contains abundant and well-preserved nannofossils, but the assemblage is not diverse and lacks any early Oligocene or late Eocene biostratigraphically significant taxa. This is also the lowest sample in the carbonate-rich Lithologic Subunit ID before the transitional Subunit IE, which is classified as primarily silty clay and organic-rich silty clay in Cores 29X and 30X; this unit is either barren of calcareous nannofossils or contains rare taxa that are not age diagnostic (i.e., Samples 29X-2, 78 cm, through 30X-CC, 16–21 cm; 259.93–267.81 m CSF-B). In the lowermost part of Subunit IE, which is described as clayey nannofossil ooze (see **Sedimentology**), Sample 31X-1, 47 cm (277.37 m CSF-B), contains very few calcareous nannofossils, but the presence of *Discoaster lodoensis* and *Discoaster sublodoensis* and the absence of *Blackites inflatus* indicates the sample is early middle Eocene within Zone CNE6. This sample is assigned an age of 48.22 Ma (Gradstein et al., 2020) according to the top of *D. lodoensis*, but it could be as old as 48.80 Ma (base age of *D. sublodoensis*; Gradstein et al., 2020). We therefore interpret the barren/depauperate clay-rich

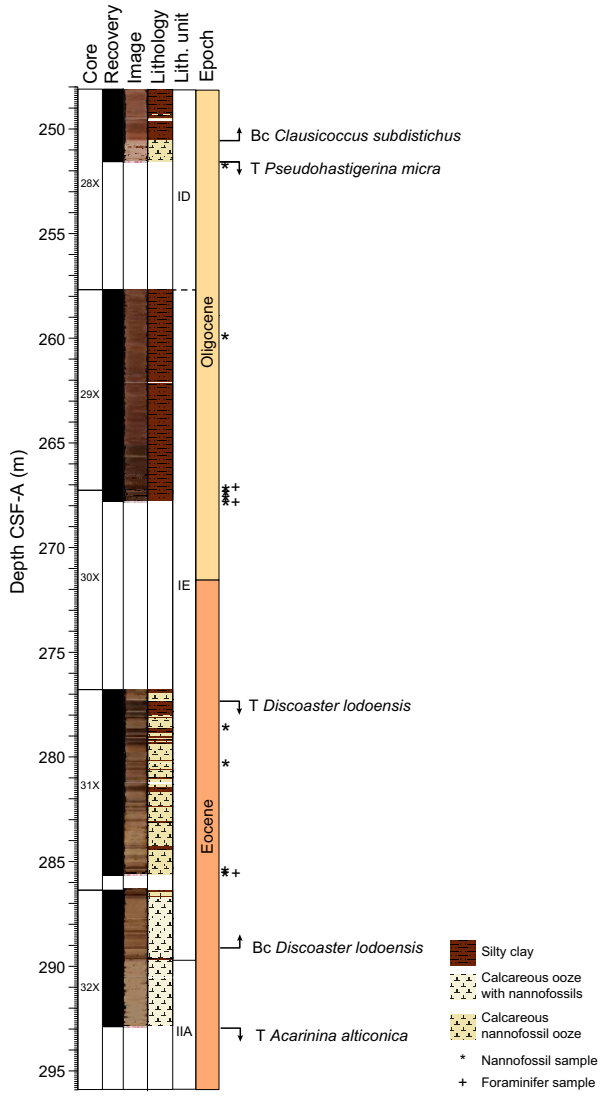

Figure F66. Integrated sedimentology and biostratigraphy for Eocene–Oligocene showing lithologic changes and calcareous microfossil samples and bioevents, Hole U1557B. Bc = base common occurrence; T = top occurrence.

Table T8. Occurrences of important calcareous nannofossils, Site U1557. **Download table in CSV format.**

interval from Cores 29X to 30X, below the base common of *C. subdistichus* (dated to 33.88 Ma; Gradstein et al., 2020), to represent a large condensed interval spanning ~15 My that encompasses nannofossil Zones CNE20–CNE7 as well as the Eocene/Oligocene boundary (dated at 33.90 Ma;

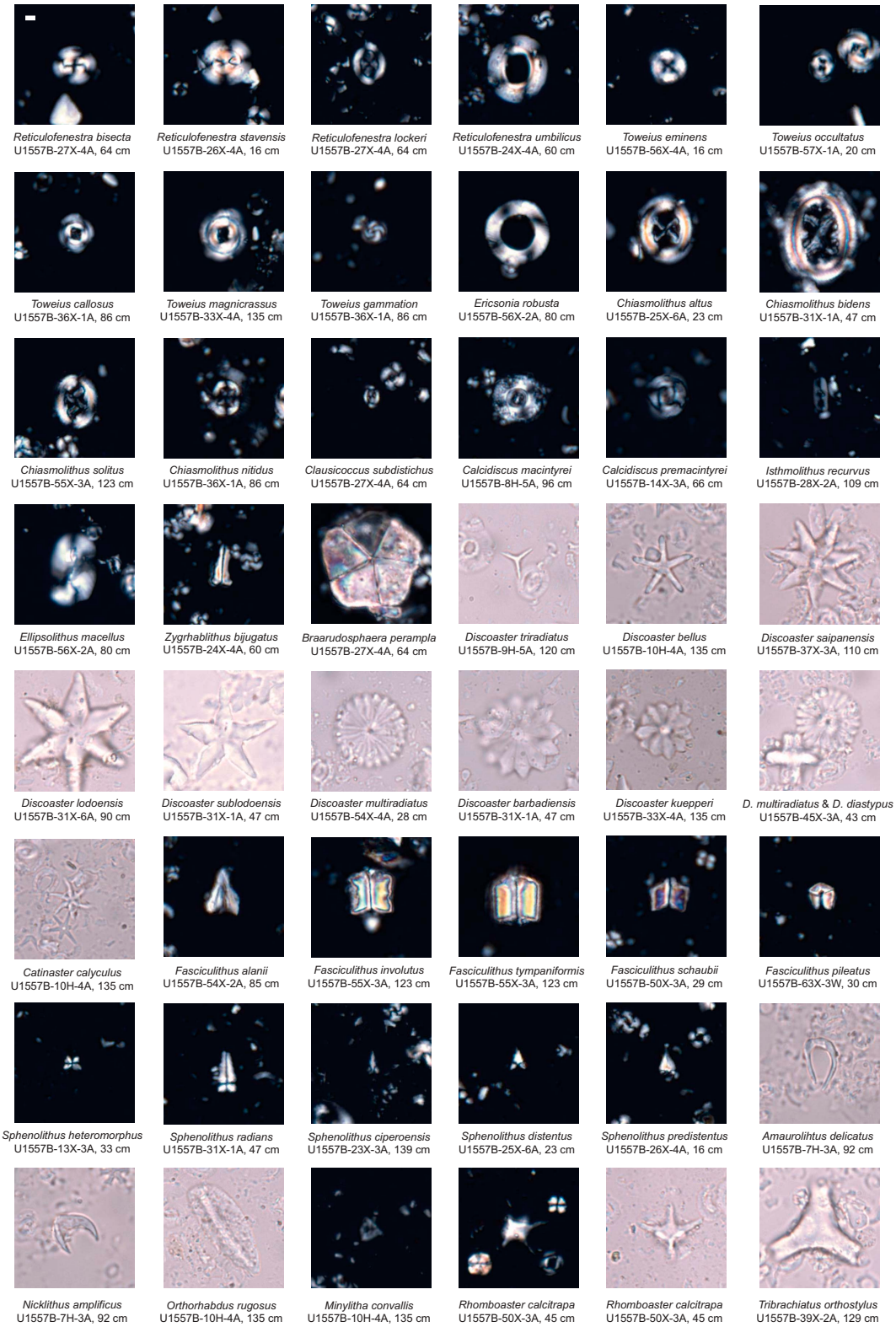

Figure F67. Biostratigraphically important and other notable calcareous nannofossil taxa, Site U1557 (XPL/PPL at 1000× magnification). Scale bar = 2 µm.

Gradstein et al., 2020). Figure **F66** provides an overview of lithologic changes and microfossil sampling and events through this Eocene–Oligocene interval.

Nannofossil preservation in Samples 390C-U1557B-31X-1, 47 cm, through 32X-2, 121 cm (277.37–289.15 m CSF-B), alternates between poor and good; these samples comprise an assemblage of relatively robust early Eocene taxa including *Tribrachiatus orthostylus, Sphenolithus radians*, and the large discoasters *D. lodoensis* and *D. sublodoensis*. The absence of a prominent central boss in the discoasters suggests these samples are affected by dissolution. The base common occurrence of *D. lodoensis* is recorded in Sample 32X-CC, 11–16 cm (293.08 m CSF-B), and marks the top of Zone CNE3. The sample contains a more diverse early Eocene assemblage, including a variety of Eocene *Chiasmolithus* species. All Eocene samples analyzed below this depth contain abundant and diverse calcareous nannofossils.

Interval 390C-U1557B-33X-4, 135 cm, through 49X-CC, 16–21 cm (301.94–454.19 m CSF-B), contains abundant moderately to well-preserved early Eocene calcareous nannofossil assemblages representing Zones CNE3–CNE1. These zones are identified based on the bioevents base of *Toweius gammation* in Sample 36X-4, 138 cm (330.79 m CSF-B), base of *S. radians* in Sample 37X-3, 110 cm (338.60 m CSF-B), base of *T. orthostylus* in Sample 41X-1, 60 cm (373.50 m CSF-B), and base of *Discoaster diastypus* in Sample 45X-3, 43 cm (414.72 m CSF-B).

The base of the genus *Rhomboaster* (Zone CNP11) is recorded in Sample 390C-U1557B-50X-3, 45 cm (461.25 m CSF-B), and multiple species are present including *Rhomboaster bramlettei, Rhomboaster calcitrapa*, and *Rhomboaster cuspis*. This genus is one of the classic markers for the PETM, which is dated at 56.00 Ma (Gradstein et al., 2020). Other excursion taxa, including the *Discoaster araneus* group, are not observed in Hole U1557B; however, identification of the PETM (in Subunit IIC) is supported by lithologic and physical properties data (see **Sedimentology** and **Sediment** in Physical properties and downhole measurements).

Below the PETM section (Samples 390C-U1557B-51X-1, 110 cm, through 60X-CC, 41–46 cm; 468.50–545.79 m CSF-B), Zones CNP11–CNP8 are recognized from the base common of *Discoaster multiradiatus* in Sample 55X-3, 123 cm (505.25 m CSF-B), base of *Ericsonia robusta* in Sample 58X-1, 24 cm (527.54 m CSF-B), top of *Heliolithus kleinpellii* in Sample 59X-1, 60 cm (533.40 m CSF-B), base of *Discoaster mohleri* in Sample 59X-2, 91 cm (535.21 m CSF-B), and base of *H. kleinpellii* in Sample 60X-2, 64 cm (544.54 m CSF-B). Paleocene nannofossil assemblages in this interval are generally diverse with moderate to good preservation.

The preservation state of calcareous nannofossils deteriorates slightly in the lowermost three cores of Hole U1557B (Sample 390C-U1557B-61X-4, 40 cm, through 63X-2, 25 cm; 551.36–564.17 m CSF-B), but the top of *Fasciculithus pileatus* is recorded in Sample 62X-1, 70 cm (553.50 m CSF-B), and the presence of *Fasciculithus tympaniformis* in the lowermost sample (63X-2, 25 cm; 551.36–564.15 m CSF-B) place these samples in Zone CNP7 within the Selandian/Thanetian Stages. This zonation correlates to the planktic foraminiferal biostratigraphy in Hole U1557B as well as the lowermost sediment samples at Sites U1556 and U1561, and it is close to the estimated crustal age of ~61 Ma (see **Background and objectives**).

7.3. Planktic foraminifera

Planktic foraminifera analysis at Site U1557 was predominantly reliant on shore-based investigation of core catcher samples, supplemented by three working-half samples from Core 390C-U1557B-63X, which was split on board the R/V *JOIDES Resolution* during Expedition 390. As such, the zonation scheme is strongly biased by preservation because many core catchers happened to collect pelagic clays and foraminiferal-poor nannofossil oozes from Lithologic Unit I (0–289.84 m CSF-B), which is composed of alternating calcareous and clay-rich layers (see **Sedimentology**). Table **T9** shows the occurrences of biostratigraphically significant species and other notable taxa. Overall, the succession of species appears to match that of Site U1556, where ship-

Table T9. Occurrences of biostratigraphically relevant planktic foraminifera, Holes U1557A and U1557B. **Download table in CSV format.**

board sampling of Hole U1556C provided a more complete biostratigraphic succession that likely also exists in the unsampled carbonate intervals at Site U1557. Preservation and foraminiferal abundance improve in the Eocene and Paleocene sections of Unit II (289.84–564.76 m CSF-B), but the absence of some marker taxa prevents identification of some early Eocene zones. Calcareous nannoplankton do not indicate any significant hiatuses in this interval, so we do not suspect that any time is missing here.

The mudline sample is barren, indicating the modern seafloor is below the carbonate compensation depth (CCD), as at nearby Site U1556 (6.7 km west). Deeper samples from Hole U1557B (Samples 390C-U1557B-1H-CC, 13–18 cm, through 17X-CC, 29–34 cm; 4.02–151.16 m CSF-B) are either barren pelagic clays or nannofossil oozes with very small (<125 μm) and sometimes very rare planktic foraminifera. The exception is Core 5H-CC, 71–76 cm (41.57 m CSF-B), which contains foraminiferal ooze, discussed below. In general, primary zonal markers were absent and age-diagnostic taxa were few. Sample 1H-CC, 13–18 cm, was barren of foraminifera but dominated by large broken diatoms similar to the discrete diatoms layers observed at Site U1556. Sample 390C-U1557A-1H-CC, 8–13 cm (9.45 m CSF-B), from the only core from Hole U1557A (which overshot the mudline), contains a depauperate assemblage of generally Pliocene–Pleistocene foraminifera. The first useful datum is the top of *Globorotalia margaritae* (marking the top of Zone PL2) based on the occurrence of that taxon in Sample 390C-U1557B-3H-CC, 8–13 cm (17.63 m CSF-B). The foraminiferal ooze in Sample 5H-CC, 71–76 cm (41.57 m CSF-B), contains an assemblage that is similar to that of the overlying samples and appears to still represent Zone PL2 based on the absence of *Globoturborotalita nepenthes* from this otherwise diverse population. The next biostratigraphically useful sample is Sample 10H-CC, 35–40 cm (89.55 CSF-B), which contains *Globoconella conomiozea, Globoconella miotumida*, and *Globoturborotalita decoraperta* and lacks *G. margaritae*. The presence of these taxa indicates that this sample is in Upper Miocene Zone M14. The next seven samples (11H-CC, 11–16 cm, through 17X-CC, 29–34 cm; 98.86–151.16 m CSF-B) are either barren or contain depauperate assemblages of broadly Neogene taxa.

Sample 390C-U1557B-18X-CC, 13–18 cm (161.48 m CSF-B), contains a more abundant assemblage of mostly small foraminifera that includes *Tenuitella gemma* (top in Zone O7), indicating that this sample was deposited during the Oligocene. Other taxa are generally long-ranging Oligocene to Early Miocene species including *Globorotalia siakensis, Globoturborotalita ouachitaensis, Globoturborotalita occlusa, Globigerina officinalis, Paragloborotalia nana*, and *Cassigerinella chipolensis*. Sample 21X-CC, 16–21 cm (190.45 m CSF-B), contains *Chiloguembelina adriatica*, which indicates that this sample cannot be younger than Zone O5. Sample 22X-CC, 21–26 cm (191.56 m CSF-B), contains *G. siakensis* and *Globoturborotalita brazieri*, both of which are not older than Zone O3. Likewise, the occurrence of *Paragloborotalia opima* in Sample 23X-CC, 19–24 cm (208.98 m CSF-B), restricts this sample to Zones O5–O2. Together, these three adjacent samples indicate that Cores 21X–23X are broadly mid-Oligocene in age. Samples 24X-CC, 14–19 cm, through 28X-CC, 20–25 cm (216.93–251.53 m CSF-B), are barren or contain no age-diagnostic taxa. Sample 29X-CC, 32–37 cm (267.25 m CSF-B), contains very few foraminifera, but fortunately, one of these is *Pseudohastigerina micra*, which places the sample within Zone O1 or older. Because this sample occurs at the top of the thick dark brown pelagic clay that separates the Eocene from the Oligocene at Sites U1557 and U1556 (see **Biostratigraphy** in the Site U1556 chapter [Coggon et al., 2024a]), we interpret this occurrence of *P. micra* to indicate an earliest Oligocene age for this sample.

Core 390C-U1557B-30X is barren, but Sample 31X-CC, 11–16 cm (285.75 m CSF-B), contains an abundant and diverse middle Eocene assemblage assigned to Zone E7 (based on the occurrence of *Acarinina boudreauxi*, which ranges from Zone E9 to Zone E7, and the questionable occurrence of *Acarinina alticonica*, which has a top in Zone E7). The sample is dominated by robust taxa, including *Subbotina senni*, and contains abundant test fragments that indicate that this assemblage was affected by dissolution. From Core 32X (~286 m CSF-B) to the base of the sediment section in Hole U1557B (564.68 m CSF-B), planktic foraminifera are generally much more abundant and diverse, and the average size of specimens is larger (many >125 μm). Samples 31X-CC, 11–16 cm, through 34X-CC, 31–36 cm (285.75–311.89 m CSF-B), all contain a similar assemblage indicative of Zone E7, including *Acarinina pentacamerata, Acarinina pseudosubsphaerica, Acarinina soldadoensis, A. boudreauxi*, and *Acarinina coalingensis*. *Acarinina cuneicamerata*, which

is a distinctive taxon that marks the top of Zone E6, was not present in any of our samples, so it is not clear whether Zone E6 is missing or we simply cannot identify it because the marker taxon is not found in this area. Sample 35X-CC, 27–32 cm (320.65 m CSF-B), contains *Morozovella aequa, Morozovella gracilis*, and *Morozovella marginodentata* and is tentatively assigned to Zones E5/E4. *Morozovella aragonensis*, which is another distinctive form whose extinction marks the top of Zone E5, was not observed at Site U1557, so we cannot separate Zone E5 from Zone E4. The base of Zone E4 is defined by the base of *Morozovella subbotinae*, which is present in our cores and is not found below Sample 40X-CC, 21–26 cm (369.56 m CSF-B). The Zone E3/E2 boundary is defined by the extinction of *Morozovella velascoensis*, which is also absent from Site U1557. Samples 45X-CC, 33–38 cm, through 49X-CC, 16–21 cm (416.58–454.19 m CSF-B), are therefore assigned to Zone E3/E2 undifferentiated. These samples are also characterized by some degree of reworking, where well-known Paleocene taxa like *Globanomalina pseudomenardii* co-occur with well-known Eocene taxa like *Pearsonites broedermanni*. There is sedimentary evidence for event deposits in this interval of Lithologic Unit II (including scour surfaces, coarse layers, and fining-upward sequences) (Figure **F68**; see **Sedimentology**), so we interpret this co-occurrence to be the result of Eocene reworking of Paleocene material. Care should be taken when sampling these cores to avoid intervals with evidence of bottom water flow or scouring.

Sample 390C-U1557B-50X-CC, 15–20 cm (463.65 m CSF-B), contains no Paleocene marker taxa but also lacks species limited to the Eocene, like *P. broedermanni*, and is therefore assigned to Zone P5. The top of *G. pseudomenardii*, which marks the top of Zone P4c, occurs in Sample 53X-CC, 26–31 cm (484.36 m CSF-B), although given the reworking of this taxon into the Eocene, the placement of the top of this zone is uncertain. *A. soldadoensis*, which marks the top of Zone P4b, was not identified at Site U1557B; however, *Morozovella acutispira*, which is a uniquely high-spired morozovellid that ranges Zone P4a–P4b, is present in fairly high abundance in our samples (as at Site U1556; see **Biostratigraphy** in the Site U1556 chapter [Coggon et al., 2024a]), and the highest occurrence of this taxon in Sample 57X-CC, 8–13 cm (522.04 m CSF-B), allows us to identify the top of Zone P4b at this level. The base of *Subbotina variospira*, which marks the top of Zone P4a, occurs in Core 59X-CC, 21–26 cm (535.73 m CSF-B). Zone P4a extends all the way to the base of the sedimentary succession at Site U1557. The lowest sample examined in the sediment section (Sample 63X-2, 78–80 cm; 564.68 m CSF-B) lacks both *M. acutispira* and *G. pseudomenardii*, but it contains a number of other taxa that are younger than the base of Zone P4a including *Globanomalina chapmani, Morozovella conicotruncata*, and *Morozovella occlusa*. Many of the *M. occlusa* appear transitional with *M. acutispira* but lack the distinctive knob on the raised early spiral chambers of that taxon; we therefore interpret this sample to be near the first appearance of *M. acutispira*, which would place it very close to the base of Zone P4a (the first occurrence is 95% through Zone P3b according to Olsson et al. [1999], although this particular species is not a

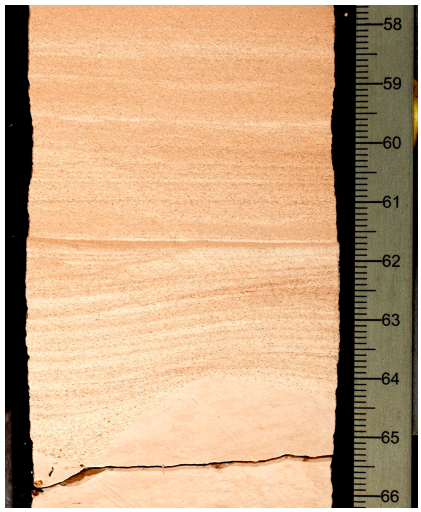

Figure F68. Example of feature indicative of microfossil reworking (390C-U1557B-50X-4). Note erosional base and fining-upward grain size. Brightness levels were adjusted in Adobe Photoshop to highlight bedding features.

well-calibrated zonal marker and Site U1557 is in the mid-latitudes, so some variability in this datum could be expected). A lowest Zone P4a age at this depth is in line with the age indicated by calcareous nannoplankton. A plate of biostratigraphically useful taxa from the base of the sediments in Hole U1557B can be found in Figure **F69**, and changes in planktic and benthic foraminiferal preservation are illustrated in Figure **F70**.

7.4. Benthic foraminifera

Onshore analysis of benthic foraminifera was conducted on core catcher samples of the cores recovered in Hole U1557B during Expedition 390C. Benthic foraminifera preservation, abundance, and assemblage composition were assessed based on the observation of depth-diagnostic calcareous species and other notable calcareous taxa. Agglutinated foraminifera were reported if identified. Benthic foraminiferal preservation and abundance are summarized in Figure **F65**, and some examples of benthic foraminiferal preservation are illustrated in Figure **F70**. The occurrence of important benthic foraminiferal species is reported in Table **T10**. Overall, the benthic foraminiferal assemblages suggest that Site U1557 could have been lying at upper abyssal depths (~2000–3000 m) during the late Paleocene and earliest middle Eocene (~61–48 Ma) and reached lower abyssal depths (>3000 m) by the Late Miocene; however, the timing of this transition is uncertain.

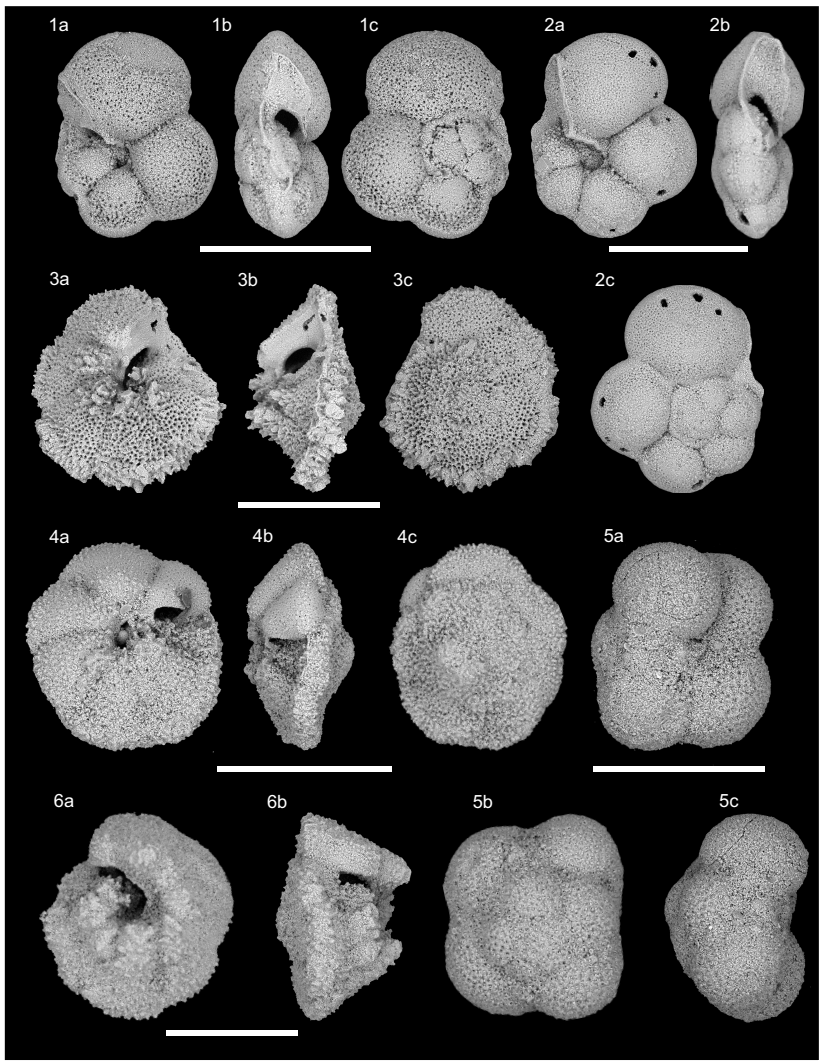

Figure F69. Scanning electron microscope images of key middle Paleocene planktic foraminifera from base of sedimentary section, Hole U1557B. Scale bars = 300 µm. 1, 2. *Globanomalina chapmani*. 3a–3c. *Morozovella occlusa*. 4a–4c. *Morozovella occlusa* aff. *Morozovella acutispira*. 5a–5c. *Parasubbotina variospira*. 6a, 6b. *Morozovella conicotruncata*. (1, 3: 63X-1, 112–116 cm. 2, 4–6: 63X-2, 78–80 cm.)

Middle and late Eocene samples are characterized by a benthic foraminiferal assemblage composed of species with a wide abyssal distribution (Holbourn et al., 2013; Tjalsma and Lohmann, 1893). In addition, a lot of late Eocene–Middle Miocene samples were barren of benthic foraminifera. However, the presence of *Nuttallides umbonifera* in one early Oligocene sample (Sample 390C-U1557B-25X-CC, 13–18 cm; 228.71 m CSF-B) implies that Site U1557 could have been lying at lower abyssal depths by the early Oligocene. This interpretation carries some uncertainties because the amount of sediment in this sample was so scarce that analysis was performed without sieving the residue and the benthic foraminiferal specimens picked were rather small (<100 µm) and of very poor preservation.

Benthic foraminifera are present in Samples 390C-U1557B-2H-CC, 8–13 cm, and 5H-CC, 71–76 cm (10.49 and 41.57 m CSF-B, respectively), including *Melonis barleeanus, N. umbonifera, Oridorsalis umbonatus, Pullenia bulloides*, and *Pullenia quinqueloba*. Sample 5H-CC, 71–76 cm, is also characterized by *Anomalinoides globosus, Cibicidoides mundulus*, and *Cibicidoides wuellerstorfi*. *N. umbonifera* is a species considered indicative of Antarctic Bottom Water (Corliss, 1979; Mackensen et al., 1995) and is the dominant species in both of these samples, implying that this site was lying at lower abyssal depths (>3000 m) from the Late Miocene.

Many samples were barren of benthic foraminifera between Samples 390C-U1557B-8H-CC, 15–20 cm, and 30X-CC, 16–21 cm (70.53 and 267.81 m CSF-B, respectively), with few exceptions. Sample 10H-CC, 35–40 cm (89.55 m CSF-B), contains a few specimens of *Cibicidoides* sp., *Lagena* sp., and *P. bulloides*, and Sample 14X-CC, 18–23 cm (122.30 m CSF-B), contains only one *Lagena* sp. specimen. In Sample 25X-CC, 13–18 cm (228.71 m CSF-B), a few specimens of *Cibicidoides* sp. and *N. umbonifera* are observed. *N. umbonifera* is an indicator of low abyssal depths, and its presence might imply that Site U1557 could have been lying at lower abyssal depths by the early Oligocene. However, this interpretation is uncertain as explained in detail above. Finally, in Sam-

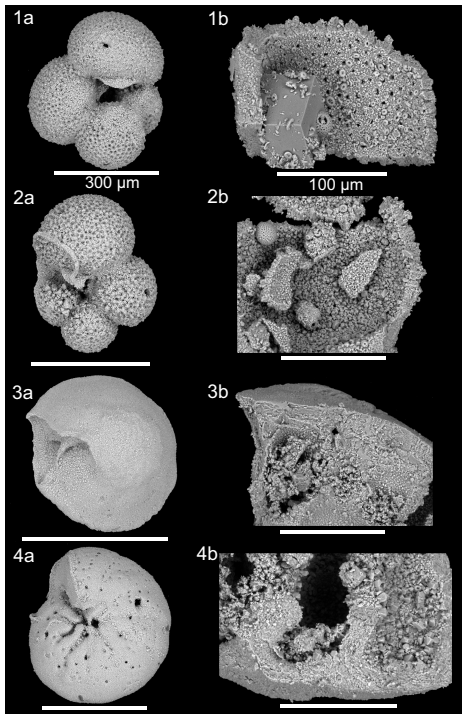

Figure F70. Scanning electron microscope images showing calcite preservation from representative planktic and benthic foraminifera at base of sedimentary section, Hole U1557B. a = 250×, b = 1000×. 1a, 1b. *Parasubbotina variospira* (note the large euhedral calcite crystal in 1b). 2a, 2b. *Parasubbotina varianta*. 3a, 3b. *Nuttallides truempyi*. 4a, 4b. *Gavelinella* sp. (1, 3: 63X-1, 112–116 cm. 2, 4: 63X-2, 78–80 cm.)

Table T10. Occurrences of important benthic foraminifera, Hole U1557B. **Download table in CSV format.**

ple 28X-CC, 20–25 cm (251.53 m CSF-B), a few specimens belonging to *O. umbonatus* and *P. bulloides* are identified.

Early middle Eocene Sample 390C-U1557B-31X-CC, 11–16 cm (285.75 m CSF-B), is characterized by abundant *Nuttallides truempyi* and *O. umbonatus* specimens. *Alabamina dissonata, Bulimina trinitatensis, Cibicidoides havanensis, Clinapertina complanata, Globocassidulina subglobosa*, and *Nonion havanense* are also observed. Sample 32X-CC, 11–16 cm (293.03 m CSF-B), is dominated by *N. truempyi* as well. *Anomalina spissiformis, Cibicidoides tuxpamensis, Cibicidoides ungerianus, Lenticulina excisa, N. havanense*, and *O. umbonatus* are present. *Pullenia coryelli* is also identified, suggesting some degree of reworking. The presence of *B. trinitatensis* and some lenticulinids in these samples suggest that Site U1557 layed at upper abyssal depths until the earliest middle Eocene (~48 Ma).

In early Eocene samples (390C-U1557B-34X-CC, 31–36 cm; 37X-CC, 13–18 cm; 42X-CC, 10–15 cm, 47X-CC, 23–28 cm; and 48X-CC, 12–17 cm; 311.89, 343.59, 388.53, and 444.19 m CSF-B, respectively), *N. truempyi* and *O. umbonatus* are commonly identified. Other observed species include *B. trinitatensis, Buliminella beaumonti, Gavelinella capitata, N. havanense, Quadrimorphina profunda*, and *P. bulloides*. Many *Cibicidoides* are also present in these samples, such as *Cibicidoides bradyi, Cibicidoides* cf. *pseudoperlucidus, Cibicidoides eoceanus, Cibicidoides hyphalus, Cibicidoides praemundulus*, and *C. ungerianus*. The presence in these samples of several diachronous species, like *Aragonia ouezzanensis, Lenticulina whitei, Neoflabellina reticulata*, and *P. coryelli* is interpreted to be evidence of reworking.

Paleocene samples (390C-U1557B-53X-CC, 26–31 cm; 58X-CC, 8–13 cm; and 62X-CC, 28–33 cm; 484.36, 530.10, and 557.11 m CSF-B, respectively) are characterized by a typical Paleocene assemblage. *N. truempyi* dominates all these samples. Numerous additional specimens belong to *Anomalina praeacuta, A. ouezzanensis, C. hyphalus, C.* cf. *pseudoperlucidus, Gavelinella beccariiformis, Gyroidinoides globosus, Gyroidinoides* cf. *quadratus, Neoeponides hillebrandti, Neoflabellina semireticulata, N. havanense, O. umbonatus, Osangularia velascoensis*, and *P. coryelli*. Buliminids (i.e., *Bulimina* cf. *trihedra, Bulimina velascoensis*, and *Bulimina* spp.) and lenticulinids (i.e., *L. excisa* and *L. whitei*) are also observed in these samples. Interestingly, *C. praemundulus* is a species that evolved in the early Eocene (Holbourn et al., 2013) and is identified in all the Paleocene samples analyzed.

8. Paleomagnetism

8.1. Sediment

The sediment package at Site U1557 was cored in Holes U1557A (a single missed mudline core) and U1557B during engineering Expedition 390C (Estes et al., 2021), during which all but the lowermost sediment cores were split, and remanence measurements were made using the superconducting rock magnetometer (SRM) (see **Paleomagnetism** in the Expedition 390/393 methods chapter [Coggon et al., 2024c]). We remeasured many of the Hole U1557B cores during Expedition 390, noting that they had previously been demagnetized to 20 mT during Expedition 390C. The natural remanent magnetization (NRM) of core sections was measured at 2 cm spacing. Three alternating field (AF) demagnetization steps (5, 10, and 20 mT) were applied, and the remanence was measured after each step. Hereafter, the intensity/inclination after demagnetization at 20 mT is referred to as the 20 mT intensity/inclination. We use these data to establish a magnetostratigraphy for the upper part of the sediment package at Site U1557. APC Cores 390C-U1557B-1H through 11H were oriented using the Icefield MI-5 core orientation tool.

Because there was no shipboard science party during Expedition 390C, discrete samples were taken only from the working halves of cores recovered from the sediment–basement transition (Cores 390C-U1557B-63X through 66X). Hence, there was no opportunity to supplement the split-core section remanence data collected during Expedition 390C with discrete sample analyses during Expedition 390.

8.1.1. Results

Measurement of the NRM and in-line AF demagnetization of APC cores (390C-U1557A-1H and 390C-U1557B-1H through 11H) and XCB cores (12X–63X) were carried out to establish a magnetostratigraphy for the entire sediment package at Site U1557. AF demagnetization of 5–20 mT generally removes a viscous overprint (Figures **F71**, **F72**). In cores recovered by scientific ocean drilling, viscous overprints are in most cases an unavoidable drilling overprint, even when nonmagnetic core barrels are employed (i.e., during APC coring), although this is not always the case. Such an overprint will manifest as a near-vertical component on an orthogonal vector plot (Zijderveld, 1967) and will bias inclinations, in this case toward more positive values. The 20 mT inclinations in Core 390C-U1557A-1H are bimodal, clustering around –46.7° or 45.3° (Figure **F73A**). The 20 mT inclinations for Hole U1557B are also bimodal and cluster around –52.2° and 49.8° (Figure **F73B**), but it is notable that there are many shallower and steeper values than those expected for a geocentric axial dipole (GAD) at this latitude (±49.1° at 30°S) (Figure **F73B**).

For both holes at Site U1557, MS and intensity correlate with lithologic variations (see **Sedimentology**); high values correspond to the silty clays, whereas lower values correspond to the biogenic carbonates. The remanence intensities for the sediment succession at Site U1557 are relatively strong for pelagic material. The single core collected from Hole U1557A has average NRM and 20 mT intensities of 2×10^{-2} and 5×10^{-2} A/m, respectively (Figure **F71**). Hole U1557B has average NRM and 20 mT intensities of 1.3×10^{-2} and 0.43×10^{-2} A/m, respectively. NRM and 20 mT intensity vary by several orders of magnitude throughout the hole. In some intervals containing drilling disturbance manifested as prominent biscuiting (see **Sedimentology**), the observed high remanence intensity may not reflect the magnetic feature of the in situ sediments. Consequently, the intensity data presented for Hole U1557B in Figure **F72** are restricted to a maximum of 4×10^{-2} A/m because values beyond this are likely spurious. Variations in 20 mT intensity downhole reflect the variable clay content of the sediments; Unit I has an average 20 mT intensity of 0.58×10^{-2} A/m, whereas the carbonate-dominated Unit II (mostly calcareous nannofossil chalk; see **Sedimentology**) has a lower average 20 mT intensity of 0.22×10^{-2} A/m.

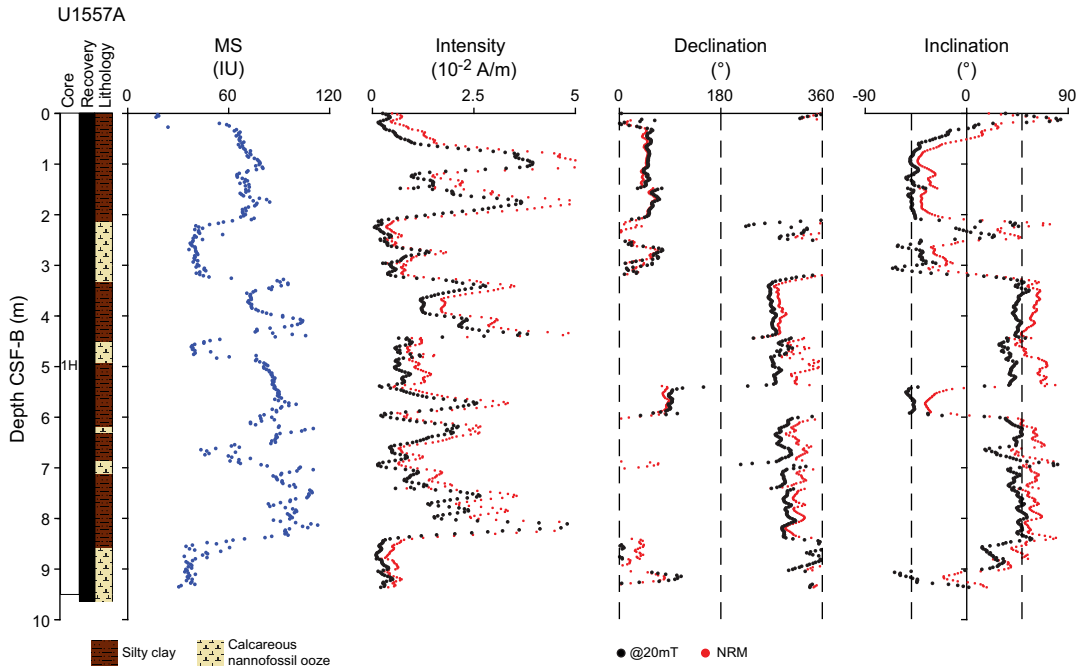

Figure F71. Archive-half MSP (MS; from SHMSL) and SRM measurements, Hole U1557A. Dashed lines on declination = values expected for normal (360°) and reversed (180°) polarity chrons, dashed lines on inclination = GAD inclination (±49.1°) expected for this latitude (~30°S). Intensity data are restricted to maximum of 5×10^{-2} A/m.

8.1.1.1. Discrete samples

Discrete sampling for magnetic investigations in Hole U1557B was limited to 5 samples from the working halves of the sediment/basement interface cores (390C-U1557B-63X through 66X; 562.4–574.0 m CSF-B).

Two of the discrete samples comprise lithified sediment collected from Core 390C-U1557B-63X above the sediment–basement transition. The other three discrete samples are basalts and a hyalo-

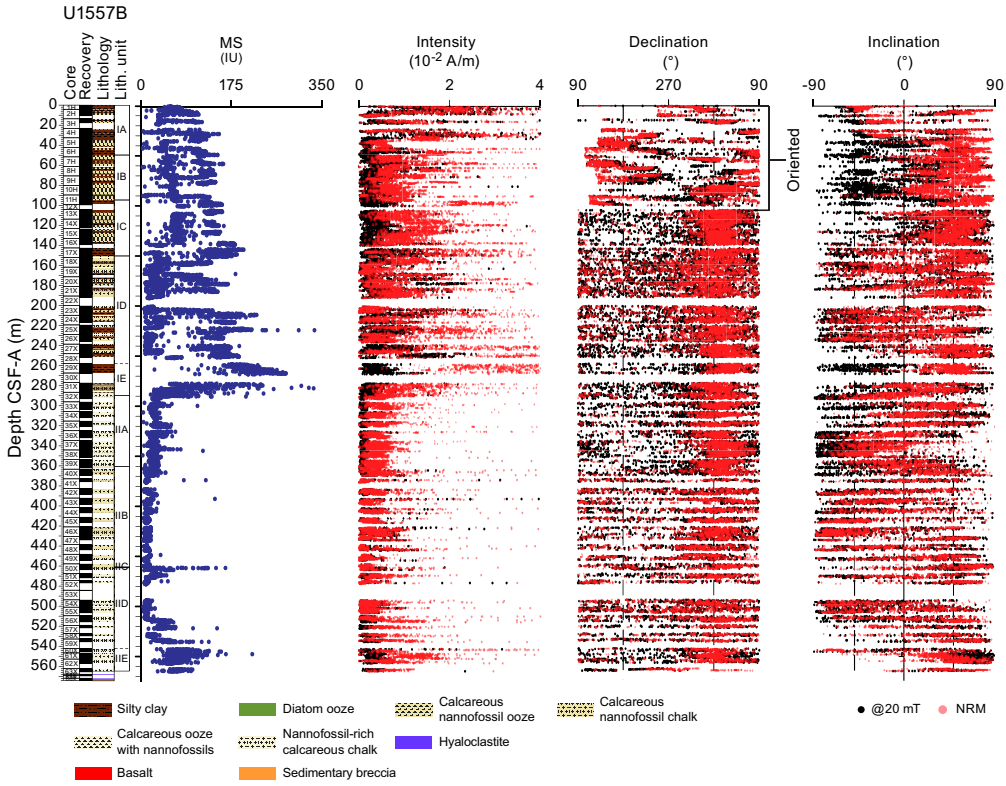

Figure F72. Archive-half MSP (MS; from SHMSL) and SRM measurements, Hole U1557B. Dashed lines on declination = values expected for normal (360°) and reversed (180°) polarity chrons, dashed lines on inclination = GAD inclination (±49.1°) expected for this latitude (~30°S). Intensity data are restricted to maximum of 4×10^{-2} A/m. Interval where declination was corrected using Icefield MI-5 core orientation tool (see Paleomagnetism in the Expedition 390/393 methods chapter [Coggon et al., 2024c]) is indicated.

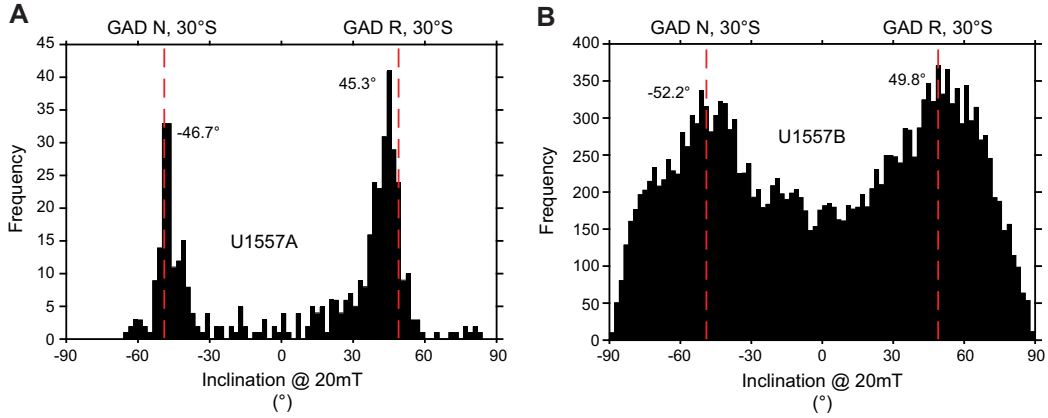

Figure F73. Histograms of SRM inclination after 20 mT AF demagnetization, Holes (A) U1557A and (B) U1557B. Positive and negative values indicate modal inclinations for the normal and reversed populations, respectively. Dashed lines = inclination (±49.1°) of GAD expected for this latitude (~30°S) during normal (N) and reversed (R) chrons.

clastite breccia from Cores 65X and 66X in basement Unit 1 (see **Basement** in this section for discussion). The discrete sediment samples were subjected to full stepwise AF demagnetization up to 100 mT. By demagnetizing the samples in a stepwise fashion, we are able to determine the characteristic remanent magnetization (ChRM) of the sample, which reflects the magnetic field direction at or soon after sediment deposition and aids in the magnetostratigraphic interpretation. The anisotropy of magnetic susceptibility (AMS) was also measured for both samples, whereas isothermal remanent magnetization (IRM) experiments were conducted only on Sample 63X-1, 112–114 cm (see **Paleomagnetism** in the Expedition 390/393 methods chapter [Coggon et al., 2024c]).

Sample 390C-U1557B-63X-1, 112–114 cm, shows a smooth demagnetization curve and a well-defined ChRM with a downward (positive) inclination, indicating a reversed polarity chron at the base of Hole U1557B (Figure **F74**). This is consistent with the Site U1557 biostratigraphic age model (see **Biostratigraphy**) and the CREST regional site survey (Kardell et al., 2019). The ChRM inclination and direction of this discrete sediment sample (inclination ≈ 37°; declination ≈ 128°) calculated using principal component analysis (PCA) (Kirschvink, 1980) between 30 and 60 mT is lower than that expected for a GAD at this latitude (30°S).

The median destructive field and coercivity spectra for these samples suggest magnetite-like phases as the dominant magnetic carrier, but future shore-based experiments are needed to confirm this.

8.1.1.2. Magnetostratigraphy

SRM measurements on the archive halves after AF demagnetization at 20 mT helped determine a preliminary partial polarity sequence for this site. Corrected declinations (Richter et al., 2007) are shown alongside the inclination data for APC Cores 390C-U1557B-1H through 11H (0–98.74 m CSF-B), whereas declinations for XCB cores (Core 12X and below) are uncorrected (Figure **F75**). Our interpretations are based on the inclination sign after the 20 mT demagnetization step. A preliminary magnetostratigraphy extends to 110 m CSF-B. Large coring gaps (up to ~9 m) are present in intervals cored using both the APC and XCB systems, and continuous drilling disturbance throughout XCB cores makes magnetostratigraphic interpretation for Hole U1557B difficult below this depth. Three intervals of normal polarity are identified in Core 390C-U1557A-1H that we correlate to the Brunhes, Jaramillo, and Cobb Mountain Chrons. Similar normal polarity intervals are also identified in the uppermost cores from Hole U1557B (Cores 390C-U1557B-1H and 2H) (Figure **F76**). MS data, along with our chron identification presented here, contribute to

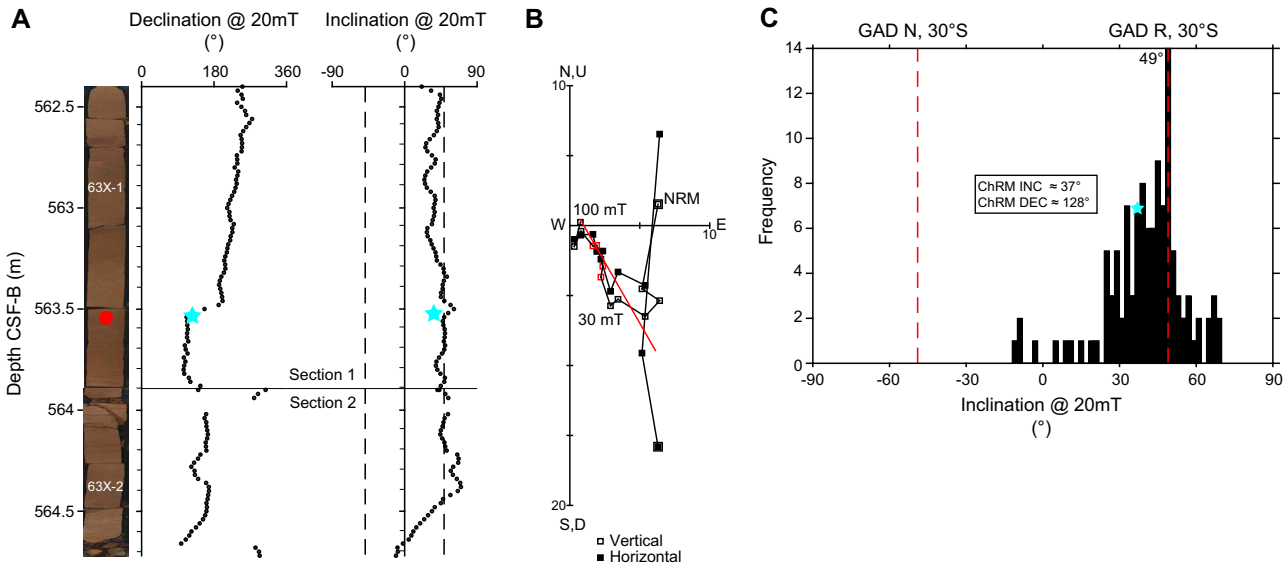

Figure F74. A. SRM declination and inclination (390C-U1557B-63X-1 and 63X-2; 562.4–564.72 m CSF-B). Red circle = discrete sample location (63X-1, 112–114 cm; 563.52–563.54 m CSF-B), stars = declination and inclination of ChRM of discrete sample, dashed lines on inclination = GAD inclination (±49.1°) expected at site latitude. B. Orthogonal vector plot for discrete sample. Red squares = remanence directions used to compute ChRM component (red line). C. Histogram of SRM 20 mT inclination (63X-1 and 63X-2). Star = fitted ChRM direction of discrete sample, dashed lines = GAD inclination expected at site latitude.

stratigraphic correlation efforts to identify missing strata in Cores 1H and 2H and the construction of a splice between the two holes (see **Physical properties and downhole measurements**). Unfortunately, the incomplete recovery of the uppermost 10 m of the sediment package in Hole

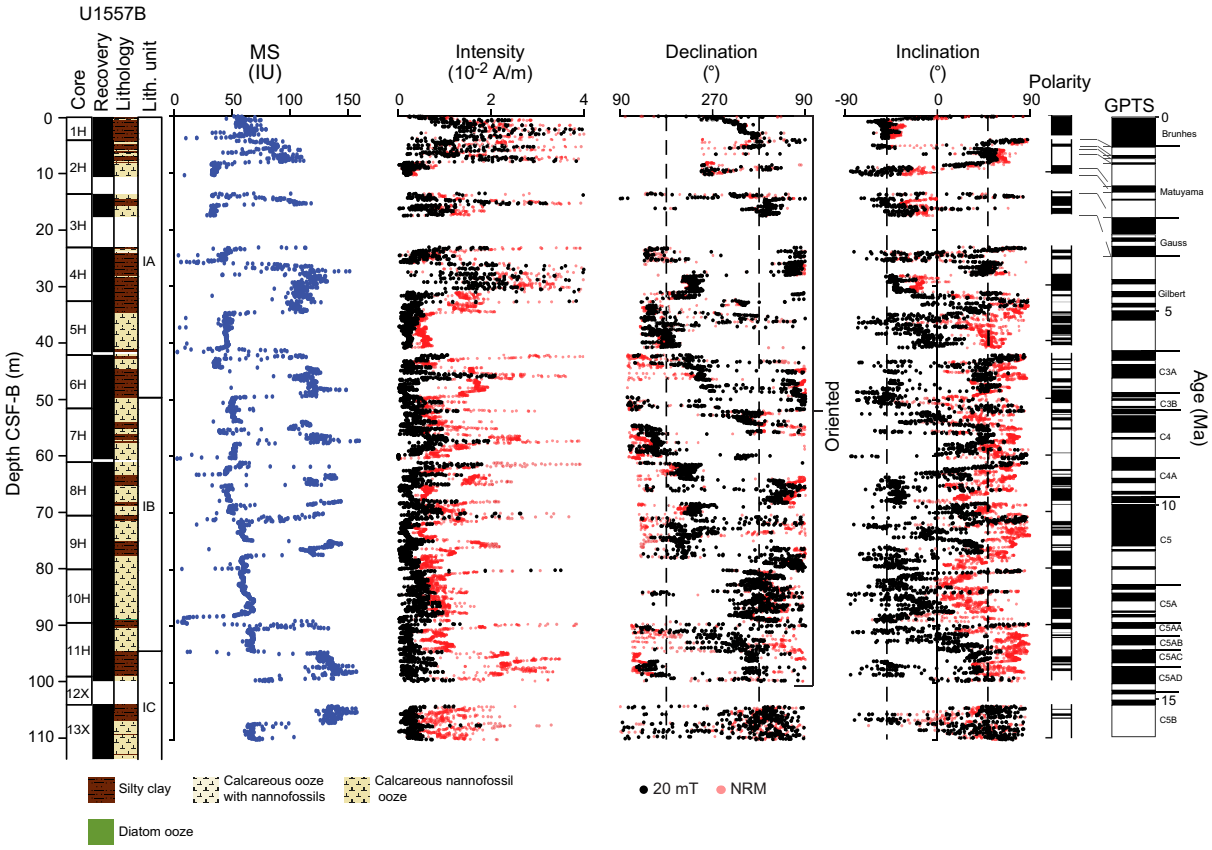

Figure F75. Archive-half MSP (MS; from SHMSL) and SRM measurements for 0–110 m CSF-B, Hole U1557B. Dashed lines on declination = values expected for normal (360°) and reversed (180°) polarity chrons, dashed lines on inclination = GAD inclination (±49.1°) expected for this latitude (~30°S). Intensity data is restricted to maximum of 4 × 10^{-2} A/m. Identified polarity sequence is matched to geomagnetic polarity timescale (GPTS; Gradstein et al., 2020) using dashed tie lines.

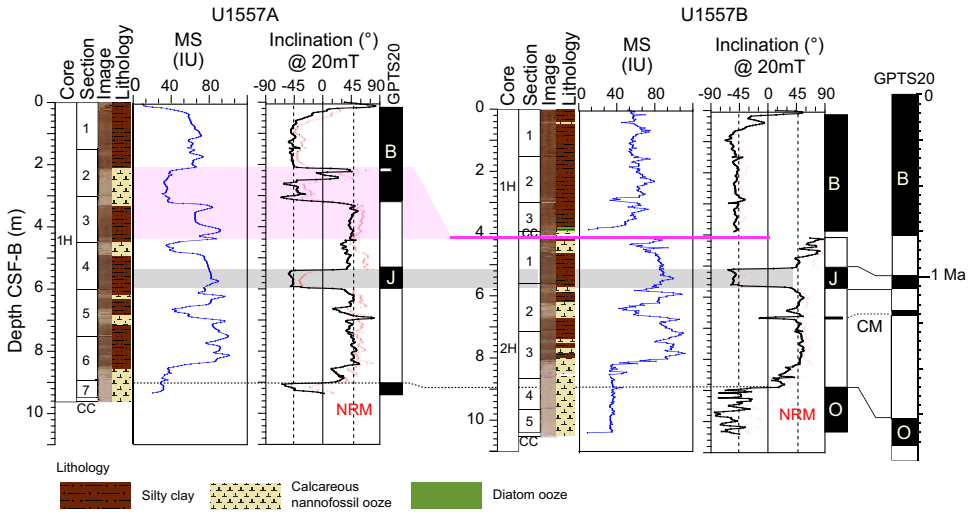

Figure F76. Archive-half MSP (MS; from SHMSL) and SRM inclinations for NRM and after 20 mT AF demagnetization from uppermost 10 m of Holes U1557A and U1557B. Dashed lines = GAD inclination (±49.1°) expected at site latitude. Shading in Hole U1557A = interval missed between Cores 1H and 2H in Hole U1557B. Pink line in Hole U1557B contains Brunhes/Matuyama boundary. B = Brunhes chron. GPTS = geomagnetic polarity timescale.

U1557B results in uncertainty in the depth estimate of the Brunhes/Matuyama Chron boundary in that hole because the reversal itself was not recovered (Figure **F76**). We have tentatively identified the onset of Chron 5Bn at ~15.2 Ma in Core 11H-5 (96.15 m CSF-B) based on a reversal pattern comparison with the current geomagnetic polarity timescale (Gradstein et al., 2020) (Figure **F75**). Biostratigraphic datums from both nannofossils and foraminifera (see **Biostratigraphy**) were used to refine this model, although there are some discrepancies between the biostratigraphic and paleomagnetic datums for Site U1557 (see **Age model and mass accumulation rates**). Magnetostratigraphic dating of the upper ~220 m of Site U1557 will be attempted during postexpedition work by incorporating the polarity sequence from Site U1556, which can be correlated quite well to the sequence at Site U1557.

8.2. Basement

Progressive AF demagnetization of basement split-core sections and discrete samples was used to characterize the paleomagnetic signal and resolve the magnetization components and history recorded in breccias at Site U1557. Remanence measurements on archive-half split cores were made at 2 cm spacing using the SRM (see **Paleomagnetism** in the Expedition 390/393 methods chapter [Coggon et al., 2024c]). Three AF steps (5, 10, and 20 mT) were applied, and the remanence was measured after each step.

The basement section in Hole U1557D comprises a sedimentary (talus) breccia with basalt clasts in a matrix of lithified pelagic sediment and/or volcanic material (see **Igneous petrology**). Discrete sampling in Hole U1557D targeted individual clasts of the breccia with diverse styles of alteration and yielded 13 discrete cube samples (8 cm^3).

Discrete breccia clast samples were used primarily to characterize the magnetic mineral assemblage. In addition, AMS was measured on all discrete samples to characterize their magnetic fabric. Acquisition of IRM and backfield IRM experiments were performed on two discrete samples.

8.2.1. Results

Measurement of the NRM and in-line AF demagnetization of Cores 390-U1557D-2R through 14R was conducted using the SRM to understand the magnetization history of the volcaniclastic sedimentary breccias. Hereafter, the intensity/inclination after demagnetization at 20 mT will be referred to as the 20 mT intensity/inclination.

AF demagnetization in the range 5–20 mT generally removes a small viscous overprint in Hole U1557D cores, observed as a consistent shift in the inclination data through the hole, although the scatter in the data makes this difficult to resolve (Figure **F77**). In cores recovered by scientific ocean drilling, viscous overprints are in most cases an unavoidable drilling overprint even when nonmagnetic core barrels are employed (i.e., during APC and RCB coring). Unlike other cores collected during Expedition 390, cores from Hole U1557D have 20 mT inclinations that are not bimodal; they instead display a Gaussian-like distribution (Figure **F78**). The inclinations measured by SRM in Hole U1557D span the full spectrum of values from −90° to 90° with a modal value around 7°. This is much shallower than the inclination expected for this latitude for a GAD (±49.1° at 30°S). This large departure from that GAD inclination is likely a function of the effect induced by the large clasts from the sedimentary breccia, which should produce randomly oriented directions if the ChRM was blocked before clast emplacement (see below).

8.2.1.1. Discrete samples

We collected ~1 discrete cube per core in Hole U1557D (13 samples total), with all discrete samples comprising basalt clasts from the sedimentary breccia. AMS was measured on all discrete cubes. AMS is routinely used as a petrofabric proxy to determine the preferred alignment of minerals in a sample.

Demagnetization of all the discrete samples in a stepwise fashion to at most 100 mT was conducted to determine the ChRM of each sample. Every discrete breccia clast sample displayed good-quality stable demagnetization data of a single component that describes a straight line to the origin, defining the ChRM (Figure **F79A**). Inclinations of the ChRM, calculated using PCA (Kirschvink, 1980), show similarly variable values to those measured by SRM. All discrete samples

gave maximum angular deviation angles <15°, which is typically considered the uppermost threshold for well-defined field directions (Table **T11**) (Butler, 1992). Two of the 13 studied samples suggest the presence of a small spurious component or overprint that is removed by either 10 or 20 mT. Stepwise demagnetization at higher fields defines the ChRM component direction, supporting the SRM data. Moreover, nearly every discrete sample was fully demagnetized by 60 mT, whereas 70% of the NRM was already removed by 30 mT, indicating the magnetic mineral assemblage consists of soft coercivity phases (e.g., titanomagnetite or titanomaghemite), probably coarser grained. Acquisition of IRM and backfield IRM experiments (Figure **F80**) further illustrate the softness of the ferrimagnetic assemblage. In the two studied samples from Hole U1557D, the coercivity of remanence (B_{cr}) values are around 20 mT. The S ratios are equal to 1, and the IRM_{100}/SIRM ratios are 0.99 and 1 (Table **T11**), suggesting the dominance of low-coercivity (soft) mineral phases (e.g., magnetite and titanomagnetite).

AMS is routinely used as a petrofabric proxy to determine the preferred orientation of the magnetic mineral assemblage in a sample and was measured on all discrete cubes. AMS indicates the presence of both oblate (planar) and prolate (linear) magnetic susceptibility ellipsoids, but there is no systematic variation in the ellipsoid shape with depth through the breccia sequence. The AMS

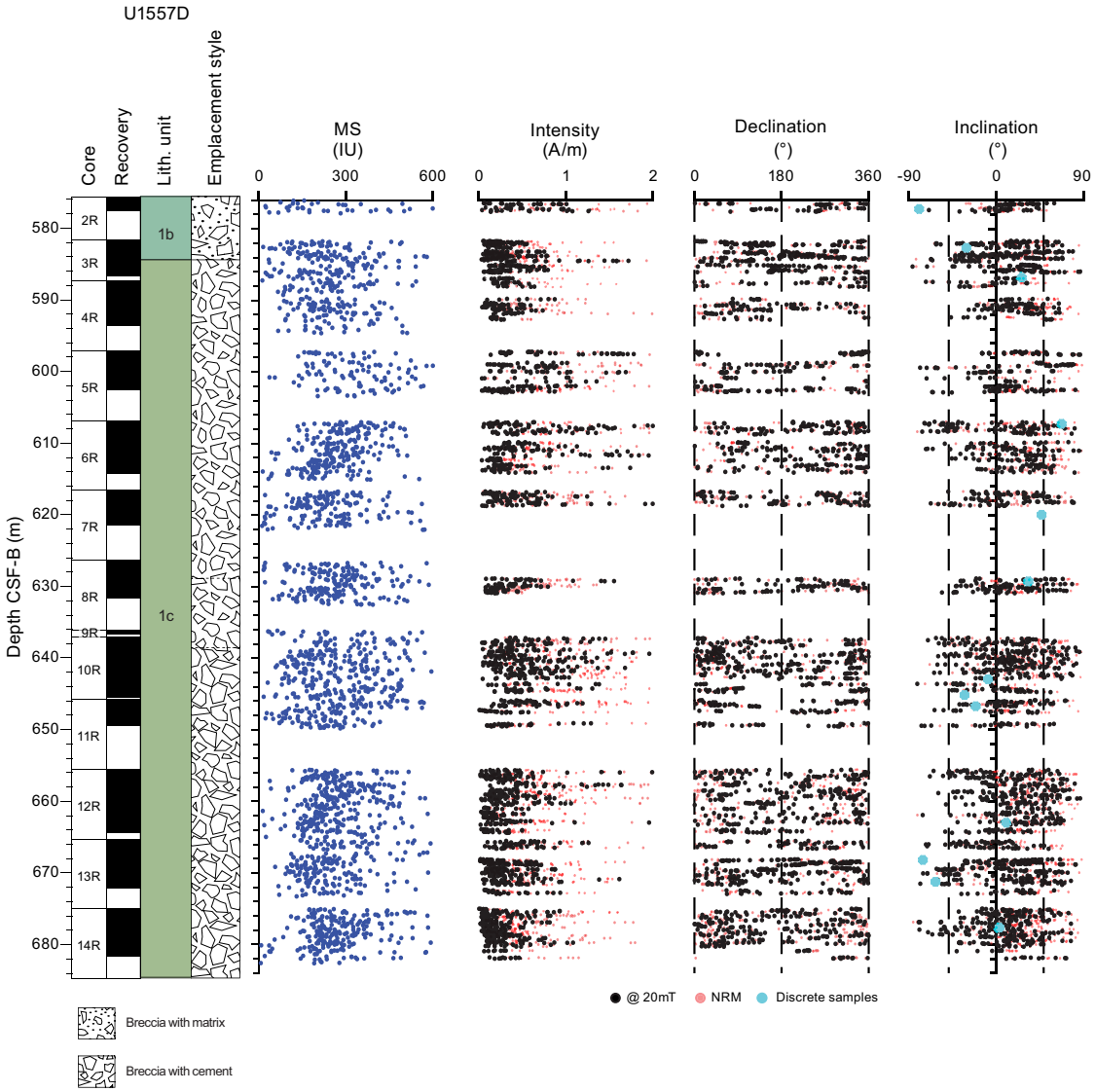

Figure F77. Archive-half MSP (MS; from SHMSL) and SRM measurements of basement, Hole U1557D. Dashed lines on inclination = GAD inclination (±49.1°) expected for this latitude (~30°S). Intensity data for Hole U1557D is restricted to maximum of 2 A/m because values beyond this are spurious, and the bulk of the signal, and thus portion of interest, lies in this constrained range.

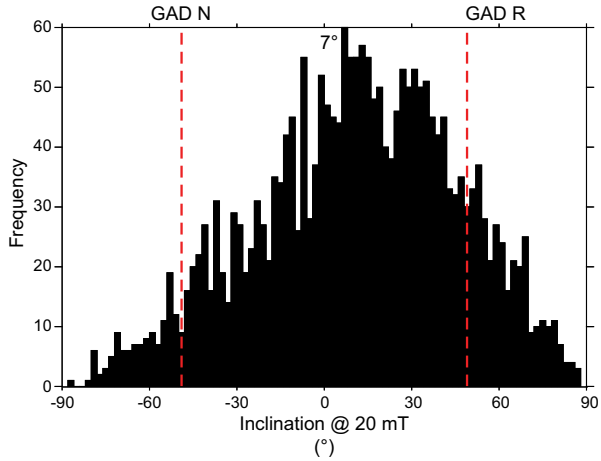

Figure F78. Histogram of inclination after 20 mT AF demagnetization of basement, Hole U1557D. Positive inclination average (7°) for bin with highest number of counts is labeled. Dashed lines = inclination (±49.1°) of GAD expected for this latitude (~30°S) during normal (N) and reversed (R) chrons.

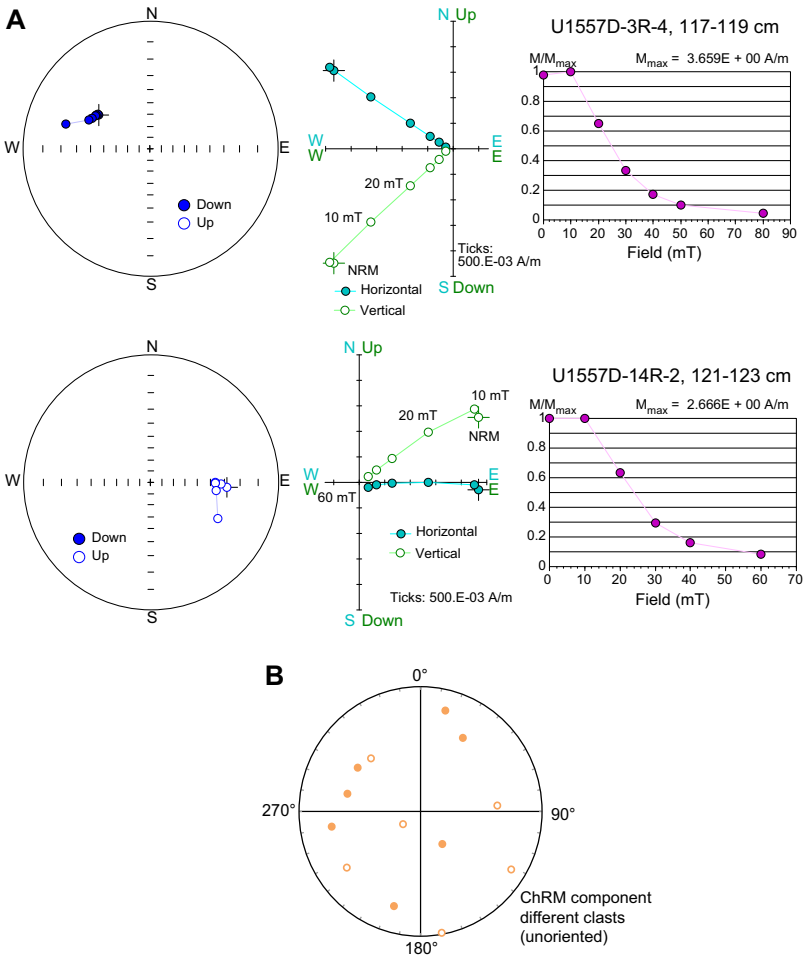

Figure F79. A. Representative AF demagnetization data for 2 discrete basalt clast samples, Hole U1557D. Left: Equal-area stereonets. Center: Orthogonal vector plots. Right: Normalized intensity decays upon stepwise demagnetization. B. Stereonet of individual fitted ChRM directions for each of 13 discrete clast samples.

Table T11. Directional data for discrete samples, Hole U1557D. **Download table in CSV format.**

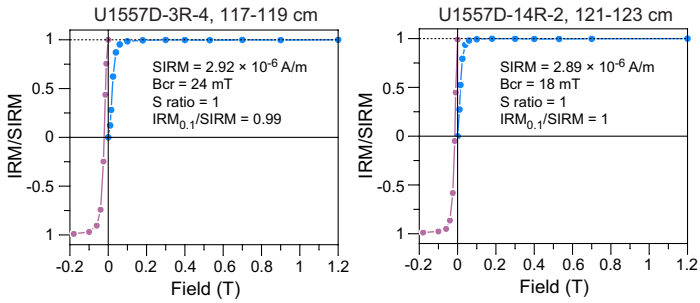

Figure F80. Normalized IRM acquisition curves up to 1.2 T and backfield IRM truncated at −0.2 T for 2 basement rock samples, Hole U1557D.

axes orientations are randomly distributed, suggesting no preferential alignment of clasts and limited transportation.

The conglomerate test was employed to test whether ChRM in the clasts was blocked prior to their emplacement in the sedimentary breccia or if ChRM was reset at a later stage (e.g., following emplacement of the breccia). Clasts that acquired ChRM prior to deposition in a conglomerate (or in this case, breccia) should give random ChRM inclinations and declinations when the clasts are oriented to their final positions in the conglomerate. Because RCB coring results in random rotation of core pieces around the core axis relative to adjacent pieces, the ChRM declinations of discrete samples from different core pieces should be random, irrespective of whether the sample material is a conglomerate. However, if their ChRM inclinations are also random, the samples pass the conglomerate test. In contrast, if samples fail the conglomerate test despite being clearly derived from a breccia, this would have required that the samples experienced remagnetization following emplacement in the breccia.

The ChRM directions of the discrete clast samples from Hole U1557D breccias plot randomly about a stereonet (Figure **F79B**), indicating the breccia clasts pass the conglomerate test and hence their ChRM was acquired prior to incorporation in the breccia and has remained stable since then.

The soft nature of the ferrimagnetic assemblage in these clasts indicates that the measured magnetic components, acquired prior to deposition in the breccia, have low stability. This in turn suggests these components resulted either from total remagnetization during alteration (e.g., maghemitization) or alternatively that they represent the primary remanent magnetization with very limited overprint. The magnetic data are thus consistent with two quite different alteration histories for the basalts prior to incorporation in the breccias. Additional postexpedition measurements are necessary to resolve the nature of the ChRM. Taken together, the paleomagnetic studies of the breccia clasts indicate there was significant reworking following original acquisition of the magnetic characteristics, but they suggest that no significant secondary magnetic mineral alteration events occurred between clast emplacement in the breccia and core retrieval during Expedition 390.

9. Age model and mass accumulation rates

9.1. Age model and linear sedimentation rates

The age model for Site U1557 is based on calcareous nannoplankton and planktic foraminiferal lowest (base) and highest (top) occurrence datums and paleomagnetic reversal datums from Hole U1557B (Figure **F81**; Table **T12**). Magnetostratigraphic reversals were only identified in the uppermost 100 m in Hole U1557B because the switch from APC to XCB coring starting with Core 390C-U1557B-12X resulted in increased drilling disturbance that prevented confident identification of paleomagnetic reversals for the remainder of the hole. Paleomagnetic investigations of sediments were limited to archive-half measurements because no discrete samples were taken during Expedition 390C. Gaps in recovery between Cores 3H and 4H and between Cores 4H and 5H were

bridged in the magnetostratigraphy by comparing Hole U1557B magnetic inclination data with that from Hole U1556A, only a few kilometers away from Site U1557, which shows an identical pattern of reversals in the uppermost 100 m of the core (see **Paleomagnetism**).

Planktic foraminifera and calcareous nannoplankton range in abundance from barren to abundant throughout the cored interval but tend to be absent entirely or rare and poorly preserved in the pelagic clays that characterize large intervals of Lithologic Unit I (see **Sedimentology** and **Biostratigraphy**). The only planktic foraminiferal samples available were those taken from core catchers collected during Expedition 390C, and these often coincided with pelagic clays that are barren of foraminifera. Planktic foraminiferal populations in the nannofossil oozes that represent the other dominant lithology of Unit I are depauperate, poorly preserved, and often only contain small specimens (Figure **F65**). As a result, foraminiferal marker species are often missing, and the ones that were identified often have very large stratigraphic error bars (Figure **F81**) due to the distance between samples with adequately preserved populations. Calcareous nannoplankton also exhibit highly variable preservation in Unit I. However, smear slide samples taken from the archive halves of Hole U1557B allowed for analysis of the higher carbonate lithologies during Expedition 390, which resulted in the identification of additional datums (see **Biostratigraphy**). In the more carbonate-rich Unit II, preservation and abundance of both fossil groups improves, although several marker species are still absent, likely due to the location of Site U1557 in the midlatitudes, outside the range of some common tropical marker species (e.g., Lam et al., 2022).

These factors make development of the age model complicated. Paleomagnetic reversal boundary datums identified within the upper 23 m were used to create the age model because they correspond well with fossil datums. However, paleomagnetic reversal datums identified between 23 and 100 m CSF-B are consistently offset from calcareous nannoplankton datums at roughly the same depths by 2–3 My near the seafloor and sometimes as much as 6 My by 100 m CSF-B. The consistent diachroneity between calcareous nannoplankton and magnetochron datums leaves us with no clear path for the age model between 23 and 100 m CSF-B, though the calcareous nannoplankton

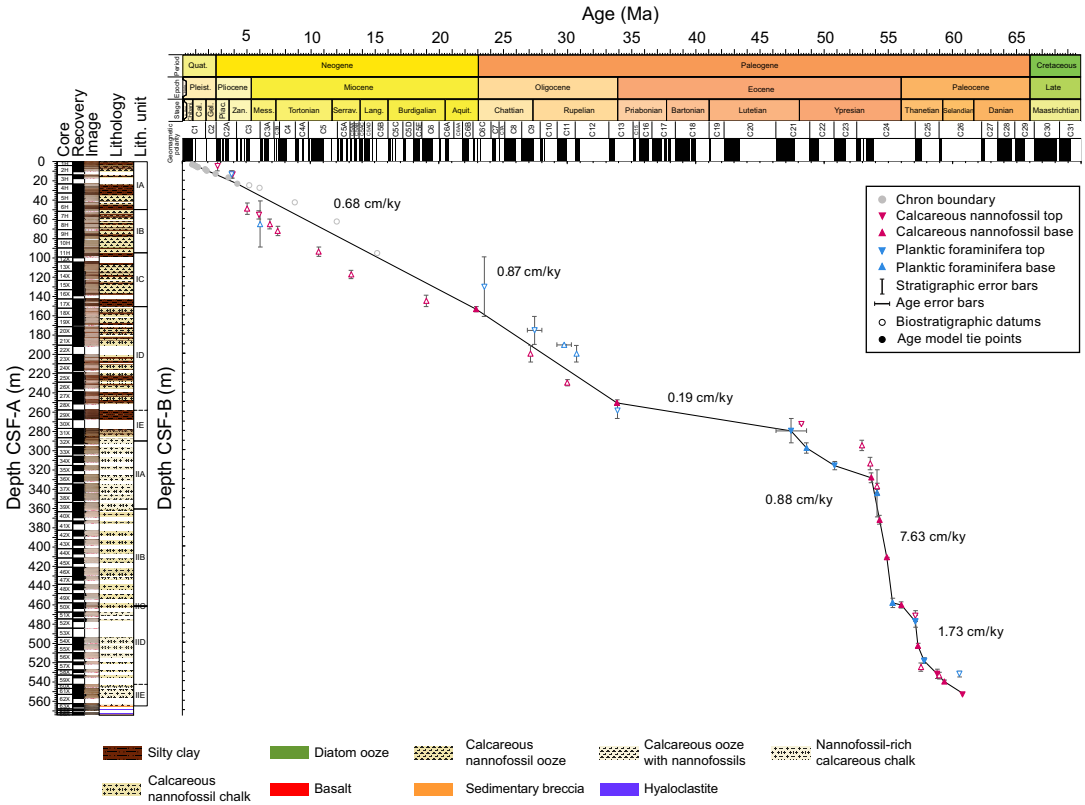

Figure F81. Age-depth model showing biostratigraphic and magnetostratigraphic datums, Hole U1557B. LSRs based on datums in Table T12 are also shown.

are preferred because assignment of magnetochrons is subjective so different magnetostratigraphic ages are possible and will be investigated in postexpedition work. Likewise, there is a consistent age offset between planktic foraminiferal and calcareous nannoplankton datums in the interval between 100 and 250 m CSF-B, likely due to the sample resolution and preservation issues with planktic foraminifera in this interval. The nannofossils likely provide a more reliable source of information because of the higher sampling resolution and identification of more datums, but the preservation and abundance of neither fossil groups is ideal in Unit I.

Table T12. Biostratigraphic and paleomagnetic datums in stratigraphic order, Hole U1557B. * = datums used to plot age model curve in Figure F81 and calculate LSRs using CSF-B depths. † = *Ch. adriatica* is uncalibrated, just "in O5," so this midpoint is between 26.9 and 28.0 ± 0.55 My. ** = *G. siakensis* is uncalibrated, just "in O3," so this midpoint is 29.2 and 30.3 Ma ± 0.55 My. ‡ = *A. alticonica* is uncalibrated, just "in E7." B of *T. frontosa* in sample below constrains this to Zone E7b, so this datum age is top of Zone E7b to top of Zone E7a, or midpoints of 46.24 to 48.62 ± 1.19 My. B = base, T = top, Bc = base common, B reversal = base of a paleomagnetic reversal event. CN = calcareous nannofossils, PF = planktonic foraminifers. **Download table in CSV format.**

Datum	Taxon/Chron (base)	Age (Ma)	Core, section	Sample depth CSF-A (m)	Sample depth CSF-B (m)	Sample above/ below	Sample above/below depth CSF-A (m)	Sample above/below depth CSF-B (m)	Midpoint depth CSF-A (m)	Midpoint depth CSF-B (m)	Depth error (±) CSF-A (m)	Depth error (±) CSF-B (m)	LSR (cm/ky)
			390C-U1557B-			390C-U1557B-							
Pmag	B reversal C1n*	0.77	1H-CC	3.89	3.89	2H-1	4.10	4.10	3.995	3.995	0.105	0.11	0.46
Pmag	T reversal C1r.1n*	1.01	2H-1	5.08	5.08	2H-1	5.08	5.08	5.08	5.08	0.00	0.00	0.85
Pmag	B reversal C1r.1n*	1.08	2H-2	5.66	5.66	2H-2	5.66	5.66	5.66	5.66	0.00	0.00	0.83
Pmag	T reversal C1r.2n*	1.19	2H-2	6.60	6.60	2H-2	6.60	6.60	6.60	6.60	0.00	0.00	0.28
Pmag	B reversal C1r.2n*	1.22	2H-2	6.69	6.69	2H-2	6.69	6.69	6.69	6.69	0.00	0.00	0.40
Pmag	T reversal C2n*	1.78	2H-4	8.91	8.91	2H-4	8.91	8.91	8.91	8.91	0.00	0.00	0.20
CN	T *Discoaster tamalis*	2.76	1H-CC	9.58	9.45	—	—	—	9.58	9.45	0.00	0.00	
PF	T *Globorotalia margaritae*	3.85	3H-CC	17.63	17.63	2H-CC	10.49	10.49	14.06	14.06	3.57	3.57	
CN	T *Amaurolithus* spp.*	3.93	3H-3	15.99	15.99	2H-CC	10.49	10.49	13.24	13.24	2.75	2.75	2.88
Pmag	T C3n*	4.3	4H-1	—	23.88	4H-1	—	23.88	—	23.88	—	0.00	0.71
CN	B *Ceratolithus cristatus*	5.08	6H-2	43.80	43.75	5H-CC	41.57	41.57	42.69	42.66	1.11	1.09	
CN	T *Nicklithus amplificus*	5.98	7H-3	55.52	55.52	6H-CC	51.86	51.55	53.69	53.54	1.83	1.99	
PF	B *Globorotalia margaritae*	6.09	5H-CC	41.57	41.57	6H-CC	51.86	51.552	46.72	46.56	5.15	4.99	
CN	B *Nicklithus amplificus*	6.82	8H-5	68.06	67.83	8H-CC	70.85	70.53	69.46	69.18	1.39	1.35	
CN	B *Amaurolithus* spp.	7.45	8H-CC	70.85	70.53	9H-5	77.80	77.56	74.33	74.05	3.47	3.52	
CN	B *Minylitha convallis*	9.75	10H-4	85.95	85.77	10H-CC	89.85	89.55	87.90	87.66	1.95	1.89	
CN	B *Discoaster bellus*	10.64	11H-2	91.75	91.75	11H-CC	98.86	98.86	95.31	95.31	3.56	3.56	
CN	B *Calcidiscus macintyrei*	13.16	14X-3	117.36	117.36	14X-CC	122.30	122.30	119.83	119.83	2.47	2.47	
CN	B *Sphenolithus belemnos*	19.01	17X-3	146.00	146.00	17X-CC	151.16	151.16	148.58	148.58	2.58	2.58	
CN	B *Sphenolithus disbelemnos**	22.9	18X-2	154.35	154.35	18X-4	156.80	156.80	155.58	155.58	1.22	1.22	0.66
PF	T *Tenuitella gemma*	23.53	18X-CC	161.48	161.48	17X-CC	151.16	151.16	156.32	156.32	5.16	5.16	
CN	B *Sphenolithus ciperoensis*	27.13	23X-3	204.49	204.49	23X-CC	208.98	208.98	206.74	206.74	2.25	2.25	
PF	T *Chiloguembelina adriatica**	27.45†	21X-CC	190.48	190.451	20X-CC	180.31	180.31	185.40	185.38	5.09	5.07	0.25
PF	B *Globorotalia siakensis**	29.75**	22X-CC	191.56	191.56	23X-CC	208.98	208.98	200.27	200.27	5.09	8.71	1.46
CN	B *Sphenolithus distentus*	30	26X-CC	235.88	235.88	27X-4	243.66	243.57	239.77	239.73	3.89	3.84	
PF	B *Paragloborotalia opima*	30.71	23X-CC	208.98	208.98	24X-CC	216.93	216.93	212.96	212.96	3.97	3.97	
CN	Bc *Clausicoccus subdistichus**	33.88	28X-3	251.04	251.04	28X-CC	251.53	251.53	251.29	251.29	0.25	0.25	0.19
PF	T *Pseudohastigerina micra*	33.9	29X-CC	267.45	267.251	30X-CC	267.81	267.81	267.63	267.53	0.18	0.28	
PF	T *Acarinina alticonica**	47.43‡	31X-CC	285.75	285.75	30X-CC	267.81	267.81	276.78	276.78	8.97	8.97	1.80
CN	T *Discoaster lodoensis*	48.22	31X-1	277.37	277.37	29X-CC	267.37	267.17	272.37	272.27	4.78	4.78	
PF	B *Turborotalia frontosa**	48.62	32X-CC	293.03	293.03	33X0CC	303.44	303.44	298.24	298.24	5.21	5.21	0.66
PF	T *Morozovella formosa*	50.81	40X-CC	369.56	369.56	38X-CC	351.44	351.44	360.50	360.50	9.06	9.06	
CN	Bc *Discoaster lodoensis*	52.93	32X-CC	293.03	293.03	33X-4	301.94	301.94	297.49	297.49	4.46	4.46	
CN	B *Discoaster lodoensis*	53.58	34X-CC	311.89	311.89	35X-3	319.52	319.52	315.71	315.71	0.75	0.75	
CN	B *Toweius gammation**	53.67	36X-4	330.79	330.79	36X-CC	332.21	332.21	331.50	331.50	0.71	0.71	6.85
CN	B *Sphenolithus radians*	54.12	37X-3	338.60	338.60	37X-CC	343.59	343.59	341.10	341.10	2.50	2.50	
PF	B *Morozovella subbotinae*	54.12	51X-CC	472.07	472.07	53X-CC	484.36	484.36	478.22	478.22	6.15	6.15	
CN	B *Tribrachiatus orthostylus**	54.3	41X-1	373.50	373.50	41X-CC	375.86	375.86	374.68	374.68	1.18	1.18	6.94
CN	B *Discoaster diastypus**	54.89	45X-3	414.72	414.72	45X-CC	416.58	416.58	415.65	415.65	0.93	0.93	9.62
PF	B *Pearsonites broedermanni**	55.34	49X-CC	454.19	454.19	50X-CC	463.65	463.65	458.92	458.92	4.73	4.73	2.38
CN	B *Rhomboaster* spp.	56	50X-3	461.25	461.25	50X-3	461.40	461.40	461.33	461.33	0.07	0.07	
PF	T *Globanomalina pseudomenardii*	57.1	53X-CC	484.36	484.36	51X-CC	472.07	472.07	478.22	478.22	6.14	6.14	
CN	T *Ericsonia robusta* (>9 µm)	57.11	52X-1	475.50	475.50	51X-CC	472.07	472.07	473.79	473.79	1.72	1.72	
CN	Bc *Discoaster multiradiatus**	57.32	55X-3	505.25	505.25	55X-CC	506.77	506.77	506.01	506.01	0.76	0.76	2.77
CN	B *Ericsonia robusta* (>9 µm)	57.54	58X-1	527.54	527.54	58X-2	529.35	529.35	528.45	528.45	0.90	0.90	
PF	T *Morozovella acutispira**	57.79	57X-CC	522.04	522.04	56X-CC	516.00	516.00	519.02	519.02	3.02	3.02	1.26
CN	T *Heliolithus kleinpellii**	58.8	59X-1	533.40	533.40	58X-CC	530.10	530.10	531.75	531.75	1.65	1.65	2.19
CN	B *Discoaster mohleri**	58.97	59X-2	535.21	535.21	59X-CC	535.73	535.73	535.47	535.47	0.26	0.26	2.49
CN	B *Heliolithus kleinpellii**	59.36	60X-2	544.54	544.54	60X-CC	545.79	545.79	545.17	545.17	0.63	0.63	0.55
PF	T *Parasubbotina variospira*	60.54	62X-CC	557.11	557.11	61X-CC	553.05	552.355	555.08	554.73	2.03	2.38	
CN	T *Fasciculithus pileatus**	60.76	62X-1	553.50	553.50	61X-CC	553.05	552.36	553.28	552.93	1.30	1.30	

To construct the age model, we therefore had to rely on our own judgment more than we would have preferred. Rather than connecting every datum through the uncertain intervals in Unit I, we drew a middle course between the datums and used datums close to this middle line to construct the age model (Figure **F81**; Table **T12**). Although we believe this to be the most accurate age model, we emphasize that there are other interpretations of the data that would generate considerably different sample ages. When constructing this age model, datums were selected to avoid age inversions and frequent fluctuations in sedimentation rate.

Linear sedimentation rates (LSRs) fluctuate through the interval, with the highest LSR values in the Eocene. Neogene LSR values are relatively stable, averaging 0.68 cm/ky. The average sedimentation rate increases slightly in the Oligocene to 0.87 cm/ky. Perhaps the most obvious feature of the age model is a large hiatus or condensed interval spanning the middle Eocene to early Oligocene (Figure **F81**) that has an average sedimentation rate (if sedimentation was continuous) of 0.19 cm/ky. This lithologic unit (Subunit IE) also separates the relatively low sedimentation rates of the Oligocene to recent (Unit I) from the high sedimentation rates of the Paleocene and Eocene (Unit II). The average sedimentation rate directly below Subunit IE is 0.88 cm/ky, nearly identical to that of the Oligocene, but below this in the earliest Eocene, sedimentation rates were significantly higher, averaging 7.63 cm/ky. Late Paleocene sedimentation rates were also relatively elevated, averaging a healthy 1.73 cm/ky.

9.2. Mass accumulation rates

Mass accumulation rates (MARs) for Hole U1557B were calculated using bulk density calculated from gamma ray attenuation (GRA) collected during Whole-Round Multisensor Logger (WRMSL) scans because no shipboard discrete dry bulk density samples were taken during Expedition 390C (see U1557B_MAR.xlsx in AGEMODEL in **Supplementary material**; also see **Age model and mass accumulation rates** in the Expedition 390/393 methods chapter [Coggon et al., 2024c]). Because of changes in the physical properties of core material during storage (drying, shrinking, etc.), it is impossible to generate useful discrete measurement data postexpedition. Data presented in Figure **F82** are binned in 1 My intervals.

MARs at Site U1557 are very high in the late Paleocene/early Eocene (peak of 10.3 g/cm^2/ky), relatively high in the early Eocene (between 0.9 and 2.1 g/cm^2/ky), and then very low during the condensed interval in the late Eocene (0.2 g/cm^2/ky). In Unit I, values are highest in the early Oligocene (1.8 g/cm^2/ky) and Early Pliocene (1.4–01.8 g/cm^2/ky) and generally hover around 0.7 g/cm^2/ky in between. The last 3 My is characterized by very low MARs (0.2 g/cm^2/ky).

9.3. Carbonate and organic carbon accumulation rates

Carbonate accumulation rates (CARs) and organic carbon accumulation rates (OCARs) were calculated by multiplying the MAR by the weight percent of carbonate and total organic carbon (TOC), respectively (see **Age model and mass accumulation rates** in the Expedition 390/393 methods chapter [Coggon et al., 2024c]). Carbonate and organic carbon samples were taken from Hole U1557B IW sample squeeze cakes after the water was extracted during Expedition 390C. Bulk density was calculated from GRA measurements collected during WRMSL scans conducted after the IW whole-round sample was taken. Thus, we do not have carbon and bulk density data from the same samples. Fortunately, all but one IW sample was taken from the bottom of one of the middle sections of each core; for these samples, MAR was interpolated from the adjacent GRA measurements above and below. These measurements were just a few centimeters away from the IW sample, and at that scale at Site U1557, bulk density can vary by a negligible amount of a few tenths of a gram per centimeter cubed. IW Sample 390C-U1557B-41X-2, 126–130 cm (375.61 m CSF-B), was taken from the bottom of a core and separated from the nearest sample below it by a 6.92 m gap in recovery. In this case, we applied the MAR from the sample directly above instead of interpolating. Bin size was increased to 2 My between 0 and 54 Ma because the low sample density and low sedimentation rate meant that many bins were empty of data.

9.3.1. Carbonate accumulation rates

On a first-order basis, CARs mirror MARs in Hole U1557B (Figure **F82**). This fits with the observation that sedimentation is driven by pelagic deposition of dust diluted by more or less pelagic carbonate. The CAR is highest in the carbonate-rich Lithologic Unit II, with a peak spanning the late Paleocene and early Eocene (0.92 g/cm^2/ky). Low sample resolution combined with low sedimentation rates means that most bins in the late Eocene condensed interval have no CAR or OCAR data, although the bin that does have data has a CAR value of 0.000006 g/cm^2/ky, appropriately low considering the low sedimentation rate and practically carbonate free sedimentology. In Lithologic Unit I, CAR values range 0.0002–00.14 g/cm^2/ky (with peaks in the early Oligocene and Early Pliocene, similar to MAR), and appear largely controlled by the relative proportion of pelagic clay versus carbonate within the bin.

9.3.2. Organic carbon accumulation rates

A surprising result in Hole U1557B is the elevated organic carbon content in Subunit IIB (late Paleocene to early Eocene; Figure **F82**) (see **Geochemistry**). TOC values as high as 3 wt% in the early Eocene suggest that this interval was characterized by high organic carbon production and preservation with an OCAR peak near 0.05 g/cm^2/ky, which is more than double the abyssal average OCAR during the Late Cretaceous Oceanic Anoxic Event 2 (Owens et al., 2018). The general correspondence of high OCARs with high CARs indicates overall high productivity in surface waters during this time interval. The OCAR is generally low throughout the Neogene and Oligocene, with the highest values reaching 0.004 g/cm^2/ky in the Oligocene and 0.017 g/cm^2/ky in the Pliocene.

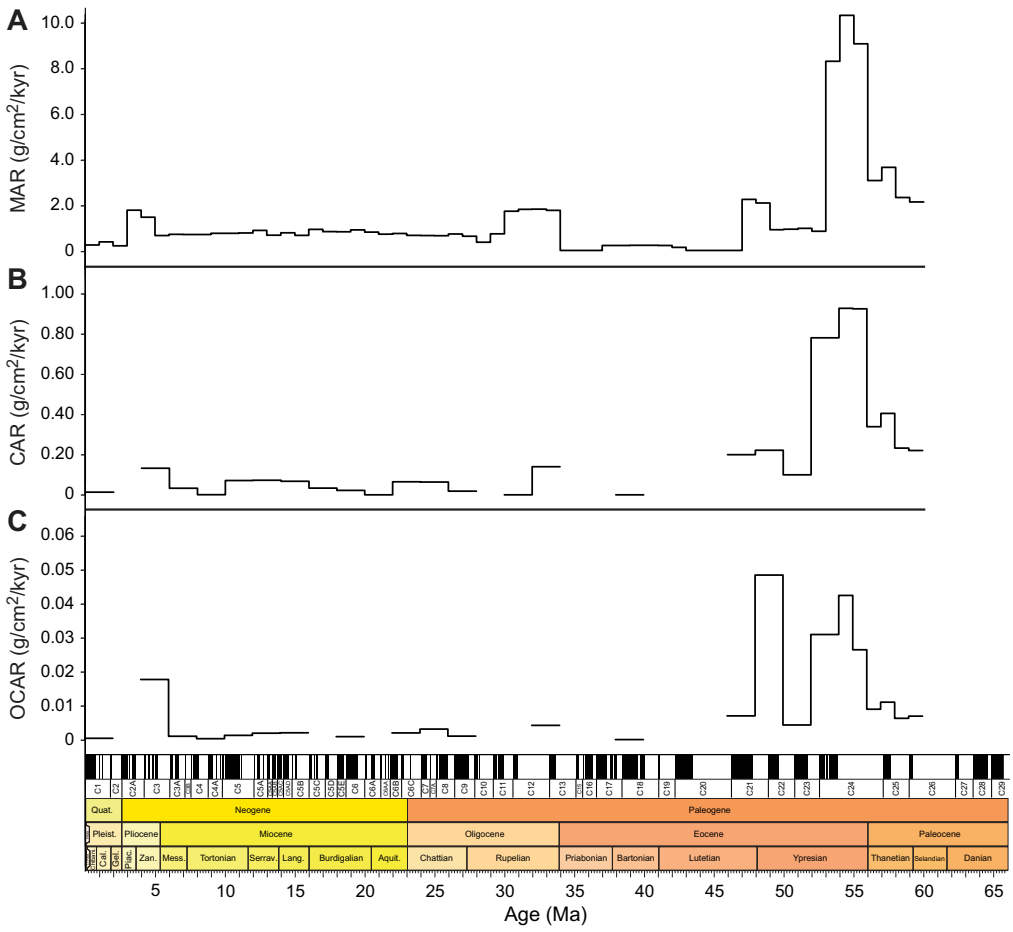

Figure F82. (A) MAR, (B) CAR, and (C) OCAR calculated at 2 My intervals between 0 and 54 Ma and at 1 My intervals between 54 and 60 Ma, Hole U1557B.

10. Physical properties and downhole measurements

10.1. Sediment

10.1.1. Physical properties

The sediment succession at Site U1557 was cored in two holes during Expedition 390C. Hole U1557A was a missed mudline that penetrated 9.63 m. Coring with the APC system in Hole U1557B proceeded through Core 390C-U1557B-11H, after which the XCB system was deployed from Core 12X to drill deeper into more lithified sediments and recover the sediment/basement interface in Hole U1557B. Site U1557 sediment physical properties measurements included whole-round NGR, GRA bulk density, MS, and compressional wave (*P*-wave) velocity measured on the WRMSL. During Expedition 390C, measurements of thermal conductivity were made in Hole U1557B (Estes et al., 2021). Discrete sampling for moisture and density (MAD) and *P*-wave velocity measurements were not carried out during Expedition 390C.

Because sediment cores from Site U1557 were collected and split during Expedition 390C, only the archive halves of Hole U1557A and U1557B cores were on board for analysis during Expedition 390. Discrete samples were not taken from Site U1557 sediment cores for MAD or *P*-wave velocity during Expedition 390 because after being in storage for 2 y the split sections would not have retained their original moisture content.

10.1.1.1. Natural gamma radiation

NGR was measured at 10 cm intervals on all whole-round core sections that exceeded 50 cm in length. Each measurement reflects integration of two separate 5 min counts (i.e., 10 min of counting per section, consisting of 5 min at each of two positions separated by 10 cm) (see **Physical properties and downhole measurements** in the Expedition 390/393 methods chapter [Coggon et al., 2024c]). NGR serves as an estimate of the content variability of radioactive elements (e.g., ^{40}K, ^{238}U, and ^{232}Th) in the cored sedimentary section. NGR from marine sediments is especially useful in distinguishing clay-rich intervals from clay-poor carbonate ooze intervals (Dunlea et al., 2013).

NGR shows high-frequency variability in Hole U1557B, ranging 7–50 counts/s shallower than 252 m CSF-B (Figure **F83**). These variations likely reflect changes in clay content: higher NGR corresponding to the silty clay layers and lower NGR corresponding to the carbonate ooze of Lithologic Unit I (see **Sedimentology**). Between 257 and 267 m CSF-B, NGR is relatively high and invariable (mean ± 1 standard deviation = 41 ± 1 count/s). This corresponds to a distinctive clay layer in Lithologic Subunit IE in Core 390C-U1557B-29X. Below this layer, NGR decreases and is uniformly lower (mean = 6 counts/s), generally ranging from 3 to <15 counts/s between 267 m CSF-B and the bottom of the sedimentary section at 565 m CSF-B. This interval is dominated by chalk, which is characteristically low in natural radioactivity. There are several sharp positive excursions (up to 31 counts/s) in this interval that generally correspond to thin (centimeter-scale) clay layers. The mean NGR, as well as variability, increases slightly below 525 m CSF-B toward the base of the sediment section (Figure **F83**).

10.1.1.2. Gamma ray attenuation bulk density

GRA is defined as the fraction of gamma rays that are not absorbed by a material, and this can be used as an approximation for bulk density. Variations in bulk density can reflect changes in mineralogy, composition, and porosity in the sedimentary section. However, drilling disturbance, expansion cracks, incomplete filling of the core liner, or any other disturbance of the cored sediment can produce spurious values not realistic of marine sediment, which is typically about 1–2 g/cm^3, depending on lithology and compaction. No data filtering to remove spurious values was done shipboard. Because spurious GRA data points are typically lower than true values, a useful method to reduce the potential influence of spurious data is to consider the upper envelope of the GRA data as a first-order estimate of bulk density and to discount unrealistically low values.

High-frequency trends in bulk density are generally anticorrelated with NGR in the depth interval above 252 m CSF-B. These variations reflect shifts between denser carbonate-rich lithologies and less dense dark clay-rich deposits. Notably, a high-density interval ranging 1.94–2.2 g/cm^3 occurs at ~190.4 m CSF-B (Section 390C-U1557B-22X-1) (Figure **F83**) above a gap in recovery. In Core

31X, bulk densities reach as high as 2 g/cm^3 and mark a transition to consistently more dense carbonate material below 281.6 m CSF-B, where values average 1.9 g/cm^3 (Figure **F83**). Drilling disturbance, known as biscuiting, is common in the cores recovered using the XCB coring system (below 99.1 mbsf). Many of the sections recovered from below this depth are reworked and unconsolidated as a result, which may also lead to erratic centimeter-scale fluctuations in density. The most notable example of this disturbance can be seen visually but also in the bulk density data of Cores 54X–56X (see **Sedimentology**).

10.1.1.3. Magnetic susceptibility

MS is an indicator of the tendency of minerals to become magnetized upon application of a magnetic field and can be considered an approximation of the concentration of magnetic minerals in the formation. Silt and clay-rich sedimentary layers generally include more magnetic minerals than carbonate sedimentary layers; therefore, higher MS typically corresponds to silt and clay lithologies, whereas lower MS typically corresponds to carbonate and siliceous lithologies. MS of cored sediments at Site U1557 was measured using the WRMSL; MSP was measured using the

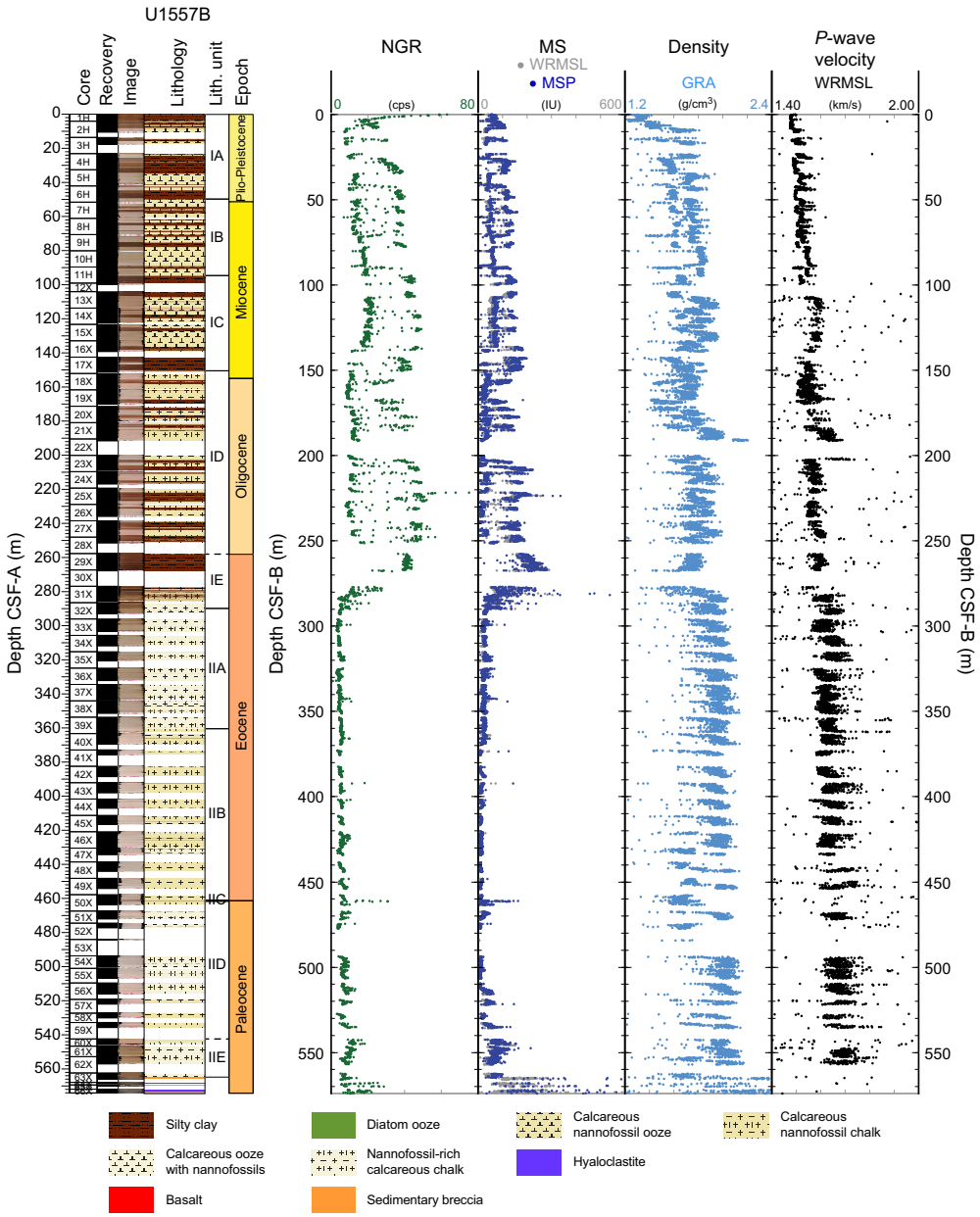

Figure F83. Summary of core physical properties data, Hole U1557B. cps = counts per second.

SHMSL. MSP measurements made on split-core sections reflect the same trends as those obtained from the WRMSL; however, MSP is on average 12.22 instrument units (IU) higher than MS determined by the WRMSL (Figure **F83**).

MS ranged from ~1 to ~300 IU (mean = 54 IU) in Hole U1557B (Figure **F83**). In the upper ~250 m of the sediment in Hole U1557B, MS alternates between 50 and 150 IU. These high-frequency MS variations likely reflect the same lithologic variability recorded in the NGR and GRA bulk density. Between ~250 and ~275 m CSF-B (Subunit IE; see **Sedimentology**), a peak in MS of ~300 IU indicates a high concentration of magnetic minerals. Between ~275 and ~500 m CSF-B, MS is low, generally less than ~50 IU, and exhibits much less variability, except for a few distinct peaks that likely reflect the more uniform carbonate chalk–dominated lithology of Lithologic Unit II compared to Lithologic Unit I. Below 500 m CSF-B, MS increases toward the sediment/basement interface, likely due to increasing clay content in these sediments.

10.1.1.4. *P*-wave velocity

P-wave velocity is a measure of the velocity with which a compressional body wave (*P*-wave) propagates through a sample. *P*-wave velocity is directly related to the bulk density, compressibility, and shearability of the material sampled. *P*-wave velocity is indirectly related to the porosity, mineralogy, and fabric of the interval or lithology represented by the material sampled. *P*-wave velocity is especially useful for a material control in correlating different scales of data, from regional seismic imaging (at the scale of tens to hundreds of meters) to downhole logs (at the centimeter to meter scale) to core-based data (at the millimeter to centimeter scale).

P-wave velocity measurements made on whole-round core sections using the WRMSL are more reliable in sediment than in basement (see **Physical properties and downhole measurements** in the Expedition 390/393 methods chapter [Coggon et al., 2024c]), but spurious values still occur. Similar to the GRA measurement, *P*-wave velocity is adversely affected by drilling disturbance, expansion cracks, incomplete filling of the core liner, or any other disturbance of the cored sediment. Marine sediment *P*-wave velocity should typically be between 1.48 and ~1.80 km/s, depending on compaction and lithology. Spurious *P*-wave velocities from the whole-round core section are typically both higher and lower, and the best approximation of true velocity is to use the clustering of values and disregard any outliers.

At Site U1557, *P*-wave velocity measured with the WRMSL ranges from ~1.48 to ~1.80 km/s (mean = 1.59 km/s when excluding erroneously high or low values). In general, velocity increases with depth and is positively correlated with bulk density (Figure **F83**).

10.1.1.5. Thermal conductivity

Thermal conductivity is a measure of the potential for conductive heat flow through a material. Thermal conductivity in sediment and basement is affected by the mineralogy, porosity, density, and fabric of the lithology being measured. Measurements of thermal conductivity help develop an understanding of thermal insulation and heat dissipation processes from the underlying igneous crust through the sediment to the ocean. The thermal conductivity of sediment is an essential parameter required to calculate conductive heat flow through marine sediments from in situ temperature measurements. A total of 182 individual thermal conductivity measurements were made at 60 depths during Expedition 390C (Estes et al., 2021), yielding values averaging 1.4 ± 0.25 W/(m·K) (Figure **F84A**). Three individual measurements are used to calculate an average thermal conductivity for each sample. In general, measurements were taken at a frequency of about one per core on the most representative lithology.

10.1.2. Stratigraphic correlation

During Expedition 390C, two holes were drilled at Site U1557 using APC and XCB coring techniques: Holes U1557A and U1557B. Hole U1557A consists of a single core that missed the mudline and thus the top of the sediment pile, reaching 9.5 m drilling depth below seafloor (DSF). The mudline was recovered on a second attempt in Hole U1557B, which consists of 66 cores for a total of 574 m DSF. Hole U1557B crossed the uppermost basement at 564 m DSF. A total of 9.6 m and 412 m of sediment were recovered from Holes U1557A and U1557B with recovery of 101% and 73%, respectively.

Physical properties data from Holes U1557A and U1557B were compared to establish a core composite depth below seafloor (CCSF) scale only for the uppermost sediment record. The lack of correspondence in the physical properties between Cores 390C-U1557A-1H and 390C-U1557B-1H suggests at least 4.1 m is missing from the top of Hole U1557A (Figure **F85**). However, there is good correspondence in bulk density, MS, NGR, and lightness (L*) data between Sections 390C-U1557A-1H-5 and 390C-U1557B-2H-2 (Figure **F85**). Comparison with core images confirmed that these signals represented transitions between clay- and carbonate-rich layers in both holes. Therefore, a tie point was assigned at 10.8 m CCSF aligning the two holes (Table **T13**). This shifted Hole U1557B cores down (except Core 390C-U1557B-1H), producing a 4.5 m core gap (4.1–8.6 m CCSF) between Cores 1H and 2H (Table **T14**). This correlation allowed construction of a partially continuous splice for the upper 15 m at Site U1557 (Figure **F85**), with a gap present between the bottom of Core 390C-U1557B-1H and the top of Core 390C-U1557A-1H at ~4 m CCSF.

10.1.3. Downhole measurements

10.1.3.1. Downhole temperature

Formation temperature measurements were made at Site U1557 during Expedition 390C using the advanced piston corer temperature (APCT-3) tool (Estes et al., 2021). Three APCT-3 measurements were taken in Hole U1557B (Table **T15**; Figure **F86**). Although the records show that the APCT-3 tool could not remain stable during the full length of any of its deployments, each deployment included long enough stable intervals of thermal recovery to calculate reasonable fits to theoretical models and derive formation temperature data, suggesting a geothermal gradient of 36°C/km (Figure **F84C**).

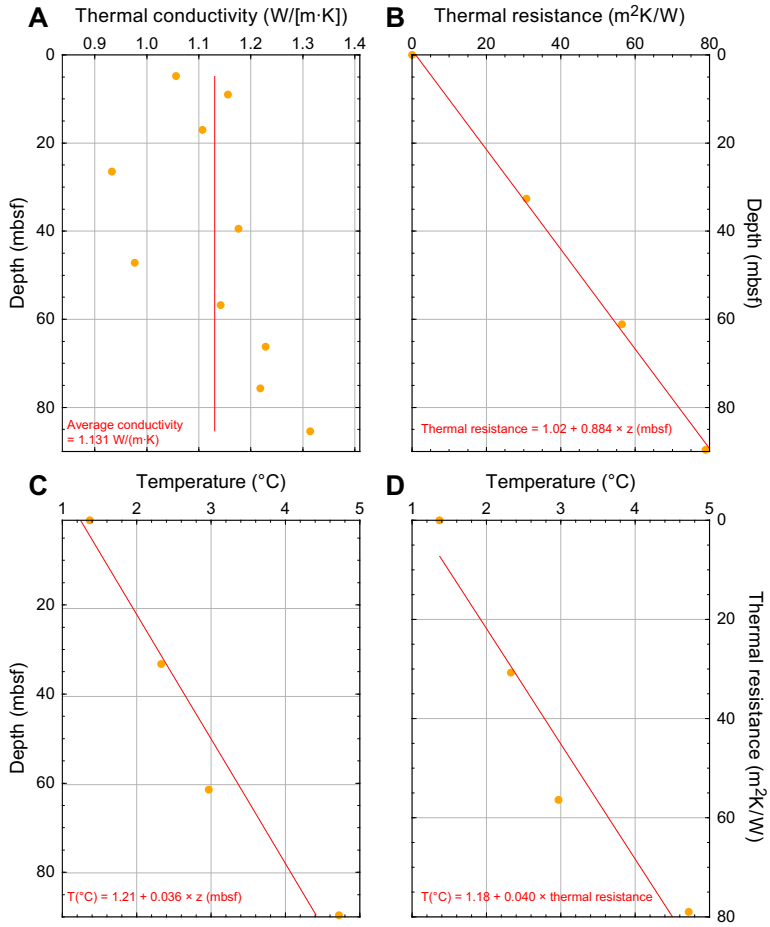

Figure F84. Estimation of conductive heat flow, Site U1557. A. Mean measured thermal conductivity on cores. B. Calculated thermal resistance with linear regression. C. Temperature measured using APCT-3 tool with linear regression. D. Bullard plot of measured temperature vs. calculated thermal resistance. Slope of regression line is conductive heat flow for Site U1557.

10.1.3.2. Heat flow

Conductive heat flow for Site U1557 was calculated using discrete thermal conductivity measurements to calculate thermal resistance and plotting this versus depth (Figure **F84B**). This allowed thermal resistance to be calculated at depths coincident with temperature measurements made during APC drilling in Hole U1557B (see **Physical properties and downhole measurements** in the Expedition 390/393 methods chapter [Coggon et al., 2024c]). The intercept (T_0) of a linear trend on a plot of temperature versus thermal resistance, known as a Bullard plot (Pribnow et al., 2000) (e.g., Figure **F84D**), is the temperature at depth 0 m in the sediment succession (i.e., at the seafloor). The slope of such a regression line is equal to the conductive heat flow, which is calculated to be 40 mW/m^2 in Hole U1557B, similar to that observed in nearby Hole U1556A (42 mW/m^2). Table **T15** summarizes these results.

10.1.3.3. Logging operations

Logging operations for Site U1557 began after the completion of RCB coring in Hole U1557D to a total depth of 684.7 m DSF. In preparation for logging, an additional 50 barrel mud sweep was circulated in the hole to clean out any cuttings, the pipe was raised above the reentry cone, the RCB bit was released on the seafloor, and the borehole was reentered and filled with seawater (see **Operations**). The drill pipe was raised to 30 m DSF for logging. Sea conditions were moderate,

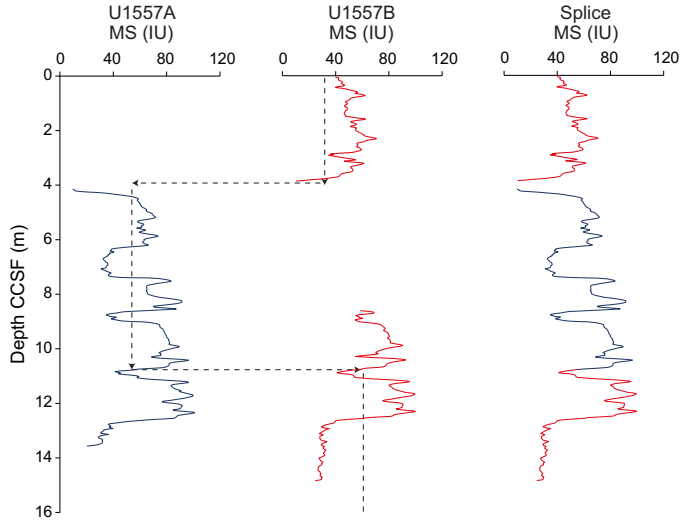

Figure F85. Construction of Site U1557 CCSF composite depth scale and splice using MS from Holes U1557A and U1557B. Dashed lines = correlation tie points aligning similar stratigraphies between holes. Spliced MS color scheme indicates which hole contributes to each interval of splice. Only 16 m CCSF is shown because there is no splice below that depth.

Table T13. Splice table, Site U1557. **Download table in CSV format.**

Table T14. Affine table, Holes U1557A and U1557B. **Download table in CSV format.**

Table T15. Formation temperature measurements, derived temperature gradient, and heat flow, Site U1557. TCON = thermal conductivity. **Download table in CSV format.**

Site/Core	Measurement depth (mbsf)	Equilibrium temperature (°C)	Gradient (°C/km)	Average TCON (W/[m·K])	Heat flow from gradient (mW/m^2)	Heat flow from Bullard plot (mW/m^2)
390C-U1557B-						
4H	32.6	2.33				
7H	61.1	2.97				
10H	89.6	4.72				
Site U1557			36	1.13	41	40

with heave in the 1–2 m range, and the wireline heave compensator was used for the entirety of logging operations.

Because of time limitations, wireline logging operations were limited to a single tool string run in Hole U1557D. The sedimentary section in Hole U1557D was cased during Expeditions 390C and 395E (Estes et al., 2021; Williams et al., 2021) (see **Background and objectives**). The primary target of wireline logging at this site was the open hole below 572 m DSF in the Site U1557 hard rock section. However, the gamma ray wireline logging tool received adequate signal through casing below the depth of the pipe during logging operations to record spectral gamma ray data from the sedimentary formation. Gamma ray data from wireline logging operations in Hole U1557D provide information about the nature of the sediments at Site U1557 that can be correlated with properties of the sediment cores from Hole U1557B. However, logs recorded through casing were used primarily qualitatively because of the attenuation of the incoming signal. Full detail on wireline logging operations and basement results are provided in the basement section for Site U1557 (see **Wireline logging**).

10.1.3.4. Logging data through casing

Gamma ray logs recorded the contributions of U, K, and Th to the total gamma ray signal through the cased interval of sediments in Hole U1557D reflect changes in sediment properties, primarily the distinct alternations in lithology between silty clay and nannofossil ooze/chalk that are likely the primary sedimentary characteristic affecting both in situ and core physical properties data at Site U1557. Silty clay layers have higher NGR relative to the carbonate-rich intervals. The pattern of alternating higher and lower gamma ray from downhole logging is also seen in physical properties measurements of cores from Hole U1557B (Figure **F83**), which enables the downhole gamma ray logs from Hole U1557D to be correlated to the core data from Hole U1557B with a slight depth offset on the order of a few meters (Figure **F87**). Discrepancies between the drilling core depth and wireline logging depth may occur because of core expansion, incomplete core recovery, incomplete heave compensation, wireline stretch, drill pipe stretch, and tidal changes.

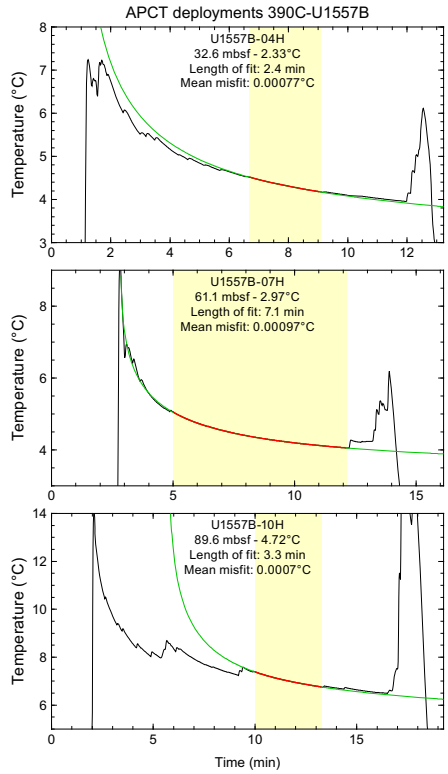

Figure F86. APCT-3 temperature records, Site U1557. Highlighted time intervals show where best-fit temperature decay model (green curve) was calculated to derive equilibrium temperature for each deployment. In situ formation temperature value for each record is extrapolated from best-fit model.

Lithologic unit boundaries correspond to clear changes in core physical properties data, and these boundaries are also evident in gamma ray logs. There is good agreement between core data from Hole U1557B and trends in logging gamma ray data recorded in the cased interval of Hole U1557D below the depth at which the drill pipe was set for wireline logging (29 m WMSF). Between 29 and ~270 m WMSF, the gamma ray log shows clearly defined intervals of higher and lower gamma ray, consistent with the presence of alternating silty clay and ooze/chalk, respectively, in Lithologic Unit I (see **Sedimentology**). Logging data, which is continuous downhole, resolves both sharp boundaries (e.g., 171 m WMSF) and transitional changes (e.g., 97–102 m WMSF) between silty clay and carbonate-dominated intervals throughout Lithologic Unit I. Gamma ray decreases gradually from 270 to 288 m WMSF with low-amplitude variability. In the interval below 298 m WMSF, which likely corresponds to the Lithologic Unit I/II boundary described in Hole U1557B (see **Sedimentology**), gamma ray is generally low, consistent with the carbonate-dominated lithology of Lithologic Unit II described in Hole U1557B cores. A local peak in the gamma ray log centered around 470 m WMSF occurs at approximately the same depth as a distinct clay-bearing layer described as being deposited during the PETM (see **Lithologic correlations**). Gamma ray increases slightly between 540 and 562 m WMSF, with locally elevated values that are consistent with both the presence of sand-sized igneous clasts and organic-rich laminations in Hole U1557B cores. A distinct peak in the gamma ray log at 558 m WMSF may correspond to the first appearance of basalt in Hole U1557D, consistent with the signature of the gamma ray peak in core-based data from Hole U1557B that corresponds to the first appearance of basalt in that hole. The depth of the gamma ray peak in Hole U1557D logs is ~6 m shallower than the first appearance of basalt

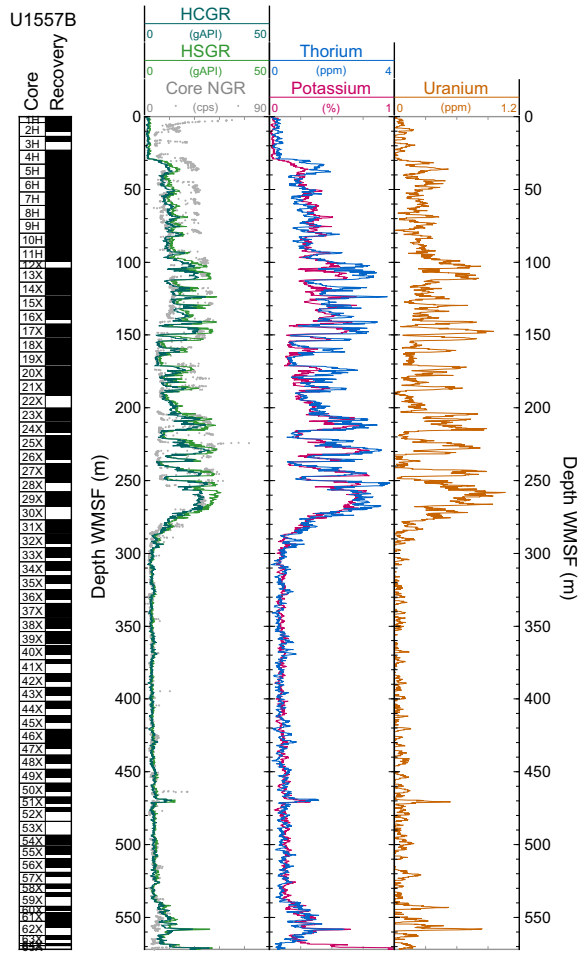

Figure F87. NGR logs recorded in casing, Hole U1557D. Gamma ray log signal is attenuated by drill pipe and casing in Hole U1557D, but relative changes correlate well with core-based gamma ray data. Core-based NGR data (Hole U1557B) have been shifted by +2.5 m for a better fit with logging data, shown on logging depth scale. HCGR = computed (U-free) gamma ray, HSGR = standard (total) gamma ray, cps = counts per second.

in Hole U1557B cores, but this could be explained by a number of factors, including slight differences in the basement topography between holes, a gap in core recovery in Hole U1557B (Core 390C-U1557B-62X), and small-scale discrepancies between core and logging depth scales. The return to lower gamma ray below 558 m WMSF at the base of the cased interval suggests that there is an additional interval of carbonate-rich sediment before the appearance of significant basement intervals, further described in **Basement** in Physical properties and downhole measurements.

Spectral data from the gamma ray logging tool show variations in the relative contributions of the radioactive isotopes of U, K, and Th to the total gamma ray signal (Figure **F87**). At Site U1557, the total gamma ray signal comes mostly from the radioactive isotopes of potassium, with additional contributions from thorium throughout Lithologic Unit I of the logged sedimentary section. Thorium is a trace element typically associated with clays and heavy minerals, and spectral gamma ray data show relatively higher contributions from thorium in the more clay-rich intervals that define the lithologic unit (Figure **F87**; see **Sedimentology**). There is also a contribution from uranium in the higher gamma ray intervals throughout the logged interval, which is likely associated with higher organic carbon in silty clay layers.

10.1.4. Data integration

10.1.4.1. Lithologic correlations

Physical properties data show distinct changes in the sedimentary section cored at Site U1557 that correspond closely with the lithologic units (see **Sedimentology**). Lithologic Unit I (0–251.53 m CSF-B) exhibits centimeter-scale alternations in NGR, MS, and bulk density that are likely associated with the primary alternating lithologies that characterize that unit. Higher NGR and MS and lower bulk density throughout this interval are associated with silty clays, which contain more naturally radioactive and magnetic minerals, whereas lower NGR and MS and higher bulk density are associated with nannofossil oozes.

MS and GRA bulk density display a distinct change in character at the Unit I/II boundary (Figure **F83**). A peak in MS and a low in bulk density, indicative of a clay-rich layer, seem to bracket the Unit I/II boundary at 289.84 m CSF-B, which was defined on the basis of sedimentologic observations (see **Sedimentology**). A gap in Hole U1557B core recovery occurs at the Unit I/II boundary and inhibits more definitive analyses. Converting CSF-B depth to two-way traveltime (TWT) using the depth-averaged velocity of seawater and sediment, the Unit I/II boundary occurs at 7.0 s TWT, which is coincident with a seismic reflector identified by Estep et al. (2020) to represent a regional unconformity.

Physical properties data show distinct variation in Lithologic Unit II (257.7–564.76 m CSF-B). Low NGR and MS below ~275 m CSF-B are representative of the carbonate ooze that dominates the lithology of that unit. Locally elevated NGR in this lithologic unit corresponds to layers with higher silty clay within the calcareous nannofossil oozes (e.g., 422–430 m CSF-B in Core 390C-U1557B-46X) (Figure **F83**). Elevated NGR may also correspond to intervals with a higher proportion of organic particles (e.g., 510–520 m CSF-B in Core 56X).

10.1.4.2. Carbonate dissolution events

In sedimentary Unit II, three sections (390C-U1557B-37X-6, 40X-2, and 50X-3) show abrupt increases in NGR and MS above respective baseline values (Figure **F88**). An increase in NGR suggests a greater proportion of clay versus carbonate because of the greater radioactive element content of clays. Sedimentary core descriptions (see **Sedimentology**; also see **Core descriptions**) and core images show dark orange layers in these three sections, validating the increased clay content suggested by NGR. Higher MS in the same intervals indicate a greater proportion of magnetic minerals in the sediments, perhaps due to more Fe-bearing minerals hosted in these clay intervals. These abrupt changes in the physical properties occur in carbonate-dominated Unit II, making these short-lived clay intervals stand out as possible carbonate dissolution events associated with shoaling of the CCD at the time of deposition.

The clay-rich interval in Section 390C-U1557B-50X-3 (460.5–462 m CSF-B) is the thickest interval of the three possible carbonate dissolution events and has the highest NGR and MS (Figure **F88**). In a sample taken from Section 50X-3, 45 cm (461.25 m CSF-B), specimens of *Rhomboaster*

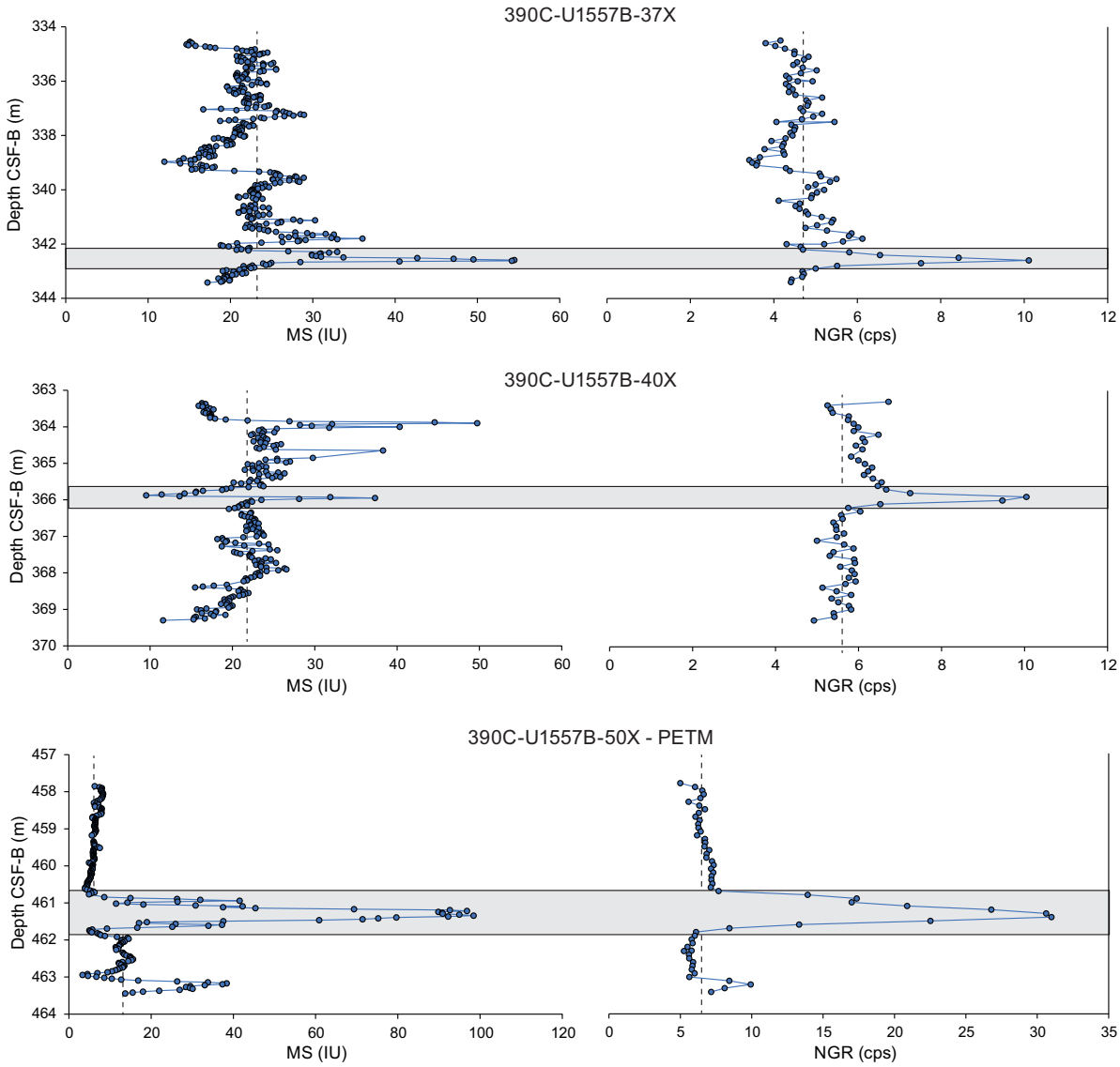

Figure F88. MS and NGR records (390C-U1557B-37X, 40X, and 50X). Gray bars = abrupt increases in both properties above respective baselines (dashed lines) at correlative depths, suggesting carbonate dissolution. cps = counts per second.

spp., short-lived excursion taxa that lived during the PETM, are present (see **Biostratigraphy**). The two clay-rich intervals in Sections 37X-6 (342–343 m CSF-B) and 40X-2 (365.5–366.5 m CSF-B) have more condensed clay layers with lower NGR and MS relative to the PETM section, but both are elevated relative to their respective baselines (Figure **F88**). The lowest occurrence datum for *S. radians* at Site U1557 occurs at 338.6 m CSF-B in Section 37X-3 and has an age of 54.12 Ma (Gradstein et al., 2020) (see **Biostratigraphy**). The preliminary Site U1557 age model (see **Age model and mass accumulation rates**) tentatively points toward three possible carbonate dissolution events during the early Eocene. Similarly, clay layers with high NGR and MS were identified during Ocean Drilling Program Leg 208 at Walvis Ridge in the southeast Atlantic across the Eocene/Paleocene boundary (Shipboard Scientific Party, 2004), confirmed as evidence to support carbonate dissolution during shoaling of the CCD during the PETM by Zachos et al. (2005).

10.2. Basement

10.2.1. Physical properties

Physical properties characterization in the basement section at Site U1557 is based on cores from Holes U1557B and U1557D. The basement sequence at Site U1557 consists of sedimentary breccia

composed of basalt and volcanic glass clasts and a matrix of variable proportions of pelagic sediment, calcite, lithic fragments, and zeolites (see **Igneous petrology** and **Alteration petrology**). For physical properties characterization, matrix is defined as the material between large clasts, which actually comprises small basalt and altered glass clasts, fine-grained matrix, and/or cement (see **Igneous petrology**). Whole-round core section measurements included NGR, GRA bulk density, and MS (see **Physical properties and downhole measurements**). Archive halves of all split-core sections were measured for MSP. A total of 36 discrete sample cubes were taken for *P*-wave velocity and MAD measurements. Most of these discrete samples were also used for paleomagnetic measurements (see **Paleomagnetism**). Nondestructive thermal conductivity measurements were made on representative samples (individual pieces) from split cores. Full-circumference, true color images of whole-round core exteriors were recorded with the DMT CoreScan3 system. A summary of the physical properties data from Hole U1557D, which recovered the longest basement interval at this site, is shown in Figure **F89**.

10.2.1.1. Natural gamma radiation

NGR serves as an estimate of the variability in concentration of radioactive elements (^{40}K, ^{238}U, and ^{232}Th) in the cored basement section. Because radioactive element concentrations are generally low in fresh basalts, potassium added via secondary mineral precipitation is likely to be the main component in the NGR variability (Alt, 1995). Assuming that is the case, NGR may serve as a proxy for alteration in oceanic crust (Bartetzko et al., 2001).

In Hole U1557D, NGR ranges 0.4–35.6 counts/s (mean = 15.9 counts/s) (Figure **F89**). Because of the lithologically mixed nature of the breccia encountered at Site U1557, scatter in the physical properties data is expected and trends are difficult to distinguish. However, lower NGR appears to

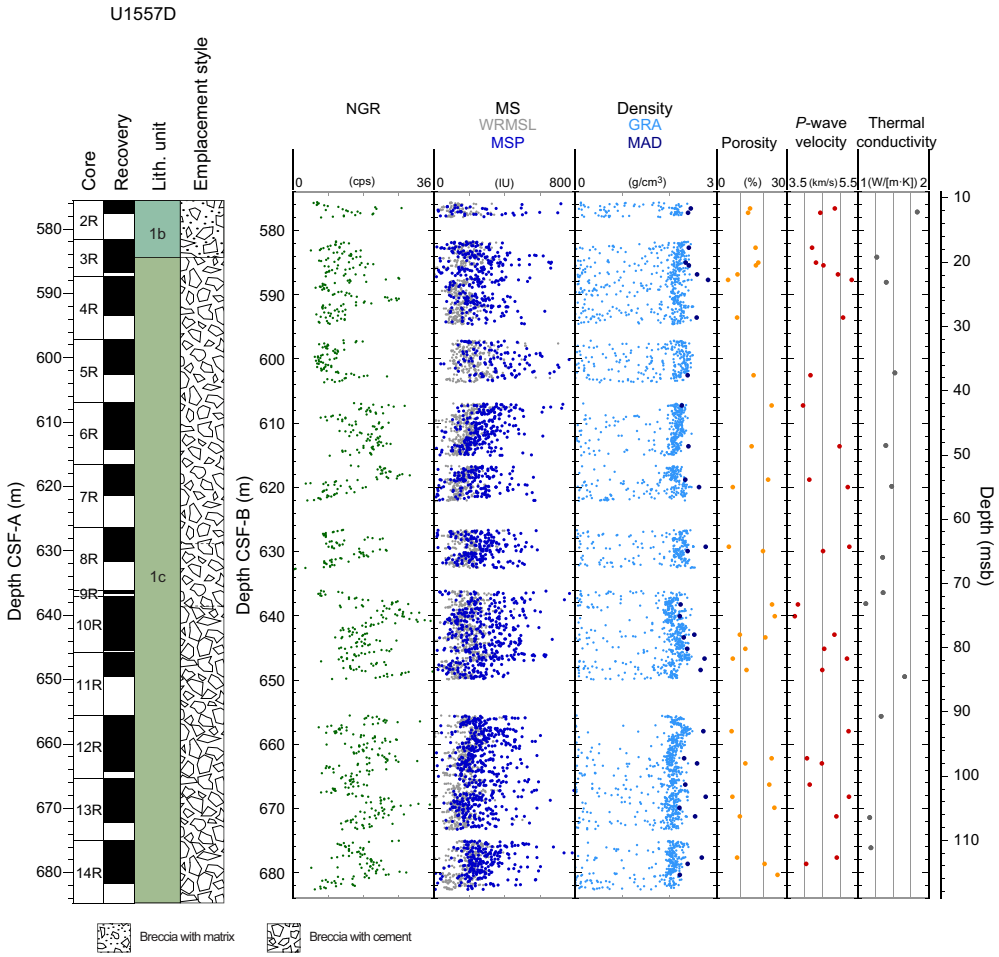

Figure F89. Summary of core physical properties data in basement, Hole U1557D. cps = counts per second.

coincide with relatively (macroscopically) fresh basalt clasts in the breccia, whereas higher values, particularly above 30 counts/s, coincide with altered glass-bearing, clay-rich intervals (see **Igneous petrology**). Zeolites commonly form in association with altered glass clasts, and intervals with higher NGR in Hole U1557D may reflect the presence of a potassium-rich end-member such as phillipsite (see **Alteration petrology**).

10.2.1.2. Gamma ray attenuation bulk density

Variations in bulk density can reflect changes in mineralogy, composition, and porosity within basement units. GRA bulk density from Holes U1557B and U1557D ranges from 0 to ~2.6 g/cm^3. Values < 1 g/cm^3 are considered spurious because they have a lower density than seawater (~1.03 g/cm^3) and are likely associated with irregularly sized core pieces, gaps between individual core pieces, and/or core liner dividers inserted between core bins (see **Curatorial core procedures and sampling depth calculations** in the Expedition 390/393 methods chapter [Coggon et al., 2024c]). Most of the coherent data cluster at the higher end of the reported range (Figure **F89**). At Site U1557, there is no major downhole trend in GRA bulk density. However, the basement recovered at Site U1557 was a single unit of breccia >100 m thick (see **Igneous petrology**), so the compositional difference observed within the breccias (i.e., the different proportions of clast type or matrix type) had very minor influence on the bulk density.

10.2.1.3. Magnetic susceptibility

MS is an indicator of the tendency of minerals to become magnetized upon application of a magnetic field; thus, it can be considered an approximation of the abundance of magnetic minerals within the rock. MS at Site U1557 was measured on whole-round core sections using a pass-through sensor on the WRMSL and on split-core sections using a point-contact sensor on the SHMSL. Both the pass-through and point-contact data are similar in character. MS ranges from 0 to ~800 IU. Whole-round data from Hole U1557D have a mean MS of 168 IU, and discrete data have a mean MS of 277 IU. Figure **F89** shows substantial scatter in both measurements, which reflects the mixed composition of basalts and matrix in the breccia.

10.2.1.4. Thermal conductivity

Thermal conductivity measurements in the basement offer a means of calculating potential conductive heat flow through oceanic crust. Thermal conductivity is controlled by basement properties such as chemical composition, porosity, density, and fabric of the basement rocks.

Thermal conductivity in Hole U1557D ranges from 1.84 W/(m·K) in the uppermost core (Section 390-U1557D-2R-2) to 1.11 W/(m·K) in Section 10R-1. Four thermal conductivity measurements were taken below the sediment/basement interface in Hole U1557B, in which the sediment/basement interface was captured with the XCB system, and values were consistent with data from Hole U1557D (Table **T16**; Figure **F90**). At 0.26 msb, a thermal conductivity of 2.18 W/(m·K) was determined for a sample from Hole U1557B. The shallowest basement measurement in Hole U1557D was relatively high as well (1.8 W/[m·K]). First-order analysis of core images seemed to indicate that higher thermal conductivity coincides with breccia containing clasts of fresher basalt, whereas samples that contained a higher proportion of more altered basalt had lower conductivity.

10.2.1.5. Moisture and density

MAD procedures include high-precision, high-accuracy measurements of discrete sample mass and volume that allow calculations of the bulk density, grain density, and porosity. Porosity is particularly useful for determining the volume of water that could potentially be stored in the interval or lithology represented by a discrete sample. Bulk density, in part, controls seismic wave velocity. Grain density is related to the mineralogy of the sample, so it is useful for mineralogical analyses and alteration studies.

Discrete samples for MAD analysis were generally taken twice per core and were selected to be representative of both the basalt clasts and the matrix of the breccia recovered at Site U1557. There were intervals within the breccia that contained significant void space that was greater in volume than the 2 cm^3 sampling size for the MAD cubes; therefore, MAD porosity measurements are not representative of the total pore space in the formation and should be considered the lower limit of true porosity in the basement material at Site U1557. Four discrete samples were taken

from below the sediment/basement interface in Hole U1557B (from Cores 390C-U1557B-63X, 65X, and 66X) that recovered the uppermost volcaniclastic breccia (see Estes et al., 2021). A total of 32 discrete samples were taken from Hole U1557D cores: 16 samples from the basalt clasts and 16 samples from the breccia matrix (defined here as the material between large clasts, which actually comprises small basalt and altered glass clasts, fine-grained matrix, and/or cement; see **Igneous petrology**). The analyses reported here are of samples from Hole U1557D, in which the majority of the talus breccia recovered at Site U1557 was cored.

Table T16. Thermal conductivity measurements on basement rocks, Site U1557. Thermal conductivity was measured on selected pieces of split core, chosen to be representative of the primary igneous lithology for each core in Holes U1557B (Expedition 390C) and U1557D (Expedition 390). Mean values are the arithmetic mean of three replicate measurements on the same core piece. TCON = thermal conductivity. **Download table in CSV format.**

Core, section, interval (cm)	Top depth CSF-B (m)	Depth (msb)	TCON, mean (W/[m·K])	TCON, standard deviation (W/[m·K])	Primary lithology
390C-U1557B-					
63X-3, 17	565.03	0.26	2.184	0.04	Breccia
64X-1, 4	567.94	3.17	1.45	0.008	Breccia
65X-1, 25	569.65	4.88	1.582	0.013	Breccia
66X-1, 79	572.615	7.845	1.487	0.008	Breccia
390-U1557D-					
2R-2, 22	577.10	12.33	1.839	0.052	Breccia
3R-2, 106	584.126	19.356	1.266	0.02	Breccia
4R-1, 63	588.03	23.26	1.401	0.009	Breccia
5R-4, 90	602.18	37.41	1.52	0.026	Breccia
6R-5, 139	613.45	48.68	1.393	0.019	Breccia
7R-3, 46	619.84	55.07	1.476	0.008	Breccia
8R-4, 80	630.89	66.12	1.352	0.01	Breccia
9R-1, 30	636.40	71.63	1.357	0.028	Breccia
10R-1, 108	638.118	73.348	1.109	0.016	Breccia
11R-3, 82	649.47	84.70	1.663	0.014	Breccia
12R-1, 13	655.63	90.86	1.33	0.004	Breccia
13R-5, 47	671.39	106.62	1.166	0.029	Breccia
14R-1, 112	676.12	111.35	1.185	0.008	Breccia

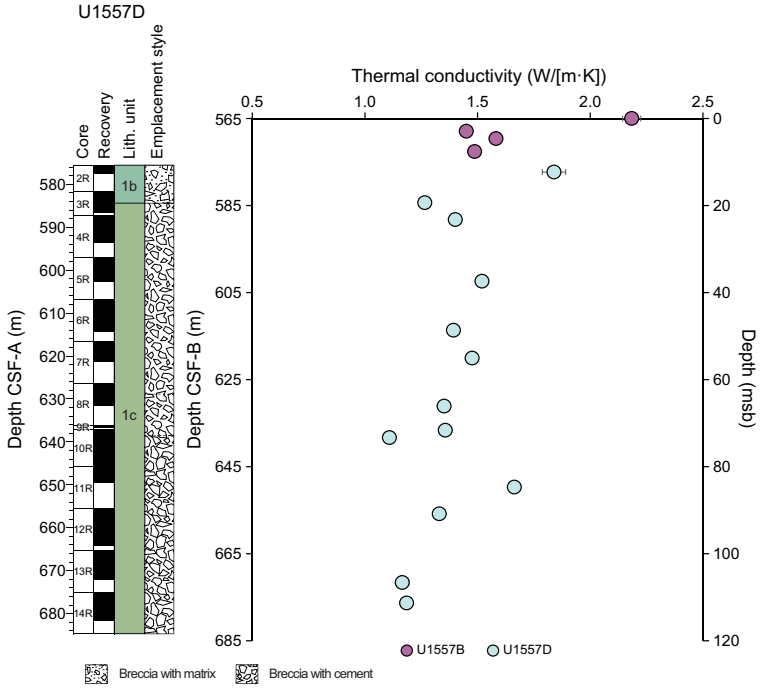

Figure F90. Thermal conductivity data in basement, Holes U1557B and U1557D. Error bars = ±1 standard deviation uncertainty unless uncertainty is smaller than symbol width. See Table T16.

The mean porosity of all Hole U1557D discrete samples is 15% (Table **T17**) (mean clasts = 9%; mean matrix = 21%). The porosity of the clast samples does not change systematically downhole, but the porosity of the matrix samples increases downhole (Figure **F91A**). A linear regression of porosity as a function of depth for the matrix samples has R^2 = 0.54 and a p value = 0.001, indicating a significant relationship.

The mean grain density of the discrete samples is 2.71 g/cm^3 (Table **T17**) (mean clasts = 2.77 g/cm^3; mean matrix = 2.66 g/cm^3). Although the grain density of the matrix samples shows little variation from the mean (standard deviation = 0.04 g/cm^3), the clast samples show more variation (standard deviation = 0.11 g/cm^3) (Figure **F91B**). The variation in grain density of the clast samples could reflect different basalt types or different degrees of alteration.

10.2.1.6. *P*-wave velocity

P-wave velocity is the velocity of a seismic compressional wave (*P*-wave) propagating through a sample. *P*-wave velocity is directly controlled by the bulk density, compressibility, and shearability of the material sampled and is indirectly related to the porosity, mineralogy, grain fabric, or lithology of a discrete sample. *P*-wave velocity was measured on the discrete samples used for MAD analyses, allowing direct comparison of porosity and density with velocity. Determining the *P*-wave velocity of discrete samples is also especially useful when correlating the downhole logging velocities and regional seismic imaging to the core measurements.

P-wave velocity was measured on the *x*-, *y*-, and *z*- axes of the discrete sample cubes, and no evidence of anisotropy was observed. Therefore, the mean three-axis velocity was used for each of the discrete samples (Table **T17**). The mean *P*-wave velocity of the clast samples is 4.90 ± 0.36 km/s

Table T17. Summary of physical properties, clast lithology, and matrix classification of discrete sample cubes, Hole U1557D. Mean velocity is the arithmetic mean of manual *P*-wave velocities from the three axes (*x*, *y*, *z*) for each sample. Clast color and matrix type were determined by shipboard igneous petrologists based on visual assessment. NA = not applicable for this sample or sample type. **Download table in CSV format.**

Core, section, interval (cm)	Top depth CSF-B (m)	Bulk density (g/cm^3)	Grain density (g/cm^3)	Porosity (vol%)	*P*-wave velocity (km/s)	Sample lithology	Type	Clast color	Matrix type	Text ID
390-U1557D-										
2R-1, 97	576.57	2.448	2.682	14.1	4.83	Breccia	Matrix	NA	Pelagic	CUBE11577111
2R-2, 34	577.22	2.388	2.598	13.3	4.47	Breccia	Clast	Brown	NA	CUBE11577071
3R-1, 99.5	582.65	2.412	2.686	16.5	4.25	Breccia	Clast	Orange/Brown	NA	CUBE11577121
3R-3, 65	585.01	2.342	2.624	17.6	4.28	Breccia	Matrix	NA	Pelagic	CUBE11577131
3R-3, 108	585.42	2.406	2.684	16.7	4.57	Breccia	Matrix	NA	Calcite	CUBE11577141
3R-4, 117	586.83	2.585	2.737	8.8	4.98	Breccia	Clast	Brown	NA	CUBE11577151
4R-1, 28	587.68	2.816	2.908	4.9	5.38	Breccia	Clast	Gray	NA	CUBE11577311
4R-5, 40	593.53	2.576	2.722	8.6	5.06	Breccia	Clast	Brown	NA	CUBE11577341
5R-4, 128	602.56	2.382	2.635	15.7	4.28	Breccia	Matrix	NA	Calcite/Zeolite	CUBE11577301
6R-1, 34	607.24	2.256	2.632	23.4	3.94	Breccia	Matrix	NA	Calcite/Zeolite	CUBE11577351
6R-6, 1	613.57	2.402	2.643	14.9	4.95	Breccia	Matrix	NA	Calcite	CUBE11577411
7R-2, 84.5	618.79	2.330	2.697	21.9	4.17	Breccia	Matrix	NA	Calcite/Zeolite	CUBE11577541
7R-3, 56	619.94	2.623	2.741	6.9	5.20	Breccia	Clast	Brown	NA	CUBE11577561
8R-3, 39	629.25	2.768	2.864	5.2	5.31	Breccia	Clast	Gray	NA	CUBE11577581
8R-3, 106	629.92	2.382	2.712	19.6	4.48	Breccia	Matrix	NA	Calcite/Zeolite	CUBE11577611
10R-1, 119	638.22	2.233	2.605	23.5	3.87	Breccia	Matrix	NA	Calcite/Zeolite	CUBE11581571
10R-3, 21.5	640.06	2.220	2.610	24.6	3.70	Breccia	Matrix	NA	Zeolite/Compact	CUBE11581601
10R-5, 42	642.94	2.524	2.688	9.8	4.83	Breccia	Clast	Brown	NA	CUBE11581631
10R-5, 88	643.37	2.302	2.632	20.6	NA	Breccia	Matrix	NA	Zeolite/Compact	CUBE11581641
10R-6, 138	645.13	2.372	2.556	12.1	4.61	Breccia	Clast	Brown	NA	CUBE11581651
11R-1, 89	646.69	2.739	2.863	6.8	5.18	Breccia	Clast	Gray	NA	CUBE11581681
11R-2, 118	648.42	2.658	2.893	12.6	4.56	Breccia	Clast	Orange/Brown	NA	CUBE11581721
12R-3, 61	657.95	2.717	2.832	6.4	5.31	Breccia	Clast	Gray	NA	CUBE11582001
12R-7, 70	662.17	2.309	2.700	23.3	3.91	Breccia	Matrix	NA	Zeolite/Compact	CUBE11582031
12R-8, 35	662.97	2.585	2.800	12.1	4.60	Breccia	Clast	Gray	NA	CUBE11582041
13R-1, 96.5	666.27	2.335	2.710	22.3	3.98	Breccia	Matrix	NA	Zeolite/Compact	CUBE11582061
13R-3, 6.5	668.17	2.769	2.893	6.6	NA	Breccia	Clast	Gray	NA	CUBE11582101
13R-4, 28	669.88	2.206	2.589	24.5	3.59	Breccia	Matrix	NA	Zeolite/Compact	CUBE11582121
13R-5, 30	671.22	2.545	2.711	9.9	4.89	Breccia	Clast	Brown	NA	CUBE11582141
14R-2, 121	677.62	2.682	2.841	8.7	NA	Breccia	Clast	Gray	NA	CUBE11582161
14R-3, 84.5	678.61	2.383	2.730	20.3	3.98	Breccia	Matrix	NA	Zeolite/Compact	CUBE11582181
14R-4, 110	680.36	2.219	2.636	25.9	3.64	Breccia	Matrix	NA	Zeolite/Compact	CUBE11582191

(±1 standard deviation), and the mean velocity of the matrix samples is 4.14 ± 0.42 km/s. The *P*-wave velocity of the discrete samples from clasts in the breccia shows little downhole trend (Figure **F91C**), but the velocity of the discrete samples from the breccia matrix between the larger basalt clasts decreases downhole (Figure **F91C**). A linear regression with R^2 = 0.52 and a p value = 0.002 indicates a clear decrease in velocity with increasing depth for the matrix samples, which is consistent with the observed increase in porosity downhole (Figure **F91A**).

10.2.2. Digital imaging

Hard rock cores collected at Site U1557 were well consolidated, and pervasive fracturing was rare. This resulted in cylindrical cores particularly suitable for imaging. A total of 99.3% of the recovered material could be scanned on the DMT CoreScan3. Image exposure was also improved compared to Site U1556 because all automatic processing done by the CoreScan3 software was disabled and a blackout curtain was installed to create a more controlled imaging environment. Unlike the section-half images taken using the SHIL (see **Core image processing** in the Expedition 390/393 methods chapter [Coggon et al., 2024c]), high-resolution images of the whole-round core preserve 3-D geometries of alteration features and greater data coverage (360°) of the original core. Both image data sets could be used for quantifying the proportion of rock types using machine learning and computer vision (Fu et al., 2022), although the high-resolution DMT images collected during Expedition 390 provide a unique suite of images for training machine learning algorithms.

10.2.3. Wireline logging

Three logging runs were initially planned to follow basement coring in Hole U1557D: the triple combo, Formation MicroScanner (FMS)-sonic, and Ultrasonic Borehole Imager tool strings (see

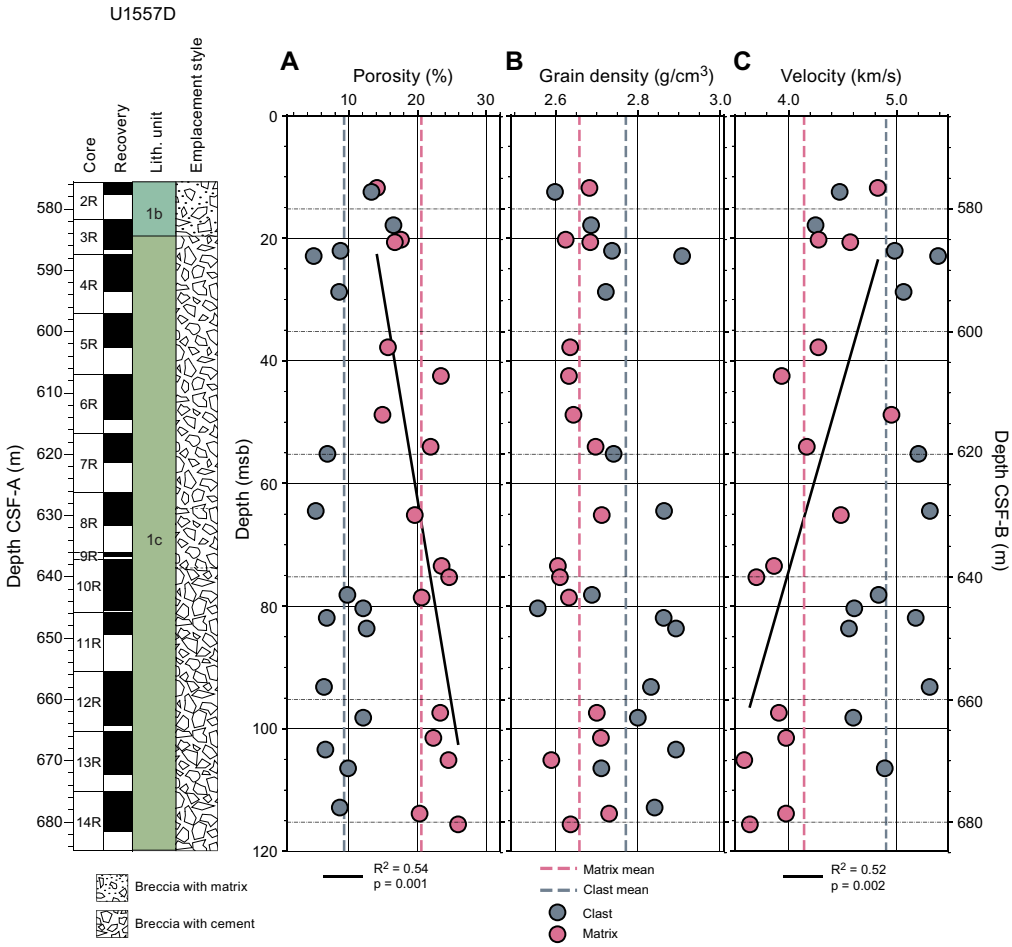

Figure F91. Physical properties of discrete rock samples, Hole U1557D. A. Porosity. Black line = linear regression through matrix samples. B. Grain density. C. *P*-wave velocity. Black line = linear regression through matrix samples. See Table T17.

Wireline logging operations in the Expedition 390/393 methods chapter [Coggon et al., 2024c]). However, to recover time lost to weather during Site U1557 operations and preserve time for operations at Site U1559, only one logging tool string was run in Hole U1557D (see **Operations**). The triple combo tool string recorded a primary set of measurements (gamma ray spectroscopy, density, electrical resistivity, and MS) to assess hole conditions and characterize the drilled formation. Drilling conditions prior to completion of coring had been good, the sea state was favorable, and the triple combo was deployed successfully, providing good quality data over two full passes of the drilled breccia interval.

10.2.3.1. Wireline operations

Logging operations for Site U1557 began after completion of RCB coring in Hole U1557D to a total depth of 684.7 m DSF on 17 May 2022. In preparation for logging, a final mud sweep was circulated in the hole, the pipe was raised above the reentry cone, the RCB bit was released on the seafloor, and the borehole was reentered and filled with seawater (see **Operations**). The drill pipe was raised to 30 m DSF for logging. Sea conditions were moderate, with heave in the 1–2 m range, and the wireline heave compensator was used for the entire logging operation.

The triple combo was rigged up and run into the hole at 0835 h (local time) on 18 May. A downlog was recorded from just above the seafloor (identified by a step in the gamma ray log) to the bottom of the hole at 5711 mbrf. The first upward pass started at 1215 h and continued through the open hole until the entire tool string was pulled back into the casing. The tool string was immediately run back into the hole for the second (main) upward pass. The main pass began at 1250 h at 5711 mbrf and continued up through the casing until the entire tool string passed above the seafloor. The main pass was completed at 1731 h, and the triple combo tool string was returned to the surface. All tools were rigged down by 1815 h, and the drill floor was returned to drilling operations at 1845 h on 18 May.

10.2.3.2. Data overview

A summary of the main data recorded from the triple combo is shown in Figures **F92** and **F93**. The quality of downhole logging data is typically affected by hole diameter. The caliper log in Figure **F92** shows that the borehole was in excellent condition with a diameter close to RCB MS size. A larger diameter drill bit was used during the earlier phases of drilling in Hole U1557D when casing was installed (Estes et al., 2021; Williams et al., 2021), which is reflected by the enlarged interval at the top of the basement section (~572–580 m WMSF).

The quality of the logs can also be assessed by comparison with measurements made on cores from the same hole. Total natural gamma ray from the triple combo shows good agreement with NGR data from cores, with a slight depth offset of a few meters (Figure **F92**). Discrepancies between the drilling core depth and wireline logging depth may occur because of core expansion, incomplete core recovery, incomplete heave compensation, wireline stretch, drill pipe stretch, and tidal changes. The density log generally follows the upper envelope of the scattered GRA data from core, which are affected by variable core recovery and incomplete filling of the core liner (see **Physical properties** in Basement). The MS log similarly follows the outer envelope of the scattered MS measurements on both whole-round and half-section cores.

Total gamma ray generally increases with depth in the breccia of Hole U1557D, with local variations on the order of 5–20 gAPI. Two intervals of higher gamma ray (640–644 and 652–654 m WMSF) occur within ±5 m of a fault zone described in **Igneous petrology** and **Alteration petrology** (Core 390-U1557D-11R) and may reflect a local increase in clay minerals associated with fault gouge materials. Spectral data show changes in individual contributions of Th, K, and U to the total gamma ray signal (Figure **F93**), which seems to be driven primarily by the contributions of K and to a lesser extent Th. Detailed core-log correlation of the gamma ray data may allow for more precise spectral characterization of the different breccia styles recovered in Hole U1557D.

The resistivity log indicates that there is significant variability in formation conductivity (5–2000 Ωm) within the breccia interval (Figure **F92**). The alternating character of the resistivity log is consistent with the presence of open and mineral-filled pore spaces (low resistivity) throughout the breccia lithology. Resistivity is relatively high in Lithologic Subunits 1a and 1b and the top of Subunit 1c (see **Igneous petrology**). A distinct interval of decreasing resistivity (630–644 m

WMSF) coincides with a transition zone in lithology and corresponding transition in alteration (see **Alteration petrology**; Figure **F54**). The deepest recovered breccia in Subunit 1c has slightly lower mean resistivity than overlying breccias but the same variable character, alternating between intervals of lower and higher resistivity.

10.2.4. Data integration

10.2.4.1. Image analysis

Perhaps the most interesting feature of the rocks recovered from Site U1557 is that they are dominated by porous breccia, predominantly partially cemented by $CaCO_3$. Estimating the proportion of basalt of different generations as well as the proportion of cement present encasing these clasts will be a valuable means of understanding the alteration history and nature of fluid flow in these ridge flank deposits as they age. High-resolution images captured during Expedition 390 provide a unique data set that enables not only visual estimates of alteration extent but also a means of training machine learning algorithms to automate the quantification of these features (Fu et al., 2022). Core-log integration between DMT images and downhole logging data could also be useful, particularly because recovery was high in the basement sections at Site U1557, which may provide groundtruthing for electrofacies determined from downhole logs (e.g., Tominaga et al., 2009).

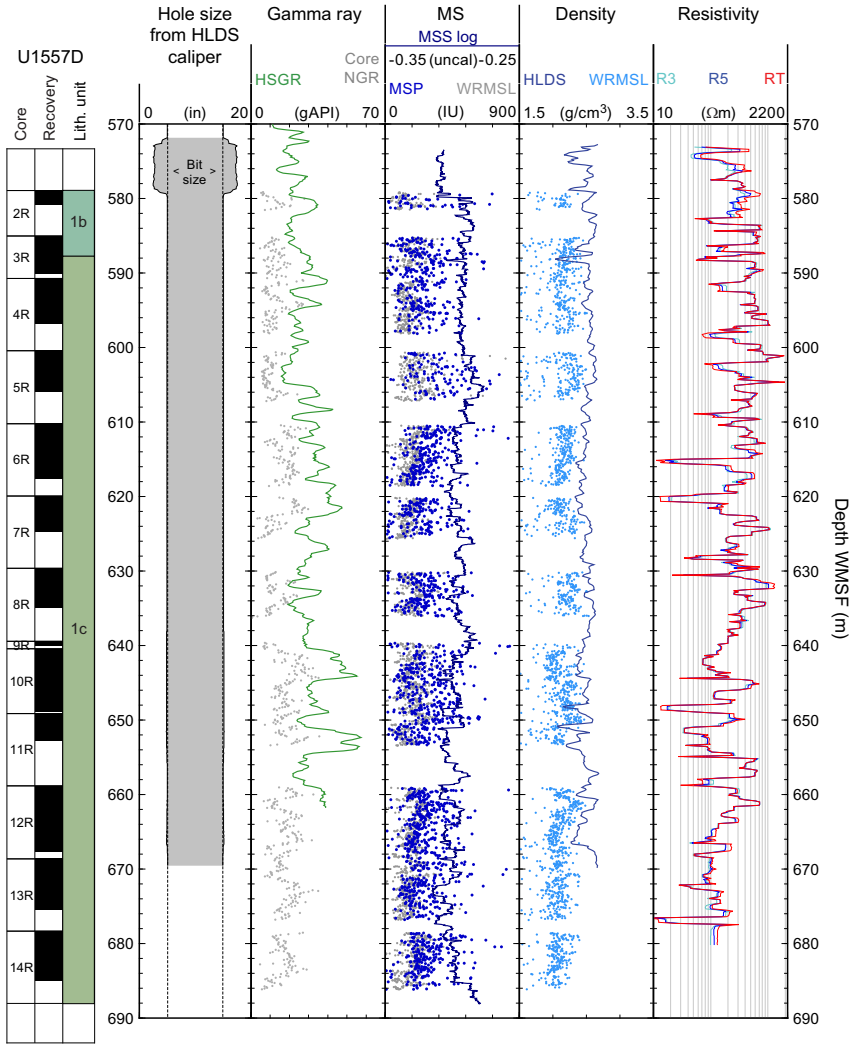

Figure F92. Summary of logging data recorded with triple combo logging tool string, Hole U1557D. Note that logging data are on logging depth scale; core data have been shifted from CSF-A depths by +3.5 m for better correspondence with logging data. HLDS = Hostile Environment Litho-Density Sonde, HSGR = standard (total) gamma ray log, uncal = uncalibrated units for Magnetic Susceptibility Sonde (MSS). R3 = medium resistivity reading of High-Resolution Laterolog Array Tool; R5 = deepest resistivity; RT = true resistivity, modeled from all depths of investigation.

10.2.4.2. Discrete sample comparisons

Discrete samples used for MAD and *P*-wave analyses were classified in terms of their matrix type and color to characterize any relationships or trends within the breccia recovered at Site U1557 (Table **T17**). Figure **F94** shows crossplots of *P*-wave velocity versus porosity and grain density versus porosity for both samples of breccia matrix (Figure **F94A, F94C**) and breccia clasts of basalt (Figure **F94B, F94D**). For the matrix samples (defined here as the material between large clasts, which actually comprises small basalt and altered glass clasts, fine-grained matrix, and/or cement; see **Igneous petrology**), the dominant composition of the matrix was classified to correspond to petrologic observations (see **Igneous petrology** and **Alteration petrology**). In general, matrix composition changed downhole from mostly pelagic sediment at the top to sparry calcite to an authigenic calcite/zeolite mix and finally to a mostly zeolitic composition at the bottom of the hole. The observed porosity increase and velocity decrease downhole (Figure **F91A, F91C**) therefore correspond to distinct properties for different matrix-sample classes, with pelagic sediment and sparry calcite samples having the highest *P*-wave velocity and lowest porosity, whereas the samples with more zeolite-rich cements have the lowest *P*-wave velocity and highest porosity (Figure **F94A**). The grain density of the matrix samples does not vary systematically with porosity regardless of how porosity varies with matrix classification. Note that the observation that measured porosity increases downhole is contrary to core-based observations that indicate a tendency

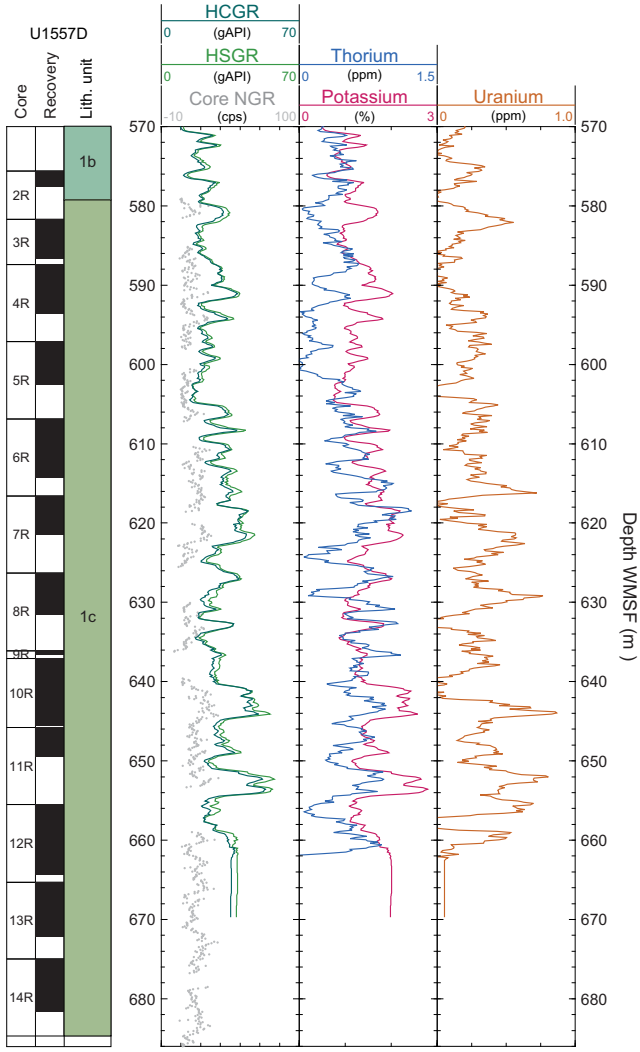

Figure F93. Summary of spectral gamma ray logs recorded with triple combo tool string, Hole U1557D. Note that logging data are on logging depth scale; core NGR data have been shifted from CSF-A depths by +3.5 m for better correspondence with logging data. HCGR = computed (U-free) gamma radiation, HSGR = standard (total) gamma ray, cps = counts per second.

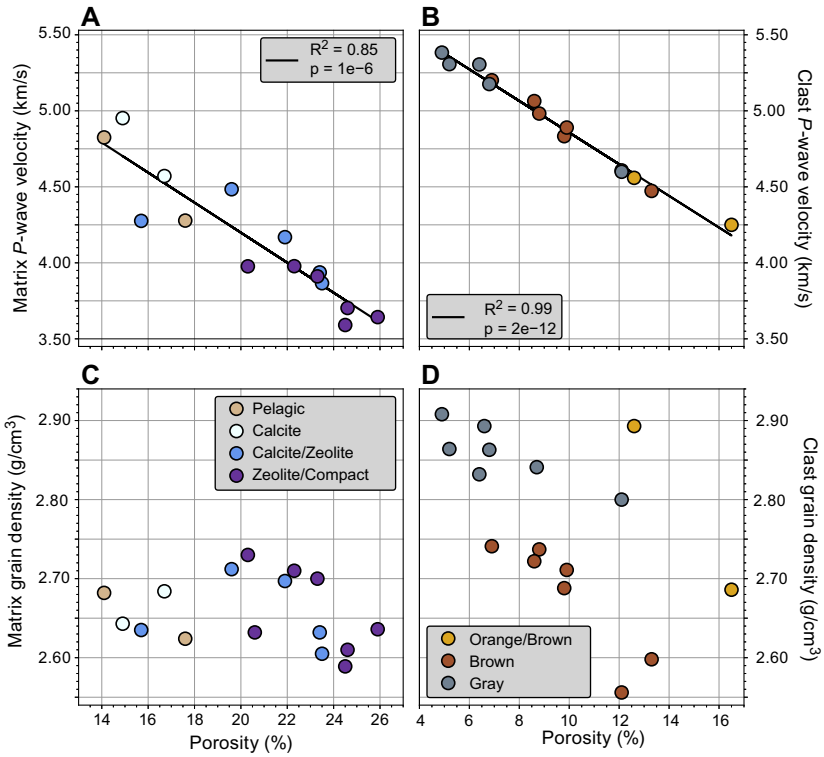

Figure F94. *P*-wave velocity vs. porosity for (A) matrix and (B) basalt clast discrete samples, Hole U1557D. Grain density vs. porosity for (C) matrix and (D) basalt clast discrete samples.

for calcite cement and vuggy porosity to be higher toward the top of Subunit 1c and compaction to be greater toward the bottom of Subunit 1c (see **Igneous petrology**; Figure **F17**). This raises questions regarding the nature of porosity measured for the discrete samples, which was also noted at Site U1556 (see **Basement** in Physical properties and downhole measurements in the Site U1556 chapter [Coggon et al., 2024a]).

The discrete clast samples were classified based on color following the scheme (orange, brown, or gray) used in Hole U1557D macroscopic core descriptions (see **Igneous petrology**). Although no orange clasts were taken as discrete samples, gray and brown clasts were sampled for physical properties analyses. Additionally, two somewhat anomalous, highly plagioclase phyric clasts with a high degree of background alteration were taken and classified as orange/brown. A very strong correlation exists between porosity and *P*-wave velocity for the clast samples, illustrating the control porosity plays on seismic velocities (Figure **F94B**). Generally, gray clasts have the lowest porosity and highest *P*-wave velocity and brown and orange/brown clasts have the highest porosity and lowest *P*-wave velocity. Comparing grain density to porosity suggests that the gray clasts are less altered given their higher mean grain density (2.86 g/cm^3), whereas the brown clasts are more altered given their lower mean grain density (2.68 g/cm^3), regardless of the porosity of either clast classification (Figure **F94D**). The two clast samples classified as orange/brown have different grain densities, one is more similar to the gray clasts and the other is more similar to the brown clasts.

11. Geochemistry

11.1. Sediment

11.1.1. Interstitial water sampling

The ~564 m sedimentary succession at Site U1557 was cored in Hole U1557B during Expedition 390C, with one sample per core taken for headspace gas analysis and one IW whole-round per

core. A mudline sample was taken with Core 390C-U1557B-1H. A total of 61 IW samples were squeezed under laboratory atmosphere from whole-round samples from 0 to 554.2 m core depth below seafloor, Method A (CSF-A). The whole-round sample length was increased from 5 to 10 cm from Core 19X downhole to obtain enough water for shipboard analyses. Sediment lithology alternates between brown silty clays and calcareous nannofossil ooze in Lithologic Unit I and calcareous nannofossil chalk in Unit II (Table **T3**). No specific lithology was targeted during IW sampling because the pore water profiles of pelagic sediments are usually independent of lithology changes (Hesse and Schacht, 2011). Shipboard analyses of the squeezed IW (see **Geochemistry** in the Expedition 390/393 methods chapter [Coggon et al., 2024c]) include pH, salinity, alkalinity, major cations and anions (sodium, calcium, magnesium, potassium, chloride, and sulfate) measured by ion chromatography (IC), major and minor elements measured by ICP-AES, and nutrients (phosphate and ammonium) measured by spectrophotometry. Carbonate and total carbon (TC) were subsequently analyzed on the solid residue after IW squeezing (squeeze cakes). All data from shipboard analyses on IW and squeeze cakes are shown in Tables **T18** and **T19**, and select pore water profiles are shown in Figures **F95**, **F96**, **F97**, **F98**, and **F99**. Major cations (Na, K, Ca, and Mg) were measured by both ICP-AES and IC. Data from the two methods are very similar for Mg, K, and Ca. We thus present data from both techniques on the same plot and primarily focus on IC data in the discussion for easier comparison with major elemental compositions at other sites. Sodium concentrations from ICP-AES are slightly lower (~470 mM) than the International Association for the Physical Sciences of the Oceans (IAPSO) standard seawater value (480.7 mM); thus, we only discuss sodium IC data in the following sections.

11.1.2. Interstitial water results

Downcore variability of pore water concentrations is controlled by a combination of physical (e.g., vertical and lateral diffusion and/or advection of fluids), geochemical (e.g., sorption and desorption onto clay minerals, calcium carbonate dissolution and recrystallization, and biogenic silica dissolution), and biological processes (e.g., microbial reduction of Mn oxides, Fe oxyhydroxides, and sulfate for organic carbon respiration; Mottl, 1989). Here, we show depth profiles of pore water chemistry from Hole U1557B to identify the reactions that may have occurred during and after sediment deposition.

11.1.2.1. Salinity, chloride, sodium, and potassium

Salinity varies around 34–35 throughout the hole, with lower salinity in intervals at 130–190 and ~250–400 m CSF-A (Table **T18**). Chloride (Cl) concentrations range 540–595 mM, and sodium (Na) concentrations range 460–509 mM (Figure **F95A**). Potassium (K) concentrations decrease from 11.4 mM near the seafloor to 6.6 mM at ~262 m CSF-A (Figure **F95B**). The concentration gradient may be associated with K incorporation during the transformation of smectite into illite; postexpedition research will verify the extent to which this reaction is occurring at Site U1557. Below sediment Unit I, K concentrations increase to a maximum of 11.5 mM at ~510 m CSF-A, below which they decrease again toward ~9.2 mM at the sediment/basement interface (Figure **F95C**).

11.1.2.2. pH, alkalinity, magnesium, calcium, and strontium

The pH value of 8.1 in the mudline of Hole U1557B is consistent with overlying seawater (Figure **F96A**). Below the mudline, pH is relatively constant at ~7.5 throughout the hole. Alkalinity is relatively uniform throughout the majority of Hole U1557B, ranging 2.2–3.9 mM; however, a maximum value of 12.4 mM occurs just above basement, coinciding with an increase in Ca (see below) and is possibly associated with calcium carbonate dissolution (Figure **F96B**). In Unit I, magnesium (Mg) concentrations decrease from seawater concentrations (55.07 mM) near the seafloor to 44.3 mM at ~184 m CSF-A (Figure **F96C**). Below Unit I, Mg concentrations gradually increase to 50.6 mM at ~554 m CSF-A. At the base of the hole, significant variability is observed in Mg concentrations, which range ~41–50 mM at the Subunit ID/IE boundary.

Table T18. Interstitial water geochemistry results, Site U1557. **Download table in CSV format.**

Table T19. Geochemical analyses of sediment samples, Site U1557. **Download table in CSV format.**

Strontium (Sr) and calcium (Ca) concentration gradients are opposite those observed for Mg and K (Figure **F96D, F96E**). Sr and Ca concentrations in the mudline sample are 95.6 µM and 10.9 mM, respectively, and increase to 270.6 µM and 16.8 mM at 216 m CSF-A. Sr and Ca concentrations are relatively invariant from 216 to ~400 m CSF-A, below which the concentrations gradually decrease until ~530 m CSF-A. In Subunit IIE, Ca concentrations are highly variable, ranging ~11–18.5 mM. This variance coincides with the chemical variability observed in Mg. Sr/Ca increases from the mudline value (8.5 µM/mM) to ~16 µM/mM near 200 m CSF-A, where it remains until the base of Subunit IIC (Figure **F96F**). It then decreases toward the basement, with

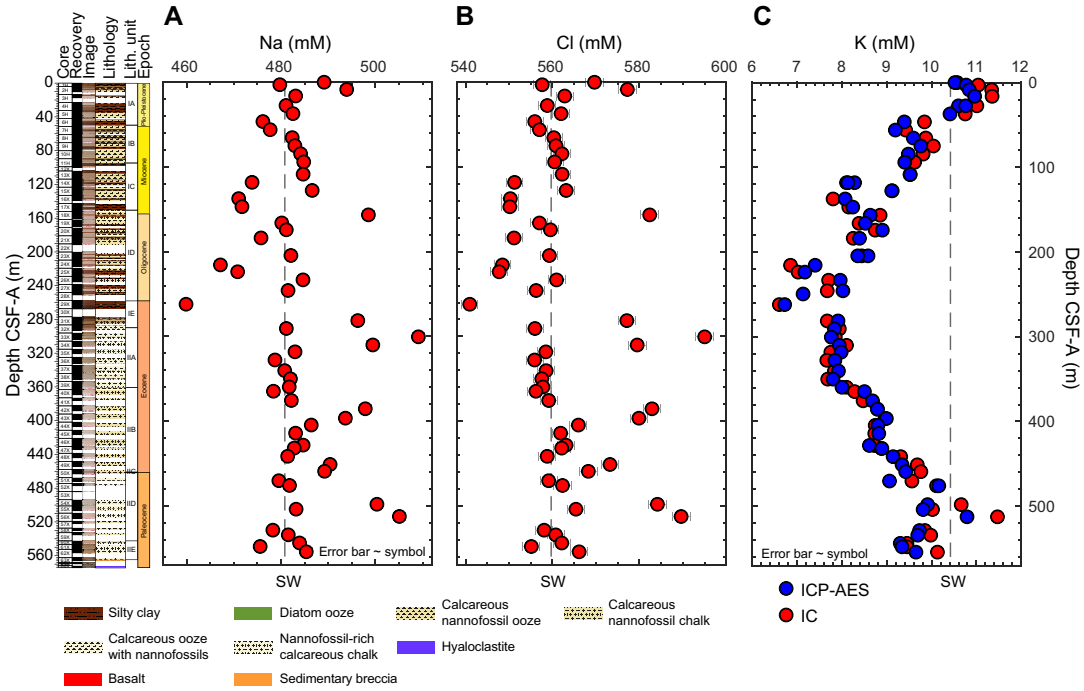

Figure F95. IW profiles of (A) sodium, (B) chloride, and (C) potassium, Site U1557. Seawater (SW) reference values correspond to IAPSO standard composition.

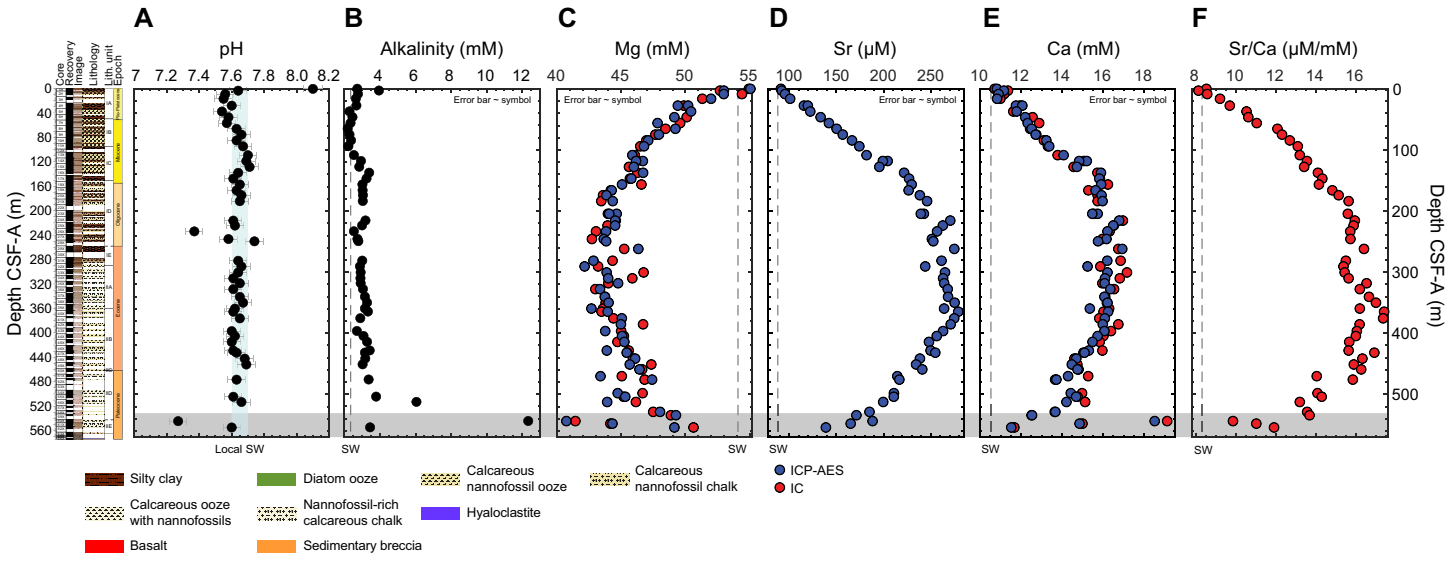

Figure F96. IW profiles of (A) pH, (B) alkalinity, (C) magnesium, (D) strontium, (E) calcium, and (F) Sr/Ca, Site U1557. Gray shading highlights abrupt changes observed in Mg, Ca, and Sr/Ca in Subunit IIE. Blue shaded area in A = range in pH observed for bottom seawater at this location (7.6–7.7 at ~31°S; Ríos et al., 2015). Vertical dashed lines = IAPSO seawater (SW) standard reference values.

a value of ~9 µM/mM near the sediment/basement interface. Increases in Sr/Ca ratios in the upper ~200 m coincide with decreases in pore water Mg concentrations and are likely a result of recrystallization from low-Mg biogenic carbonate typical of nannofossil ooze to higher Mg diagenetic calcite (e.g., Baker et al., 1982). The decrease in Sr/Ca ratios below ~400 m CSF-A, with ratios returning to the mudline value, may indicate the influence of seawater-like basement fluids in these pore fluids.

11.1.2.3. Boron, lithium, and silica

Boron (B) concentrations range ~400–725 µM in Unit I. The concentration range narrows to 346–478 µM in Unit II (Figure **F97A**). B concentrations are highly variable below ~500 m CSF-A, ranging 459–1892 µM. In contrast, pore water Li concentrations are generally less variable in Unit I (~27–38 µM), moderately variable in Unit II (33–42 µM), and highly variable below ~500 m CSF-A (~30–90 µM) (Figure **F97B**; Subunits IID and IIE). Overall, silica (Si) concentrations gradually increase from the surface to the bottom of Hole U1557B with a range of ~21–744 µM. Exceptions include two local maxima in Si content, one at ~3 m CSF-A (~420 µM) and another at ~166 m CSF-A (625 µM). These concentration maxima coincide with a diatom ooze layer in Core 390C-U1557B-1H and diatoms present in smear slides (e.g., Sample 14X-1, 85–87 cm; see **Sedimentology**), suggesting biogenic silica dissolution. The increase in Si concentrations deeper than ~500 m CSF-A (in Subunits IID and IIE) (Figure **F97C**) does not coincide with the presence of diatoms or calcareous nannofossil chalk (see **Sedimentology**). Another possibility for increased Si concentrations in sediments is Si input from basement fluids (e.g., Wheat and MeDuff, 1994; Wells and Ghiorso, 1991); the increase in Si near basement coincides with sharp changes in B, Li, Ca, Sr, sulfate, pH, and alkalinity.

11.1.2.4. Sulfate, manganese, ammonium, and phosphate

Sulfate (SO_4^{2-}) concentrations decrease from seawater value (~29 mM) at the mudline to 23.8 mM at ~246 m CSF-A (Figure **F98A**). Although sample-to-sample variability is high below this depth, sulfate concentrations overall gradually increase to ~26 mM at ~450 m CSF-A. Below ~459 m CSF-A, sulfate concentrations are highly variable and include both an increase toward seawater

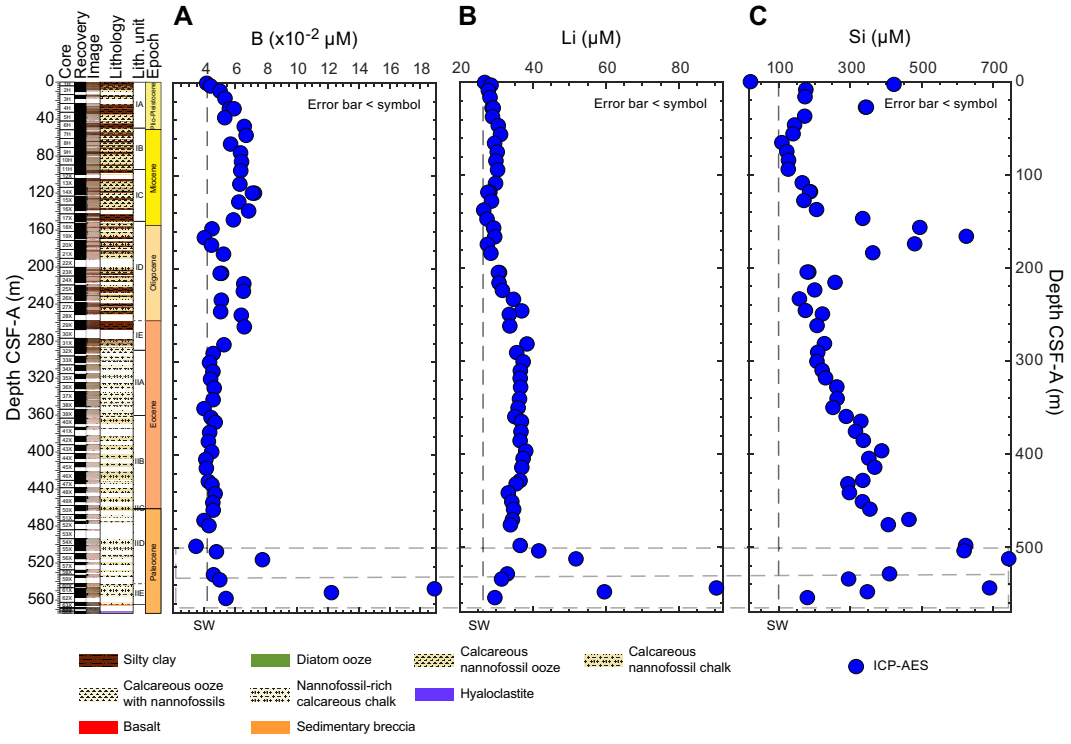

Figure F97. IW profiles of (A) boron, (B) lithium, and (C) silica, Site U1557. Dashed rectangles highlight concomitant changes in B, Li, and Si. Seawater (SW) reference values for B and Li correspond to IAPSO standard composition; local Si concentration is sourced from World Ocean Atlas (Boyer et al., 2018).

value and a decline to their lowest value of 20 mM at ~540 m CSF-A. Coincident with the decrease in sulfate concentrations in the uppermost ~100 m of Hole U1557B, dissolved Mn concentrations increase to a maximum of ~120 µM at ~27 m CSF-A (Figure **F98B**), suggesting reduction of Mn oxides and sulfate by organic carbon respiration in reducing pore waters. Broad peaks in Mn concentrations also occur at ~100–190 and ~190–280 m CSF-A, possibly due to continued Mn oxide reduction to dissolved Mn(II) during organic carbon respiration under low-oxygen/anoxic conditions. Below ~280 m CSF-A (near the bottom of Subunit IE), dissolved Mn is uniformly <5 µM. Ammonium (NH_4^+) concentrations increase linearly from 33.78 µM near the seafloor to 325.76 µM at ~75 m CSF-A (Figure **F98C**), consistent with production during organic carbon decay. Below this point, ammonium concentrations decrease linearly to 65.6 µM at ~550 m CSF-A. Phosphate (PO_4^{3-}) varies between 6.2 and 9.0 µM with no clear trend downcore (Figure **F98D**).

11.1.3. Sediment bulk geochemistry

11.1.3.1. Calcium carbonate

Calcium carbonate ($CaCO_3$) concentrations were measured once per core from Cores 390C-U1557B-1H through 62X and 65X, except for Cores 12H, 22X, 23X, and 57X, for a total of 56 analyses (Table **T19**; Figure **F99A**). The average carbonate content (39.5 ± 34.4 wt%, ±1 standard deviation [σ], n = 25) is highly variable in upper Lithologic Unit I, which is composed of alternating clay and carbonate layers, with a minimum value of 0.13 wt% in a clay layer (Core 29X) and a maximum value of 80.3 wt% in a carbonate layer (Core 26X). Carbonate concentrations were considerably higher through Unit II (average = 83.0 ± 16.1 wt%, ±1σ, n = 31; maximum = 92.1 wt%).

11.1.3.2. Total organic carbon

TOC was calculated for all samples measured for $CaCO_3$ as the difference between TC and total inorganic carbon (TIC) (see **Geochemistry** in the Expedition 390/393 methods chapter [Coggon et al., 2024c]). TOC concentrations in Unit I (0.25 ± 0.28 wt%, ±1σ, n = 21) are generally low (<1 wt%, excluding one sample in Core 390C-U1557B-3H) compared to those in Unit II (0.52 ± 0.65 wt%, ±1σ, n = 31) (Table **T19**; Figure **F99B**). A maximum of 2.7–3.1 wt% TOC occurs in the upper portion of Unit II at ~291–300 m CSF-A.

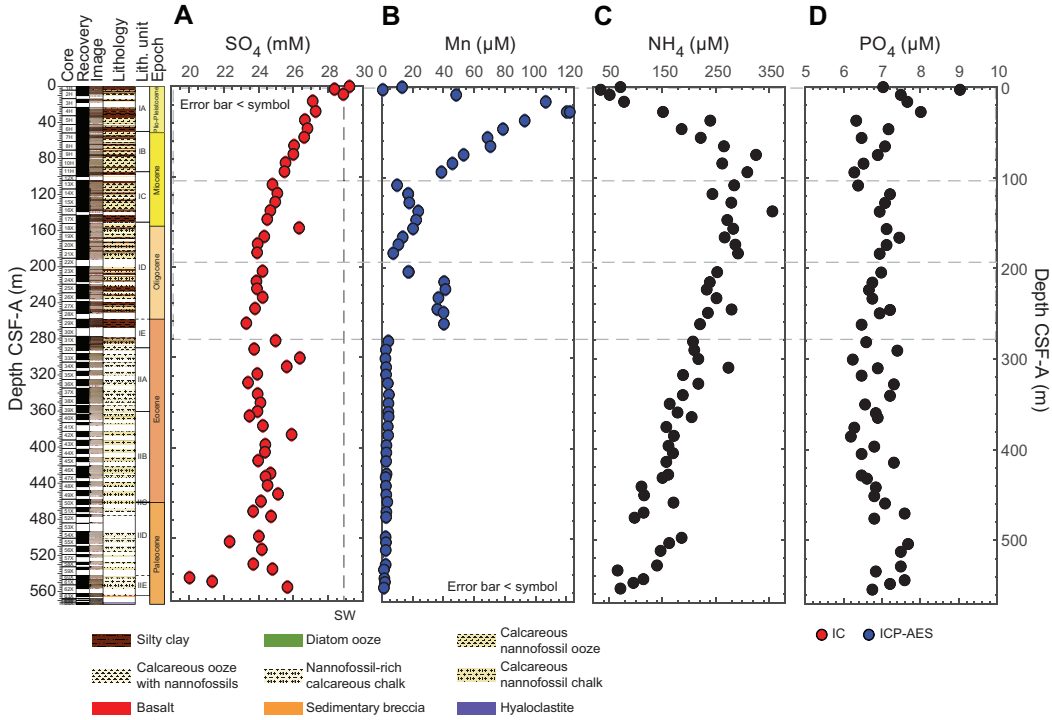

Figure F98. IW profiles of (A) sulfate, (B) manganese, (C) ammonium, and (D) phosphate, Site U1557. Dashed rectangles = intervals where increases in dissolved Mn concentrations are observed. Seawater (SW) reference value corresponds to IAPSO standard composition.

11.1.3.3. Total nitrogen

Total nitrogen (TN) content was measured concurrently with the TC analyses for each sample (Table **T19**). TN concentrations are low throughout Hole U1557B (0.010 ± 0.011 wt%, ±1σ, n = 40) with a range from below the detection limit to 0.032 wt% (Table **T19**; Figure **F99C**). Although low, the concentration of TN in Unit I (0.013 ± 0.011 wt%, ±1σ, n = 25) is an order of magnitude higher than the average concentration in Unit II (0.002 ± 0.006 wt%, ±1σ, n = 15). The trend of generally higher TN in Unit I is antithetic to the pattern of higher TOC in Unit II (Figure **F100**). If organic matter in the sediment is derived from surface productivity, then the relative proportions of TOC and TN should approximate the Redfield ratio (where C:N = 106:12). A regression between TOC and TN would then result in a positive relationship that intersects the origin (Figure **F100**) (Schubert and Calvert, 2001). Postexpedition research will confirm this deviation from the Redfield ratio and explore possible mechanisms.

11.1.4. Sediment gas sampling

Routine safety hydrocarbon measurements were made in Hole U1557B during Expedition 390C (Estes et al., 2021) at a sampling resolution of one analysis per core from Cores 390C-U1557B-1H through 63X (Table **T19**). No gas was detected in any of the samples.

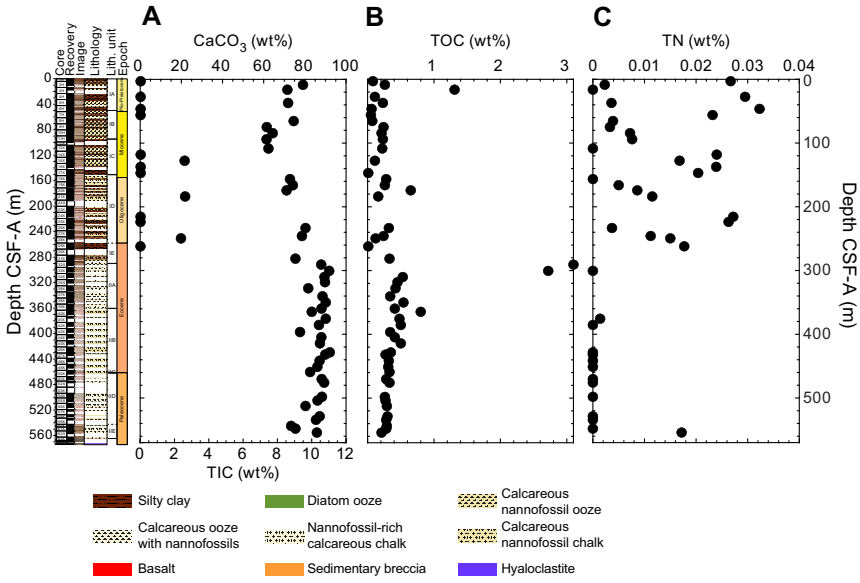

Figure F99. Sediment (A) calcium carbonate and TIC, (B) TOC, and (C) TN, Site U1557.

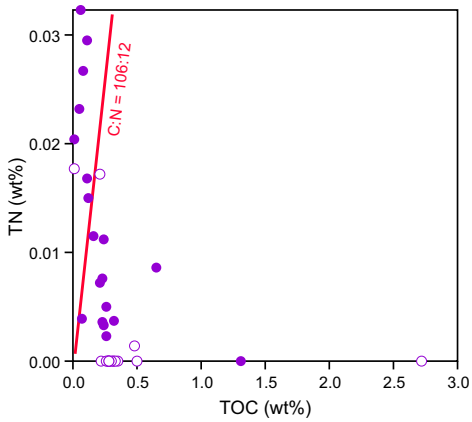

Figure F100. TOC vs. TN, Site U1557. Solid symbols = Unit I, open symbols = Unit II, red line = Redfield ratio (where C:N = 106:12).

11.2. Basement

11.2.1. Sampling strategy and sample classification

A 109 m basement succession was cored in Hole U1557D during Expedition 390. Representative samples were taken from the least altered basaltic clasts in the sedimentary breccia in an attempt to obtain a downhole record of compositional variations. Clast lithology includes aphyric, plagioclase-olivine sparsely to moderately phyric, and microcrystalline basalts (see **Igneous petrology**). The least altered basalt samples were targeted for sampling where possible, although basaltic clasts from breccias in Hole U1557D have all experienced significant and variable degrees of alteration (see **Alteration petrology**). The sample set was supplemented with basalt samples that exhibited different styles of alteration to investigate the effects of alteration on elemental concentrations. One basalt sample was also taken from the Hole U1557B sediment/basement interface, cored during Expedition 390C and sampled on the ship during Expedition 390 (see **Background and objectives**).

Because the sampled basalts experienced variable degrees of alteration, they were categorized as follows for simplicity in this chapter (see **Alteration petrology**):

- Slightly altered basalt: minimal phenocryst and groundmass alteration (i.e., typically <10% of the rock).
- Moderately altered basalt: macroscopic phenocryst and groundmass alteration (i.e., typically 10%–50% of the rock).
- Highly altered basalt: significant macroscopic phenocryst and groundmass alteration (i.e., typically >50% of the rock).

The 21 samples selected include 1 slightly altered basalt, 16 moderately altered basalts, and 4 highly altered basalts, including 1 sample pair taken from different portions of a single basaltic clast in the breccia that display different styles or extents of alteration to investigate alteration effects on the bulk rock composition (Samples 390-U1557D-3R-2, 56.5–58.5 and 58.5–61 cm) (Figure **F101**). Rocks with thin fresh glassy margins that preserve primary magma compositions and samples of distinct alteration domains will be analyzed postexpedition.

Loss on ignition (LOI) was first determined on the selected samples by ignition at 1025°C for 4 h, and concentrations of major (SiO_2, TiO_2, Al_2O_3, Fe_2O_3, MnO, MgO, CaO, Na_2O, K_2O, and P_2O_5) and minor/trace (Ba, Co, Cr, Cu, Ni, Sc, Sr, V, Zn, and Zr) elements were then measured on the ignited samples using ICP-AES (see **Geochemistry** in the Expedition 390/393 methods chapter [Coggon et al., 2024c]). Results are reported on a volatile-free basis as weight percent for major

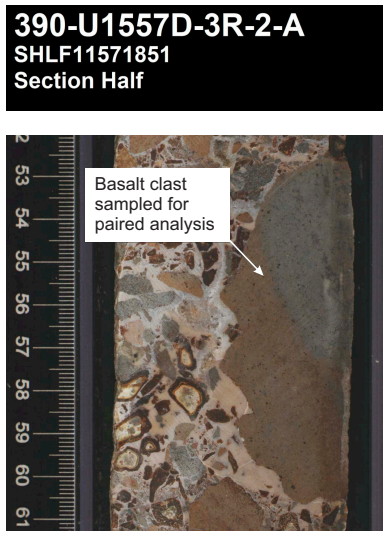

Figure F101. Core photograph of Hole U1557D basalt clast selected to examine impacts of differing styles or alteration extent on bulk rock composition. Paired samples were taken from intervals 3R-2, 56.5–58.5 and 58.5–61 cm.

element oxides and LOI and as parts per million for minor/trace elements in Table **T20**. Major oxide analyses were not normalized to 100%.

11.2.2. Lava geochemistry

11.2.2.1. Variations with depth

Figure **F102** summarizes the major element variations for the rocks from Site U1557 as a function of depth. The data are predominantly from Hole U1557D, but one sample was analyzed from Hole U1557B. This sample is included for completeness, plotting at the top of each graph. For simplicity, when discussing the data we will refer to a single hole (i.e., Hole U1557D), but the sample from Hole U1557B is included throughout unless otherwise stipulated. For comparison, the compositional range for N-MORB, depleted MORB (D-MORB), E-MORB, and mean MORB from Gale et al. (2013) is shown as a gray bar. As explained in **Basement** in Geochemistry in the Site U1556 chapter (Coggon et al., 2024a), this means the gray bar is of variable width, reflecting the compositional variation that is observed among these different MORB groups. The gray bar shown for LOI represents the estimated H_2O content following the recommendation of Langmuir et al. (2006)

Table T20. Major and minor/trace elements and LOI, , Holes U1557A and U1557B. **Download table in CSV format.**

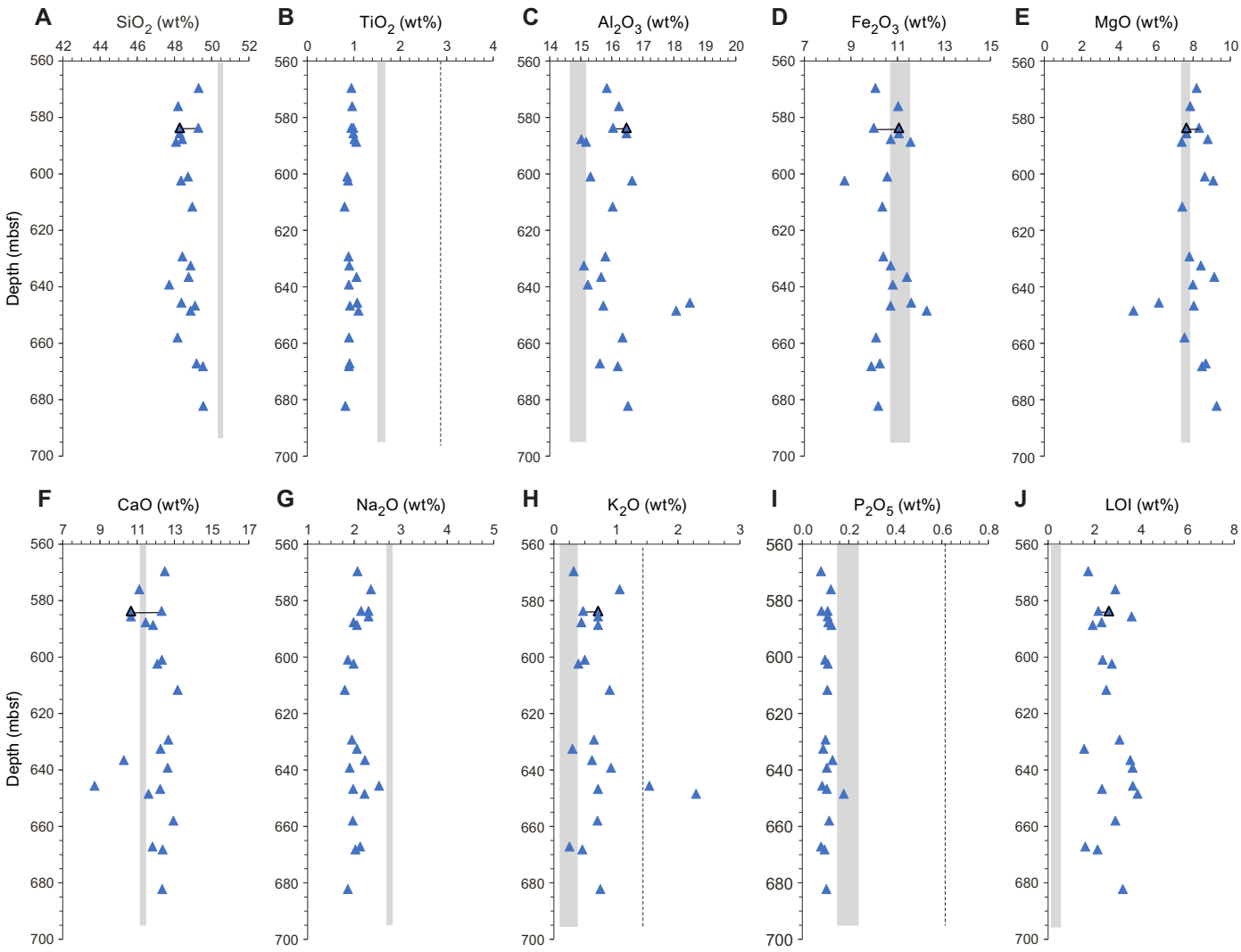

Figure F102. A–J. Major element concentrations and LOI of representative Hole U1557D basalt samples. Paired samples from basalt clast chosen to investigate alteration effects on elemental concentrations are connected by black tie lines; more altered sample of pair is indicated by black outline. Gray bars span range of N-MORB, D-MORB, E-MORB, and mean MORB from Gale et al. (2013). Dashed lines = OIB composition (Sun and McDonough, 1989).

(i.e., H_2O_{est} = 1.5 × K_2O; it does not account for CO_2). Also shown for comparison is the average composition for ocean-island basalt (OIB; black dashed lines) from Sun and McDonough (1989).

Figure **F102** shows the limited major element variation in basement rocks from the top to the bottom of Hole U1557D. The basalt clasts are compositionally similar to Stratigraphic Sequence C (H-POPP) from Site U1556 (Figure **F147** in the Site U1556 chapter [Coggon et al., 2024a]), plotting close to the range of average MORBs but not overlapping the range for D-MORB, N-MORB, E-MORB, and mean MORB for most elements. Unlike the shallower lavas at Site U1556, none of the Site U1557 samples have compositions consistent with OIB (see **Basement** in Geochemistry in the Site U1556 chapter [Coggon et al., 2024a]).

Instead, the Hole U1557D samples are depleted in incompatible elements such as TiO_2, Na_2O, and P_2O_5 (i.e., lower than average MORBs) and enriched in Al_2O_3, MgO, and CaO (i.e., higher than average MORBs). Two samples (390-U1557D-10R-6, 138–140 cm, and 11R-2, 121–123 cm) deviate from the main group, exhibiting significantly higher Al_2O_3 and K_2O but lower MgO and CaO. These two samples are described as completely altered based on thin section petrography (see Site U1557 thin sections in **Core descriptions**), suggesting that their compositional distinctiveness reflects hydrothermal alteration processes and not primary magmatic differences.

Trace elements also show limited systematic variation with depth (Figure **F103**) and reinforce the observation based on major elements that the rocks are depleted relative to average MORB com-

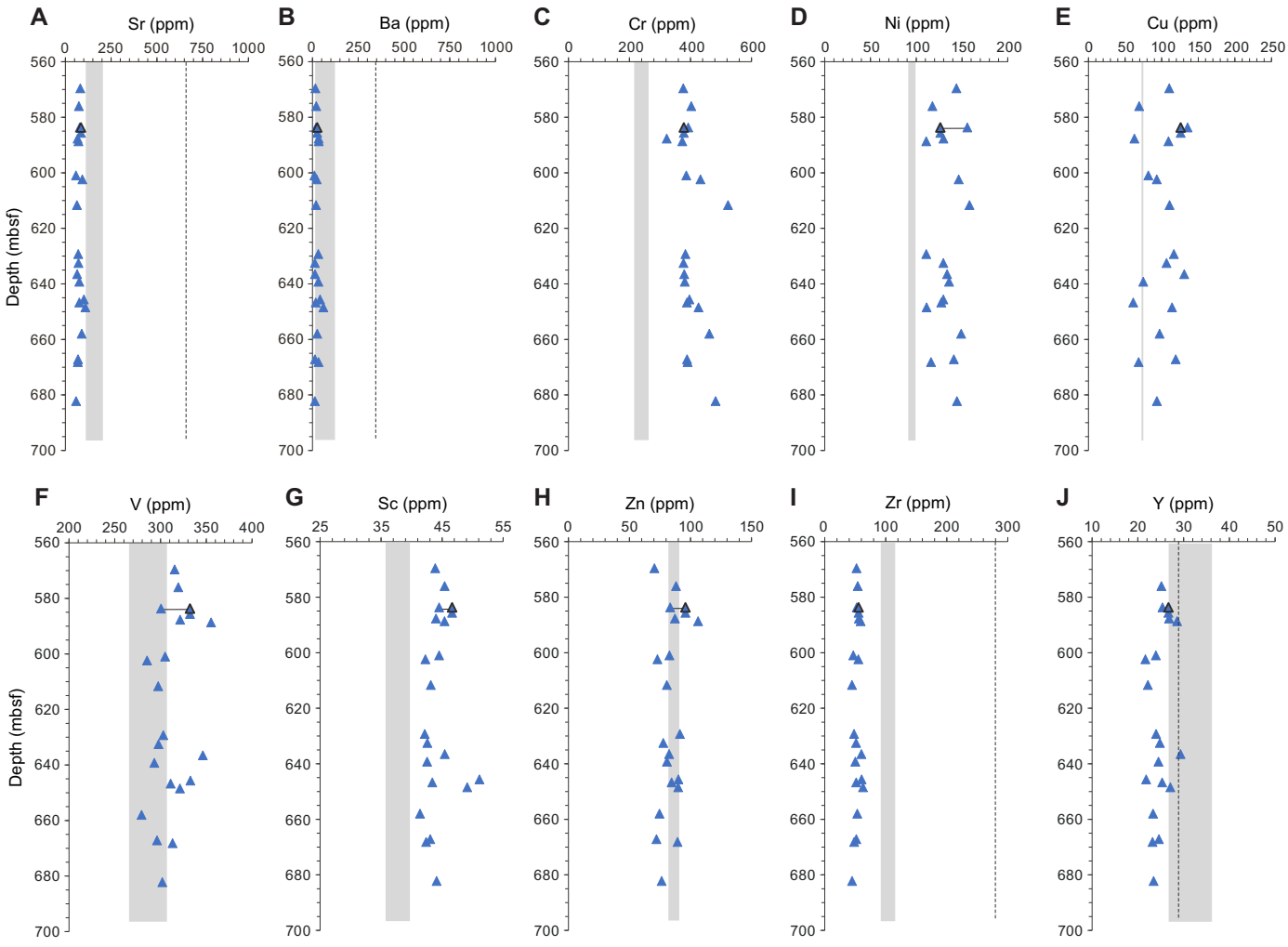

Figure F103. A–J. Trace element concentrations of representative Hole U1557D basalts. Paired samples from basalt clast chosen to investigate alteration effects on elemental concentrations are shown connected by black tie lines; more altered sample of pair is indicated by black outline. Gray bars span range of N-MORB, D-MORB, E-MORB, and mean MORB from Gale et al. (2013). Dashed lines = OIB composition (Sun and McDonough, 1989).

positions. In common with H-POPP basalts from Site U1556 (Stratigraphic Sequence C; Figure **F148** in the Site U1556 chapter [Coggon et al., 2024a]), incompatible trace element concentrations (e.g., Zr and Y) are even lower than average D-MORB, whereas compatible trace element concentrations (e.g., Cr and Ni) are higher than average D-MORB (i.e., the lower and upper boundaries of each gray bar in Figure **F103**). The transition metals Cu, V, and Sc show variable behavior, and concentrations are predominantly higher than the range of average MORB groups (Figure **F103**); only Zn predominantly overlaps the range of average MORBs.

11.2.2.2. Paired analyses of basalt clasts with variable alteration

Two different portions of a single basalt clast that exhibits differing styles and/or extents of alteration were analyzed to examine the effect of alteration on bulk rock composition. These paired samples are from Samples 390-U1557D-3R-2, 56–59 and 3R-2, 59–61 cm (Figure **F101**). Based on macroscopic observation, Sample 3R-2, 59–61 cm, is from an orange halo (see **Alteration petrology**) and is inferred to be more altered than Sample 3R-2, 56–59 cm. Where the compositional difference between the paired samples is large enough to be seen on the downhole plots (Figures **F102**, **F103**), the two analyses are linked by a tie line and the more altered sample is outlined by a thick black line. The figures show that for many elements the compositional differences between the two samples are relatively small and within the size of the symbols used. Nonetheless, SiO_2, MgO, and CaO are noticeably lower in the more altered portions of the basalt clast and Al_2O_3, Fe_2O_3, Sr, and LOI are higher. Transition metals (V, Sc, Cu, and Zn) and high-field-strength elements (HFSE) (Zr and Y) are largely indistinguishable. The alkali elements Na_2O and K_2O have higher concentrations in the more altered sample. These variations are consistent with those expressed even more strongly by the two completely altered samples described above (i.e., Samples 10R-6, 138–140 cm, and 11R-2, 121–123 cm). They are also consistent with those observed for the paired samples analyzed from Site U1556 (see **Basement** in Geochemistry in the Site U1556 chapter [Coggon et al., 2024a]).

As noted for samples from Site U1556, the geochemical data indicate that as a result of hydrothermal and/or seafloor alteration basalt samples from Hole U1557D will appear to be more evolved (i.e., lower MgO and higher Fe_2O_3), more alkaline (i.e., lower SiO_2 and generally higher K_2O), and possibly more enriched in some trace elements than their original compositions, necessitating care when interpreting primary petrology.

11.2.2.3. Classification

The sampled basalt clasts from Site U1557 are plotted on a total alkalis versus silica (TAS) diagram in Figure **F104A**. The data show a distribution that ranges from alkaline to subalkaline, although

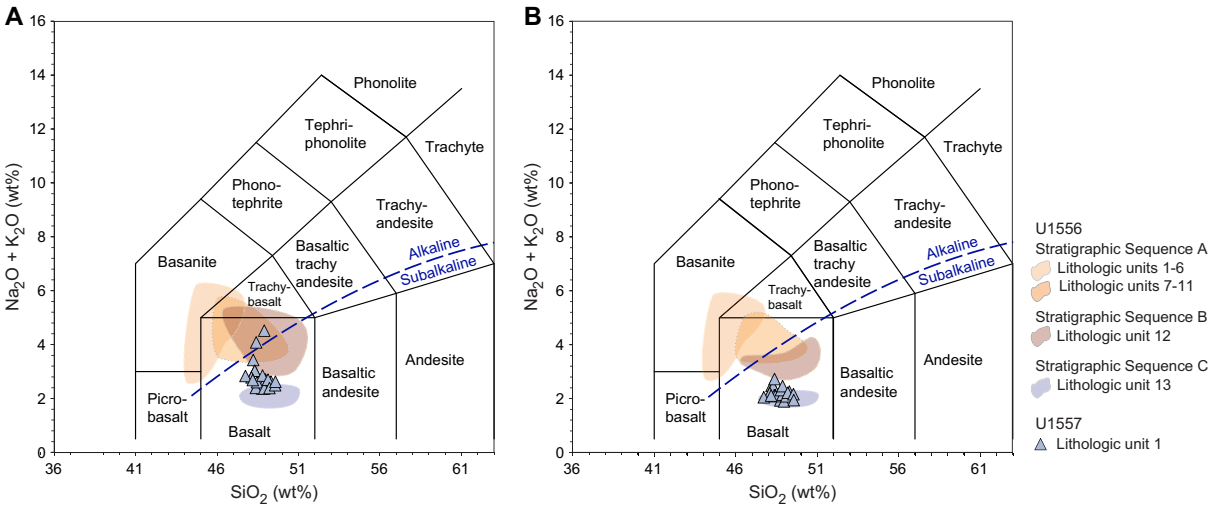

Figure F104. TAS diagram, Hole U1557D lavas. Classification is from Le Maitre et al. (2002). A. Uncorrected. B. K_2O concentration has been corrected (designated K_2O^*) to remove secondary alteration by extrapolating between adjacent elements Ba and Sr from Figure F105. Dashed line = alkaline/subalkaline rock series division (Miyashiro, 1978). Data are shown relative to fields for Stratigraphic Sequences A, B, and C from Site U1556 (Figure F150 in the Site U1556 chapter [Coggon et al., 2024a]).

most samples plot in the subalkaline basalt field. Hole U1557D basalts overlap the field for Hole U1556B Stratigraphic Sequence C (H-POPP), but most exhibit higher $Na_2O + K_2O$ than the rocks from the bottom of Hole U1556B.

Like the basalts from Site U1556, LOI values are high throughout (1.6–3.9 wt%) (Table **T20**). Such high LOI values indicate significant degrees of alteration, particularly for subalkaline basalts. As explained in **Basement** in Geochemistry in the Site U1556 chapter (Coggon et al., 2024a), Gale et al. (2013) estimate that mean MORB has H_2O content of only ~0.24 wt%, which is more than an order of magnitude lower than the average for basalts from Site U1557.

The alkali elements are particularly susceptible to hydrothermal alteration, as highlighted in a mean MORB–normalized multielement plot (Figure **F105**). The figure shows that the average concentration of K_2O in Hole U1557D basalts is nearly 4 times that of H-POPP (Stratigraphic Sequence C from Site U1556) and nearly 5 times that of mean MORB. More importantly, it is more than an order of magnitude higher than predicted by the shape of the multielement pattern (i.e., the concentration predicted by projection of the slope of the fluid-immobile trace elements Zr, Ti, and Y that occur to the right of K in the multielement diagram; red dotted line).

Using the same approach as that described for Site U1556 basalts, we used the pattern of the multielement plot to apply a correction to the K_2O concentration. As noted previously, this approach rests on the assumption that adjacent elements (Ba and Sr) are not affected by alteration. Figure **F106** shows Sr, K_2O, and Ba concentrations versus silica saturation index (SSI) relative to fields for basalts from Site U1556. A description of the SSI value and how it is calculated is provided in **Basement** in Geochemistry in the Site U1556 chapter (Coggon et al., 2024a). In common with H-POPP basalts, the basalts from Site U1557 show limited variation in Sr and Ba concentration, but the corresponding SSI values show a much wider range. Indeed, one sample from Site U1557 has an SSI value <1, plotting in the alkaline basalt field. This sample (390-U1557D-11R-2, 121–123 cm) is one of the completely altered basalts flagged in Figures **F102** and **F103**. In contrast to the limited compositional variation shown by Sr and Ba, K_2O shows a wide range of values (Figure **F106B**), and the sample with the lowest SSI value (11R-2, 121–123 cm) also has the highest K_2O content. This suggests that the higher degree of alteration, particularly enrichment in K_2O, has a greater impact on the calculated SSI value for Site U1557 basalts than seen for the Site U1556 basalts.

However, the limited ranges in Ba and Sr concentrations (Figure **F106A, F106C**) suggest that these elements are either largely unaffected by alteration or they have been altered to the same degree for all basalt clasts at Site U1557, regardless of style of alteration. We think the latter is

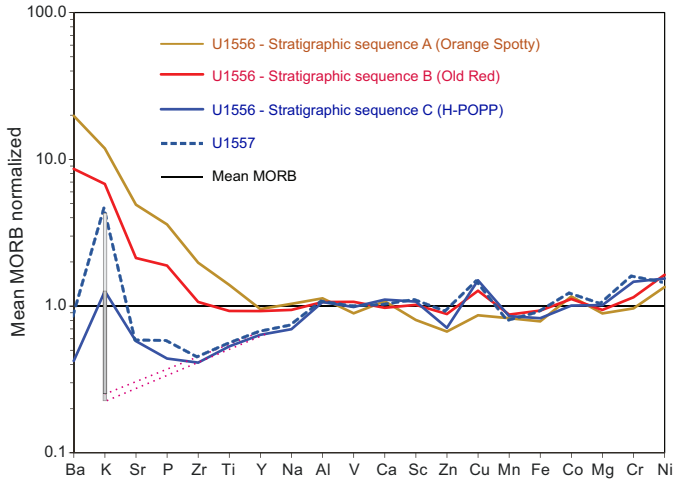

Figure F105. Mean MORB–normalized incompatible trace element diagram for average composition of Site U1557 basalt clasts. Data are shown relative to average compositions for Stratigraphic Sequences A, B, and C from Site U1556. Stratigraphic Sequence A average excludes interval of mixed lithologies (Units 7–11). Normalizing values from Gale et al. (2013). See text for discussion.

unlikely given the wide variation in K_2O (Figure **F106B**), so for this exercise we assume that their concentrations can be used to at least partially correct for the K_2O added during alteration (Figure **F105**).

Figure **F104B** shows the distribution of data in the TAS diagram using the corrected K_2O contents compared to the fields for corrected data for Stratigraphic Sequences A–C from Site U1556. After correction, all basalts from Site U1557 plot within the subalkaline field and most overlap the field for H-POPP (Stratigraphic Sequence C in Hole U1556B). Prior to correction of the K_2O values, classification implied that the lavas at Site U1557 ranged from alkaline to subalkaline, which has significant implications for understanding source composition and degree of partial melting. After K_2O correction, all samples plot within the subalkaline field, consistent with a normal MORB-type composition throughout the section.

11.2.2.4. Comparison of basalts from Sites U1557 and U1556

Figure **F105** summarizes average compositions for the basalts from Site U1557 relative to the three stratigraphic sequences from Site U1556 on an extended multielement plot, normalized to mean MORB composition of Gale et al. (2013). A first-order observation from this diagram is that the basalts from Site U1557 are similar to H-POPP basalts (Stratigraphic Sequence C in Hole U1556B) and show N-MORB-like compositions for most elements to the right of Na (i.e., concentrations plot near a mean MORB–normalized value of 1) with some variation in the transition metals (Zn, Cu, Mn, and Fe) and elevated concentrations of compatible elements Cr and Ni. However, the most incompatible elements (Ba to Y) show distinct depletion relative to mean MORB except for K. The latter shows a strong positive anomaly relative to adjacent LILEs due to hydrothermal alteration, as discussed above. Collectively, the data for Site U1557 basalts suggest they were derived from a mantle source that was significantly more depleted than normal MORB, indeed, more depleted even than D-MORB (Figures **F101**, **F102**), but they have been secondarily enriched in (some) LIL elements, particularly K, by hydrothermal alteration. The ratio of V/Sc,

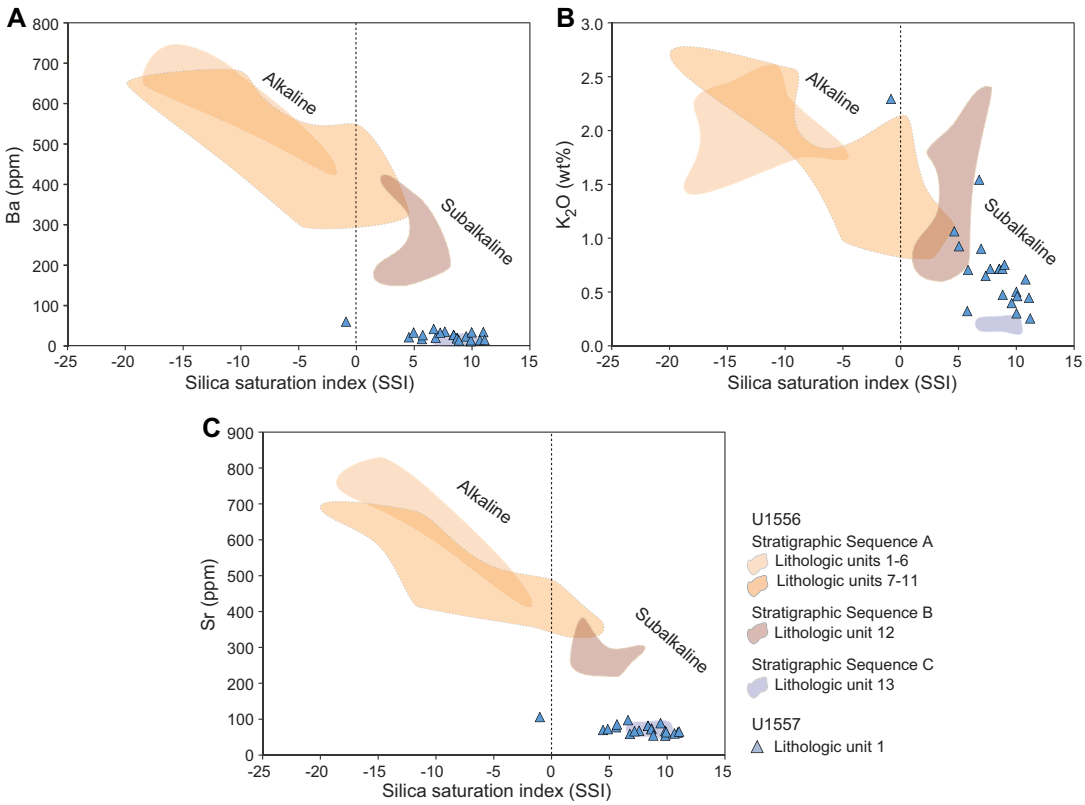

Figure F106. SSI vs. (A) Ba, (B) K_2O, and (C) Sr. Data for Site U1557 are shown relative to fields for Stratigraphic Sequences A, B, and C (see Figure F152 in the Site U1556 chapter [Coggon et al., 2024a]). SSI is calculated following equation in Gill and Fitton (2022).

often cited as a sensitive recorder of the oxygen fugacity of MORB-source mantle, averages ~7 for Site U1557 basalts, similar to H-POPP basalts (Stratigraphic Sequence C) from Site U1556, which is within the range for average MORB (6.74 ± 1.11) (Li and Lee, 2004), melting in the spinel lherzolite stability field at slightly below quartz-magnetite-fayalite (Mallmann and O'Neill, 2009). However, other transition metals (i.e., Zn and Cu) show unusual negative and positive anomalies, respectively. These variations are interesting because the differences among D-MORB, N-MORB, and mean MORB averages (Gale et al., 2013) are <3 ppm for both elements, whereas Site U1557 basalts are up to 7 ppm lower and 248 ppm higher in Zn and Cu, respectively, relative to mean MORB. This suggests the variations observed in Site U1557 basalts are due to something other than typical MORB-source melting or magma chamber processes. Whether this is due to secondary alteration processes, unusual source conditions, or possibly analytical uncertainty in the shipboard data will require detailed shore-based research.

Given that all Hole U1557D samples are hydrothermally altered, some significantly so as indicated by their high LOI and K_2O contents, we rely on ratios of HFSEs to provide insights into magmatic compositional variations because these ratios are not strongly affected by fractional crystallization or alteration (e.g., Gill and Fitton, 2022). In this context we note that the Zr/TiO_2 ratio (parts per million/weight percent) for paired basalt samples from both Holes U1556B (see Table **T31** in the Site U1556 chapter [Coggon et al., 2024a]) and U1557D (Table **T20**) are similar, regardless of the degree of alteration, suggesting this ratio reflects the primary magmatic compositions of the basalts.

The Zr/TiO_2 ratios of basalt clasts from Site U1557 are summarized graphically in Figure **F107**. The data show limited variation in this ratio from the top to the bottom of the hole (56 ± 2 ppm/wt% on average). Unlike the variations in Zr and TiO_2 systematics on the basis of pXRF analyses of core archive-half surfaces reported in **Igneous petrology**, which suggest mobility of Ti in some samples, we do not see comparable mobility for the samples analyzed by ICP-AES. This may be due to our focus on fresher sample material or that a larger volume of rock is homogenized for ICP-AES analysis. Regardless, the limited variation provides confidence that the Zr/TiO_2 ratios are representative of the original igneous compositions. The Site U1557 basalt average is slightly higher than that for Hole U1556B Stratigraphic Sequence C (H-POPP; 54 ± 0.6 ppm/wt%). It is similar to the N-MORB composition of Sun and McDonough (1989) (i.e., 58 ppm/wt%) but lower than mean MORB of Gale et al. (2013) (70 ppm/wt%). Of the average values reported by Gale et al.

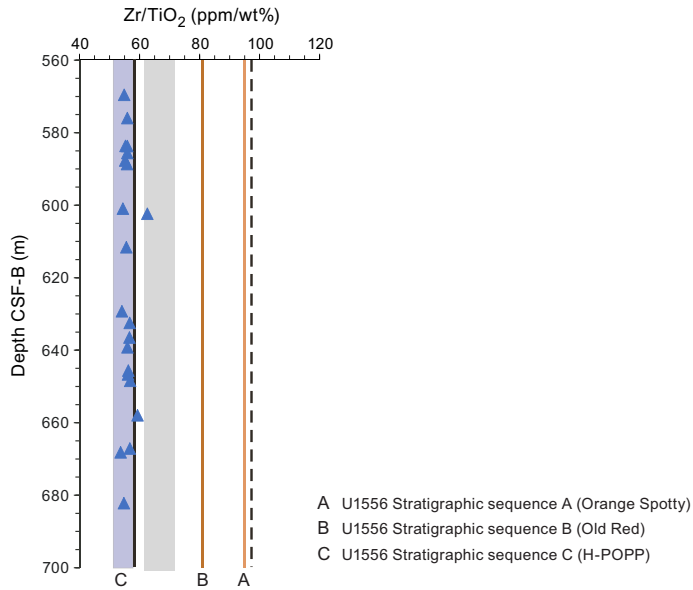

Figure F107. Zr/TiO_2 ratios for representative Hole U1557D basalt samples shown relative to range of Zr/TiO_2 values for Site U1556 Stratigraphic Sequence C and average values for Site U1556 Stratigraphic Sequences A and B. Average value for Stratigraphic Sequence A excludes mixed lithology interval (Units 7–11). Gray bar spans range of N-MORB, D-MORB, E-MORB, and mean MORB from Gale et al. (2013). Dashed line = OIB composition (Sun and McDonough, 1989).

(2013), the Site U1557 basalts are most similar to average D-MORB (i.e., 61 ppm/wt%). The data indicate the Hole U1557D talus pile reflects a stratigraphic sequence of lavas that sampled a relatively homogeneous D-MORB-like mantle source throughout.

12. Microbiology

Microbiology sampling in basement at Site U1557 during Expedition 390 focused on exploring evidence for life using culture-based and culture-independent approaches. For Hole U1557D, sampling efforts aimed at collecting a single whole-round core sample from each 9.5 m advance that would be processed and subsampled for different analyses. The number of subsamples able to be processed for each analysis type depended on the amount of material available from each parent sample (Table **T21**). The aim was to generate a suite of samples that were representative of the different rock and alteration types that comprise the basement stratigraphy of the site (see **Igneous petrology**). In total, 12 whole-round samples (8–15 cm long) were collected for microbiological analysis (Figure **F108**). All of the samples were sedimentary breccia containing clasts of hydrothermally altered basalt and volcanic glass.

12.1. Microbiological sample processing and experiments

12.1.1. Cell counts

A total of 12 samples were processed for cell enumeration. Performing shipboard cell counts on rock samples is difficult and time consuming; therefore, shipboard cell counts were not attempted during Expeditions 390 and 393. Cell count samples were instead broken into small chips and/or powder and preserved for postexpedition analysis in a 20% vol/vol slurry in 5 mL total of rock and 5% Epredia Formal-Fixx in 3× phosphate-buffered solution.

12.1.2. Microbial community structure

A total of 12 samples were preserved for shore-based DNA (polymerase chain reaction [PCR] amplicon-based and metagenomes) and/or RNA (PCR amplicon-based and/or metatranscriptomes) analysis, 8 samples were preserved for single cell genomics, and 7 samples were collected for lipid analysis (Table **T21**). Material for DNA, RNA, and lipid-based analyses of microbial community composition was collected and preserved following the procedures described in **Microbiology** in the Expedition 390/393 methods chapter (Coggon et al., 2024c).

12.1.3. Microbial incubation experiments

To attempt to isolate new microbial species that can be characterized and used in future laboratory-based experiments, isolation experiments using enrichment media in Petri dishes were initiated. Samples 390-U1557D-5R-5, 37.5–48.5 cm, and 7R-3, 0–9.5 cm, were used to initiate enrichment experiments on 1/10 ZoBell Marine Agar media (Table **T21**). This media selects for heterotrophic marine microorganisms and is commonly used to isolate new microorganisms. These culturing experiments were prepared as described in **Microbiology** in the Expedition 390/393 methods chapter (Coggon et al., 2024c), incubated at 9.5°C with the tops facing down for the duration of Expedition 390, and then shipped to shore for postexpedition research.

To detect the metabolically active microbes in basaltic basement, Samples 390-U1557D-6R-3, 39–49 cm, and 8R-3, 52–63 cm, were used to initiate stable isotope probing (SIP) experiments (Table **T21**). Similar methods were used to reveal the presence of active microorganisms in sediments as old as 101.5 Ma during Integrated Ocean Drilling Program Expedition 329 to the South Pacific Gyre (Morono et al., 2020). The aim is to determine whether microbial cells are active in the basement at Site U1557, determine growth rate, and quantify how many cells take up C and N substrates. These SIP experiments were conducted according to the procedure outlined in **Microbiology** in the Expedition 390/393 methods chapter (Coggon et al., 2024c). Samples were incubated at 10°C until shipment to shore at the end of Expedition 390. Individual experimental vials will be killed at three time points (2, 3, and 6 months) prior to analysis.

Table T21. Microbiology whole rounds and subsamples, Hole U1557D. **Download table in CSV format.**

12.2. Microbiological contamination monitoring

Perfluoromethyldecalin (PFMD) tracer was not run during coring at Site U1557 because of insufficient volume of PFMD available for use at all sites during Expeditions 390 and 393. We chose to forego running tracer specifically at Site U1557 because we expected to recover material similar to what was found at nearby Site U1556 (Figure **F108**). Although all cores recovered from Hole U1557D comprised sedimentary talus breccia, which is different in regard to total hole composition compared to Hole U1556B, the breccia recovered from Hole U1557D was comparable to that recovered from Hole U1556B and therefore still allows for comparison of trends of contamination in similar lithology across the two holes. Likewise, core pieces with obvious open porosity (centimeter scale) through which drilling fluid would have infiltrated were not sampled for microbiology.

Sample	Top depth CSF-B (mbsf)	Lithostratigraphic unit and lithology	Color of basalt	Photo
390-U1557D-2R2, 0-12 cm	576.88	Unit 1: Sedimentary breccia, supported with basaltic clasts that are highly to completely altered.	Gray to brown	
390-U1557D-4R4, 136.5-148 cm	593.02	Unit 1: Sedimentary breccia, supported with basaltic clasts that are highly to completely altered.	Dark gray to yellowish brown to strong brown	
390-U1557D-5R5, 37.5-48.5 cm	603.13	Unit 1: Sedimentary breccia, supported with basaltic clasts that are highly to completely altered	Dark gray to yellowish brown to strong brown	
390-U1557D-6R3, 39-49 cm	609.55	Unit 1: Sedimentary breccia, supported with basaltic clasts that are highly to completely altered	Gray to yellowish brown to strong brown	
390-U1557D-7R2, 136-144 cm	619.3	Unit 1: Sedimentary breccia, supported with basaltic clasts that are highly to completely altered	Yellowish brown to strong brown	
390-U1557D-7R3, 0-9.5 cm	619.38	Unit 1: Sedimentary breccia, supported with basaltic clasts that are highly to completely altered	Yellowish brown to strong brown	

Figure F108. Samples collected for shore-based microbiology research, Hole U1557D. (Continued on next page.)

To determine the number of microorganisms present in drilling fluid and also generate a database of potential contaminants, we collected drilling fluid from a pipe on the rig floor three times during coring operations in Hole U1557D: during coring of Core 390-U1557D-2R (586 mbsf), during coring of Core 11R (645 mbsf), and during coring of Core 14R (676 mbsf). Samples were preserved for cell counts, and an additional 500 mL of drilling fluid was filtered onto two separate 0.20 µm pore size, 47 mm diameter filters and frozen at –80°C for shore-based molecular biology analysis to determine the microorganisms present in drilling fluid.

Sample	Top depth CSF-B (mbsf)	Lithostratigraphic unit and lithology	Color of basalt	Photo
390-U1557D-8R3, 52-63 cm	629.38	Unit 1: Sedimentary breccia, supported with basaltic clasts that are highly to completely altered	Gray to grayish brown to strong brown	
390-U1557D-10R2, 14.5-29.5 cm	638.83	Unit 1: Sedimentary breccia with abundant palagonite	Green	
390-U1557D-11R1, 131-144 cm	647.11	Unit 1: Sedimentary breccia with basaltic clasts that are highly to completely altered	Gray to yellow brown to grayish brown	
390-U1557D-12R9, 53.5-67 cm	664.43	Unit 1: Sedimentary breccia with basaltic clasts that are highly to completely altered	Gray to brown	
390-U1557D-13R2, 7.5-19.5 cm	666.97	Unit 1: Sedimentary breccia with abundant palagonite. Basalt clasts are highly altered.	Green	
390-U1557D-14R5, 42-57 cm	681.15	Unit 1: Sedimentary breccia supported with basaltic clasts	Gray to brown to brownish yellow	

Figure F108 (continued).

References

Agnini, C., Fornaciari, E., Raffi, I., Catanzariti, R., Pälike, H., Backman, J., and Rio, D., 2014. Biozonation and biochronology of Paleogene calcareous nannofossils from low and middle latitudes. Newsletters on Stratigraphy, 47(2):131–181. **https://doi.org/10.1127/0078-0421/2014/0042**

Alt, J.C., 1995. Subseafloor processes in mid-ocean ridge hydrothermal systems. In Humphris, S.E., Zierenberg, R.A., Mullineaux, L.S., and Thomson, R.E. (Eds.), Seafloor Hydrothermal Systems: Physical, Chemical, Biological, and Geological Interactions. Geophysical Monograph, 91: 85–114. **https://doi.org/10.1029/GM091p0085**

Backman, J., Raffi, I., Rio, D., Fornaciari, E., and Pälike, H., 2012. Biozonation and biochronology of Miocene through Pleistocene calcareous nannofossils from low and middle latitudes. Newsletters on Stratigraphy, 45(3):221–244. **https://doi.org/10.1127/0078-0421/2012/0022**

Baker, P.A., Gieskes, J.M., and Elderfield, H., 1982. Diagenesis of carbonates in deep-sea sediments; evidence from Sr/Ca ratios and interstitial dissolved Sr^{2+} data. Journal of Sedimentary Research, 52(1):71–82. **https://doi.org/10.1306/212F7EE1-2B24-11D7-8648000102C1865D**

Bartetzko, A., Pezard, P., Goldberg, D., Sun, Y.-F., and Becker, K., 2001. Volcanic stratigraphy of DSDP/ODP Hole 395A: An interpretation using well-logging data. Marine Geophysical Researches, 22(2):111–127. **https://doi.org/10.1023/A:1010359128574**

Boyer, T.P., García, H.E., Locarnini, R.A., Zweng, M.M., Mishonov, A.V., Reagan, J.R., Weathers, K.A., Baranova, O.K., Paver, C.R., Seidov, D., and Smolyar, I.V., 2018. World Ocean Atlas 2018. NOAA National Centers for Environmental Information. **https://www.ncei.noaa.gov/archive/accession/NCEI-WOA18**

Butler, R.F., 1992. Paleomagnetism: Magnetic Domains to Geologic Terranes: Boston (Blackwell Science Publishing). **https://www.geo.arizona.edu/Paleomag/**

Christeson, G., and Reece, R., 2020. Bathymetric site survey gridded data in support of IODP Expeditions 390 and 393, South Atlantic Transect (MGL1601, CREST). Interdisciplinary Earth Data Alliance (IEDA). **https://doi.org/10.26022/IEDA/327528**

Christeson, G.L., Goff, J.A., and Reece, R.S., 2019. Synthesis of oceanic crustal structure from two-dimensional seismic profiles. Reviews of Geophysics, 57(2):504–529. **https://doi.org/10.1029/2019RG000641**

Christeson, G.L., Reece, R.S., Kardell, D.A., Estep, J.D., Fedotova, A., and Goff, J.A., 2020. South Atlantic transect: variations in oceanic crustal structure at 31°S. Geochemistry, Geophysics, Geosystems, 21(7):e2020GC009017. **https://doi.org/10.1029/2020GC009017**

Coggon, R.M., Sylvan, J.B., Teagle, D.A.H., Reece J., Christeson, G.L., Estes, E.R., Williams, T.J., and the Expedition 390 Scientists, 2022a. Expedition 390 Preliminary Report: South Atlantic Transect 1. International Ocean Discovery Program. **https://doi.org/10.14379/iodp.pr.390.2022**

Coggon, R.M., Sylvan, J.B., Teagle, D.A.H., Reece, J.S., Christeson, G.L., Estes, E.R., and Williams, T., 2022b. Expedition 390/393 Scientific Prospectus Addendum: South Atlantic Transect. International Ocean Discovery Program. **https://doi.org/10.14379/iodp.sp.390393add.2022**

Coggon, R.M., Sylvan, J.B., Estes, E.R., Teagle, D.A.H., Reece, J., Williams, T.J., Christeson, G.L., Aizawa, M., Borrelli, C., Bridges, J.D., Carter, E.J., Dinarès-Turell, J., Estep, J.D., Gilhooly, W.P., III, Grant, L.J.C., Kaplan, M.R., Kempton, P.D., Lowery, C.M., McIntyre, A., Routledge, C.M., Slagle, A.L., Takada, M., Tamborrino, L., Wang, Y., Yang, K., Albers, E., Amadori, C., Belgrano, T.M., D'Angelo, T., Doi, N., Evans, A., Guérin, G.M., Harris, M., Hojnacki, V.M., Hong, G., Jin, X., Jonnalagadda, M., Kuwano, D., Labonte, J.M., Lam, A.R., Latas, M., Lu, W., Moal-Darrigade, P., Pekar, S.F., Robustelli Test, C., Ryan, J.G., Santiago Ramos, D., Shchepetkina, A., Villa, A., Wee, S.Y., Widlansky, S.J., Kurz, W., Prakasam, M., Tian, L., Yu, T., and Zhang, G., 2024a. Site U1556. In Coggon, R.M., Teagle, D.A.H., Sylvan, J.B., Reece, J., Estes, E.R., Williams, T.J., Christeson, G.L., and the Expedition 390/393 Scientists, South Atlantic Transect. Proceedings of the International Ocean Discovery Program, 390/393: College Station, TX (International Ocean Discovery Program). **https://doi.org/10.14379/iodp.proc.390393.103.2024**

Coggon, R.M., Sylvan, J.B., Estes, E.R., Teagle, D.A.H., Reece, J., Williams, T.J., Christeson, G.L., Aizawa, M., Borrelli, C., Bridges, J.D., Carter, E.J., Dinarès-Turell, J., Estep, J.D., Gilhooly, W.P., III, Grant, L.J.C., Kaplan, M.R., Kempton, P.D., Lowery, C.M., McIntyre, A., Routledge, C.M., Slagle, A.L., Takada, M., Tamborrino, L., Wang, Y., Yang, K., Albers, E., Amadori, C., Belgrano, T.M., D'Angelo, T., Doi, N., Evans, A., Guérin, G.M., Harris, M., Hojnacki, V.M., Hong, G., Jin, X., Jonnalagadda, M., Kuwano, D., Labonte, J.M., Lam, A.R., Latas, M., Lu, W., Moal-Darrigade, P., Pekar, S.F., Robustelli Test, C., Ryan, J.G., Santiago Ramos, D., Shchepetkina, A., Villa, A., Wee, S.Y., Widlansky, S.J., Kurz, W., Prakasam, M., Tian, L., Yu, T., and Zhang, G., 2024b. Site U1561. In Coggon, R.M., Teagle, D.A.H., Sylvan, J.B., Reece, J., Estes, E.R., Williams, T.J., Christeson, G.L., and the Expedition 390/393 Scientists, South Atlantic Transect. Proceedings of the International Ocean Discovery Program, 390/393: College Station, TX (International Ocean Discovery Program). **https://doi.org/10.14379/iodp.proc.390393.104.2024**

Coggon, R.M., Teagle, D.A.H., Sylvan, J.B., Reece, J., Estes, E.R., Williams, T.J., Christeson, G.L., Aizawa, M., Albers, E., Amadori, C., Belgrano, T.M., Borrelli, C., Bridges, J.D., Carter, E.J., D'Angelo, T., Dinarès-Turell, J., Doi, N., Estep, J.D., Evans, A., Gilhooly, W.P., III, Grant, L.J.C., Guérin, G.M., Harris, M., Hojnacki, V.M., Hong, G., Jin, X., Jonnalagadda, M., Kaplan, M.R., Kempton, P.D., Kuwano, D., Labonte, J.M., Lam, A.R., Latas, M., Lowery, C.M., Lu, W., McIntyre, A., Moal-Darrigade, P., Pekar, S.F., Robustelli Test, C., Routledge, C.M., Ryan, J.G., Santiago Ramos, D., Shchepetkina, A., Slagle, A.L., Takada, M., Tamborrino, L., Villa, A., Wang, Y., Wee, S.Y., Widlansky, S.J., Yang, K., Kurz, W., Prakasam, M., Tian, L., Yu, T., and Zhang, G., 2024c. Expedition 390/393 methods. In Coggon, R.M., Teagle, D.A.H., Sylvan, J.B., Reece, J., Estes, E.R., Williams, T.J., Christeson, G.L., and the Expedition 390/393 Scientists, South Atlantic Transect. Proceedings of the International Ocean Discovery Program, 390/393: College Station, TX (International Ocean Discovery Program). **https://doi.org/10.14379/iodp.proc.390393.102.2024**

Coggon, R.M., Teagle, D.A.H., Sylvan, J.B., Reece, J., Estes, E.R., Williams, T.J., Christeson, G.L., Aizawa, M., Albers, E., Amadori, C., Belgrano, T.M., Borrelli, C., Bridges, J.D., Carter, E.J., D'Angelo, T., Dinarès-Turell, J., Doi, N., Estep, J.D., Evans, A., Gilhooly, W.P., III, Grant, L.J.C., Guérin, G.M., Harris, M., Hojnacki, V.M., Hong, G., Jin, X., Jonnalagadda, M., Kaplan, M.R., Kempton, P.D., Kuwano, D., Labonte, J.M., Lam, A.R., Latas, M., Lowery, C.M., Lu, W., McIntyre, A., Moal-Darrigade, P., Pekar, S.F., Robustelli Test, C., Routledge, C.M., Ryan, J.G., Santiago Ramos, D., Shchepetkina, A., Slagle, A.L., Takada, M., Tamborrino, L., Villa, A., Wang, Y., Wee, S.Y., Widlansky, S.J., Yang, K., Kurz, W., Prakasam, M., Tian, L., Yu, T., and Zhang, G., 2024d. Expedition 390/393 summary. In Coggon, R.M., Teagle, D.A.H., Sylvan, J.B., Reece, J., Estes, E.R., Williams, T.J., Christeson, G.L., and the Expedition 390/393 Scientists, South Atlantic Transect. Proceedings of the International Ocean Discovery Program, 390/393: College Station, TX (International Ocean Discovery Program). **https://doi.org/10.14379/iodp.proc.390393.101.2024**

Coggon, R.M., Teagle, D.A.H., Sylvan, J.B., Reece, J., Estes, E.R., Williams, T.J., Christeson, G.L., Aizawa, M., Albers, E., Amadori, C., Belgrano, T.M., Borrelli, C., Bridges, J.D., Carter, E.J., D'Angelo, T., Dinarès-Turell, J., Doi, N., Estep, J.D., Evans, A., Gilhooly, W.P., III, Grant, L.J.C., Guérin, G.M., Harris, M., Hojnacki, V.M., Hong, G., Jin, X., Jonnalagadda, M., Kaplan, M.R., Kempton, P.D., Kuwano, D., Labonte, J.M., Lam, A.R., Latas, M., Lowery, C.M., Lu, W., McIntyre, A., Moal-Darrigade, P., Pekar, S.F., Robustelli Test, C., Routledge, C.M., Ryan, J.G., Santiago Ramos, D., Shchepetkina, A., Slagle, A.L., Takada, M., Tamborrino, L., Villa, A., Wang, Y., Wee, S.Y., Widlansky, S.J., Yang, K., Kurz, W., Prakasam, M., Tian, L., Yu, T., and Zhang, G., 2024e. Site U1559. In Coggon, R.M., Teagle, D.A.H., Sylvan, J.B., Reece, J., Estes, E.R., Williams, T.J., Christeson, G.L., and the Expedition 390/393 Scientists, South Atlantic Transect. Proceedings of the International Ocean Discovery Program, 390/393: College Station, TX (International Ocean Discovery Program). **https://doi.org/10.14379/iodp.proc.390393.109.2024**

Coggon, R.M., Teagle, D.A.H., Sylvan, J.B., Reece, J., Estes, E.R., Williams, T.J., Christeson, G.L., and the Expedition 390/393 Scientists, 2024f. Supplementary material, **https://doi.org/10.14379/iodp.proc.390393supp.2024.** In Coggon, R.M., Teagle, D.A.H., Sylvan, J.B., Reece, J., Estes, E.R., Williams, T.J., Christeson, G.L., and the Expedition 390/393 Scientists, South Atlantic Transect. Proceedings of the International Ocean Discovery Program, 390/393: College Station, TX (International Ocean Discovery Program).

Corliss, B.H., 1979. Recent deep-sea benthonic for aminiferal distributions in the southeast Indian Ocean: Inferred bottom-water routes and ecological implications. Marine Geology, 31(1):115–138. **https://doi.org/10.1016/0025-3227(79)90059-8**

Dunlea, A.G., Murray, R.W., Harris, R.N., Vasiliev, M.A., Evans, H., Spivack, A.J., and D'Hondt, S., 2013. Assessment and use of NGR instrumentation on the JOIDES Resolution to quantify U, Th, and K concentrations in marine sediment. Scientific Drilling, 15:57–63. **https://doi.org/10.2204/iodp.sd.15.05.2013**

Estep, J., Reece, R., Kardell, D.A., Christeson, G.L., and Carlson, R.L., 2019. Seismic Layer 2A: evolution and thickness from 0- to 70-Ma crust in the slow-intermediate spreading South Atlantic. Journal of Geophysical Research: Solid Earth, 124(8):7633–7651. **https://doi.org/10.1029/2019JB017302**

Estep, J., Reece, R., Kardell, D.A., Perez, N.D., Christeson, G.L., and Carlson, R.L., 2020. Intraplate deformation of oceanic crust near the Rio Grande Rise in the South Atlantic. Tectonophysics, 790:228543. **https://doi.org/10.1016/j.tecto.2020.228543**

Estes, E.R., Williams, T., Midgley, S., Coggon, R.M., Sylvan, J.B.,Christeson, G.L., Teagle, D.A.H., and the Expedition 390C Scientists, 2021. Expedition 390C Preliminary Report: South Atlantic Transect Reentry Systems. International Ocean Discovery Program. **https://doi.org/10.14379/iodp.pr.390C.2021**

Fu, D., Su, C., Wang, W., and Yuan, R., 2022. Deep learning based lithology classification of drill core images. PloS One, 17(7):e0270826. **https://doi.org/10.1371/journal.pone.0270826**

Gale, A., Dalton, C.A., Langmuir, C.H., Su, Y., and Schilling, J.-G., 2013. The mean composition of ocean ridge basalts. Geochemistry, Geophysics, Geosystems, 14(3):489–518. **https://doi.org/10.1029/2012GC004334**

Gill, R., and Fitton, G., 2022. Igneous Rocks and Processes: A Practical Guide, 2nd Edition: Chichester, UK (John Wiley & Sons, Ltd).

Gradstein, F.M., Ogg, J.G., Schmitz, M.D., and Ogg, G.M. (Eds.), 2020. The Geologic Time Scale 2020: Amsterdam (Elsevier BV). **https://doi.org/10.1016/C2020-1-02369-3**

Hesse, R., and Schacht, U., 2011. Early diagenesis of deep-sea sediments. In HüNeke, H., and Mulder, T. (Eds.), Deep-Sea Sediments. Developments in Sedimentology, 63: 557–713. **https://doi.org/10.1016/B978-0-444-53000-4.00009-3**

Holbourn, A., Henderson, A.S., and MacLeod, N., 2013. Atlas of Benthic Foraminifera: United Kingdom (John Wiley & Sons, Ltd.). **https://doi.org/10.1002/9781118452493**

Kamenetsky, V.S., Crawford, A.J., and Meffre, S., 2001. Factors controlling chemistry of magmatic spinel: an empirical study of associated olivine, Cr-spinel and melt inclusions from primitive rocks. Journal of Petrology, 42(4):655–671. **https://doi.org/10.1093/petrology/42.4.655**

Kardell, D.A., Christeson, G.L., Estep, J.D., Reece, R.S., and Carlson, R.L., 2019. Long-lasting evolution of Layer 2A in the western South Atlantic: evidence for low-temperature hydrothermal circulation in old oceanic crust. Journal of Geophysical Research: Solid Earth, 124(3):2252–2273. **https://doi.org/10.1029/2018JB016925**

Kastner, M., 1979. Zeolite minerals. In Burns, R.G. (Ed.), Marine Minerals. Reviews in Mineralogy, 6:111–112.

Kirschvink, J.L., 1980. The least-squares line and plane and the analysis of palaeomagnetic data. Geophysical Journal International, 62(3):699–718. **https://doi.org/10.1111/j.1365-246X.1980.tb02601.x**

Korenaga, T., and Korenaga, J., 2008. Subsidence of normal oceanic lithosphere, apparent thermal expansivity, and seafloor flattening. Earth and Planetary Science Letters, 268(1):41–51. **https://doi.org/10.1016/j.epsl.2007.12.022**

Kruber, C., Thorseth, I.H., and Pedersen, R.B., 2008. Seafloor alteration of basaltic glass: textures, geochemistry, and endolithic microorganisms. Geochemistry, Geophysics, Geosystems, 9(12):Q12002. **https://doi.org/10.1029/2008GC002119**

Lam, A.R., Crundwell, M.P., Leckie, R.M., Albanese, J., and Uzel, J.P., 2022. Diachroneity rules the mid-latitudes: a test case using Late Neogene planktic foraminifera across the Western Pacific. Geosciences, 12(5):190. **https://doi.org/10.3390/geosciences12050190**

Langmuir, C.H., Bézos, A., Escrig, S., and Parman, S.W., 2006. Chemical systematics and hydrous melting of the mantle in back-arc basins. In Christie, D.M., Fisher, C.R., Lee, S.-M., and Givens, S. (Eds.), Back-Arc Spreading Systems: Geological, Biological, Chemical, and Physical Interactions. Geophysical Monograph, 166: 87–146. **https://doi.org/10.1029/166GM07**

Le Maitre, R.W., Steckeisen, A., Zanettin, B., Le Bas, M.J., Bonin, B., and Bateman, P. (Eds.), 2002. Igneous Rocks: A Classification and Glossary of Terms (Second edition): Cambridge, UK (Cambridge University Press). **https://doi.org/10.1017/CBO9780511535581**

Li, Z.-X.A., and Lee, C.-T.A., 2004. The constancy of upper mantle fO_2 through time inferred from V/Sc ratios in basalts. Earth and Planetary Science Letters, 228(3):483–493. **https://doi.org/10.1016/j.epsl.2004.10.006**

Mackensen, A., Schmiedl, G., Harloff, J., and Giese, M., 1995. Deep-sea foraminifera in the South Atlantic Ocean: ecology and assemblage generation. Micropaleontology, 41(4):342–358. **https://doi.org/10.2307/1485808**

Mallmann, G., and O'Neill, H.S.C., 2009. The Crystal/Melt Partitioning of V during Mantle Melting as a Function of Oxygen Fugacity Compared with some other Elements (Al, P, Ca, Sc, Ti, Cr, Fe, Ga, Y, Zr and Nb). Journal of Petrology, 50(9):1765–1794. **https://doi.org/10.1093/petrology/egp053**

Martini, E., 1971. Standard Tertiary and Quaternary calcareous nannoplankton zonation. Proceedings of the Second Planktonic Conference, Roma, 1970:739–785.

Marty, J.C., and Cazenave, A., 1989. Regional variations in subsidence rate of oceanic plates: a global analysis. Earth and Planetary Science Letters, 94(3):301–315. **https://doi.org/10.1016/0012-821X(89)90148-9**

Miyashiro, A., 1978. Nature of alkalic volcanic rock series. Contributions to Mineralogy and Petrology, 66(1):91–104. **https://doi.org/10.1007/BF00376089**

Morono, Y., Ito, M., Hoshino, T., Terada, T., Hori, T., Ikehara, M., D'Hondt, S., and Inagaki, F., 2020. Aerobic microbial life persists in oxic marine sediment as old as 101.5 million years. Nature Communications, 11(1):3626. **https://doi.org/10.1038/s41467-020-17330-1**

Mottl, M.J., 1989. Hydrothermal convection, reaction, and diffusion in sediments on the Costa Rica Rift flank: porewater evidence from ODP Sites 677 and 678. In Becker, K., Sakai, H., et al., Proceedings of the Ocean Drilling Program, Scientific Results. 111: College Station, TX (Ocean Drilling Program), 195–213. **https://doi.org/10.2973/odp.proc.sr.111.125.1989**

Olson, P., Reynolds, E., Hinnov, L., and Goswami, A., 2016. Variation of ocean sediment thickness with crustal age. Geochemistry, Geophysics, Geosystems, 17(4):1349–1369. **https://doi.org/10.1002/2015GC006143**

Olsson, R.K., Berggren, W.A., Hemleben, C., and Huber, B.T., 1999. Atlas of Paleocene Planktonic Foraminifera: Washington, DC (Smithsonian Institution Press). **https://doi.org/10.5479/si.00810266.85.1**

Owens, J.D., Lyons, T.W., and Lowery, C.M., 2018. Quantifying the missing sink for global organic carbon burial during a Cretaceous oceanic anoxic event. Earth and Planetary Science Letters, 499:83–94. **https://doi.org/10.1016/j.epsl.2018.07.021**

Parsons, B., and Sclater, J.G., 1977. An analysis of the variation of ocean floor bathymetry and heat flow with age. Journal of Geophysical Research (1896-1977), 82(5):803–827. **https://doi.org/10.1029/JB082i005p00803**

Pribnow, D.F.C., Kinoshita, M., and Stein, C.A., 2000. Thermal data collection and heat flow recalculations for ODP Legs 101-180: Hannover, Germany (Institute for Joint Geoscientific Research, GGA). **http://www-odp.tamu.edu/publications/heatflow/**

Reece, R., Christeson, G., Amara, A., Estep, J., Greene, J., Koch, C., Henning, L., Worman, W., and Wright, A., 2016. CREST: Crustal Reflectivity Experiment southern transect South Atlantic multichannel seismic and ocean bottom seismometer experiment, 4 Jan–25 Feb 2016 Cruise Report. **http://www.iris.washington.edu/data/reports/2016/16-003/CREST_2016-01-04-2016-02-25_MGL1601_CruiseReport.pdf**

Reece, R., and Estep, J., 2019. Processed MCS (PSTM) data from the Mid-Atlantic Ridge (MAR) to the Rio Grande Rise, South Atlantic Ocean, acquired by the R/V Marcus G. Langseth in 2016 (MGL1601) **https://doi.org/10.1594/IEDA/500255**

Richter, C., Acton, G., Endris, C., and Radsted, M., 2007. Handbook for shipboard paleomagnetists. Ocean Drilling Program Technical Note, 34. **https://doi.org/10.2973/odp.tn.34.2007**

Ríos, A.F., Resplandy, L., García-Ibáñez, M.I., Fajar, N.M., Velo, A., Padin, X.A., Wanninkhof, R., Steinfeldt, R., Rosón, G., and Pérez, F.F., 2015. Decadal acidification in the water masses of the Atlantic Ocean. Proceedings of the National Academy of Sciences, 112(32):9950–9955. **https://doi.org/10.1073/pnas.1504613112**

Schubert, C., and Calvert, S., 2001. Nitrogen and carbon isotopic composition of marine and terrestrial organic matter in Arctic Ocean sediments. Deep Sea Research, Part I: Oceanographic Research Papers, 48:789–810. **https://doi.org/10.1016/S0967-0637(00)00069-8**

Shipboard Scientific Party, 2004. Leg 208 summary. In Zachos, J.C., Kroon, D., Blum, P., et al., Proceedings of the Ocean Drilling Program, Initial Reports. 208: College Station, TX (Ocean Drilling Program). **https://doi.org/10.2973/odp.proc.ir.208.101.2004**

Spinelli, G.A., Giambalvo, E.R., and Fisher, A.T., 2004. Sediment permeability, distribution, and influence on fluxes in oceanic basement. In Davis, E.E., and Elderfield, H. (Eds.), Hydrogeology of the Oceanic Lithosphere. Cambridge, UK (Cambridge University Press), 151–188.

Straume, E.O., Gaina, C., Medvedev, S., Hochmuth, K., Gohl, K., Whittaker, J.M., Abdul Fattah, R., Doornenbal, J.C., and Hopper, J.R., 2019. GlobSed: updated total sediment thickness in the world's oceans. Geochemistry, Geophysics, Geosystems, 20(4):1756–1772. **https://doi.org/10.1029/2018GC008115**

Sun, S., and McDonough, W.F., 1989. Chemical and isotopic systematics of oceanic basalts: implications for mantle composition and processes. In Saunders, A.D., and Norry, M.J. (Eds.), Magmatism in the Ocean Basins. Geological Society Special Publication, 42: 313–345. **https://doi.org/10.1144/GSL.SP.1989.042.01.19**

The Shipboard Scientific Party, 1970. Summary and conclusions. In Maxwell, A.E., et al., Initial Reports of the Deep Sea Drilling Project. 3: Washington, DC (US Government Publishing Company), 441–471. **https://doi.org/10.2973/dsdp.proc.3.113.1970**

Tjalsma, R.C., and Lohmann, G.P., 1983. Paleocene-Eocene Bathyal and Abyssal Benthic Foraminifera from the Atlantic Ocean. Micropaleontology, Special Publication, 4.

Tominaga, M., Teagle, D.A.H., Alt, J.C., and Umino, S., 2009. Determination of the volcanostratigraphy of oceanic crust formed at superfast spreading ridge; electrofacies analyses of ODP/IODP Hole 1256D. Geochemistry, Geophysics, Geosystems, 10(1):Q01003. **https://doi.org/10.1029/2008GC002143**

Wade, B.S., Pearson, P.N., Berggren, W.A., and Pälike, H., 2011. Review and revision of Cenozoic tropical planktonic foraminiferal biostratigraphy and calibration to the geomagnetic polarity and astronomical time scale. Earth-Science Reviews, 104(1–3):111–142. **https://doi.org/10.1016/j.earscirev.2010.09.003**

Walton, A.W., and Schiffman, P., 2003. Alteration of hyaloclastites in the HSDP 2 Phase 1 Drill Core 1: description and paragenesis. Geochemistry, Geophysics, Geosystems, 4(5):8709. **https://doi.org/10.1029/2002GC000368**

Wells, J.T., and Ghiorso, M.S., 1991. Coupled fluid flow and reaction in mid-ocean ridge hydrothermal systems: the behavior of silica. Geochimica et Cosmochimica Acta, 55(9):2467–2481. **https://doi.org/10.1016/0016-7037(91)90366-D**

Wheat, C.G., and MeDuff, R.E., 1994. Hydrothermal flow through the Mariana Mounds: dissolution of amorphous silica and degradation of organic matter on a mid-ocean ridge flank. Geochimica et Cosmochimica Acta, 58(11):2461–2475. **https://doi.org/10.1016/0016-7037(94)90024-8**

Williams, T., Estes, E.R., Rhinehart, B., Coggon, R.M., Sylvan, J.B., Christeson, G.L., and Teagle, D.A.H., 2021. Expedition 395E Preliminary Report: Complete South Atlantic Transect Reentry Systems. International Ocean Discovery Program. **https://doi.org/10.14379/iodp.pr.395E.2021**

Zachos, J.C., Röhl, U., Schellenberg, S.A., Sluijs, A., Hodell, D.A., Kelly, D.C., Thomas, E., Nicolo, M., Raffi, I., Lourens, L.J., McCarren, H., and Kroon, D., 2005. Rapid acidification of the ocean during the Paleocene-Eocene Thermal Maximum. Science, 308(5728):1611–1615. **https://doi.org/10.1126/science.1109004**

Zijderveld, J.D.A., 1967. AC demagnetization of rocks: analysis of results. In Runcorn, S.K.C., Creer, K.M., and Collinson, D.W. (Eds.), Methods in Palaeomagnetism. Developments in Solid Earth Geophysics, 3: 254–286. **https://doi.org/10.1016/B978-1-4832-2894-5.50049-5**